# A VIBRO-ACOUSTIC CAE APPROACH FOR ACTIVE NOISE CONTROL PREDICTION

by

AHMAD A. ABBAS

A dissertation submitted in partial fulfillment of the
requirements for the degree of

DOCTOR OF PHILOSOPHY IN MECHANICAL ENGINEERING

2024

Oakland University
Rochester, Michigan

Doctoral Advisory Committee:

Zissimos P. Mourelatos, Ph.D., Chair
Michael Latcha, Ph.D.
Lianxiang Yang,, Ph.D.
Dorin Drignei, Ph.D.
Francisco Sturla, Ph.D.

*To the memory of my beloved father,*
*Abdulsattar Abbas Al-sawaedi (1951-1982)*

## ACKNOWLEDGMENTS

First, I would like to express my sincere gratitude to my advisor, Dr. Zissimos P. Mourelatos, for his dedication and guidance throughout my PhD studies. His wisdom and extensive knowledge, along with his continuous support of my PhD studies and research, provided a significant source of inspiration during my years at OU.

Also, I would like to thank all the members of my Ph.D. committee - Drs. Michael Latcha, Dorin Drignei, and Francisco Sturla - for their suggestions and feedback, as well as for the help they provided whenever needed.

In addition, I would like to thank my colleague and adjunct professor at Oakland University Wael Elwali Ph.D. and Dr. Syed Haider for their help and suggestions during this research.

Ahmad A. Abbas

ABSTRACT

A VIBRO-ACOUSTIC CAE APPROACH FOR ACTIVE NOISE CONTROL PREDICTION

by

AHMAD A. ABBAS

Adviser: Zissimos P. Mourelatos, Ph.D.

This research focuses on a comprehensive analysis and prediction of Active Noise Cancellation (ANC) system performance in vehicles, with particular emphasis on the structural and acoustic aspects. While acknowledging the significance of electronic components and control algorithms in ANC systems, this study focuses on predicting the ANC performance using a full vibro-acoustic vehicle model. Additionally, the integration of noise management supplier control systems with CAE ANC models is explored. The development of a predictive CAE methodology is demonstrated using a road noise cancellation example. The process involves several steps including the structural behavior of the Trim Body in White (TBIW) structure, the development of a vehicle cavity model, the derivation of accurate speaker models, the assessment of speaker integration with vehicle doors, and the development of Transfer Paths (TP) from speakers to microphones. A novel methodology is presented to quantify the door stiffness requirements for optimal speaker ANC performance, incorporating substructuring methods and physical testing. The accuracy of the developed CAE models is validated using physical testing of circular and oval-shaped speakers integrated into vehicle doors and the calculation of transfer paths between each door speaker and microphone locations

is demonstrated. The significance of microphone and speaker locations relative to driver or passenger ear positions highlights their influence on ANC performance. Finally, a controller is developed to test the CAE model and illustrate its functionality using a supplier's controller for sound management. Overall, this research establishes a reliable vibro-acoustic CAE ANC model capable of predicting ANC system performance accurately by integrating a full vehicle vibro-acoustic model with an ANC controller. Such a predictive capability enables optimization and enhancement of vehicle performance for noise cancellation, unlocking its full potential in mitigating vehicle noise.

TABLE OF CONTENTS

TABLE OF CONTENTS—Continued

LIST OF ABBREVIATIONS

| | |
|---|---|
| CAE | Computer Aided Engineering |
| FEM | Finite Element Method |
| FE | Finite Element |
| ANC | Active Noise Canceling |
| IR | Impulse Response |
| DOE | Design of Experiment |
| TBIW | Trimmed Body in White |
| IC | Internal Combustion |
| BEV | Battery Electric Vehicle |
| PHEV | Plug-in Hybrid Electric Vehicle |
| $t$ | Time |
| $p$ | Pressure |
| $P$ | Pressure Magnitude |
| $\bar{P}$ | Phasor of Pressure Magnitude |
| $\gamma$ | Ratio of the Specific Heat |
| $\rho$ | Density |
| $L_{cz}$ | Rectangular Cavity Length is X direction |
| $L_{cy}$ | Rectangular Cavity Length is Y direction |
| $L_{cz}$ | Rectangular Cavity Length is Z direction |
| $L_{py}$ | Moving Cone Dimension in Y direction |

| | |
|---|---|
| $L_{pz}$ | Moving Cone Dimension in Z direction |
| $p_0$ | Static Pressure |
| $R_g$ | Gas Constant |
| $T_g$ | Absolute Temperature |
| $u$ | Velocity |
| $\nabla$ | Gradient Operator |
| $\omega$ | Angular frequency |
| $k$ | Wave number |
| $\lambda$ | Wavelength |
| $\dot{q}$ | Mass Rate (Mass per Time) |
| $c$ | Speed of Wave |
| $\dot{Q}$ | Volumetric Acceleration |
| $\dot{Q}_0$ | Volumetric Acceleration Amplitude |
| $\delta$ | Dirac Delta Function |
| $x_s$ | Coordinate Location of Monopole Acoustic Source in X Direction |
| $y_s$ | Coordinate Location of Monopole Acoustic Source in Y Direction |
| $z_s$ | Coordinate Location of Monopole Acoustic Source in Z Direction |
| $x_{d1}$ | Coordinate Location of Dipole’s First Monopole in X Direction |
| $y_{d1}$ | Coordinate Location of Dipole’s First Monopole in Y Direction |
| $z_{d1}$ | Coordinate Location of Dipole’s First Monopole in Z Direction |

| | |
|---|---|
| $x_{d1}$ | Coordinate Location of Dipole's First Monopole in X Direction |
| $y_{d1}$ | Coordinate Location of Dipole's First Monopole in Y Direction |
| $z_{d1}$ | Coordinate Location of Dipole's First Monopole in Z Direction |
| $N$ | Mode Shape Number |
| $A_N$ | Mode Participation |
| $\bar{A}_N$ | Phasor of $A_N$ |
| $\psi_N$ | Mode Shape |
| $r$ | Radial distance spherical coordinate system |
| $\theta$ | Polar angle spherical coordinate system |
| $\varphi$ | Azimuthal angle spherical coordinate system |
| $a$ | Monopole Radius |
| $u_s$ | Radial Surface Velocity |
| $U$ | Phasor of the volume velocity |
| $Q$ | Acoustic Volumetric Velocity |
| $Q_0$ | Acoustic Volumetric Velocity Amplitude |
| $U_0$ | Acoustic Surface Velocity Amplitude |
| $W$ | Acoustic Power |
| $f$ | Frequency |
| $d$ | Dipole – Pole distance |
| $h$ | Step Faction |

| | |
|---|---|
| $v_x$ | Moving Cone Velocity in X Direction |
| $V_x$ | Magnitude of the Harmonic Velocity in X Direction |
| $\alpha_d$ | Damping Coefficient |
| $S$ | Surface of the moving cone (piston) |
| $\alpha_d$ | Damping Coefficient |
| $R(f, \beta)$ | Directivity |
| $\beta$ | Polar Angle Spherical Coordinate System from Center of Moving Cone |
| $\tau$ | Azimuthal Angle Spherical Coordinate System on Plane of Moving Cone |
| $P_0$ | The Observation Point from Moving Cone |
| $P_o'$ | Project Observation Point on Moving Cone |
| $h_c$ | Distance from $P_o$ to dS |
| $r_c$ | Distance from $P_o$ to Center of Moving Cone |
| $\alpha_c$ | Radius of Moving Cone |
| $H_1$ | First Struve Function |
| $J_n(z)$ | $n^{th}$ Bessel Function |
| $\xi$ | Speaker sensitivity |
| $P_{AU}$ | Acoustic Power |
| $P_{EE}$ | Electrical Power |
| $\eta$ | Speaker Efficiency |
| M | Total mass of speaker |

| | |
|---|---|
| $X_{max}$ | Maximum Linear Travel of Speaker Cone |
| Fs | Speaker Resonant Frequency Far Field |
| CMS | Mechanical Compliance |
| MR | Mechanical Resistance |
| $R_{imp}$ | Speaker Impedance |
| $V_{max}$ | Max planed voltage for ANC system |
| $A_{speaker}$ | Surface Area of the Speaker Diaphragm |
| $F(t)$ | Force Function |
| x(t) | Displacement Function |
| $\bar{F}$ | Phasor of Force Function |
| $F_{MC}$ | Force Function on Diaphragm with Moving Cone Assumption |
| $\overline{F_{MC}}$ | Phasor Force Function on Diaphragm with Moving Cone Assumption |
| $\bar{X}$ | Phasor of Displacement Function |
| H | Substructure |
| $H_D$ | FRF of the door |
| $\bar{X}_1$ | Phasor of displacement speaker diaphragm |
| $\bar{X}_2$ | Phasor of displacement at the interface between the door and $m_d$ |
| $\bar{F}_D$ | Phasor of the force on the door at the interface |
| $u^*(t)$ | Distorted Speaker Diaphragm Velocity |
| $\overline{u^*}(t)$ | Distorted Speaker Diaphragm Velocity Phasor |

| | |
|---|---|
| $P_{EE}$ | Electric Power in Watts |
| [C] | Damping Matrix |
| [M] | Mass Matrix |
| [K] | Stiffness Matrix |
| SPIS | Speaker Power Input |
| PL | The power limit |
| SPRN | Sound Pressure from Road Noise |
| RSP | Resulting Sound Pressure |

LIST OF TABLES

TABLE OF FIGURES

TABLE OF FIGURES – Continued

TABLE OF FIGURES – Continued

# CHAPTER ONE

# INTRODUCTION

The significance of Noise, Vibration, and Harshness (NVH) concerns in modern vehicle development cannot be overstated. Numerous manufacturers are prioritizing quieter vehicles, recognizing the direct correlation between sound quality and the customer's perceived quality. Consequently, substantial time and resources are being invested by vehicle manufacturers to enhance the comfort and tranquility of the vehicle cabin. Vehicle cabin noise originates from various sources, including powertrain, road, wind, cooling system, pumps, and other systems. Powertrain and road noise pose the greatest challenges in terms of control. As much of this noise is transmitted through a structure-borne transfer path, it predominantly falls within the low-frequency range and comes in a wide range of low frequencies.

Traditionally, passive control methods have been employed to mitigate noise. While effective at middle and high frequencies, they often struggle to address low-frequency noise adequately. Passive control solutions are typically made of heavy materials, leading to increased vehicle weight. Recently, there has been a growing demand for lightweighting vehicles, particularly for Battery Electric Vehicles (BEV). BEV vehicles tend to feature stiffer tires compared to Internal Combustion Engine (ICE) vehicles, which can exacerbate low-frequency noise transmission to the cabin if combined with lighter vehicle structures. In such cases, Active Noise Control (ANC) methods show promise as evidenced by many applications in the market by noise management suppliers such as Harman [1] and Bose [2] . ANC is particularly effective at mitigating low-frequency noise, offering a viable solution to the evolving challenges in vehicle NVH management.

The current vehicle development process in automotive manufacturers extensively relies on virtual analysis. With the decreasing duration of the vehicle development cycle, Computer-Aided Engineering (CAE) has gained increased significance [3]. Consequently, vehicle development teams prioritize early access to information during the product development phase. This early insight facilitates prompt product adjustments to attain the desired performance standards. Anticipating potential issues and performance outcomes at an early stage offers cost and time benefits, ensuring a smooth vehicle launch process. For example, the vibrations and sound from a vehicle cooling module operating at different fan speeds can be accurately predicted using a specific CAE methodology [4].

In recent times, ANC technology has been integrated into diverse vehicle segments, expanding beyond its previous confinement to luxury vehicles [5]. ANC employs the sound emitted by speakers to counteract unwanted noise within the vehicle. Rooted in acoustics and noise principles, this technology utilizes microphones. The signals captured by these microphones undergo analysis, leading to the generation of canceling noise using the vehicle's speakers, as shown in

Figure 1.1. In reality, the vehicle noise is very complex described by a spectrum of varying amplitudes across the frequency range. Consequently, to generate anti-noise to counter each waveform effectively, the ANC system requires an individual filtration of each spectrum, with delineation of its frequency range, generation of out-of-phase

frequency noise signals with suitable amplitudes, and a subsequent integration with the original signal to reduce cabin noise levels [6].

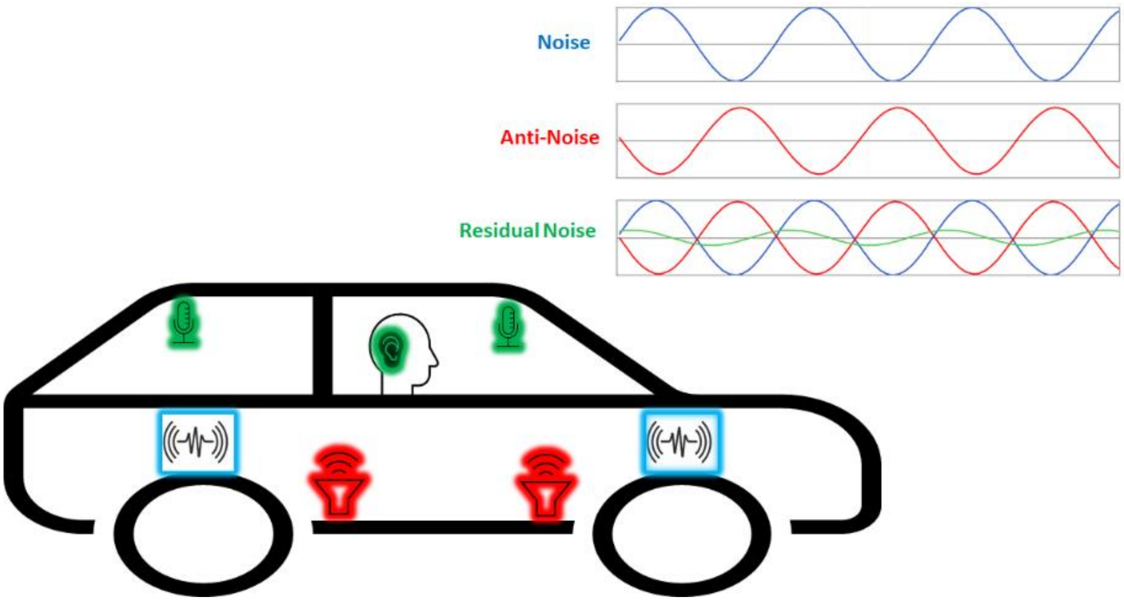


*Figure 1.1* Schematic of a ANC system

Given the multitude of frequencies within a vehicle noise signal, complete cancellation of all frequencies becomes unfeasible. Instead, the ANC system selectively targets a narrow band of frequencies and produces an average cancellation. This approach notably aids in mitigating vehicle noise. However, it does not cancel the entire noise signal. Figure 1.2 shows an example of active noise cancellation for vehicle powertrain noise at idle. The absence of active noise cancellation during idle noise is indicated by the black line, denoting the noise level detected at the driver microphone location. If the ANC system is activated, the noise recorded at the microphone location is shown by the red line. The figure demonstrates that noise cancellation is not consistently uniform across the engine's RPM spectrum. Specifically, at 700 and 1000 RPM, the cancellation effect is minimal, while in the range of 800 to 950 RPM the ANC system demonstrates over 15 dB of noise cancellation.

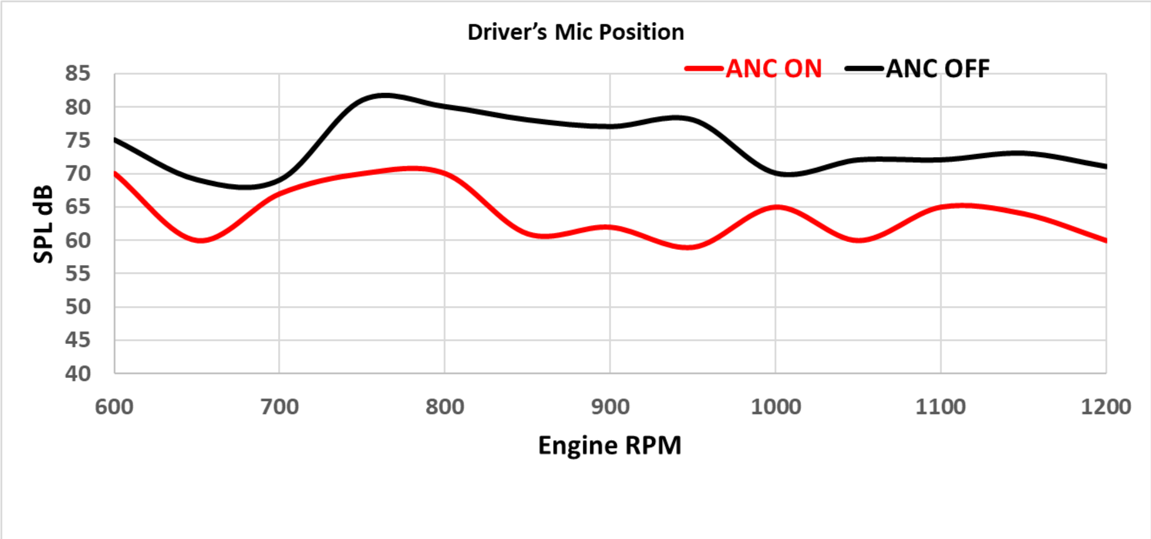


*Figure 1.2* A noise canceling example

Several vehicle structural and acoustic features yield a significant influence on the effectiveness of ANC. These characteristics can constrain the ANC system's ability to effectively reduce noise across specific frequency bands or within distinct areas inside the vehicle cabin. As of now, the ANC system development occurs relatively late in the vehicle development timeline, relying extensively on hardware availability and intricate calibration processes. The vehicle ANC development usually starts with prototype vehicles that can be challenging for NVH performance evaluation due to sealing and content maturity. Thus, audio engineers typically work on tuning ANC systems after the first preproduction vehicles are available. This development approach limits any pre-hardware design. The number and location of microphones, speakers, amplifier requirements, and other ANC system requirements cannot be predetermined.

Additionally, ANC performance cannot be predicted, limiting engineering teams to rely on ANC noise reduction for cost and weight optimization, as most vehicle NVH attributes are designed and evaluated using numerical methods prior to hardware availability.

The currently available CAE methods for ANC are insufficient, providing limited pathways to obtain optimal designs for ANC performance. Moreover, further constraints emerge from the vehicle development schedule, where critical aspects of the vehicle's structure such as door configurations, door carrier modules, and speaker placements are finalized during ANC system development. Consequently, any attempts to enhance ANC performance through alterations become both economically burdensome and arduous.

# CHAPTER TWO

# PROBLEM DESCRIPTION AND RESEARCH SCOPE

The ANC system includes many components which are purely electronic parts and the quality of their hardware and software is a limiting factor for the ANC system performance. Some of these limitations are related to system cancelation strategy algorithms, memory, delay, and software among other factors [7]. Other components are electromechanical, and their performance directly influences the ANC system capacity. In this research, the focus is not in the electronic or control system algorithm domain, but on the virtual prediction of ANC performance using a full vibro-acoustic vehicle model. Moreover, understanding the structural and acoustics design of vehicle would allow for an improved vibro-acoustic design of an ANC system. We will also show that the noise management supplier control system can be coupled with a CAE ANC model.

Figure 2.1 is used as an example to describe the development process of an ANC predictive CAE methodology. The example shows the setup for a simple road noise cancelation problem.

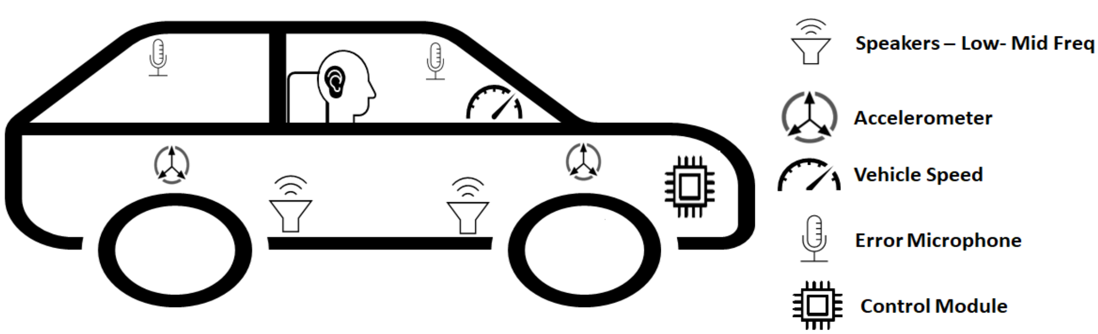


*Figure 2.1* Simplified road noise cancelation setup

In this road noise example, the accelerometers detect the vibration from the road input and the controller analyzes the signal. Then, based on specific predefined functions in the ANC algorithm the amplifier sends anti-noise signal to speakers. The algorithm can also be based on other inputs such as vehicle speed. Subsequently, a perceived anti-noise by the driver and error mic is generated and the error mic sends a feedback to the controller to adjust the anti-noise signal to speakers. The simplified process schematic is shown in Figure 2.2.

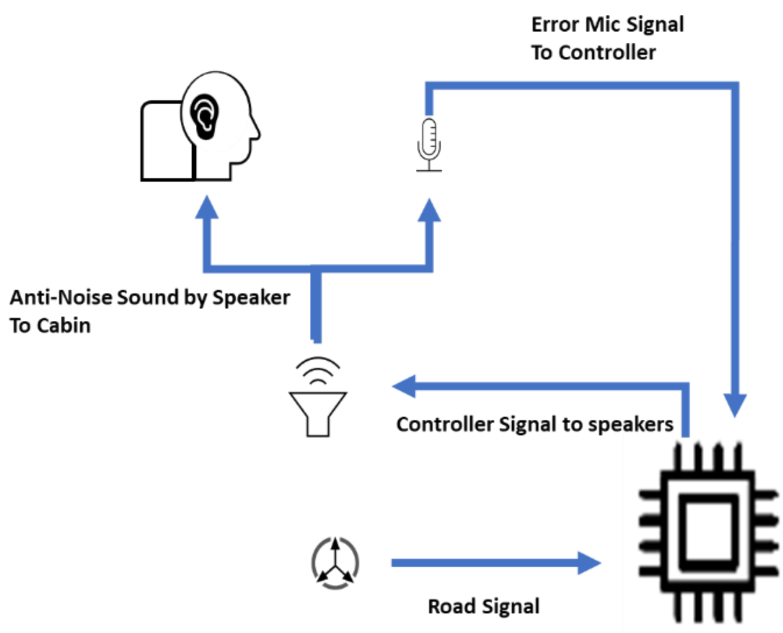


*Figure 2.2* Simplified road noise cancelation schematics

Based on this simple setup it’s clear that we need to develop a CAE modeling process that captures the multi-physics nature of this problem described by the following six steps.

<u>First step:</u> The structural part of the vehicle must be studied. This vehicle part is usually called Trim Body in White (TBIW). It includes the body structure and the trims

as shown in Figure 2.3. A TBIW FE (Finite Element) vibration model must be created and verified for correctness and the TBIW modes must be identified and correlated.

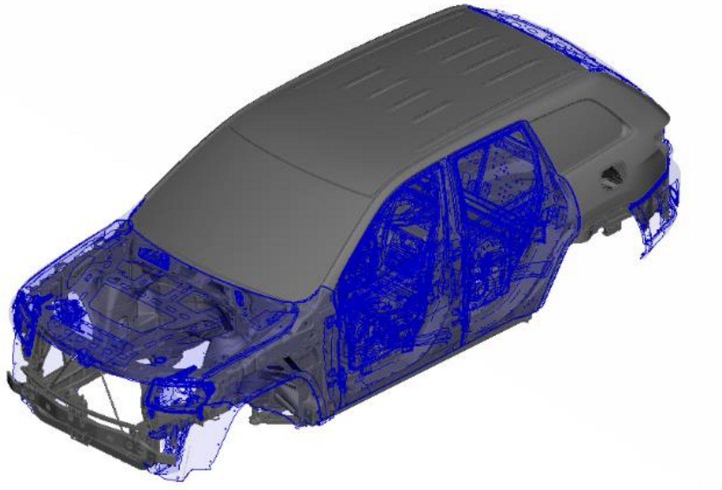

*Figure 2.3* Vehicle TBIW FE model – body structure (gray), trims (blue)

<u>Second step:</u> Development and verification of a vehicle cavity. Since the speakers, microphones and structure are coupled with the cavity it is very important to have an accurate vehicle cavity model that can capture the acoustic modes and transfer paths as shown in Figure 2.4. In this research, a detailed mathematical modeling of such a cavity is demonstrated.

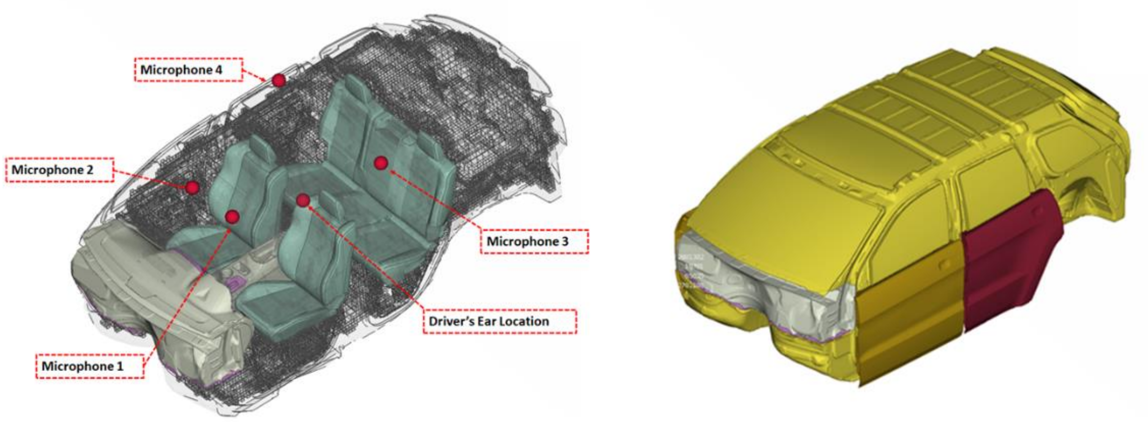


*Figure 2.4* Vehicle cavity with relative error mic locations

Third step: Development of a speaker model capable to accurately predict the acoustics of the vehicle cabin. This model translates specific electrical signals into corresponding acoustic outputs. Consequently, it is imperative to establish a CAE methodology capable of precisely generating Impulse Responses (IR) from the speakers to microphone locations. These IRs are also known as Transfer Paths (TP). During the development of ANC systems, these TPs are acquired through physical tests, necessitating the utilization of full vehicle hardware. Among the various electromechanical components of the ANC system, speakers play a paramount role, as they produce the sound required to mitigate unwanted noise in the vehicle cabin. Assessing the performance of speakers within a vehicle mandates the implementation of a CAE methodology for speaker modeling, thus constituting one of the primary objectives of this research. We have developed various speaker modeling techniques in order to establish the most accurate one which was verified experimentally.

Fourth step: Demonstration that the stiffness of the speaker attachment plays an important role in sound signal alteration. Typically, speakers are placed in vehicle doors and are supported by door carrier modules, as shown in

Figure 2.5. The door carrier module has a specific stiffness and vibration response to acoustic loading generated by the speaker. This response can interfere with the speaker output. Additionally, the door cavity can influence the speaker output since it exhibits acoustic modes and interact with various panels and door components. Thus, a specific speaker modeling methodology is required to understand the effect of speaker integration with the door and vehicle. In this step, we established a novel methodology to quantify the door stiffness requirement for optimal speaker ANC performance using a

substructuring method. The speaker-door interaction CAE modeling was verified by physical testing with circular and oval-shaped speakers. As an example, Figure 2.6 shows two doors with different speakers.

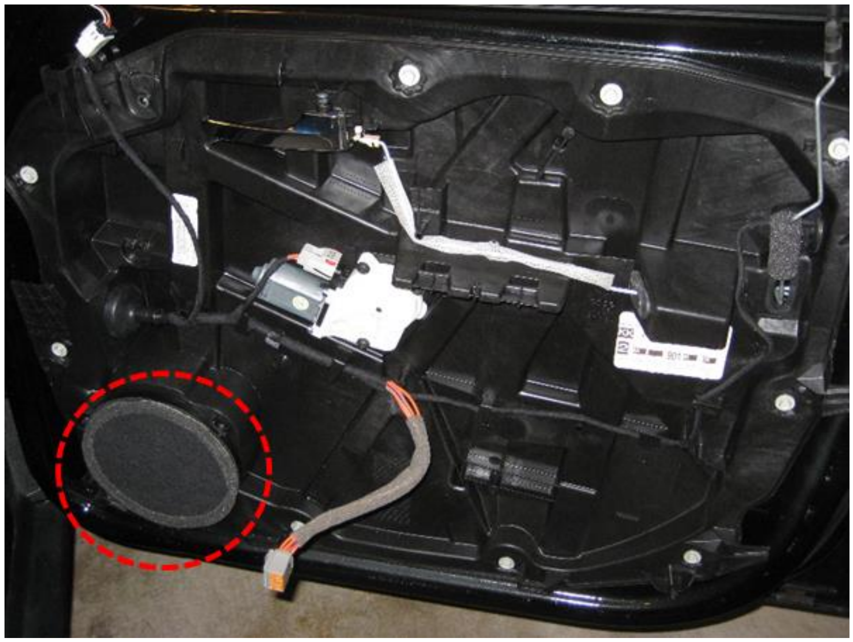

*Figure 2.5* Typical door speaker system

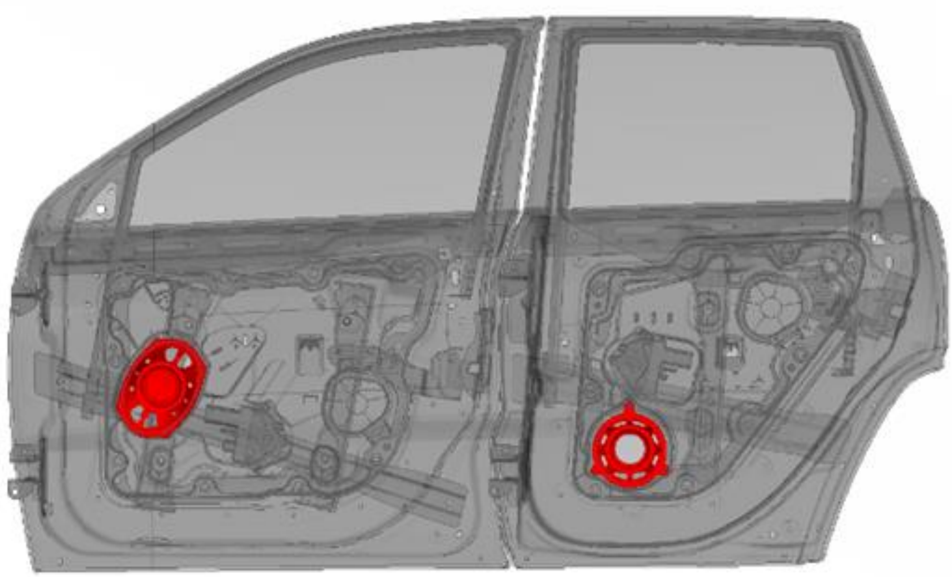

*Figure 2.6* Vehicle with oval and circular speakers

Fifth step: Representation of the TP from speaker to microphone locations. Using the developed TBIW, cavity, and speaker models, we demonstrated how the TP can be developed for each speaker to all microphones in the vehicle. The microphone locations used in this research are shown in Figure 2.7. From the FE model, the TP between each door speaker and microphone was calculated, and the results were verified experimentally. Because the ANC system cannot cancel noise that it cannot detect, the microphones and accelerometer locations relative to the driver's or passenger's ear location are very important. The ANC system relies on speakers to cancel undesirable noise. Thus, the location of the speakers is fundamentally important for ANC performance as well.

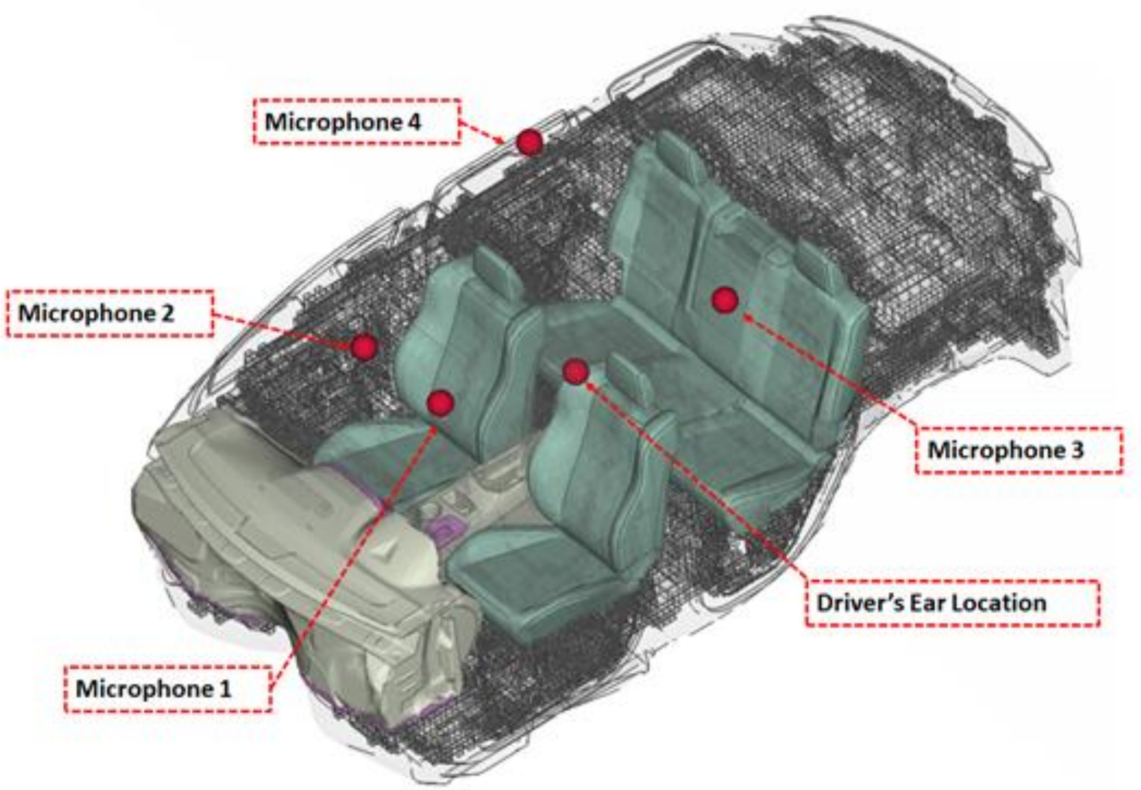


*Figure 2.7* Example vehicle microphone locations

Sixth step: Development of a basic controller to test the CAE model before sharing the model results with a sound management supplier. The objective of developing a simple controller is to understand the factors influencing the controller using the CAE model. The basic controller is also used to illustrate the CAE model for sound management suppliers.

In summary, the scope of this research is to develop a methodology to create a reliable vibro-acoustic CAE ANC model that can predict the ANC performance. When the vibro-acoustic performance of the ANC system is correctly predicted, changes can be introduced to optimize the ANC performance and achieve a more effective system.

# CHAPTER THREE

# LITERATURE REVIEW

The earliest experiments on superimposing sound fields were conducted around 1878 by Lord Rayleigh, who observed interference patterns using synchronized tuning forks [8]. While these experiments demonstrated the interference of coherent sound fields, patent applications by Coanda and Lueg in the late 19th century aimed at noise reduction, with Lueg's proposal being particularly realistic. Lueg's writings are considered the first documents of active sound control [9].

Although Lueg suggested using electroacoustic components, laboratory experiments were not documented until Olson's work in 1953, where he also envisioned potential applications [10]. However, a technical implementation was hindered by limitations in electronic equipment and the nonlinear response of human ears to sound pressure as shown in Olson’s patent [11].

Achieving significant noise reduction requires precise amplitude and phase control across all frequencies, a challenge exacerbated by the logarithmic relationship between sound pressure and perceived loudness. Overcoming these obstacles took time, with the advent of digital adaptive filters in recent years proving to be a breakthrough for coherent-active compensation systems, also known as anti-sound [12].

Guicking [13] provides an overview of the coherent active control of noise and vibration, tracing its development over time. His approach involves either canceling or enhancing sound and vibration by adding anti-phase or in-phase signals from external sources. Critics historically questioned the efficacy of canceling sound fields, arguing that adding secondary sound sources would only augment the primary field energy rather than nullify it, as proposed by the active noise control theory. However, Guicking demonstrated that with proper placement and driving of secondary sources, the primary energy can be indeed absorbed. In some cases, sources interact to influence radiation impedance, reducing sound production.

ANC has been commonly employed in ICE cars to mitigate the unwanted noise generated by the engine. Utilizing microphones strategically placed within the vehicle's cabin, ANC systems detect the specific frequencies of the engine noise. Subsequently, these frequencies are analyzed and categorized into different orders, representing the harmonics produced by the engine. ANC systems then generate sound waves of opposite phase through speakers positioned throughout the cabin, targeting each order of engine noise individually. By producing these anti-noise waves, ANC effectively cancels out the unwanted engine noise across multiple orders, resulting in a quieter and more comfortable driving experience for the passengers. This technology not only enhances the overall quality of the ride but also contributes to reducing driver fatigue and improving the vehicle's acoustic environment. S. Kuo and D.R. Morgan provide an overview of such applications [14].

Recently, Road Noise Cancelation (RNC) technology is gaining traction in vehicle development [2]. Road noise, typically impact the comfort and tranquility of the driving experience. Road noise canceling systems utilize accelerometers strategically placed inside the vehicle to detect and analyze the specific frequencies of road forces resulting in road noise. Using error microphones and advanced algorithms sound waves are then generated with opposite phases through speakers positioned throughout the cabin, effectively canceling out the unwanted noise. This technology is particularly crucial for Battery Electric Vehicles (BEVs), where the absence of an internal combustion engine accentuates other sources of noise, including road and wind noise. By minimizing these disturbances, road noise canceling enhances the overall driving experience in BEVs, ensuring a quieter and more refined ride for passengers. Recently, the practical implementation of RNC technology was discussed by F. Valeri and C. Stirlen [2].

The main purpose of this research is to develop a vehicle vibro-acoustic FE model with all input and output channels coupled with the audio management supplier's control system to enable the prediction of ANC system performance. J. Bean [15] has developed a modeling method for headset noise canceling using control engineering by applying a limited FE methodology to evaluate the ANC performance. Since the near field in the headset problem is important, both plane wave and diffuse fields were considered. Even though this work is very interesting, it is not directly applicable in solving our research problem. J. Lefèvre and U. Gabbert [16] have shown the theoretical background of a general finite element simulation tool for the design of actively controlled thin structures to reduce the noise radiating and presented a basic FE implementation and vibro-acoustic coupling providing a beneficial insight in understanding the needed formulation to solve our research problem.

V. Auweraer et al [17] have developed an extensive optimization tool for FE-based design of ANC systems. Their approach revolves around reducing the structural model to an equivalent low-order state-space model using mathematical reduction techniques and curve fitting. In their methodology, the reduced FE model is utilized for vibro-acoustics, with the addition of actuators, sensors, and control 1-D simulation elements as supplementary optimization parameters. Additionally, they incorporated operational data analysis, transfer path analysis (TPA), and panel contribution analysis (PCA) approaches into their solution. This integrated approach allows for the selection and optimization of the actual location and number of actuators and sensors by employing simplified or idealized actuation and control models using "secondary sources" in the structural and vibro-acoustical simulation models. However, this approach employs a reduced system model for the complete vibro-acoustic mesh, resulting in loss of information. Furthermore, the use of rigid boundaries for the acoustic cavity may lead to additional loss of information, as fluid-structure interaction (FSI) significantly influences the ANC system performance.

As of present, there has been no proposed methodology for the virtual evaluation of the ANC system by integrating a comprehensive Finite Element (FE) vibroacoustic model with an audio management control system. Upon reviewing the current literature, a detailed, systematic, and clear method has yet to be proposed for the comprehensive examination of the structural, acoustical, and vibro-acoustic aspects of vehicles for ANC. Researchers have not presented an effective method for analyzing complex cavities and addressing high modal density in the higher frequency range. Additionally, the methods provided do not encompass an integrated FE modeling technique and analysis method capable of predicting the ANC performance of vehicles for different noise sources or combined sources of noise to evaluate real-world conditions.

The modeling method proposed in this research is not focused on the electronics of ANC system, the power management, ANC filters or specific noise cancelling algorithms. These topics have been extensively researched and are well understood [18-22]. Furthermore, it is understood that even though the design of an ANC system is usually aiming for maximum attenuation of vehicle cabin noise, in certain cases some limitations are considered. For example, in an electric battery vehicle (BEV), it is desirable to have a residual error so the driver can have some audible information about the Electric Drive Motor (EDM) speed.

An Active Noise Control (ANC) system encompasses various components, including input and output channels such as microphones, accelerometers, speakers, subwoofers, amplifiers, and controllers. Creating an accurate representation of these physical components in a CAE model requires the utilization of detailed Finite Element (FE) modeling techniques. Assuming an accurate FE model and loading, acceleration, and acoustic responses are readily available, the modeling of microphones and accelerometers may not be necessary. However, achieving precise modeling of speakers poses a significant challenge.

One of the most critical components of an ANC system is the speaker. The transfer path between the speaker and the microphones, along with the positions of the driver and passengers, represents essential data used by sound management suppliers. Many researchers have utilized Finite Element (FE) methods to construct speaker models, facilitating the assessment of speaker performance based on the physical characteristics of its components.

A loudspeaker (speaker) is an electroacoustic transducer that converts a specific electrical signal into audible sound. First order electro-dynamic behavior of a speaker can be described using a classical Thiele and Small 1D model [23, 24]. The analysis of ANC systems requires a detailed Finite Element (FE) model of the speaker that accurately predicts the acoustic output for the input electrical signal. Many speaker models have been introduced [25-34]. Most of these models have been developed in commercial acoustics analysis tools, focusing on the acoustic output of the speaker, and researchers have linked acoustic analysis solutions with structural vibratory analysis by coupling commercial acoustics and structural analysis codes such as Actran, Abaqus, Cosmol, and Nastran [35-40].

Y. Hu [41] has provided insights into modeling various components of the speaker, focusing on the cone, the cone edge, and the behavior of air around the voice coil. However, his FE model is valuable for the design of the speaker but not substantial enough to be integrated into a full TBIW model. Y. Shiozawa et al [42] have demonstrated hybrid testing, FE, and Boundary Element (BE) methodology to model the loudspeaker by incorporating the experimental modal information of the speaker membrane. Their coupled electro-vibro-acoustic model of a loudspeaker considers the complexity of the speaker's electric circuit and integrates it into the model. Since their aim was to capture the performance of the speaker at higher frequencies, they included experimentally obtained speaker diaphragm mode shapes into the model. Their modeling strategy provides insights into the functional behavior of the speaker with electromotive force (EMF) and back EMF, and the influence of the baffled speaker with vibro-acoustic coupling is also shown. The experimental verification of the model shows good prediction trends, and in many frequency bands the numerical results correlate with testing results. However, in the low ANC frequency operating range (20 to 300 Hz), there are discrepancies of about 5 dB or higher that must be understood.

The solution for speaker modeling provided by researchers requires detailed modeling of speaker components, such as the exact geometry of the speaker diaphragm, surround speaker suspension, speaker spider suspension data, speaker moving mass, moving air mass, as well as the speaker magnet and coil data [43-45]. These detailed models can accurately predict the acoustic output of the speaker but require considerable effort to construct. Some researchers have worked on predicting high-frequency noise of loudspeakers by examining the nonrigid modes of the loudspeaker diaphragm [46-49].

When OEMs acquire speakers from audio suppliers, they usually get very limited data for the speakers. Many design parameters and the exact geometry of the speaker are their intellectual property and are therefore very reluctant to share. For this reason, one of the main objectives of our speaker model development for ANC analysis is the ability to model the speaker with limited data that are readily available. To achieve this constraining objective a ground up approach for speaker modeling was considered. Starting with the most basic acoustic source of a monopole, a closed form solution for free field and closed cavity was obtained. Despite existing studies on the theoretical and experimental correlation of a monopole source [50, 51], a detailed relationship between finite element modeling parameters and theoretical solutions has not been well established.

Furthermore, researchers have shown that the dipole acoustic source represents the most fundamental speaker model capable of providing information regarding sound directivity [50, 51]. Although a strong agreement between theoretical and experimental results is shown, similar to the monopole acoustic source, the influence of finite element modeling parameters remains unclear. Researchers have also explored modeling the speaker as a moving piston [53]. While a closed-form solution for the baffled speaker model with a moving cone was provided by F. Jacobsen et al [54], the closed-form solution for the unbaffled case was not clearly defined. For both the baffled and unbaffled cases, finite element modeling parameters were not well-defined for free field and closed cavity scenarios. Additionally, researchers investigated the propagation of low-frequency near-field sound from speakers [55], although finite element modeling details for the moving cone model are unclear. Hence, the necessity for a speaker modeling methodology for ANC FE applications is evident.

Following the development of a comprehensive vibro-acoustic finite element (FE) speaker model, it was crucial to consider the impact of the speaker mounting location on speaker's performance. The door carrier module exhibits a distinct vibration response to acoustic loading generated by the loudspeaker. This response has the potential to interfere with loudspeaker output, resulting in an alteration of sound known as "distortion." Moreover, the loudspeaker may induce buzz, squeak, and rattle issues in the door. Researchers have examined the structural vibration of doors and carrier modules in lightweight structures, demonstrating that door stiffness can significantly contribute to speaker sound distortion [56].

Researchers have extensively investigated Buzz, Squeak, and Rattle (BSR) occurrences in doors resulting from audio input [57-63]. They explored the complexities involved in detecting and mitigating squeak and rattle issues caused by structural vibrations transmitted through speakers in passenger vehicles. Elevated expectations for enhanced perceived quality have necessitated stringent standards for minimal interior noise and superior speaker sound quality within vehicles. They advocated for the application of finite element methods to accurately simulate speaker-induced structural vibrations, extending the analysis to predict potential issues in door systems where speakers are mounted. Additionally, they pinpointed the root causes of buzz, squeak, and rattle issues and devised effective countermeasures to enhance audio quality by reinforcing the door structure. Validation of these methods was conducted through correlation with observed issues in physical tests, with audio tests confirming the efficacy of the implemented countermeasures. Their findings underscored that reinforcing the door inner panel near the speaker mounting significantly reduces speaker-induced buzz, squeak, and rattle noise. Emphasizing the significance of addressing speaker-induced structural vibrations to achieve desired audio quality benchmarks in passenger vehicles, they employed straightforward load assumptions, simplified speaker models, and experimental data to assess BSR. Utilizing experimental measurements and numerical analysis, they evaluated rattle and squeak in vehicle door trim under varying audio system inputs. BSR was quantified using a microphone and a vibration sensor attached to the door trim, employing a sweep sine signal across frequencies ranging from 20 Hz to 100 Hz. Results indicated a strong dependence of BSR on the frequency and sound pressure level (SPL) of the input signal, with peaks observed at lower frequencies. Detailed modal analysis of the door trim identified resonant frequencies closely aligning with those producing the highest BSR, offering insights into potential mitigation strategies. Many analysis tools for such BSR problems were developed, with the E-Line being one of most used BSR methods, first introduced by J. Weber and I. Benhayoun [64].

Moreover, researchers have investigated the impact of door structure on audio quality [65]. They have examined the challenges associated with achieving optimal audio quality in car audio systems, with a specific focus on the response of the car door to audio load. Their findings revealed that while the door functions as a cabinet, influencing the loudspeaker response, it also emits undesirable sound through the inner door panel. Employing FE modeling as a tool to address the acoustic response of the loudspeaker and the door, they proposed a hybrid modeling approach. This approach integrates a classical Thiele and Small 1D model for the loudspeaker with a 3D finite element model for the door. Furthermore, they validated the effectiveness of this approach using experimental frequency response functions, demonstrating strong agreement between measured and computed responses. They have claimed that the proposed model could also predict instances of squeak and rattle resulting from audio system operation. However, their proposed methodology necessitates highly detailed information about the loudspeaker. Also, the integration of the 1D speaker model into the 3D vibro-acoustic FE model remains a challenge [66-67].

Other researchers have employed detailed loudspeaker, door, and vehicle Finite Element (FE) models to assess sound quality parameters such as clarity and loudness [68]. They have provided an overview of various sound-field simulation tools suitable for modeling acoustic and vibro-acoustic phenomena occurring when loudspeakers interact with passenger compartments and door cavities. The study incorporates vibro-acoustic effects, including speaker membrane vibrations coupled with door cavity acoustic pressures and vibrations on the door trim, utilizing coupled structural and acoustic FE methods and Boundary Element formulations. Additionally, they utilized beam-tracing algorithms to synthesize binaural impulse responses and derive interaural cross-correlation coefficient (IACC) maps for modeling high-frequency sound fields. The performance of a vehicle audio system at low frequencies is closely linked to cabin modes, emphasizing the importance of positioning woofer loudspeakers to couple with these modes. The researchers demonstrated that door vibrations significantly impact sound quality at frequencies below 500 Hz. Furthermore, they highlighted the significance of door acoustics and the challenges associated with mounting loudspeakers in inner door panels. Beyond 500 Hz, the sound field within vehicle interiors is primarily influenced by intricate interference effects between direct and reflected waves from surfaces such as glass windows, dashboards, carpet floors, and rooflines. These reflections contribute to sound coloration and influence the subjective perception of sound image and sound stage. In conclusion, they asserted that sound-field simulation software can expedite development processes and enhance in-vehicle audio sound quality by predicting acoustic and vibro-acoustic parameters of small rooms, cabin modes, and door acoustics. Numerous efforts were done to reduce the vehicle door weight, as highlighted in [69] investigating the impacts of different materials and manufacturing processes on door module carrier stiffness. The findings reveal that the utilization of advanced materials like carbon fiber or composites, alongside advanced manufacturing techniques such as injection molding, can notably enhance stiffness while simultaneously reducing weight.

Researchers further explored the door's crashworthiness, examining how door module carrier stiffness influences vehicle crash safety [70]. Their investigation concluded that a stiffer door module carrier can effectively distribute impact forces more evenly during a crash, thereby mitigating the risk of passenger injury. Overall, this study shows that enhancing the stiffness of the vehicle door module carrier can enhance vehicle safety performance. However, determining the optimal stiffness level may depend on various factors including vehicle design, materials, and manufacturing processes. Additionally, researchers observed that augmenting the door module carrier stiffness can enhance the vehicle overall structural rigidity, thereby diminishing noise, vibration, and harshness levels. Consequently, this improvement can contribute to a more comfortable driving experience for passengers.

In summary, the existing literature does not provide a comprehensive overview or methodology to comprehend the diverse distortions that could impact the door speaker and vehicle system. Furthermore, there is no proposed methodology for evaluating the stiffness requirements for door speaker attachment points at the component level for optimal active noise cancelation system performance.

CHAPTER FOUR

# DEVELOPMENT AND VERIFICATION OF CAE TBIW MODEL

## 4.1 Review of the Full TBIW Vehicle FE Model

To showcase the capability of predicting active noise cancellation within a comprehensive vehicle framework, we employ a complete vehicle example. A vehicle NASTRAN FE model represents a full-size unibody Sport Utility Vehicle (SUV), including all TBIW vehicle components. This presentation outlines the TBIW model verification process for accuracy, and highlights some of the correlation studies between physical testing and FE modeling.

The accuracy of the TBIW model for vibro-acoustic analysis has been evaluated. Figure 4.1 shows the structural finite element model with approximately 11 million degrees of freedom (DOFs). The model has a relatively large number of DOFs. Many components such as IP, IP trims, steering, seats, carpet, and other trim are included yielding a relatively large model.

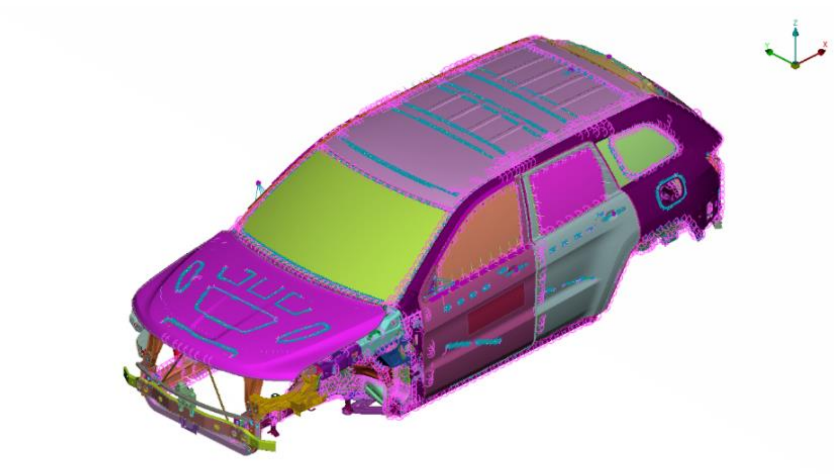

*Figure 4.1* TBIW FE model

### 4.1.1 Element Types for Structural Model

Table 4.1 lists all structural element types used in constructing the TBIW model, and the number of each element type. The elements utilized in constructing this TBIW FE NASTRAN model are common in the automotive industry.

Table 4.1

*TBIW Element Types*

| Element Type | Number of Elements |
|---|---|
| CBAR | 202 |
| CBEAM | 1183 |
| CBUSH | 7 |
| CELAS1 | 2620 |
| CELAS2 | 29 |
| CONM2 | 1922 |
| CQUAD4 | 1410391 |
| CTRIA3 | 99299 |
| RBE2 | 56002 |
| RBE3 | 102051 |

### 4.1.2 Number of Modes in the TBIW Model

Figure 4.2 and Figure 4.3 show the modal density of the TBIW in the 0 to 300 Hz range, indicating approximately 3000 modes. As anticipated, the modal density increases at higher frequencies. At lower frequencies, the structural response tends to be dominated by global, low-frequency modes, resulting in relatively fewer modes within the given frequency range. However, as the frequency rises, the structural behavior becomes more localized and intricate, leading to the emergence of numerous higher-frequency modes. These modes capture the finer details of the structural response, including localized deformations, resonances, and interactions between different components.

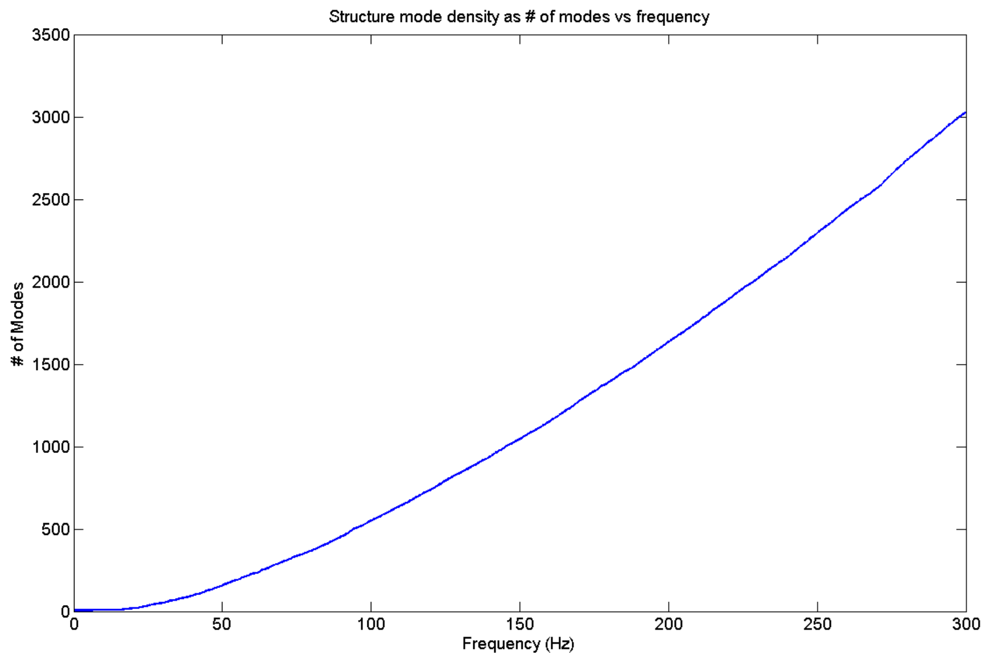


*Figure 4.2* Mode density of TBIW structural model

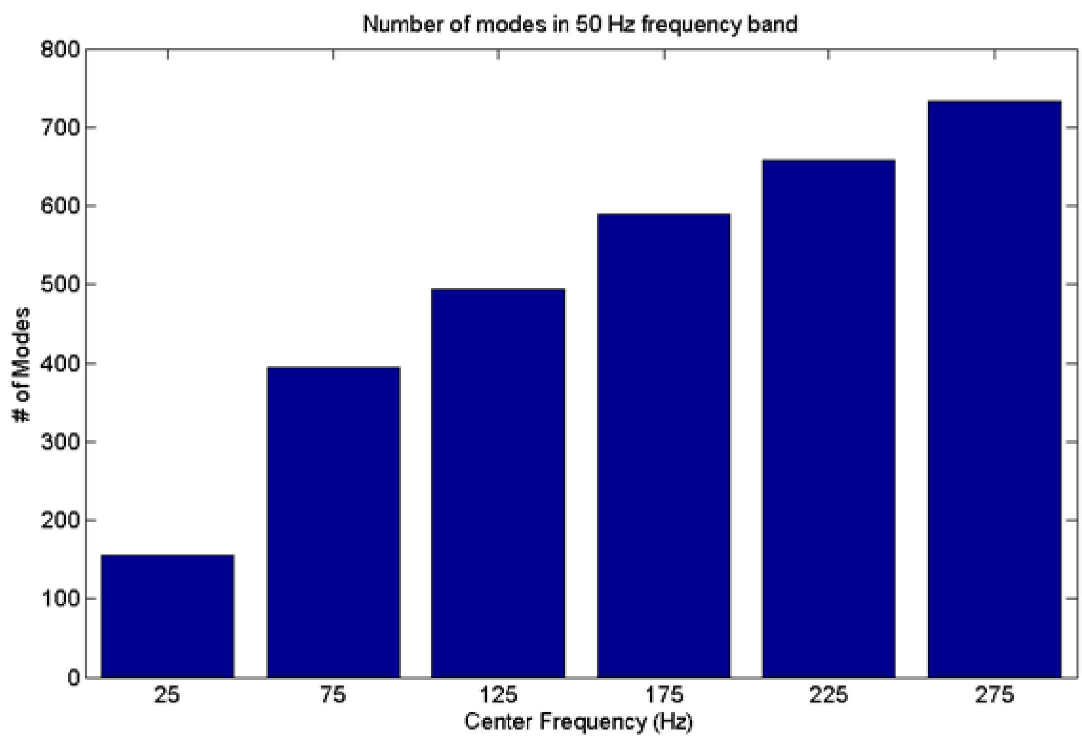


*Figure 4.3* Histogram of mode density of TBIW structural model

### 4.1.3 Sufficient Element Size in Frequency Range of Interest

Linear vibrations are the result of traveling linear waves at a specific rotational frequency $\omega$ (rad/sec) or wave number $k$

$$\omega=2\pi f=kc \quad where \quad k=\frac{2\pi}{\lambda} \tag{4.1}$$

where $f$ is the frequency in Hz, $\lambda$ is the wavelength, and $c$ is the wave speed of the medium (air for acoustics, and steel for example for a structural part). Combining the two equations yields

$$\lambda = \frac{c}{f}$$

indicating that the wavelength $\lambda$ is inversely proportional to the frequency $f$. As it was shown by S. Roth [71] , to represent accurately a harmonic wave of length $\boldsymbol{\lambda}$, we must have an element size of $\frac{\lambda}{16}$; i.e., we must have 16 elements per wavelength. In our model, to be accurate up to 300 Hz in linear acoustics in air ($c$ = 341 m/s), the element size must be smaller than $\frac{1}{16}\frac{341}{300} = 0.071\ m$ or 71.2 mm. For a structural part made of steel, the wave speed is 5100 m/s resulting in an element size of $\frac{1}{16}\frac{5100}{300} = 1.06\ m$ for accuracy up to 300 Hz. This element size is obviously impractical and cannot capture the modes in vehicle structure. This is because this element size does not capture the vibration characteristics of structures with complicated geometry subjected to specific boundary conditions.

It is known that a structural vibratory motion is a linear combination of the modes up to the frequency of interest. This is the basic idea of a “modal” model. It is important therefore, to accurately represent all mode up to the highest frequency of interest. The following approach is recommended.

Using a generated mesh based on "common practice" rules, we calculate all modes of interest – both natural frequencies and corresponding mode shapes. Some modes are local, and some are global. For the former, the mode shape is almost zero everywhere in the structure except at a local region. From a visual inspection of the mode, we can estimate an "effective" length $l_i$ and the number of nodes $n$ (location with zero displacement) along the effective length $l_i$. To capture the shape of the mode between two subsequent nodes, we may use 4 to 6 elements resulting in an average element length of $l_i/4$ if four elements are used. The $l_i/4$ length provides an average element size for an appropriate mesh density to accurately estimate that local mode.

As an example, consider the longitudinal vibration of a fixed-free rod of length $l$ [72].

| End Conditions of Bar | Boundary Conditions | Frequency Equation | Mode Shape (Normal Function) | Natural Frequencies |
|---|---|---|---|---|
| Fixed-free | $u(0,t)=0$<br>$\frac{\partial u}{\partial x}(l,t)=0$ | $\cos\frac{\omega l}{c}=0$ | $U_n(x)=C_n\sin\frac{(2n+1)\,\pi x}{2l}$ | $\omega_n=\frac{(2n+1)\,\pi c}{2l}$;<br>$n=0,1,2,\ldots$ |

With the n$^{th}$ mode shape being

$$U_n(x)=\frac{C_n sin\,(2n+1)\pi x}{2l} \tag{4.2}$$

indicating that the length between two nodes for the $n^{th}$ mode shape is $\frac{2l}{(2n+1)}$. Thus, the required average element size to capture the $n^{th}$ mode accurately is $\frac{1}{4}\frac{2l}{(2n+1)}$. In our vehicle FE model, a similar approach was used to evaluate the mesh size for various components.

#### 4.1.4 TBIW Model Quality

The TBIW model underwent a rigorous evaluation using diverse techniques to confirm its quality and accuracy. An initial assessment used the rigid body modes to validate the accuracy of the TBIW FE model. In an error-free, unconstrained model, the initial six modes are expected to be rigid body modes, theoretically possessing a zero frequency. However, practical constraints such as numerical errors and finite mesh size could prevent the attainment of a zero frequency. As such, these six rigid body modes should be at least four orders of magnitude lower than the first elastic mode to ensure model integrity. A free-free model necessitates the presence of precisely six rigid body modes. Failure to meet this criterion renders the model unsuitable for analysis. Moreover, the presence of more than six modes with frequencies nearing zero suggests the existence of mechanisms, often attributable to suboptimal mesh quality, such as disconnected meshed components.

Since the TBIW model first flexible mode is 10 Hz, the rigid body modes should be ideally at frequencies less than 1.0E-03 Hz. The frequencies of the first six structural modes of the base TBIW model are listed in Table 4.2. clearly indicating rigid body modes.

Table 4.2

*First six modes of TBIW structural model*

| Mode Number | Frequency (Hz) |
|---|---|
| 1 | 1.19E-04 |
| 2 | 1.05E-04 |
| 3 | 1.53E-04 |
| 4 | 2.67E-04 |
| 5 | 6.30E-04 |
| 6 | 6.49E-04 |

The second quality assessment was the 1G-test, which examines the model's connectivity. This evaluation determines whether any subsystems are inadequately attached or if there are unexpected alterations in mass distribution. Employing a suitable array of boundary conditions, specifically, fixtures at the front and rear shock nodes, the structure underwent loading equivalent to a unit gravity force. The resulting displacement profile, shown in Figure 4.4, reveals a maximum displacement of approximately 1mm, suggesting the model's overall validity. Notably, no segments of the structure exhibit disproportionately large displacements, affirming its coherence and reliability.

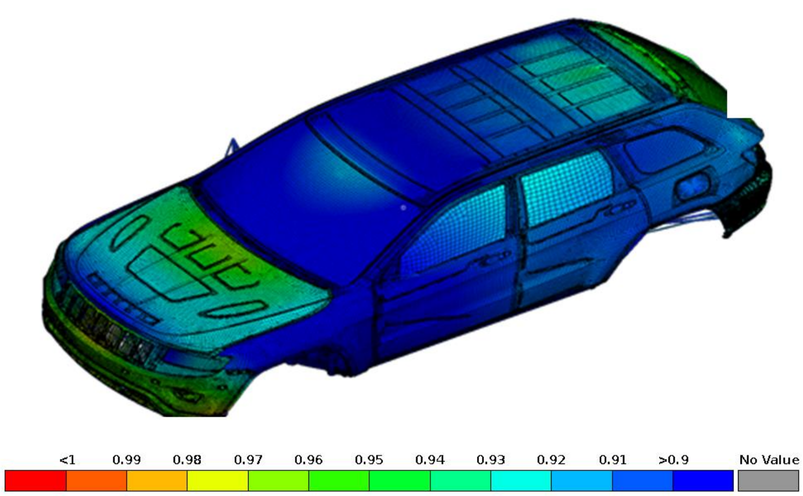


*Figure 4.4* TBIW displacement response plot for the 1G load test

The third validation check for the TBIW FE model is the enforced displacement test, designed to assess the structural rigidity across all nodes. This examination involves fixing a single node at the front shock location in all six degrees of freedom (DOFs), while permitting unrestricted movement for all other nodes within the model. Subsequently, an enforced displacement was applied sequentially to each DOF of the designated node, with our study focusing on the left front shock node.

For each of the six tests conducted (one per DOF), both visual and numerical analyses were performed on the displacement counter plots for the entire model. Specifically, the expected displacement for all grids in that DOF upon applying a unit displacement in a particular DOF (e.g., x-axis), should be equal to 1.

In the case of extensive structures like the TBIW model, this verification process is efficiently executed using a post-processing tool to visualize the deformed shape. Figure 4.5 shows the displacement contour plot resulting from a unit displacement in the x-axis DOF of the front shock node while the remaining five DOFs of the node remained constrained.

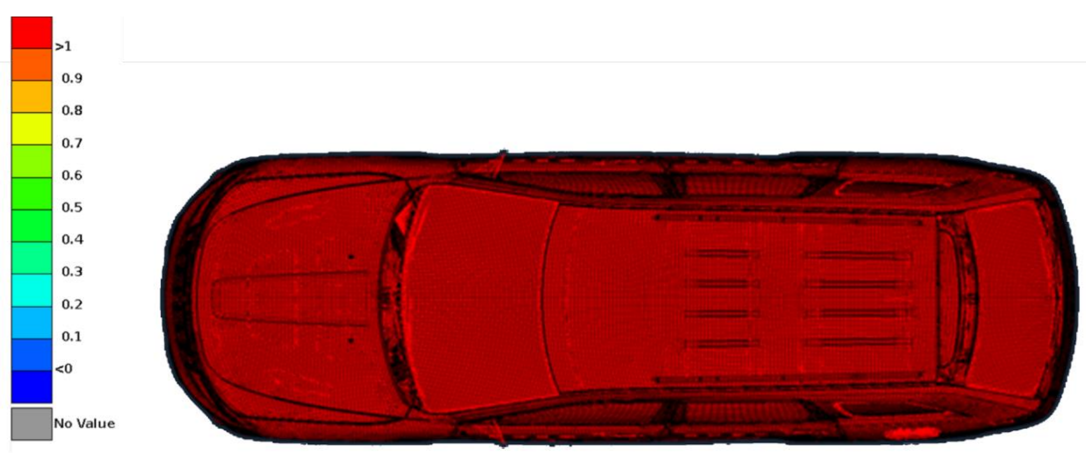


*Figure 4.5* Displacement contour plot for a unit displacement of first DOF front shock

As shown, all nodes of the vehicle exhibit a unit displacement of 1.0 in the x direction. The same is observed when the unit displacement is enforced on the front shock node in the other 5 DOFs one by one.

### 4.1.5 TBIW Structural Damping Assumptions

Damping in materials is due to energy dissipation from the friction among the molecules as the material flexes. The exact physical mechanism of damping is almost impossible to model theoretically. For this reason, approximate damping models are used which at best are calibrated using experimental results from modal analysis. The latter is used to measure among others, the so called "modal damping" which represents the damping at a particular resonance condition only. The measured modal damping for two resonances (one at a low frequency and one at a high frequency) is commonly used to estimate two parameters in the so-called "structural damping" (or "proportional damping") approximation model. Modal damping assumes that the damping matrix in the time domain is proportional to the stiffness matrix and the mass matrix as shown in Equation (4.3).

$$[C] = \alpha[M] + \beta[K] \tag{4.3}$$

where $[C]$ is the damping matrix and $[M]$ and $[K]$ are the mass and stiffness matrices, respectively. The two constants $\alpha$ and $\beta$ are calculated using the two measured modal damping values at a low and a high frequency, respectively. For metallic structures, the modal damping at any resonance is between 2% and 3% [73]. In this study, we assume a 3% modal damping at all resonances based on past experience.

## 4.2 TBIW Vehicle Model Correlation with Physical Testing

Global modes are of paramount importance in Finite Element Analysis (FEA) for vehicle full-body structural design. These modes represent the fundamental vibrational characteristics of the entire vehicle body, including its BIW structure and trims interconnected components. Understanding and accurately predicting these global modes is critical in FEA modeling to show the fundamental mass and stiffness matrix are representative of the physical vehicle. To ensure the vehicle FE model is accurate we used a four-post shaker to excite the vehicle TBIW modes. A four-post shaker is a specialized testing equipment used to simulate various road conditions and vibrations experienced by vehicles. It employs four hydraulic or electromagnetic actuators to replicate real-world forces on the vehicle chassis. This setup allows for precise control over frequency, amplitude, and direction of vibrations. The results show good agreement between frequency and mode shape of the vehicle TBIW as shown in Table 4.3.

Table 4.3

*TBIW mode comparison between test and CAE*

| Mode Description | Frequency difference between Experimental and FE, Hz |
|---|---|
| Torsion | 0.1 |
| Lateral Bending | 0.6 |
| Vertical Bending | 0.2 |

The mode shape comparison for the global modes between physical testing and FE model show good agreement as shown in Figure 4.6 to Figure 4.8. Moreover, a comprehensive verification of numerous system and panel modes, including those of the sunroof and liftgate, was conducted. It was observed that the frequency associated with the sunroof mode exhibited a small deviation of 0.2 Hz between physical testing and FE model simulation. Furthermore, the mode shape derived from the FE model closely resembled the observed physical testing mode, as illustrated in the Figure 4.9. These results show good correlation between TBIW FE model and the physical testing.

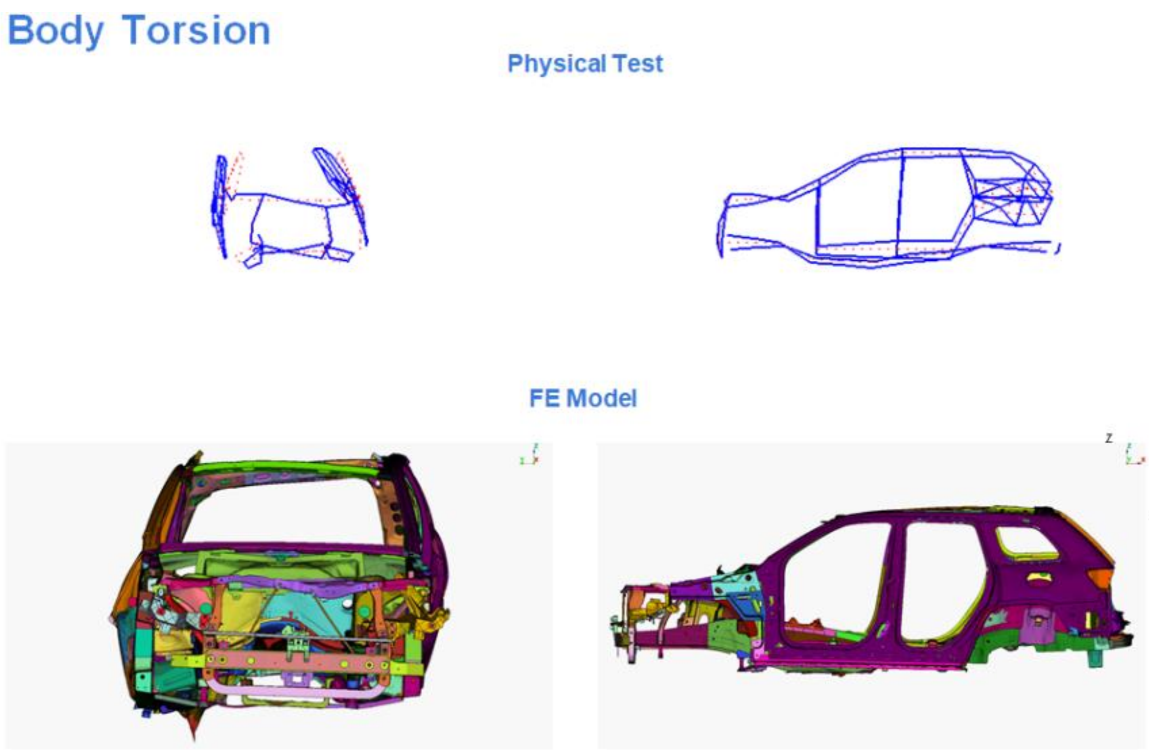


*Figure 4.6* TBIW global torsion mode

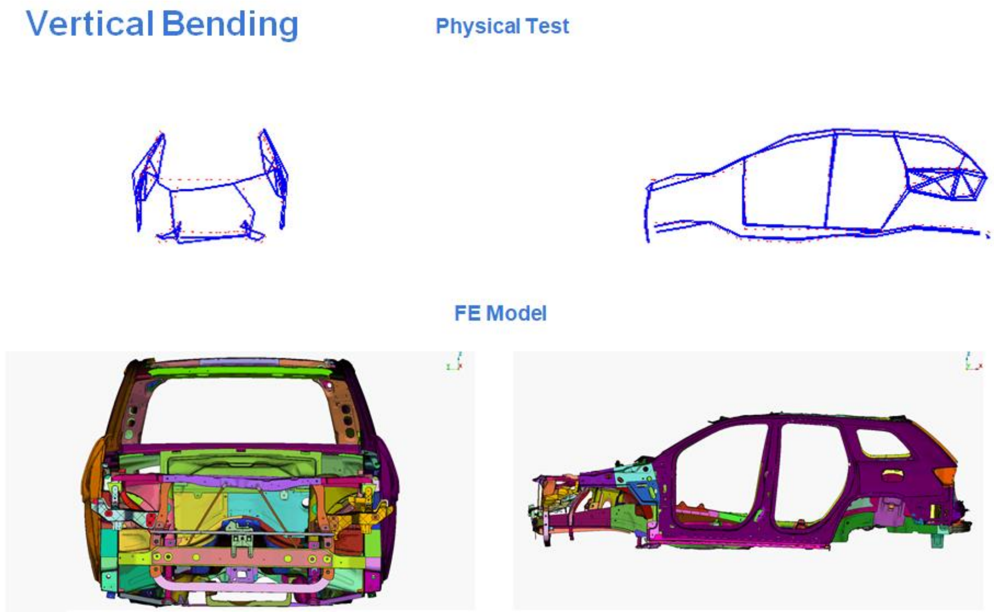


*Figure 4.7* TBIW global bending mode

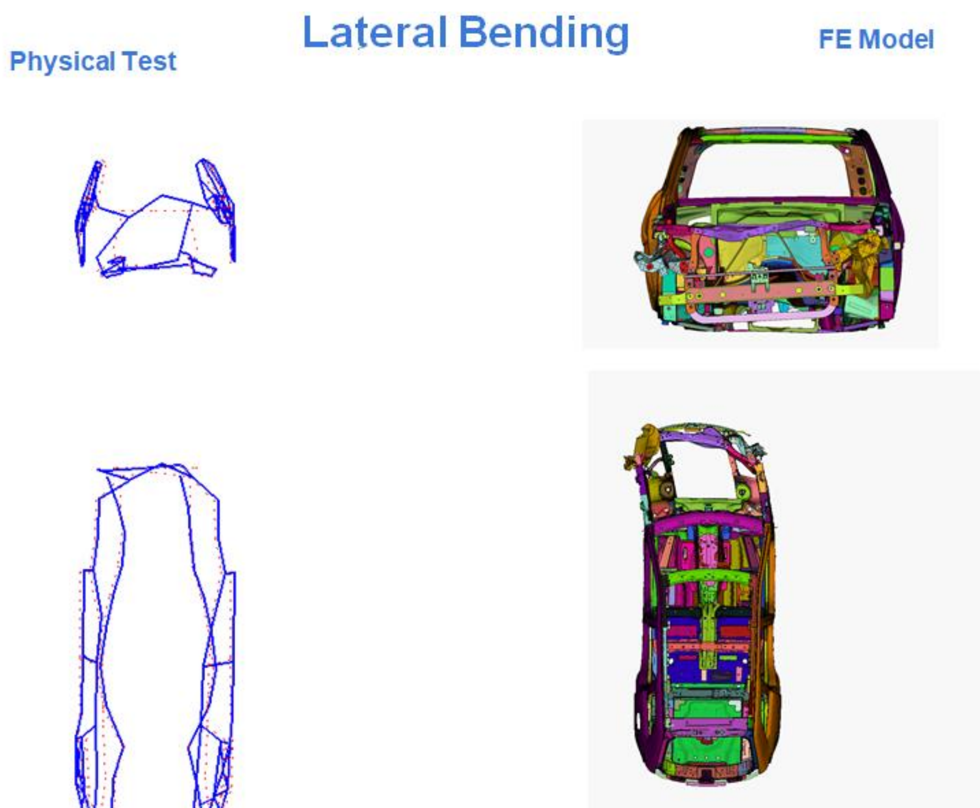


*Figure 4.8* TBIW global lateral mode

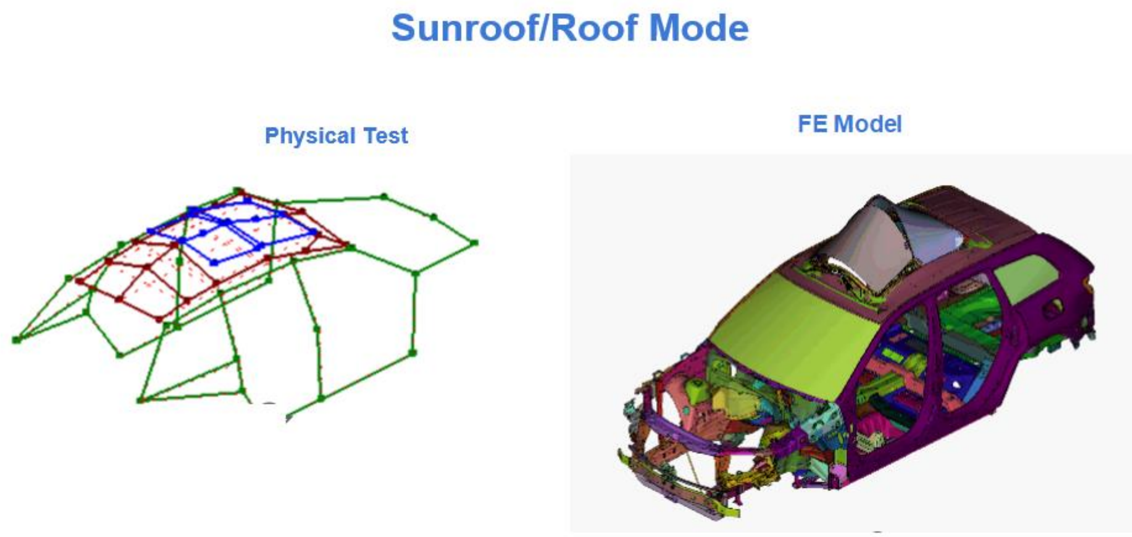


*Figure 4.9* Sunroof / roof mode

4.3 Summary

This Chapter presented details of the full TBIW vehicle FE model used in this research, indicating its accuracy compared to verification tests. The structural finite element model has approximately 11 million degrees of freedom, reflecting a detailed representation of various vehicle components. Modal density analysis reveals approximately 3000 modes in the 0 to 300 Hz range. To ensure accuracy, a mesh size evaluation was conducted based on mode shapes and their frequencies.

Quality assessments included a rigid body mode analysis, 1G-tests, and enforced displacement tests, all confirming the model's validity and accuracy. Correlation with physical testing, particularly concerning global modes and panel modes, showed good agreement in frequency and mode shape between the FE model and experimental results.

# CHAPTER FIVE

# DEVELOPMENT AND VERIFICATION OF CAE CLOSED CAVITY MODEL

This chapter provides a comprehensive overview of the vehicle cavity acoustic analysis. It starts with the wave equation and the derivation of its normal modes for one-dimensional (1-D) closed cavities. Subsequently, a CAE model is developed to validate the efficacy of the employed CAE methodology. Next, the solution from the 1-D closed cavity model is extended to consider a three-dimensional (3-D) closed cavity model. To verify the accuracy of the CAE modeling approach for 3-D closed cavities, a CAE model is established. Additionally, leveraging a monopole acoustic source formulation which is discussed in Chapter 6, and utilizing physical testing of vehicle cavities, a high level of agreement between test results and Finite Element (FE) analysis is observed.

## 5.1 Importance of Acoustic Mode Shape and Cavity Excitation Characteristics

The cavity mode shapes provide very important information about the cavity acoustic characteristics. For a cavity mode the pressure distribution and acoustic modal points provide useful information.  An acoustic modal node is a point where the wave has zero amplitude. The opposite is an acoustic modal anti-node; i.e. a point where the amplitude of the standing wave is maximum. Figure 5.1 illustrates this using the first three flexible modes of an one-dimensional cavity.

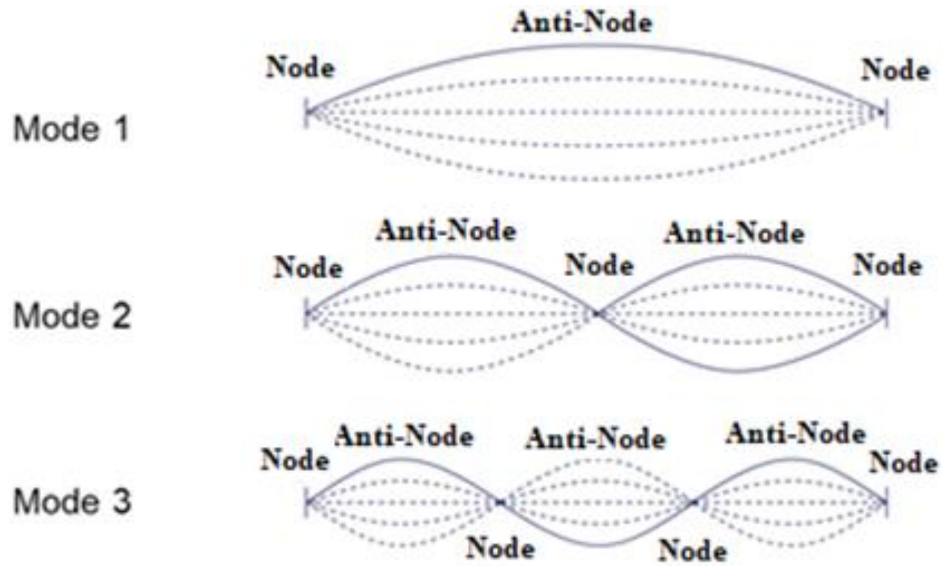


*Figure 5.1* Acoustic modal nodes and anti-nodes

If the system is excited at a node, the response is zero. In contrast, if it is excited at an anti-node the response is maximum. In general, regardless of the point of excitation, the node points always have a very low response. Figure 5.2 shows the characteristics of the first flexible mode of an SUV acoustic cavity and the corresponding mode shape.

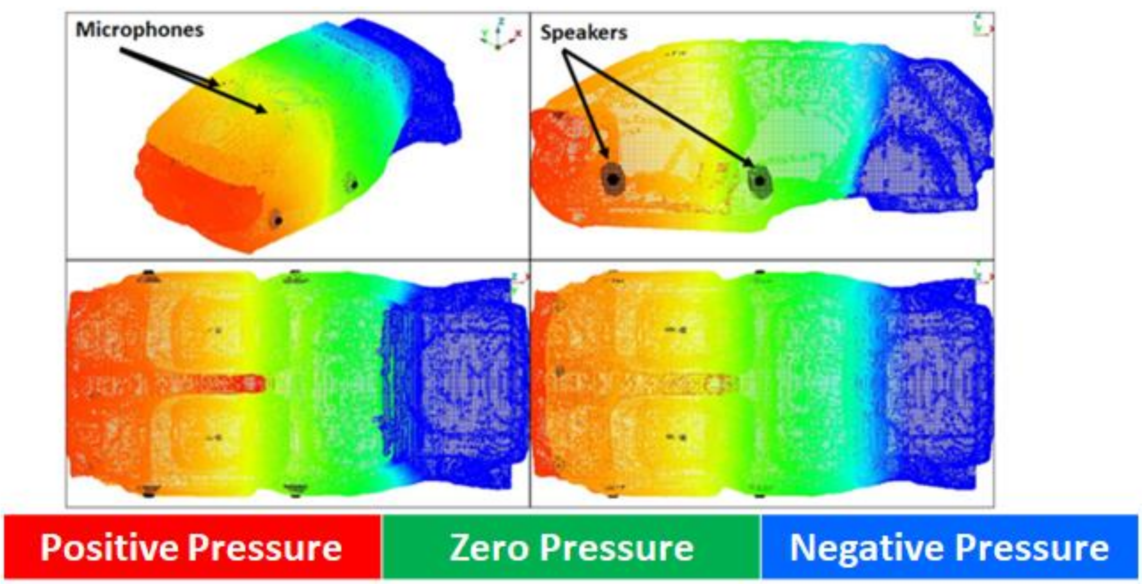


Figure 5.2 Typical pressure distribution for 1st flexible cavity mode of a SUV

The second flexible mode of the acoustic cavity and corresponding mode shape is shown in Figure 5.3.

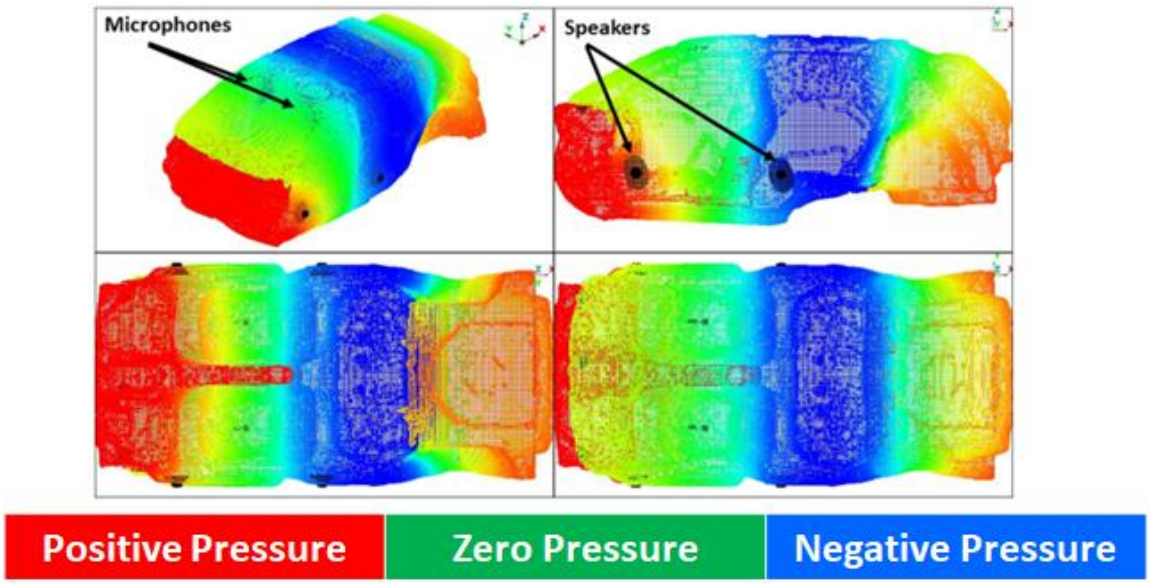


*Figure 5.3* Typical pressure distribution for 2nd flexible cavity mode of a SUV

As expected, the first and second cavity modes in this example have different nodal points. For the first mode, the rear speakers are at a nodal point and thus the cavity excitation form these speakers is expected to be minimal. Thus, it would be difficult to produce canceling noise using the rear speakers around the first flexible mode frequency band.  In contrast, in frequency range dominated by the second flexible mode both rear and front speakers could produce maximal canceling noise in ANC since both are at an anti-node nodal point. In later sections, the number of speaker and microphone locations will be further considered regarding the vehicle cavity distortion effect.

## 5.2  The Wave Equation

A mathematical description of the wave equation can be obtained by combining the equations of conservation of mass, Euler momentum equation and the state equation for an ideal gas (air) under adiabatic conditions. Because the acoustic pressure is several orders of magnitude smaller than the atmospheric pressure, a linearized wave equation can be obtained which is partial differential equation of second order in terms of the sound pressure *p* [74]

$$\frac{\partial^2 p}{\partial x^2} + \frac{\partial^2 p}{\partial y^2} + \frac{\partial^2 p}{\partial z^2} = \frac{1}{c^2}\frac{\partial^2 p}{\partial t^2} \tag{5.1}$$

in a Cartesian (*x*, *y*, *z*) coordinate system. Here, *t* denotes time and c is the speed of sound expressed as

$$c = \sqrt{\frac{\gamma p_0}{\rho}} = \sqrt{\gamma R_g T_g} \tag{5.2}$$

where *p* is in Pascals (1 Pa = 1 N/m^2), $\rho$ is the density and $\gamma$ is the ratio of the specific heat at constant pressure to that at constant volume ( $\gamma$ =1.401 for air). $R_g$ is the gas constant ($R_g$ = 287 J·kg$^{-1}$K$^{-1}$ for air), $p_0$ is the atmospheric pressure (101.3 kPa for air under normal ambient conditions), and $T_g$ is the absolute temperature [75]. From Equation (5.2), we have

$$\rho = \frac{p_0}{R_g T_g} \tag{5.3}$$

At 293.15 K (= 20°C) the speed of sound in air is 343 m/s. Under normal ambient conditions (20°C, 101.3 kPa) the density of air is 1.204 kgm$^{-3}$.

The linearity of the wave equation implies that a sinusoidal source will generate a sound field in which the pressure at all positions varies sinusoidally. It also implies linear superposition. The wave equation can be solved using appropriate boundary conditions which are often expressed in terms of the particle velocity. For example, the normal component of the particle velocity $u$ is zero on a rigid surface. Therefore, we need an additional equation that relates the particle velocity to the sound pressure. This relation is known as the *Euler's momentum equation*,

$$\rho \frac{\partial u}{\partial t} + \nabla p = 0 \tag{5.4}$$

which is simply Newton's second law for fluids. The operator $\nabla$ denotes the gradient. Note that the particle velocity is a vector and the sound pressure is a scalar.

5.3 Pressure Equation (Sound Plane Waves)

The plane wave is a central concept in acoustics. For plane waves, any acoustic variable at a given time is a constant on any plane perpendicular to the direction of propagation. Such waves exist in a duct, for example. It should be noted spherical wave in the far field can be approximated by plane waves. The plane wave is a solution to the following one-dimensional wave equation, which is simply derived from Equation (5.1)

$$\frac{\partial^2 p}{\partial t^2} = c^2 \frac{\partial^2 p}{\partial x^2} \tag{5.5}$$

It is easy to show that

$$p = f_1(ct - x) + f_2(ct + x) \tag{5.6}$$

where $f_1$ and $f_2$ are arbitrary functions, is the general solution to Equation (5.5). Since the argument of $f_1$ is constant if $x$ increases as $ct$ increases, the first term of this expression represents a wave that propagates in the positive $x$-direction with constant speed, $c$, whereas the second term represents a similar wave travelling in the opposite direction. Thus, $f_1$ represents a forward moving wave and $f_2$ represents a backward moving wave.

The special case of a harmonic forward moving plane wave is of great importance. It represents the solution of the linear wave equation which can be easily obtained using the separation of variables solution method. Harmonic waves are generated by sinusoidal sources such as a loudspeaker driven with a pure tone. A harmonic plane wave pressure propagating in the *x*-direction can be written as

$$p = p_1 \sin\left(\frac{\omega}{c}(ct - x) + \varphi\right) = p_1 \sin(\omega t - kx + \varphi) \tag{5.7}$$

where $\omega = 2\pi f$ is the angular (or radial) frequency and $k = \omega / c$ is the (angular) *wave number*. The quantity $p_1$ is the amplitude of the wave, and $\varphi$ is a phase angle. At any position in this sound field, the sound pressure varies sinusoidally with the angular frequency $\omega$ and at any fixed time the sound pressure varies sinusoidally with *x* with the spatial period

$$\lambda = \frac{c}{f} = \frac{2\pi c}{\omega} = \frac{2\pi}{k} \tag{5.8}$$

where $\lambda$ is the *wavelength* defined as the distance travelled by the wave in one cycle. Note that the wavelength is inversely proportional to the frequency. The audible frequency range is approximately from 20 Hz to 20 kHz, implying that wavelengths (in air) are in the range of 17 m at the lowest audible frequency to 17 mm at the highest audible frequency. The wave analysis can be simplified if the wavelength is very long or very short compared with typical dimensions.

### 5.4 Normal Modes of 1-D Cavity

The wave equation can be solved using the separation of variables approach if the response is a harmonic wave. This happens if the excitation (e.g., vibratory motion of the source) is harmonic.

Separation of variables assumes that the pressure is a product of separate functions in space and time, as

$$p(x,t) = P(x) * T(t) \tag{5.9}$$

resulting in

$$\frac{\partial^2 p}{\partial x^2} = \frac{\partial^2 [P(x) * T(t)]}{\partial x^2} = \frac{\partial^2 [P(x)]}{\partial x^2} * T(t)$$

$$and \qquad \frac{\partial^2 p}{\partial t^2} = \frac{\partial^2 [P(x) * T(t)]}{\partial t^2} = P(x) * \frac{\partial^2 [T(t)]}{\partial t^2}$$

Therefore, substitution in the wave Equation (5.5) yields

$$P(x) * \frac{\partial^2 [T(t)]}{\partial t^2} = \ c^2\, T(t) * \frac{\partial^2 [P(x)]}{\partial x^2}$$

$$\text{or} \qquad \frac{\partial^2 [P(x)]}{\partial x^2} * \frac{1}{P(x)} c^2 = \frac{\partial^2 [T(t)]}{\partial t^2} * \frac{1}{T(t)} = -\omega^2 \tag{5.10}$$

where $\omega^2$ is a constant. Because the left-hand side is a function of *x* and the right-hand side is a function of *t*, both terms must be equal to a constant. Equation (5.10) results in the following two ordinary differential equations (ODEs)

$$\frac{\partial^2 [P(x)]}{\partial x^2} + \frac{\omega^2}{c^2}\, P(x) = 0 \tag{5.11}$$

and

$$\frac{\partial^2 [T(t)]}{\partial t^2} + \omega^2\, T(t) = 0 \tag{5.12}$$

The solution to Equation (5.11) is the following harmonic function

$$P(x) = A * cos\left(\frac{\omega x}{c}\right) + B * sin\,(\frac{\omega x}{c}) \tag{5.13}$$

where *A* and *B* are constants to be calculated from boundary conditions. Similarly, the solution to Equation (5.12) is the harmonic function

$$T(t) = C * cos(\omega t) + D * sin\,(\omega t) \tag{5.14}$$

where *C* and *D* are constants to be calculated from initial conditions.

Using Equations (5.9), (5.13) and (5.14), the general solution for the acoustic pressure is

$$p(x,t) = (A * cos(kx) + B * sin(kx)) * (C * cos(\omega t) + D * sin(\omega t)) \quad (5.15)$$

where $k = \frac{\omega}{c}$ is the wavenumber.

Now a simple One-dimensional model will be considered, and the normal modes will be calculated. We assume the medium is air, as it can be seen the wave a is a compression wave traveling along L.

Now, a simple one-dimensional model is considered to calculate the normal acoustic modes. For that, only the space part of the general solution Equation (5.13) is used. For rigid wall (*x* = 0 and *x* = L) boundary conditions, the particle velocity is zero and thus the Euler's Equation (5.4) results in $\frac{\partial p}{\partial x} = 0$. Because differentiation of Equation (5.13) yields

$$\frac{dp(x)}{dx} = -Aksin(kx) + Bkcos(kx)$$

application of the boundary conditions results in $\frac{dp(0)}{dx} = \frac{dp(L)}{dx} = 0$ or $Bk = 0$ yielding B = 0 and $-kAsin(Lk) = 0$ . The latter results in $Lk = n * \pi$ where $n = 0, 1, 2, \ldots$ Since $k = \frac{\omega}{c}$ we have $\omega = \frac{n\pi}{L} c$ and $p(x) = Acos(\frac{n\pi}{L} x)$. The last relation shows that the acoustic mode shapes in the 1-D cavity corresponding to a non-zero natural frequency are:

$$cos\left(\frac{n\pi}{L} x\right), n = 1, 2, 3, \ldots \quad (5.16)$$

For a rectangular box cavity of length L = 3400 mm and of square cross section with each side equal to 100 mm, Table 5.1 shows the first exact acoustic natural frequencies.

Table 5.1

*Exact natural Frequencies of 1-D Cavity*

| n | Ang Freq (Rad) | Freq (Hz) |
|---|---|---|
| 0 | 0.00 | 0.00 |
| 1 | 314.00 | 50.00 |
| 2 | 628.00 | 100.00 |
| 3 | 942.00 | 150.00 |
| 4 | 1256.00 | 200.00 |

The above natural frequencies are verified using a FE model for this 1-D cavity. The FE analysis is based on MSC.NASTRAN version 2013 or higher [76]. The selected length of 3400 mm must be at least ten times longer than the other two dimensions (100 mm each) defining the cross-section. The element size is based on the frequency range of interest. For a specific frequency, there will be a corresponding wavelength $\lambda$ which is inversely proportional to the frequency f. To represent accurately a harmonic wave of length $\lambda$, we must have an element size of $\lambda/16$. In this example, the frequency range of interest is up to 200 Hz. Thus, the element size must be smaller than 107 mm. We have chosen 100 mm for our mesh to satisfy this requirement. The acoustic FE model consists of NASTRAN PSOLID fluid elements with 140 fluid nodes and the structural FE model includes thirty-four CHEXA solid elements.

Figure 5.4 shows the 1-D pressure eigenvectors and the corresponding natural frequencies. The red color corresponds to positive pressure values, the blue color indicates negative pressure values and the green represents zero pressure. The results show excellent correlation with the analytical natural frequencies of Table 5.1.

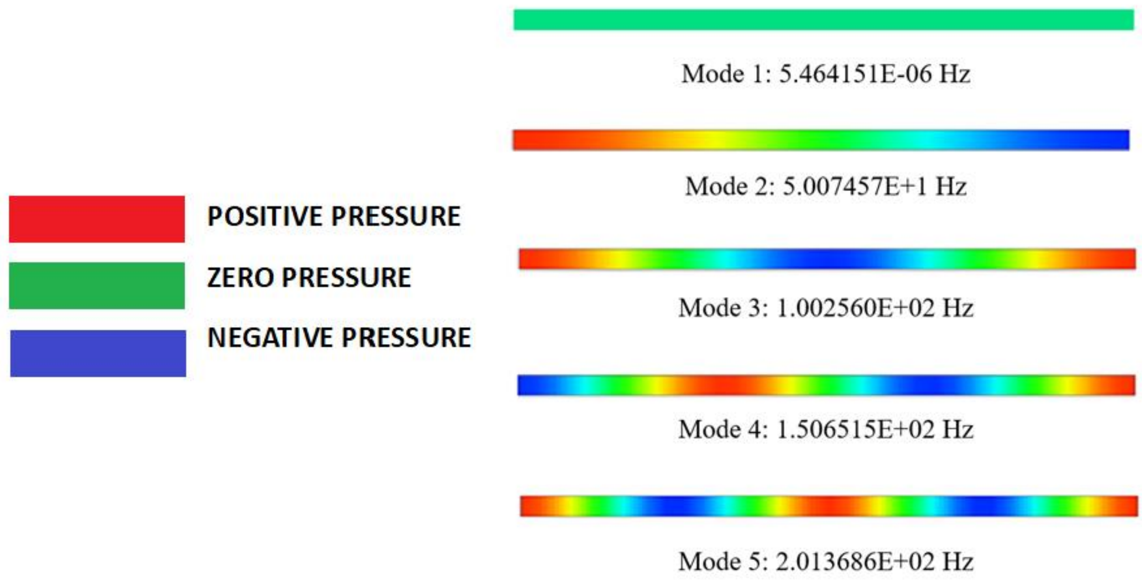


*Figure 5.4* 1-D cavity natural frequencies and eigenvectors from FE model

## 5.5 Normal Modes of a 3-D Cavity

### 5.5.1 Closed Form Solution for Modes of Three-Dimensional Cavity

We have shown that the wave equation is written as

$$\frac{\partial^2 p}{\partial t^2} = c^2 [\frac{\partial^2 p}{\partial x^2} + \frac{\partial^2 p}{\partial y^2} + \frac{\partial^2 p}{\partial z^2}]$$

or equivalently as

$$\nabla^2 p = \frac{1}{c^2}\frac{\partial^2 p}{\partial t^2} \tag{5.17}$$

We use again the separation of variables method to solve it. We assume that the solution is of the form

$$p(x, y, z, t) = P_1(x) * P_2(y) * P_3(z) * T(t) \tag{5.18}$$

resulting in

$$\frac{\partial^2 p}{\partial x^2} = \frac{\partial^2[P_1(x) * P_2(y) * P_3(z) * T(t)]}{\partial x^2}$$
$$= \frac{\partial^2[P_1(x)]}{\partial x^2} * P_2(y) * P_3(z) * T(t) \tag{5.19}$$

$$\frac{\partial^2 p}{\partial y^2} = \frac{\partial^2[P_1(x) * P_2(y) * P_3(z) * T(t)]}{\partial y^2}$$
$$= P_1(x) * \frac{\partial^2[P_2(y)]}{\partial y^2} * P_3(z) * T(t) \tag{5.20}$$

$$\frac{\partial^2 p}{\partial z^2} = \frac{\partial^2[P_1(x) * P_2(y) * P_3(z) * T(t)]}{\partial z^2}$$
$$= P_1(x) * P_2(y) * \frac{\partial^2[P_3(z)]}{\partial z^2} * T(t) \tag{5.21}$$

$$\frac{\partial^2 p}{\partial t^2} = \frac{\partial^2[P_1(x) * P_2(y) * P_3(z) * T(t)]}{\partial t^2}$$
$$= P_1(x) * P_2(y) * P_3(z) * \frac{\partial^2[T(t)]}{\partial t^2} \tag{5.22}$$

Substitution of Equations (5.19) through (5.22) in equation (5.17) and division by $P(x) * P(y) * P(z)$ yields

$$\frac{\partial^2[T(t)]}{\partial t^2}\frac{1}{T(t)} = c^2 * (\frac{1}{P(x)}\frac{\partial^2[P_1(x)]}{\partial x^2} + \frac{1}{P(y)}\frac{\partial^2[P_2(y)]}{\partial y^2}$$
$$+ \frac{1}{P(z)}\frac{\partial^2[P_3(z)]}{\partial z^2}) \tag{5.23}$$

The above equation holds only if the left-hand side and the right-hand side are each equal to a constant (say $-\omega^2$). In this case, we have

$$\frac{\partial^2[T(t)]}{\partial t^2}\frac{1}{T(t)} = -\omega^2$$

or
$$\frac{\partial^2[T(t)]}{\partial t^2} + \omega^2 T(t) = 0 \tag{5.24}$$

and
$$\frac{-\omega^2}{c^2} = \frac{1}{P(x)}\frac{\partial^2[P_1(x)]}{\partial x^2} + \frac{1}{P(y)}\frac{\partial^2[P_2(y)]}{\partial y^2} + \frac{1}{P(z)}\frac{\partial^2[P_3(z)]}{\partial z^2} \tag{5.25}$$

Then, if
$$k^2 = \frac{\omega^2}{c^2} = k_x^2 + k_y^2 + k_z^2 \tag{5.26}$$

Equation (5.25) becomes

$$-({k_x}^2 + {k_y}^2 + {k_z}^2) = \frac{1}{P(x)}\frac{\partial^2[P_1(x)]}{\partial x^2} + \frac{1}{P(y)}\frac{\partial^2[P_2(y)]}{\partial y^2} + \frac{1}{P(z)}\frac{\partial^2[P_3(z)]}{\partial z^2}$$

which is satisfied only if

$$-{k_x}^2 = \frac{1}{P(x)}\frac{\partial^2[P_1(x)]}{\partial x^2} \tag{5.27}$$

$$-{k_y}^2 = \frac{1}{P(y)}\frac{\partial^2[P_2(y)]}{\partial y^2} \tag{5.28}$$

$$-{k_z}^2 = \frac{1}{P(z)}\frac{\partial^2[P_3(z)]}{\partial z^2} \tag{5.29}$$

The solutions of the ODEs in Equations (5.27), (5.28) and (5.29) are

$$P_1(x) = Acos(k_x x) + Bsin(k_x x) \tag{5.30}$$

$$P_2(y) = Ccos(k_y y) + Dsin(k_y y) \tag{5.31}$$

$$P_3(z) = Ecos(k_z z) + Fsin(k_z z) \tag{5.32}$$

Similarly, the solution to Equation (5.24) is

$$T(t) = Gcos(\omega t) + Hsin(\omega t) \tag{5.33}$$

Substitution of Equations (5.30) through (5.33) in Equation (5.18) provides the following general solution

$$p(x,y,z,t) = \big(Acos(k_x x) + Bsin(k_x x)\big) * \Big(Ccos\big(k_y y\big) + Dsin\big(k_y y\big)\Big) * \big(Ecos(k_z z) + Fsin(k_z z)\big) * (Gcos(\omega t) + Hsin(\omega t)) \tag{5.34}$$

where the constants *A*, *B*, *C*, *D*, *E* and *F* are calculated using the boundary conditions and the constants *G* and *H* are evaluated using the initial conditions.

The acoustic mode shapes are calculated using the following time independent part in Equation (5.35).

$$p(x,y,z) = \big(Acos(k_x x) + Bsin(k_x x)\big) * \Big(Ccos\big(k_y y\big) + Dsin\big(k_y y\big)\Big) * \big(Ecos(k_z z) + Fsin(k_z z)\big) \tag{5.35}$$

### 5.5.2 Demonstration Problem for Modes of 3-D Cavity

Here we use a rectangular shape with similar dimensions to the actual full-size SUV cavity model as shown in Figure 5.5. This simplified rectangular model is used a reference model though out this research, since we can easily obtain analytical solutions and compare them with FE predictions.

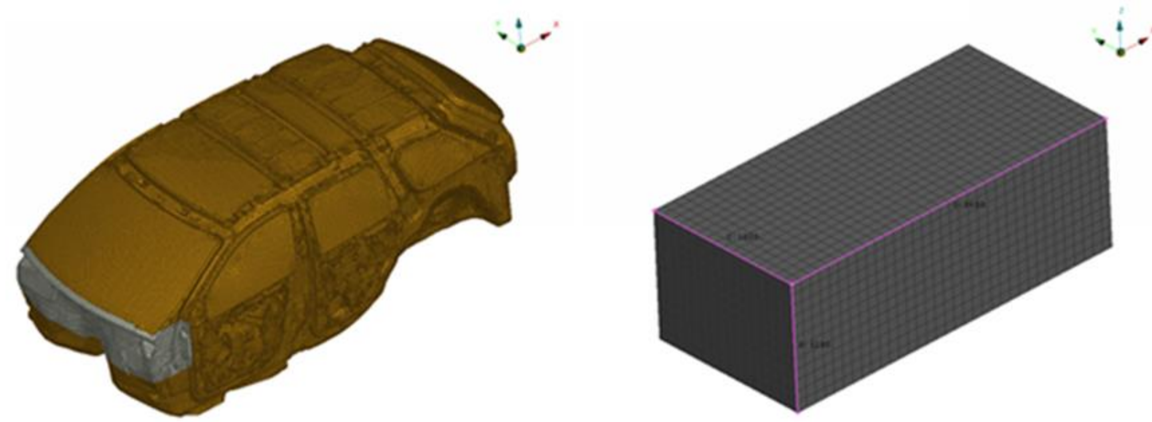

*Figure 5.5* Schematic of rectangular cavity resembling an SUV cavity

The dimensions of the rectangular cavity are $L_{cx}$ =3400 mm , $L_{cy}$=1600 mm , and $L_{cz}$= 1200 mm. Assuming rigid walls for all the boundaries, the particle velocity is zero resulting in a zero pressure gradient; i.e. $\frac{\partial p}{\partial x} = 0$ at $x = 0$ and $x = L_{cx}$. Similar boundary conditions hold in the y and z directions.

Using Equations (5.30), (5.31) and (5.32) and the derivatives of pressure in the x, y and z directions are

$$\frac{\partial[P_1(x)]}{\partial x} = -A * k * sin(k_x x) + B * k * cos(k_x x)$$

$$\frac{\partial[P_2(y)]}{\partial y} = -C * k * sin\big(k_y y\big) + D * k * cos(k_y y)$$

$$\frac{\partial[P_3(z)]}{\partial z} = -E * k * sin(k_z z) + F * k * cos(k_z z)$$

Therefore, using the boundary condition $\frac{\partial p}{\partial x} = 0$ at $x = 0$ we get $B = 0$. Using the same boundary condition at $x = L_{cx}$ we get

$$k_x L_{cx} = m * \pi, where\ m = 0,1,2, \dots \tag{5.36}$$

resulting in

$$P_1(x) = A\cos\left(\frac{m\pi x}{L_{cx}}\right) \tag{5.37}$$

Similarly,

$$k_y L_{cy} = n * \pi, where\ n = 0,1,2, \ldots \tag{5.38}$$

resulting in

$$P_2(y) = C\cos\left(\frac{n\pi y}{L_{cy}}\right) \tag{5.39}$$

and

$$k_z L_{cz} = l * \pi, where\ l = 0,1,2, \ldots \tag{5.40}$$

resulting in

$$P_3(z) = E\cos\left(\frac{l\pi z}{L_{cz}}\right) \tag{5.41}$$

Equations (5.36), (5.38) and (5.40) provide the $\omega_x$ , $\omega_y$, and $\omega_z$ components of the acoustic natural frequencies as

$$\omega_x = \frac{m\pi}{L_{cx}}\,c, \omega_y = \frac{n\pi}{L_{cy}}\,c, \omega_z = \frac{l\pi}{L_{cz}}\,c\ with\ m, n, l = 0,1,2, \ldots \tag{5.42}$$

The corresponding acoustic mode shapes are

$$p(x, y, z) = \cos\left(\frac{m\pi x}{L_{cx}}\right) * \cos\left(\frac{n\pi y}{L_{cy}}\right) * \cos\left(\frac{l\pi z}{L_{cz}}\right) \tag{5.43}$$

We can calculate ω using

$$\omega^2 = \omega_x^2 + \omega_y^2 + \omega_z^2 \tag{5.44}$$

Using Equations (5.42) and (5.44) the exact acoustic natural frequencies are calculated and shown in Table 5.2.

Table 5.2

*Exact acoustic natural frequencies for rectangular domain*

| Mode | Freq (Hz) | m | n | l |
|---|---|---|---|---|
| 1 | 0 | 0 | 0 | 0 |
| 2 | 50 | 1 | 0 | 0 |
| 3 | 100 | 2 | 0 | 0 |
| 4 | 106.25 | 0 | 1 | 0 |
| 5 | 117.4268 | 1 | 1 | 0 |
| 6 | 141.6667 | 0 | 0 | 1 |
| 7 | 145.9077 | 2 | 1 | 0 |
| 8 | 150 | 3 | 0 | 0 |
| 9 | 150.2313 | 1 | 0 | 1 |
| 10 | 173.4054 | 2 | 0 | 1 |
| 11 | 177.0833 | 0 | 1 | 1 |
| 12 | 183.818 | 3 | 1 | 0 |
| 13 | 184.0068 | 1 | 1 | 1 |
| 14 | 200.0 | 4 | 0 | 0 |

The natural frequencies of Table 5.2 were also estimated using the FE solver MSC.NASTRAN version 2013. This cavity FE model can be used for various applications as it will be shown in subsequent sections. In NVH, predicting the cavity normal modes using simulation is very important. Many forced response solutions are based on normal modes through the so-called modal model approach. Therefore, it is crucial to compare the FE model predictions with the closed-form solution to ensure the FE model is accurate.

Using the rectangular domain of Figure 5.5, the element size for a frequency range up to 200 Hz was selected similarly to the 1-D case. It was found that the element size must be smaller than 107 mm. We used 100 mm to satisfy this requirement. The cavity can be approximately represented by a rectangular box of similar dimensions with the vehicle cavity, neglecting the seats inside the cavity. We used 6548 CHEXA solid fluid elements and 7735 fluid nodes to satisfy the element size requirements. Table 5.3 compares the analytical acoustic natural frequencies with those calculated using the FE NASTRAN model. The results show excellent correlation.

Table 5.3

*Comparison of analytical and FE acoustic natural frequencies for 3-D cavity*

| Mode | Freq (Hz) Analytical | Freq (Hz) – FE Model |
|---|---|---|
| 1 | 0.0 | 0.0 |
| 2 | 50.0 | 50.1 |
| 3 | 100.0 | 100.3 |
| 4 | 106.3 | 106.5 |
| 5 | 117.4 | 117.7 |
| 6 | 141.6 | 142.2 |
| 7 | 145.9 | 146.3 |
| 8 | 150.0 | 150.7 |
| 9 | 150.2 | 150.7 |
| 10 | 173.4 | 174.0 |
| 11 | 177.1 | 177.7 |
| 12 | 183.8 | 184.5 |
| 13 | 184.0 | 184.6 |
| 14 | 200.0 | 201.4 |

## 5.6 Review of the Full Cavity Vehicle FE Model

The vehicle's structural components and the enclosed cabin air exhibit distinct modes which result in zones of varying impedance levels across the frequency spectrum of interest. The transfer of vibration energy into the cabin air depends on the impedance of the cavity at the interface with the structure. Consequently, structural vibrations may produce unwanted noise. Figure 5.6 shows the finite element mesh for the acoustic cavity model. It has approximately 0.5M DOFs. The model is typical for a ground vehicle acoustic cavity. It consists of three main components: the main cavity, the seat modeling, the instrument panel and the console sub-models. Table 5.4 shows the types and number of elements for the cavity model.

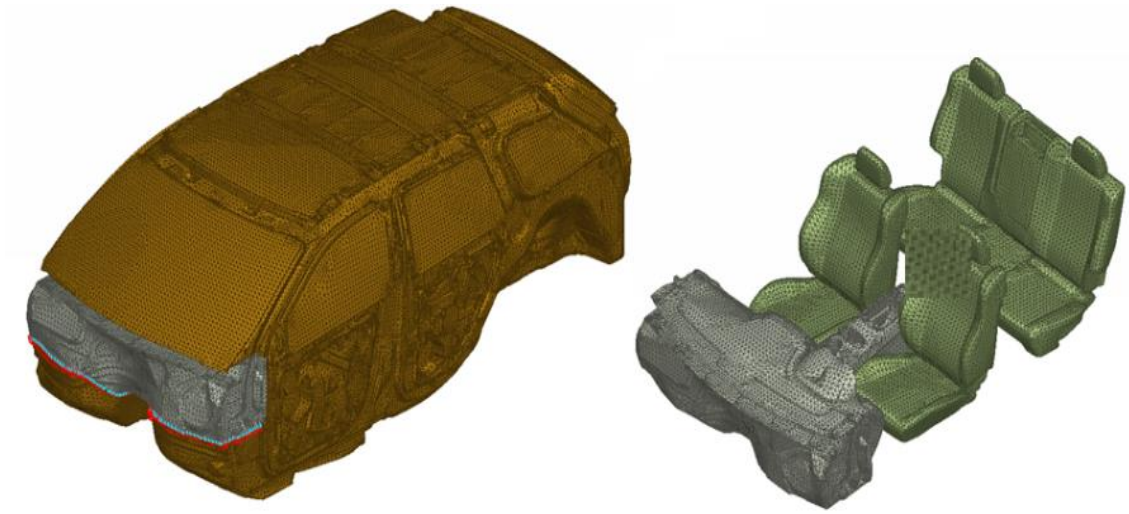

*Figure 5.6 Full vehicle cavity model*

Table 5.4

*Element type and number for vehicle acoustic cavity model*

| Element Type | Number of Elements |
|---|---|
| CHEXA | 334363 |
| CPENTA | 43682 |
| CTETRA | 1408691 |

Figure 5.7 shows a cross-section of the vehicle cavity model. The acoustic mesh exhibits a finer resolution near the outer surface and a coarser resolution towards the interior. This FE modeling approach was implemented in order to minimize the total number of acoustic elements while ensuring the integrity of the structure/acoustic interface.

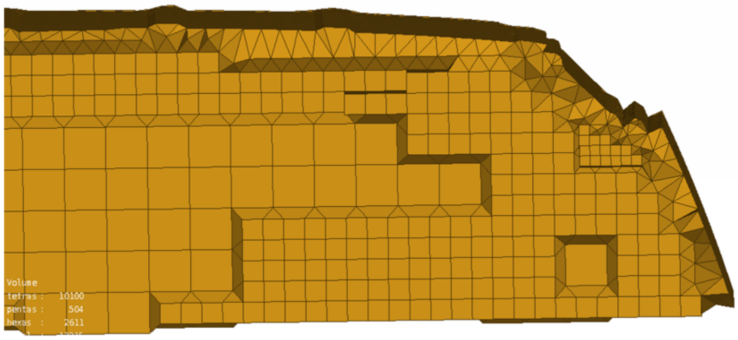


*Figure 5.7* Acoustic cavity element size transition

Figure 5.8 shows the modal density of the acoustic model. There are 44 modes in the ANC frequency range of interest from 0 to 300 Hz.

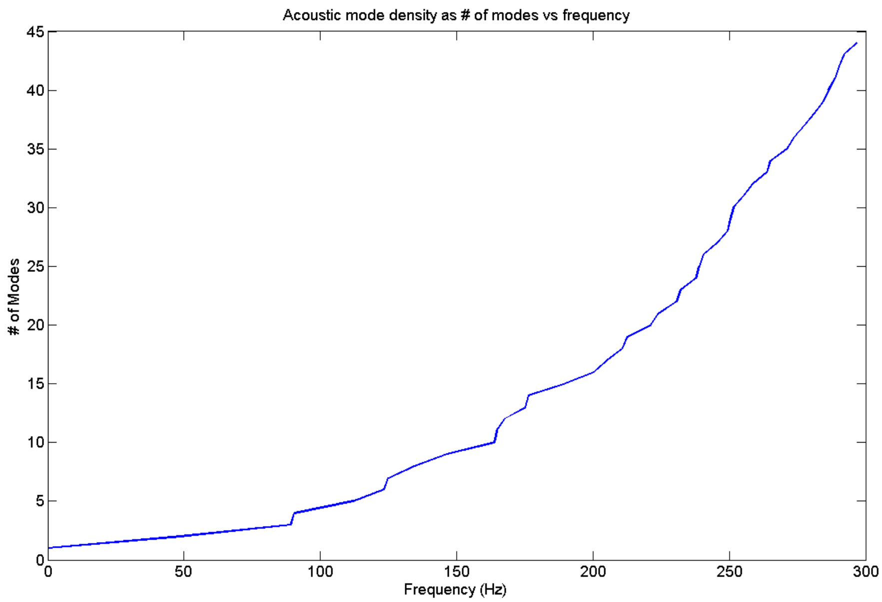


*Figure 5.8* Modal density of acoustic cavity model

### 5.6.1 Vehicle Cavity Damping Assumptions

Based on previous experimental correlations and studies frequency dependent damping ratio of 4 to 8 percent was assigned to the cavity model in the ANC frequency range.

### 5.6.2 Numerical Verification of Vehicle Cavity Modes

To verify the FE predicted vehicle acoustic cavity modes, we compare them with the modes of the simplified rectangular shape box of Section 5.5.2. The first four modes of the two models are expected to be similar since both models have the same fundamental length. Table 5.5 compares the acoustic modes between FE and simplified cavity models showing a good correlation.

Table 5.5

Comparison of acoustic modes between FE and simplified cavity models

| Mode | Vehicle Modes Freq (Hz) | Simplified Cavity Modes Freq (Hz) |
|---|---|---|
| 1 | 0 | 0 |
| 2 | 48.7 | 50.1 |
| 3 | 89.1 | 100.3 |
| 4 | 90.4 | 106.5 |

Figure 5.9 shows the first three acoustic pressure mode shapes for the vehicle and the simplified cavity models. The mode shapes are very similar indicating that that the cavity modes are reasonable.

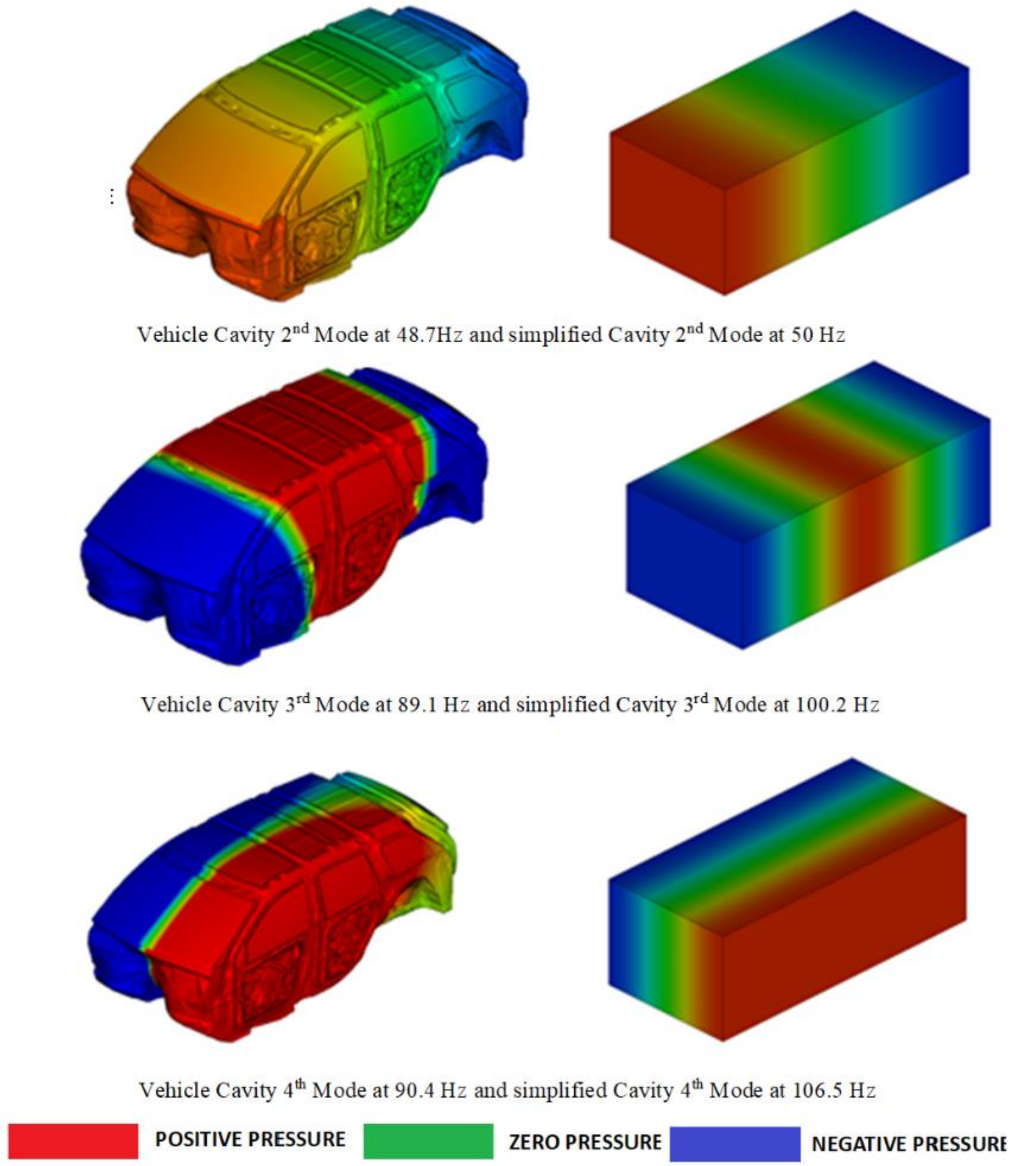


*Figure 5.9* Vehicle FE versus simplified cavity acoustic mode shapes

### 5.6.3 Fluid Structure Interaction (FSI) TBIW to Vehicle Cavity

The structure/acoustic interface is determined by an internal algorithm of NASTRAN, according to criteria such as distance, angle or predefined sets defined by the "ACMODL" NASTRAN card. Also, the parameter "SKINOUT" is used to request

NASTRAN to output the wet structure and acoustic elements and nodes at the interface. Figure 5.10 shows the structural surface elements that are in contact with the acoustic cavity.

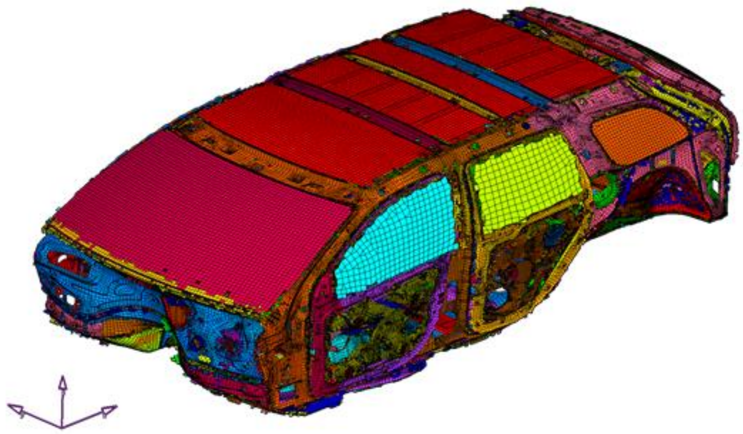

*Figure 5.10* TBIW structural elements in contact with acoustic cavity

### 5.6.4 Experimental Verification of Vehicle Cavity Modes

A monopole source was used to excite the vehicle cavity using the Simcenter Qsources hardware [77] of Figure 5.11.

*Figure 5.11* Simcenter Qsources [77] monopole source

Simcenter Qsources is a low-frequency monopole source for assessing vibro-acoustic transfer functions in vehicles. Its sound source level, coupled with its extensive frequency range, makes it very useful for NVH research and development.

The vehicle cavity acoustic FRFs (Frequency Response Functions) are expected in the range from 30 Hz to 1,000 Hz [78]. An array of microphones was strategically placed in the cavity to enable measurement of complex modes as shown in Figure 5.12. The testing procedure used has been described in detail by researchers [79].

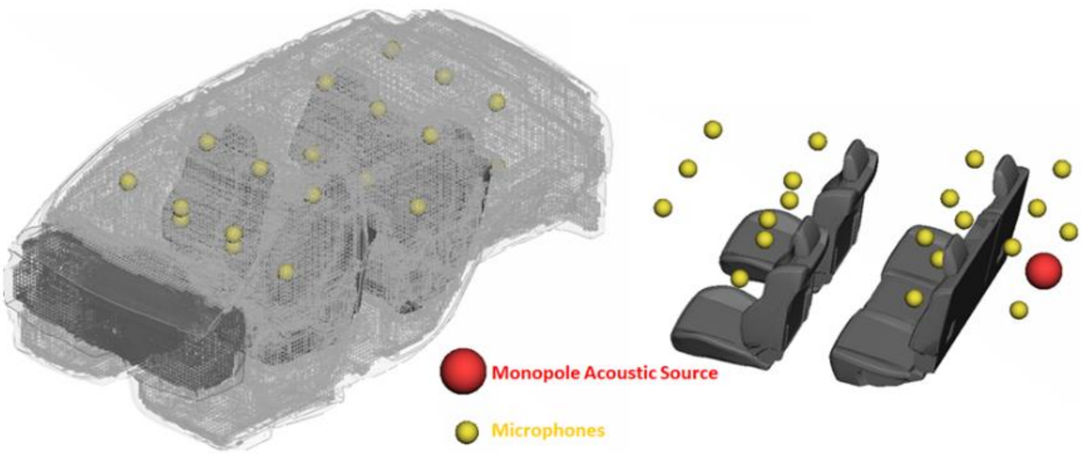


*Figure 5.12* Monopole source and microphone locations for FRF measurements

Figure 5.13 compares a measured acoustic FRF with its analytical prediction. The FRF is between the shown input volumetric acceleration source and the output microphone. The correlation is very good clearly indicating the 2nd and 3rd cavity modes.

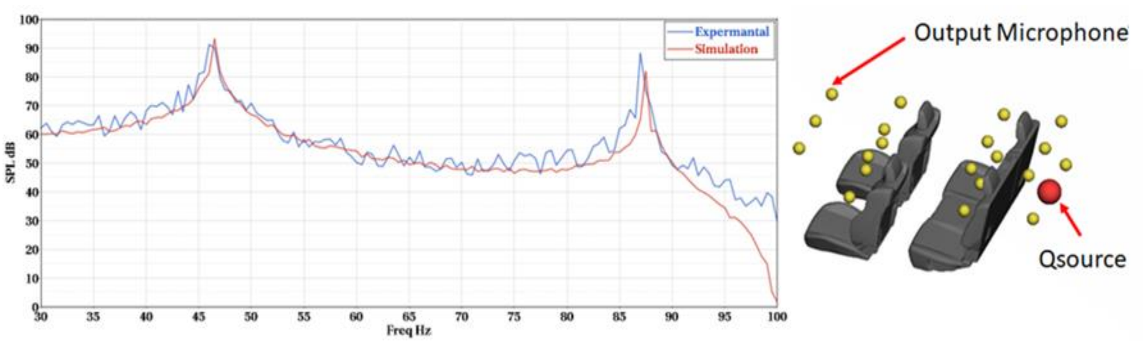


*Figure 5.13* Comparison of a measured acoustic FRF with simulation

## 5.7 Summary

This chapter described the fundamentals of vehicle cavity acoustic analysis. The wave equation was first derived and the acoustic modes for 1-D closed cavities were presented. A FE model was also constructed to validate the accuracy of calculating acoustic modes for 1-D and 3-D closed cavity models.

Demonstration problems were used to show the very good accuracy of FE models compared to analytical solutions. The Chapter also presented a full cavity vehicle FE model including mesh details, damping assumptions, and numerical verification of cavity modes. An experimental validation using monopole source testing was finally presented affirming the accuracy of the analytical and developed FE modeling approaches.

# CHAPTER SIX

# DEVELOPMENT AND VERIFICATION OF CAE SPEAKER MODEL

## 6.1 Introduction to Loudspeaker CAE Modeling Methodologies

As mentioned, an active noise cancelling system utilizes anti-noise to mitigate undesirable noise within the vehicle. This system relies on sensors to detect interior cabin noise, while vehicle loudspeakers generate cancelling sound to counteract the undesired noise, thereby enhancing cabin comfort. Consequently, an accurate modeling of the loudspeakers is critical for the virtual assessment of the active noise cancelling system.

Given the intricate nature of speaker geometry and cone shapes, coupled with diverse factors such as audio design parameters, packaging, styling, material selection, and cost, the design of speakers varies significantly. Loudspeakers, being complex electroacoustic transducers, often entail intricate internal components, details of which are typically not disclosed by loudspeaker manufacturers to vehicle OEMs. While speaker suppliers may provide rudimentary details such as the speaker's bracket geometry, finer intricacies of speaker design, including precise diaphragm shape, diaphragm materials, suspension, voice coil, magnet, and electrical characteristics, are generally withheld.

Typically, loudspeaker suppliers provide standard specifications such as sensitivity functions, impedance, mass, maximum linear travel of the cone, resonant frequency, mechanical compliance and resistance, projected area of the driver diaphragm, and moving mass. In our methodology, a FE model of the loudspeaker is developed using these fundamental specifications while excluding the intricate electromechanical system details of the loudspeaker. The primary objective of developing a speaker FE model for ANC analysis is to accurately represent the speaker using limited data. A secondary objective in speaker modeling is to create a loudspeaker FE model within a commercial platform capable of concurrently handling both acoustic and structural vibratory simulations. Thirdly, we aim to devise a simple experimental test for confirming the speaker model performance using the supplier data and FE modeling.

As demonstrated previously, a monopole source is typically used to excite the vehicle cavity and validate the modes and damping assumptions employed in the cavity FE model. In this Chapter, we first describe the modeling of a monopole acoustic source. Subsequently, the loudspeaker is modeled using a dipole source, followed by a detailed study of a moving cone (piston) model. Close-form solutions for each representation were either obtained or developed, and a FE model was constructed for each loudspeaker. A correlation between the FE models and the closed-form solutions is also presented. Our loudspeaker model provides a relationship between the electrical power input and the acoustic power output based on vibro-acoustic characteristics, thereby 'characterizing' the loudspeaker. Finally, the proposed speaker modeling approach is experimentally validated.

## 6.2 Acoustic Monopole Source

To model acoustic sources within an enclosed cavity such as a vehicle cabin, it is important to model an acoustic monopole source, as will be demonstrated in subsequent sections. As we have mentioned, a monopole acoustic source is commonly employed to excite the vehicle cavity for verification purposes, underscoring the necessity for detailed modeling.

### 6.2.1 Closed Form Solution for an Acoustic Monopole Source in a Closed Cavity

To model a monopole acoustic source, we start with the linearized wave equation [80]. From the continuity equation we have

$$\frac{\partial \rho}{\partial t} + \rho \nabla u = \dot{q} \tag{6.1}$$

where $u$ is the particle velocity vector and $\dot{q}$ is the mass rate (mass per time). The linearized Euler's equation is

$$\rho \frac{\partial u}{\partial t} = -\nabla p \tag{6.2}$$

Taking the time derivative of Equation (6.1), the divergence of Equation (6.2), and combining the two resulting equations yields

$$\frac{1}{c^2}\frac{\partial^2 p}{\partial t^2} - \nabla^2 p = \frac{\partial \dot{q}}{\partial t} \tag{6.3}$$

where
$$\dot{q} = \rho Q \delta(x - x_s)\, \delta(y - y_s)\, \delta(z - z_s) \tag{6.4}$$

with $\dot{q}$ being the mass rate at a monopole location *($x_s$, $y_s$, $z_s$)*. The ideal gas relation $p = c^2\rho$ is also used in Equation (6.4) with $c$ being the wave speed. In Equation (6.4), ρ is mass density, $Q$ is the volumetric rate (displaced volume by the monopole per unit time) and δ is the Dirac delta function. Using Equation (6.4) Equation (6.3) is written as

$$\frac{1}{c^2}\frac{\partial^2 p}{\partial t^2} - \nabla^2 p = \rho \dot{Q}\, \delta(x - x_s)\, \delta(y - y_s)\, \delta(z - z_s) \tag{6.5}$$

where $\dot{Q}$ is the displaced volume acceleration. Equation (6.5) is solved using a modal superposition approach by assuming that the acoustic pressure is the following superposition of the acoustic mode shapes

$$p(x,y,z,t) = \sum_N A_N(t) * \psi_N(x,y,z) \tag{6.6}$$

where $N$ is the mode shape number, $A_N(t)$ is the $N^{th}$ mode participation, and $\psi_N(x,y,z)$ is the $N^{th}$ mode shape. Using Equation (5.43), the mode shapes of the rectangular cavity are

$$\psi_N(x,y,z) = cos\left(\frac{m\pi}{L_{cx}}\ x\right) cos\left(\frac{n\pi}{L_{cy}}\ y\right) cos\left(\frac{l\pi}{L_{cz}}\ z\right) \tag{6.7}$$

resulting in

$$\nabla^2\psi_N(x,y,z) = -[(\frac{m\pi}{L_{cx}})^2 + (\frac{n\pi}{L_{cy}})^2 + (\frac{l\pi}{L_{cz}})^2)][cos\left(\frac{m\pi}{L_{cx}}\ x\right) cos\left(\frac{n\pi}{L_{cy}}\ y\right) cos\left(\frac{l\pi}{L_{cz}}\ z\right)]$$

If
$$k_N^2 = \frac{\omega_N^2}{c^2} = (\frac{m\pi}{L_{cx}})^2 + (\frac{n\pi}{L_{cy}})^2 + (\frac{l\pi}{L_{cz}})^2 \tag{6.8}$$

the above equation becomes,

$$\nabla^2\psi_N(x,y,z) = -\,k_N^2[cos\left(\frac{m\pi}{L_{cx}}\ x\right) cos\left(\frac{n\pi}{L_{cy}}\ y\right) cos\left(\frac{l\pi}{L_{cz}}\ z\right)] \tag{6.9}$$

Using phasor notation (representation of a harmonic function using complex numbers), we have

$$A_N(t) = Re\left[A_N * e^{j\omega t}\right]\ and\ \dot{Q}_0(t) = Re[\dot{Q}_0 * e^{j\omega t}] \tag{6.10}$$

where $A_N$ is the magnitude of $A_N(t)$ and $\dot{Q}_0$ is the magnitude of $\dot{Q}_0(t)$. The excitation angular frequency is $\omega$. From Equations (6.6) and (6.10) we get

$$\frac{\partial^2 p}{\partial t^2} = \sum_N \frac{\partial^2 A_N(t)}{\partial t^2} * \psi_N(x,y,z) = \sum_N Re[-\omega^2 A_N \psi_N(x,y,z)\, e^{j\omega t}] \tag{6.11}$$

and

$$\nabla^2 p = \sum_N A_N(t) * [-k_N^2 \psi_N(x,y,z)]$$
$$= \sum_N Re[-k_N^2 A_N \psi_N(x,y,z)\, e^{j\omega t}] \tag{6.12}$$

Using Equations (6.10), (6.11) and (6.12), Equation (6.5) becomes

$$\sum_N Re[(k_N^2 - k^2) A_N \psi_N(x,y,z)\, e^{j\omega t}]$$
$$= Re\left[\rho\left|\dot{Q}_0\right| \delta(x-x_s)\, \delta(y-y_s)\, \delta(z-z_s) e^{j\omega t}\right] \tag{6.13}$$

Equating the phasors of the above equation yields

$$\sum_N (k_N^2 - k^2) A_N \psi_N(x,y,z) = \rho\left|\dot{Q}_0\right| \delta(x-x_s)\, \delta(y-y_s)\, \delta(z-z_s) \tag{6.14}$$

Multiplying both sides of the Equation (6.14) by $\psi_M(x,y,z)$ and integrating over the entire domain (volume of rectangular cavity) yields

$$\sum_N (k_N^2 - k^2) A_N \int_V \int \quad \psi_N(x,y,z) * \psi_M(x,y,z) dV$$

$$= \rho\left|\dot{Q}_0\right| \int_V \delta(x-x_s)\, \delta(y-y_s)\, \delta(z-z_s) * \psi_M(x,y,z) dV$$

Using the orthogonality property of the acoustic mode shapes:

$$\int_V \psi_N(x,y,z) * \psi_M(x,y,z) dV = \begin{cases} 0 \; if \; N \neq M \\ \alpha \; if \; N = M \end{cases}$$

where $\alpha$ is a constant equal to one if the modes are orthonormalized, the above equation reduces to

$$(k_N^2 - k^2) A_N \int_V \psi_N^2(x,y,z) dV = \rho\left|\dot{Q}_0\right| \psi_N(x_s, y_s, z_s) \tag{6.15}$$

which yields

$$A_N = \frac{\rho|\dot{Q}_0|\psi_N(x_s, y_s, z_s)}{(k_N^2 - k^2) \quad \int_V \ \psi_N^2(x, y, z)dV} \tag{6.16}$$

Finally, the pressure at any location $(x, y, z)$ is given by

$$p(x, y, z, t) = Re\left[\sum_N A_N * \psi_N(x, y, z)\, e^{j\omega t}\right]$$

$$= Re\left[\sum_N \frac{\rho|\dot{Q}_0|\psi_N(x_s, y_s, z_s)}{(k_N^2 - k^2) \quad \int_V \ \psi_N^2(x, y, z)dV} * \psi_N(x, y, z)\, e^{j\omega t}\right] \tag{6.17}$$

indicating that the pressure is a harmonic signal with magnitude

$$p(x, y, z) = \left[\sum_N \frac{\rho|\dot{Q}_0|\psi_N(x_s, y_s, z_s)}{(k_N^2 - k^2) \quad \int_V \ \psi_N^2(x, y, z)dV} * \psi_N(x, y, z)\right] \tag{6.18}$$

To verify the formulation of this section, we use the same rectangular box mesh as in Section 5.5.2 (Figure 6.1). The monopole was placed at "Point 1" and the response (pressure) was calculated at Points 2 and 3 in the frequency domain. The model represents a pulsating sphere with volumetric acceleration in a closed cavity. The FE model represents an approximate solution to the closed form solution of Equations (6.1) and (6.2). Also, the FE model shows that the developed acoustic cavity model can fully represent an analytical 3-D cavity in the frequency range.

Using NASTRAN Solution Sequence 111 (SEMFREQ - Modal frequency response) the response at grid points 2 and 3 were calculated due to the excitation at grid point 1. RLOAD1 with DAREA NASTRAN cards were used to model the acoustic monopole volumetric acceleration.

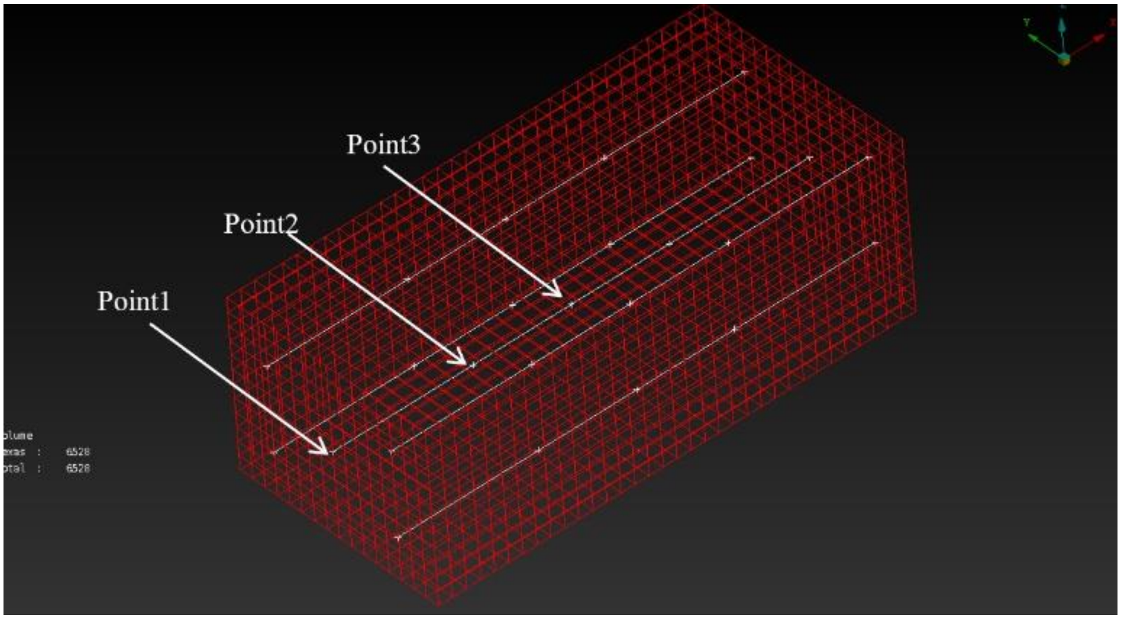


*Figure 6.1* Three locations in acoustic cavity

Figure 6.2 compares the acoustic pressure at points 2 and 3 from MATLAB (analytical formulation) and NASTRAN (FE numerical implementation). We observe a very good agreement between analytical and numerical models.

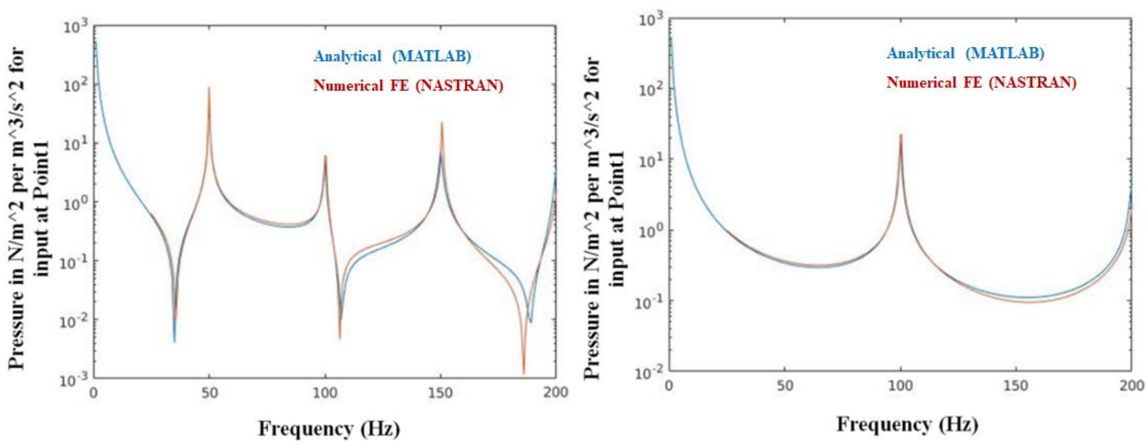


*Figure 6.2* Acoustic pressure at points 2 (left) and 3 (right). Comparison between analytical (MATLAB) and numerical (NASTRAN) results

### 6.2.2 Acoustic Monopole Source with Power Input in a Closed Cavity

Many acoustic monopole source devices require users to specify acoustic power as input. Furthermore, a key characteristic of a speaker is its efficiency defined by the ratio of acoustic power output to electric power input. Consequently, in many instances, the speaker's acoustic output is provided in terms of acoustic power.

An acoustic source is commonly assumed to be a sphere that oscillates in an infinite acoustic field. The strength of the source is characterized by a frequency-dependent flux of volume velocity defined by surface area times velocity. The source strength (volume velocity) is defined as

$$Q = \int \vec{u} \cdot \vec{n} \, dS \qquad (6.19)$$

where $Q$ , the volume velocity, is the dot product of $\vec{n}$ , a unit vector, and $\vec{u}$ , the vector of acoustic particle velocity. The volume velocity of Equation (6.19) can be expressed in terms of the input power in Watts as

$$Q = \frac{1}{2\pi f} \cdot \sqrt{\frac{8\pi c \, W(f)}{\rho}} \qquad (6.20)$$

where $W(f)$ is the input power, $c$ is the speed of sound, $\rho$ is the mass density, and $f$ is the frequency in Hz.

The formulation to obtain the acoustic pressure is the same with that of Section 6.2.1. The only difference is the expression of the volume acceleration $\dot{Q}$ in terms of the volume velocity $Q$. Considering that the former is the time derivative of the latter, we have

$$\dot{Q}(t) = Re\left[\dot{Q}_0 * e^{j\omega t}\right] = Re\left[j\omega \, Q_0 * e^{j\omega t}\right] \qquad (6.21)$$

In this case, Equation (6.13) becomes

$$\sum_N Re[(k_N^2 - k^2)\bar{A}_N \psi_N(x,y,z)\, e^{j\omega t}]$$
$$= Re[\rho j\omega Q_0 \delta(x - x_s)\, \delta(y - y_s)\, \delta(z - z_s)\, e^{j\omega t}] \tag{6.22}$$

where $\bar{A}_N$ is a complex number representing the phasor of $A_N(t)$. Equating the phasors in the above equation results in

$$\sum_N (k_N^2 - k^2)\bar{A}_N \psi_N(x,y,z) = \rho j\omega Q_0 \delta(x - x_s)\, \delta(y - y_s)\, \delta(z - z_s) \tag{6.23}$$

Using the orthogonality property of the acoustic mode shapes, the above equation yields

$$\bar{A}_N = \frac{\rho j\omega Q_0 \psi_N(x_s, y_s, z_s)}{(k_N^2 - k^2) \quad \int_V \psi_N^2(x,y,z) dV} \tag{6.24}$$

The pressure distribution at location $(x, y, z)$ is then given by

$$p(x,y,z,t) = Re\left[\sum_N \bar{A}_N * \psi_N(x,y,z)\, e^{j\omega t}\right] \tag{6.25}$$

or

$$p(x,y,z,t) = Re\left[\sum_N \frac{\rho j\omega . \frac{1}{2\pi f} \; . \sqrt{\frac{8\pi c\, W(f)}{\rho}} . \psi_N(x_s, y_s, z_s)}{(k_N^2 - k^2) \quad \int_V \psi_N^2(x,y,z) dV} \right.$$
$$\left. * \psi_N(x,y,z)\, e^{j\omega t}\right] \tag{6.26}$$

indicating that the pressure is a harmonic signal with magnitude

$$p(x,y,z) = \sum_N \frac{\rho j\omega . \frac{1}{2\pi f} . \sqrt{\frac{8\pi c\, W(f)}{\rho}} . \psi_N(x_s, y_s, z_s)}{(k_N^2 - k^2) \quad \int_V \psi_N^2(x,y,z) dV} * \psi_N(x,y,z) \tag{6.27}$$

To verify the formulation of this section, the same rectangular domain of Section 5.5.2 is used. The monopole was placed at “Point 1” with power input excitation equal to 1.0 [N*mm/s] or 0.001 [Watts] and the response (pressure) was calculated at Points 2 and 3 in the frequency domain. The model represents a pulsating sphere in a closed cavity.

To describe the load as a power input, ACSRCE and DAREA NASTRAN cards were used and using NASTRAN Solution Sequence 111 (SEMFREQ - Modal frequency response) the response at grid points 2 and 3 were calculated with power source excitation at grid point 1.

Figure 6.3 compares the acoustic pressure at points 2 and 3 from closed-form solution implemented in MATLAB and the numerical solution in NASTRAN (FE implementation). We observe a very good agreement indicating that both the developed analytical approach and the FE implementation are accurate in representing the acoustic source as a monopole with a specified input power.

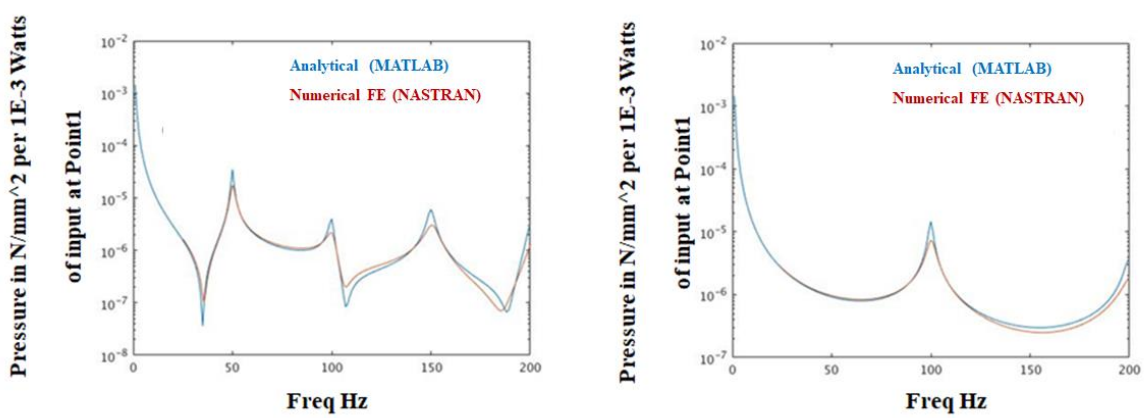


*Figure 6.3* Acoustic pressure at points 2 (left) and 3 (right). Comparison between analytical (MATLAB) and numerical (NASTRAN) for a monopole with power input

6.3 Acoustic Monopole Source in Anechoic Room

It is common to optimize subsystems instead of a full vehicle in order to streamline the development process and have a better understanding of each subsystem. The accuracy of subsystem modeling is crucial for creating realistic and predictive full vehicle models. For acoustic analysis these subsystems are studied in an anechoic room representing a far-field acoustic condition with no reverberations. In this Section, we developed a closed-form solution for a monopole acoustic source in a far field and established a general FE model which is validated using the closed-form solution. The FE model can be then used for realistic vehicle subsystem acoustic studies.

The 3-D linearized wave equation in Cartesian coordinates can be written as

$$\nabla^2 p = \frac{1}{c^2}\frac{\partial^2 p}{\partial t^2} \tag{6.28}$$

where

$$\nabla^2 = \frac{\partial^2}{\partial x^2} + \frac{\partial^2}{\partial y^2} + \frac{\partial^2}{\partial z^2}$$

For a spherical coordinate system (Figure 6.4), we have

$$x = r\, sin\theta\, cos\,\varphi\,,\, y = r\, sin\theta\, sin\,\varphi\ and\, z = r\, cos\,\theta$$

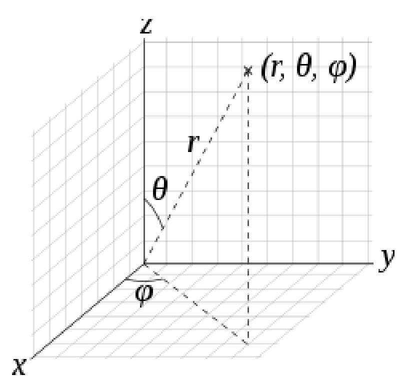


*Figure 6.4* Spherical coordinate system

where r is the radial distance, $\theta$ is the polar angle, and $\varphi$ is the azimuthal angle. Therefore,

$$\nabla^2 = \frac{\partial^2}{\partial r^2} + \frac{2}{r}\frac{\partial}{\partial r} + \frac{1}{r^2 \sin\theta}\frac{\partial(\sin(\theta)\frac{\partial}{\partial\theta})}{\partial\theta} + \frac{1}{r^2 \sin\theta^2}\frac{\partial^2}{\partial\varphi^2}$$

Because we have spherical symmetry, the wave is a function of the radial distance and time but not of angular coordinates. Therefore, the above Laplacian reduces to

$$\nabla^2 = \frac{\partial^2}{\partial r^2} + \frac{2}{r}\frac{\partial}{\partial r}$$

and the pressure equation becomes

$$\frac{\partial^2 p}{\partial r^2} + \frac{2}{r}\frac{\partial p}{\partial r} = \frac{1}{c^2}\frac{\partial^2 p}{\partial t^2} \tag{6.29}$$

or

$$\frac{1}{c^2}\frac{\partial^2(p*r)}{\partial t^2} - \frac{\partial^2(p*r)}{\partial r^2} = 0 \tag{6.30}$$

The solution of Equation (6.30) can be expressed by the following harmonic function

$$p(r,t) = \frac{\kappa}{r}e^{j(\omega t - kr)} \tag{6.31}$$

where $p$ is the acoustic pressure in [Pa], $c$ is speed of sound in air in [m/s], $\rho$ is the air density in [Kg/m$^3$], $\kappa$ is a complex value, $r$ is the radial coordinate in [m], $u$ is the radial velocity of air in [m/s], $k=\omega/c$ is the wave number, $\omega=2\pi f$ is the angular frequency in [rad/s], and $f$ is in [Hz]. Note that the pressure is proportional to $\frac{\mathbf{1}}{\boldsymbol{r}}$.

Using the acoustic momentum equation

$$\rho\frac{\partial u}{\partial t}+\frac{\partial p}{\partial r}=0 \tag{6.32}$$

the radial particle velocity $u(r,t)$ can then be calculated in terms of the pressure by substituting Equation (6.31) in Equation (6.32) yielding

$$\frac{\partial u(r,t)}{\partial t}=-\frac{\partial p(r,t)}{\partial r}*\ \frac{1}{\rho} \tag{6.33}$$

From Equation (6.32), the derivative $\frac{\partial u}{\partial t}$ of the particle velocity is expressed as

$$\frac{\partial u(r,t)}{\partial t}=-\frac{\partial p(r,t)}{\partial r}*\ \frac{1}{\rho}=-\frac{\partial\left(\frac{\kappa}{r}e^{j(\omega t-kr)}\right)}{\partial r}*\ \frac{1}{\rho}$$

$$=\ -\frac{\kappa}{\rho}\left[\frac{-krje^{j(\omega t-k_w r)}-e^{j(\omega t-kr)}}{r^2}\right]=\frac{\kappa}{\rho}\left[\frac{(1+krj)e^{j(\omega t-kr)}}{r^2}\right]$$

which after integration results in the particle velocity $u(r,t)$ as

$$u(r,t)=\int\frac{\kappa}{\rho}\left[\frac{(1+krj)e^{j(\omega t-kr)}}{r^2}\right]\,dt=\frac{\kappa}{\rho}\frac{(1+krj)}{r^2}\int\left[e^{j(\omega t-kr)}\right]dt$$

$$=\frac{\kappa}{\rho}Re[\frac{(1+krj)}{r^2}*\ \frac{1}{j\omega}\left[e^{j(\omega t-kr)}\right]]$$

or

$$u(r,t)=\frac{\kappa}{r}Re[e^{j(\omega t-kr)}*\ \frac{(1+krj)}{j\omega r\rho}]=Re[p(r,t)*\ \frac{(1+krj)}{j\omega r\rho}]$$

$$=Re[p(r,t)*\ \frac{(-j+kr)}{kcr\rho}]$$

Finally, the above equation becomes

$$u(r,t)=\frac{-jp(r,t)}{\rho ckr}(1+jkr)=\frac{1}{j\omega\rho}\left(jk+\frac{1}{r}\right)p(r,t)$$

$$u(r,t)=\frac{1}{j\omega\rho}\left(jk+\frac{1}{r}\right)p(r,t) \tag{6.34}$$

or since $\omega = ck$

We can model a monopole as a pulsating sphere of a very small radius $\alpha$. The surface of the sphere is pulsating harmonically with a radial surface velocity $u_s$ as

$$u_s(t) = U_0 e^{j\omega t}$$

Therefore, for the spherical acoustic field we have

$$u(r = \alpha\, , t) = u_s(t)$$

Applying this boundary condition to Equation (6.34), the pressure is calculated as

$$p(r,t) = j\,\frac{Q_0 \rho c k}{4\pi r}\, e^{j(\omega t - kr)} \tag{6.35}$$

where $Q_0 = U_0 * 4\pi a^2$ is the source acoustic strength amplitude (volumetric velocity) in [$m^3/s$]. Equation (6.35) indicates that the acoustic pressure amplitude is

$$|p(r,t)| = \frac{Q_0 \rho c k}{4\pi r} \tag{6.36}$$

Equation (6.36) can be also expressed in terms of volumetric acceleration $\dot{Q}_0$ as

$$|p(r,t)| = \frac{\dot{Q}_0 \rho}{4\pi r} \tag{6.37}$$

A FE model was also developed and validated using Equation (6.35). A sphere with a radius of 500 mm was used to represent the near field. The sound pressure level (SPL) was evaluated at 1000 mm (acoustic far field) using a monopole excitation $\dot{Q}_0$ (volumetric acceleration) of 10000.0 [$mm^3/s^2$].

Using NASTRAN, the far-field with the monopole source was modeled as shown in Figure 6.5. The monopole source was placed at the center of an acoustic near field meshed cavity which is part of the far-field.

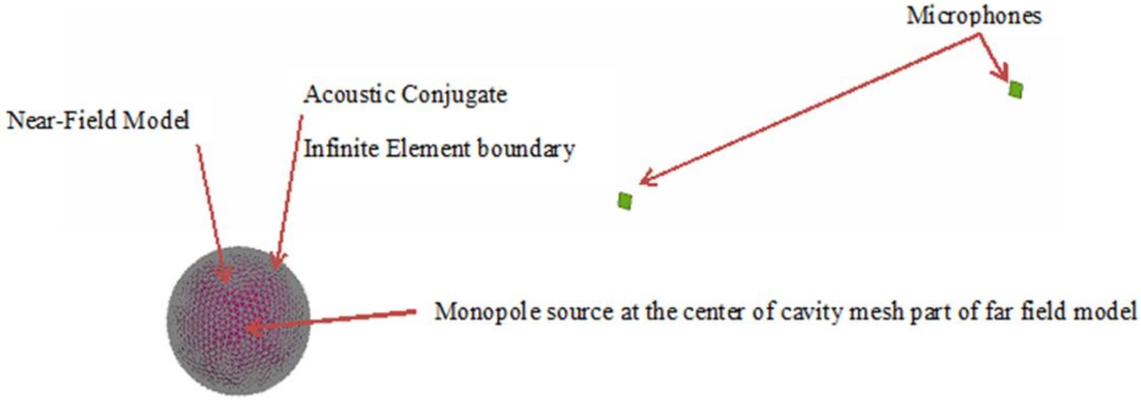


*Figure 6.5* FE modeling of a monopole source

The FE model above represents a pulsating sphere in a far field. For the near field, mesh PSOLID elements were used as shown in Figure 6.6. At the boundary of the near and far fields conjugate infinite elements (CACINF3) were used. These elements represent the transition region between near and far fields. The element normal, defined by the right-hand rule, should be pointing to the far-field as shown in Figure 6.7.

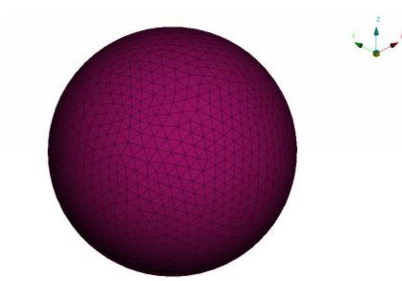

*Figure 6.6* 3-D cavity CAE mesh for acoustic near field domain

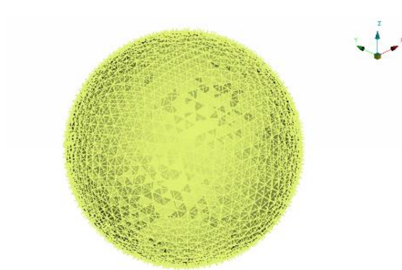

*Figure 6.7* CACINF elements

In a NASTRAN model utilizing CACINF elements, the inclusion of a PACINF card is necessary. A key parameter in the PACINF property card for far-field calculations is the RIO which denotes the radial interpolation order. The choice of RIO depends on the directivity of the pressure field. For geometrically simple shapes such as a sphere, a value ranging from 5 to 7 is considered reasonable. Opting for a higher interpolation order enhances the solution accuracy but increases the computational time significantly. The monopole is placed at the pole of PACINF interpolation at a point defining the center of the near field as shown in Figure 6.8.

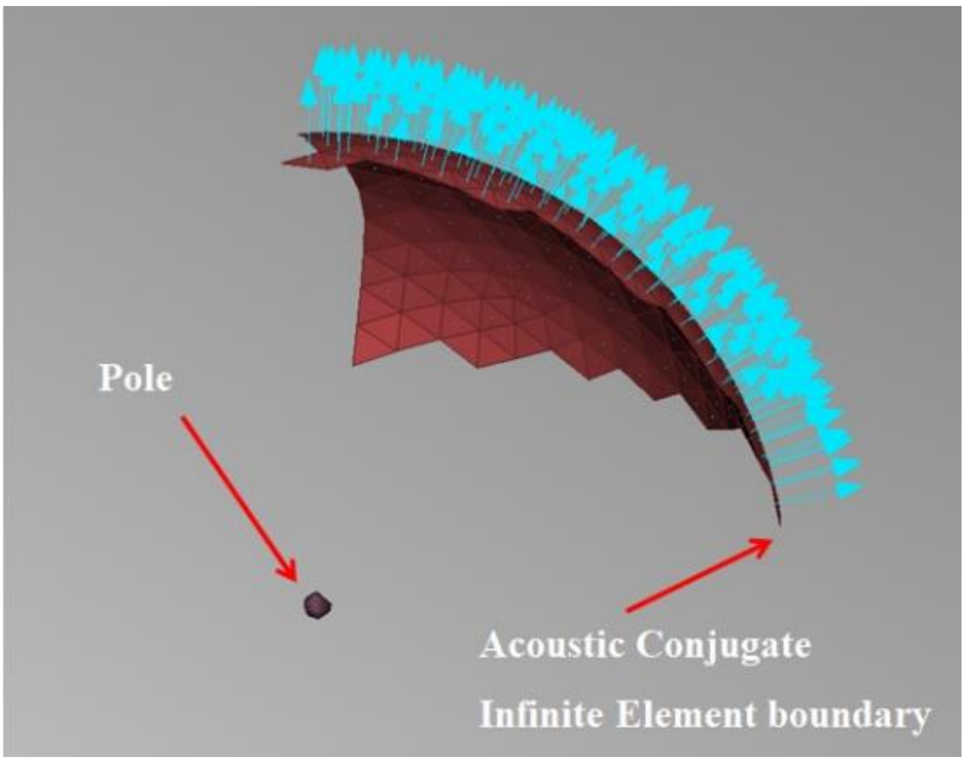


*Figure 6.8* CACINF infinite element pole

Figure 6.9 compares the closed-form solution of Equation (6.35) with the FE solution (NASTRAN). A very good agreement is observed indicating that the modeling method is correct.

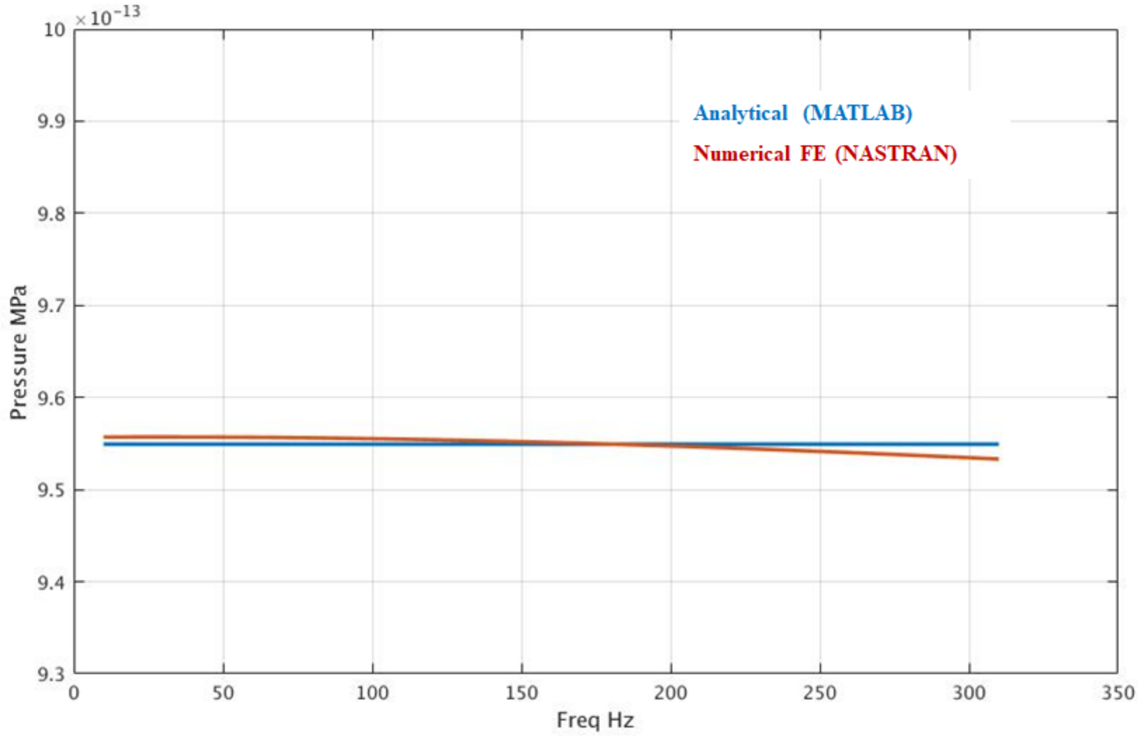


*Figure 6.9* Far-field acoustic pressure from monopole source– Numerical solution (NASTRAN) versus analytical solution

6.4 Speaker Modeling as Acoustic Dipole in Closed Cavity

An acoustic dipole is a common model of a loudspeaker. It consists of two monopoles separated by a small distance, vibrating in opposite directions. The vibration of each monopole generates alternating compressions and rarefactions in the surrounding air, effectively creating sound waves. In the context of a loudspeaker, the two sources represent the motion of the diaphragm, which moves back and forth as it converts electrical signals into sound waves. By treating the loudspeaker as an acoustic dipole, we can analyze its behavior with simplicity, focusing on the basic principles of wave propagation and radiation patterns.

The acoustic dipole model provides insights into the directional characteristics of a loudspeaker. Depending on the relative size and spacing of the sources, the radiation pattern of the sound waves can vary. For instance, in the case of a small loudspeaker driver, the dipole pattern tends to exhibit stronger radiation perpendicular to the driver's motion, resulting in more focused sound projection. Understanding these directional properties is crucial in speaker design and placement, as it influences the dispersion of sound and its interaction with the listening environment. Thus, while a loudspeaker may consist of complex components and mechanisms, the concept of the acoustic dipole offers a fundamental framework for grasping its essential behavior and performance.

A dipole source consists of two monopole sources of equal strength (same volume velocity Q) but opposite phase separated by a small distance compared with the wavelength of interest (Figure 6.10).

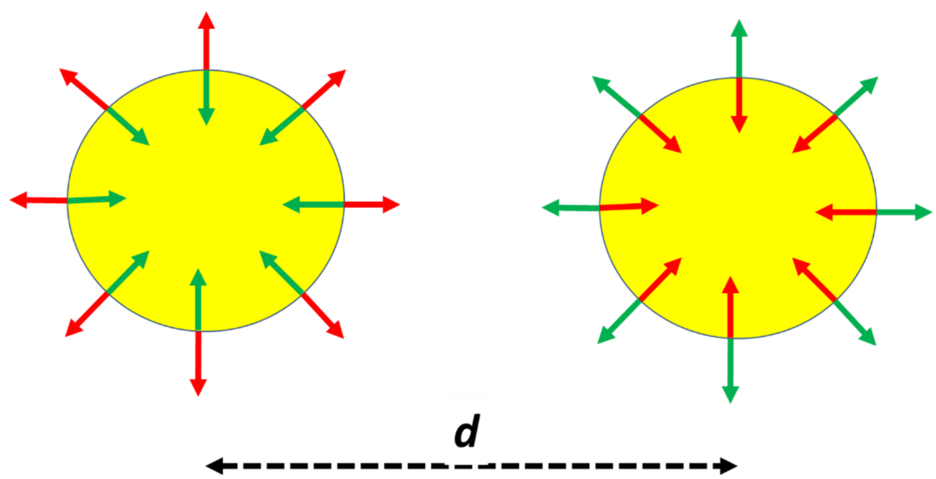


*Figure 6.10* Schematic of a dipole

In general, a point dipole is a good approximation to a small vibrating body that does not change its volume as a function of time. Such a source exerts a force on the fluid. The dipole source is typically modeled as two monopole acoustic sources that are out of phase, and they are separated by a known distance *d.* The distance *d* must be small. However, in FE modeling, a finite distance *d* must be defined clearly because of mesh size limitation. A dipole is represented by two out of phase monopoles if the variation of pressure at given frequency is low in distance between the two out of phase monopoles. For the sound cosine wave of Figure 6.11 and Figure 6.12, the wave has a wavelength λ that is determined by the frequency of the wave. At a known frequency the monopoles representing the dipole must be at a distance *d* so that the pressure difference between them is small. For Figure 6.11 the distance *d* is very large while for Figure 6.12 it is small compared to the pressure difference.

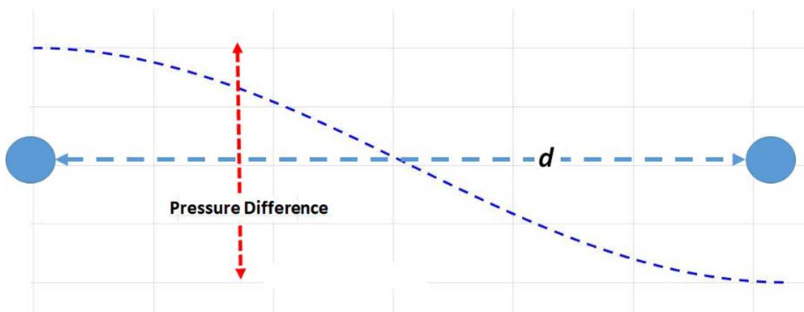


*Figure 6.11* Inadequate distance for dipole modeling

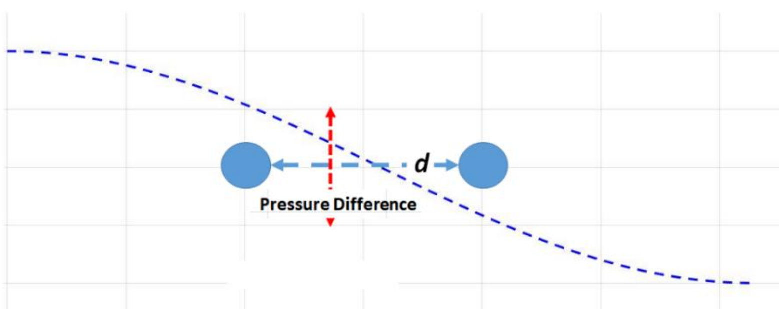


*Figure 6.12* Adequate distance for dipole modeling

The distance *d* should satisfy the relation

$$k.d \ll 1 \tag{6.38}$$

so that,

$$\frac{\omega}{c}.d \ll 1 \quad , \qquad \frac{2\pi f}{c}.d \ll 1\,, \quad \frac{2\pi}{\lambda}.d \ll 1$$

Thus, the distance must satisfy

$$d \ll \frac{c}{2\pi f} \tag{6.39}$$

Using Equation (6.17), the pressure for two acoustic monopoles representing a dipole can be expressed as

$$p(x,y,z,t) = Re\left[\sum_N \frac{\rho|\dot{Q}_0|\psi_N(x_{d1},y_{d1},z_{d1})}{(k_N^2 - k^2) \quad \int_V \ \psi_N^2(x,y,z)dV} * \psi_N(x,y,z)\, e^{j\omega t} + \sum_N \frac{\rho|\dot{Q}_0|\psi_N(x_{d2},y_{d2},z_{d2})}{(k_N^2 - k^2) \quad \int_V \ \psi_N^2(x,y,z)dV} * \psi_N(x,y,z)\, e^{j\omega t+\pi}\right] \tag{6.40}$$

where $x_{d1}, y_{d1}, z_{d1}$ and $x_{d2}, y_{d2}, z_{d2}$ are the coordinate locations of each monopole so that,

$$d = \sqrt{(x_{d2} - x_{d1})^2 + (y_{d2} - y_{d1})^2 + (z_{d2} - z_{d1})^2} \tag{6.41}$$

indicating that the pressure is a harmonic signal with magnitude,

$$p(x,y,z) = \sum_N \frac{\rho|\dot{Q}_0|[\psi_N(x_{d1},y_{d1},z_{d1}) - \psi_N(x_{d2},y_{d2},z_{d2})]}{(k_N^2 - k^2) \quad \int_V \ \psi_N^2(x,y,z)dV} * \psi_N(x,y,z) \tag{6.42}$$

In this section, we use the same rectangular box mesh as section 5.5.2 to evaluate the accuracy of a FE model using a dipole excitation in the closed cavity (Figure 6.13).

The two monopoles of the dipole were placed at “Point 1” and “Point 2” with $d$ = 100 mm and the acoustic pressure was calculated at Points 3 and 4 in the frequency domain. “Point3” is along the dipole axis and “Point4” is near the mid-plane of the dipole.

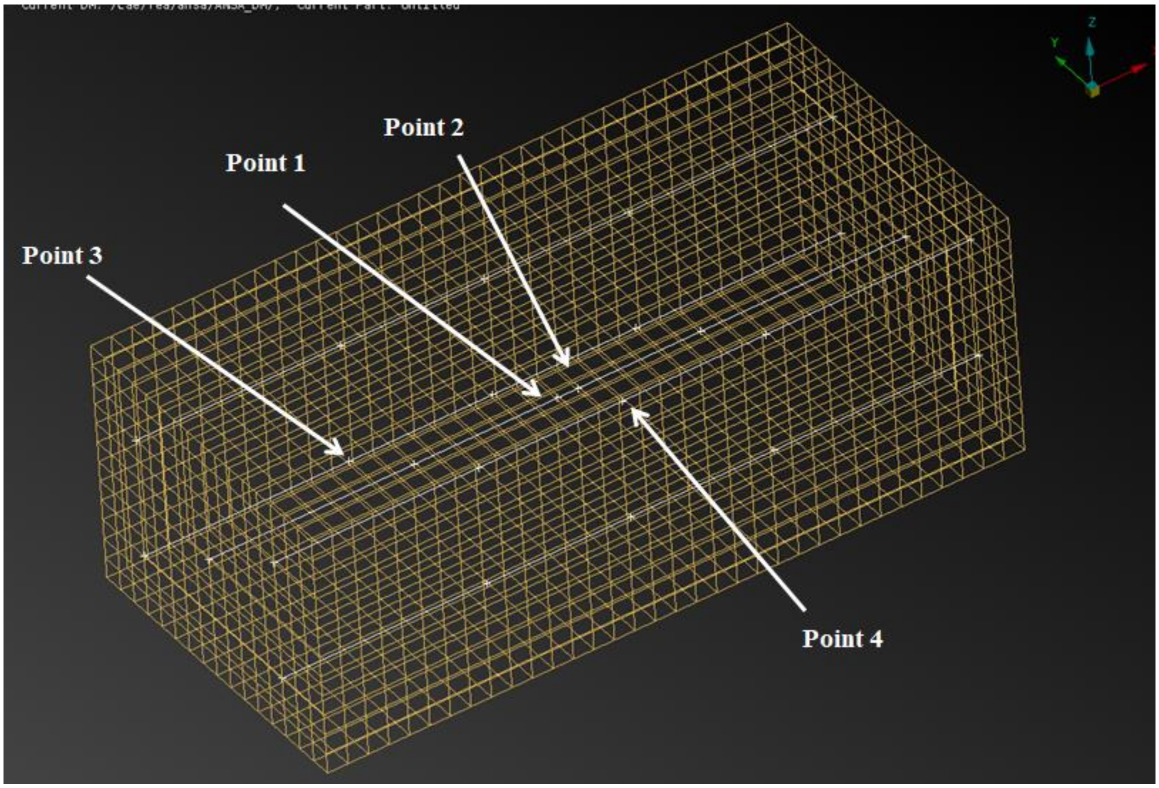


*Figure 6.13* Closed cavity with dipole acoustic source

The FE model represents a pulsating dipole in a closed cavity. At grid points 1 and 2 two out of phase monopole acoustic sources are modeled to represent a pulsating dipole with volumetric acceleration input. The out of phase condition is satisfied using NASTRAN’s DPHASE card with 180 degrees phase difference between each monopole source. Using NASTRAN Solution Sequence 111 (SEMFREQ - Modal frequency response), the SPL response at grid Points 3 and 4 were calculated.

Figure 6.14 and Figure 6.15 compare the acoustic pressure at Points 3 and 4 between the analytical solution (Equation 6.42) and the FE solution (NASTRAN). We observe a good agreement indicating that the developed analytical approach and the FE modeling are consistent.

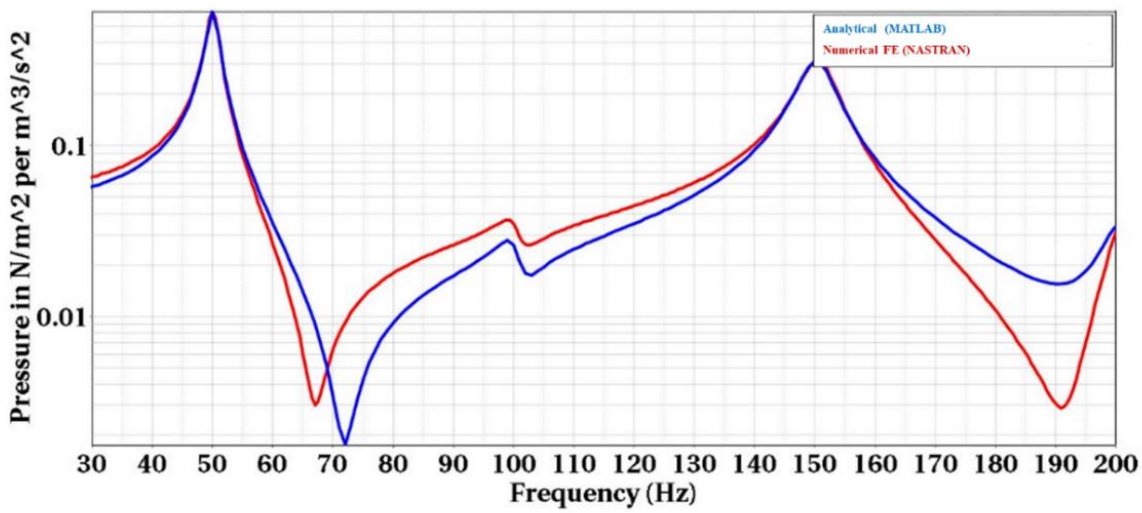


*Figure 6.14* Response at Point 3: FE model versus analytical

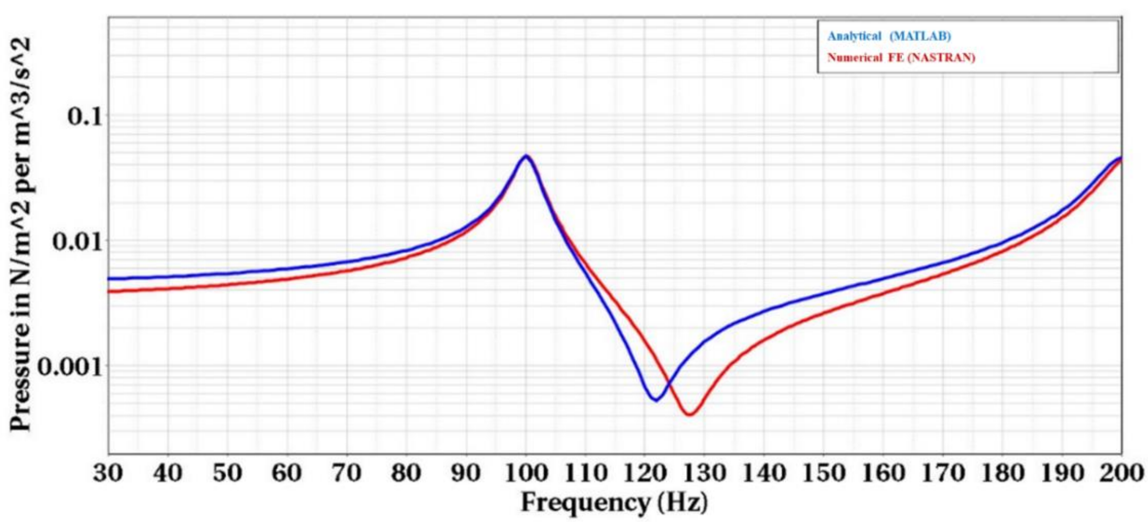


*Figure 6.15* Response at Point 4: FE model versus analytical

## 6.5 Speaker Modeling as Acoustic Dipole in Anechoic Room

### 6.5.1 Closed Form Solution for Acoustic Dipole Source in Anechoic Room

In a free field a dipole acoustic source does not radiate sound in all directions equally. The directivity pattern has a “∞“ shape (Figure 6.16). There are two regions where sound is radiated very well, and two regions where sound cancels. The sound pressure (in Pa) at some distance *r* (meters) is given by:

$$p(r,\theta,t) = Re[j\frac{Q_0\rho ck^2 d}{4\pi r}cos\theta e^{j(\omega t-kr)}] \quad (6.43)$$

where $d$ is the horizontal distance between the two sources, $\rho$ is the air density, *c* is the speed of sound, ω (= 2π *f*) is the frequency *f* in Hz, *t* is time, *k* is the wave number, and $Q$ is the source strength ($m^3$/s) which is the product of the surface area and the normal surface velocity of the monopole. The sound pressure of Equation (6.43) and the particle velocity generated by the two monopoles can be derived by adding the pressure and velocity contributions of the two monopoles using Equations (6.34) and (6.35) . The amplitude of sound pressure in Equation (6.43) is:

$$|p(r,\theta)| = \frac{Q_0\rho ck}{4\pi r} * kd * cos\theta \quad (6.44)$$

Which is interpreted as the product of the pressure amplitude $\frac{Q_0\rho ck}{4\pi r}$ radiated by a monopole, a term $kd$ which relates the radiated wavelength to the source separation, and a directivity function $cos\theta$ which depends on the angle $\theta$.

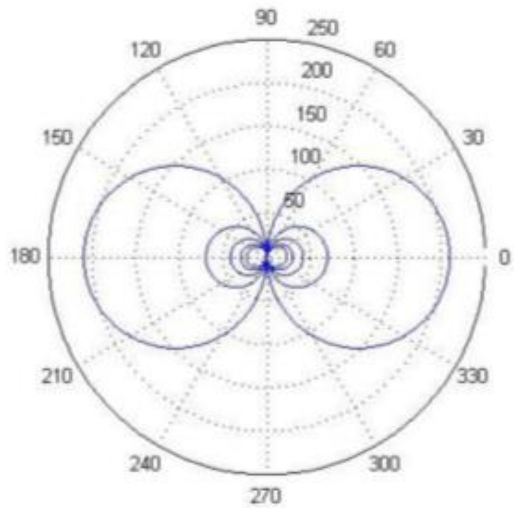


*Figure 6.16* Directivity pattern of a dipole

### 6.5.2 Demonstration Problem for Acoustic Dipole Source in Anechoic Room

We will use a formulation shown in section 6.5.1 and a FE modeling strategy to demonstrate a dipole modeling technique that directly correlates with closed form solution. The dipole was modeled with pulsating small spheres as shown in Figure 6.17. To model the far field, a small sphere of air around the dipole was used to represent near field.

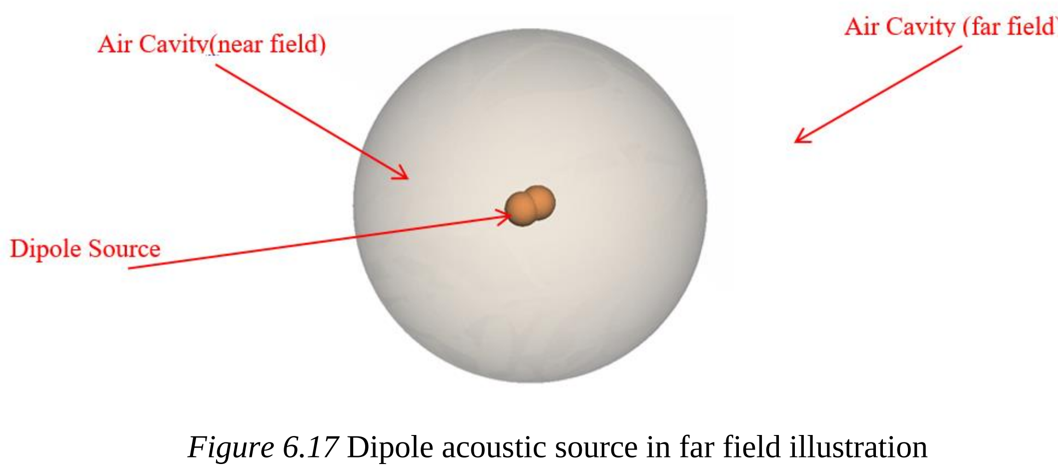


*Figure 6.17* Dipole acoustic source in far field illustration

Figure 6.18 shows the NASTRAN FE model used to model the dipole. The model uses two out of phase monopole pulsating small spheres at a known distance embedded in an acoustic sphere representing the near field. The conjugate infinite element boundary represents the start of the far field. A simplified spherical shape and two merged dipole small spheres for dipole are used. The near field cavity was constructed using NASTRAN PSOLID fluid elements as shown in Figure 6.19. Acoustic conjugate infinite elements (CACINF3) were used to represent the transition region between near and far fields. For the acoustic field point mesh, the "microphone" elements were used to evaluate the far field acoustic pressure.

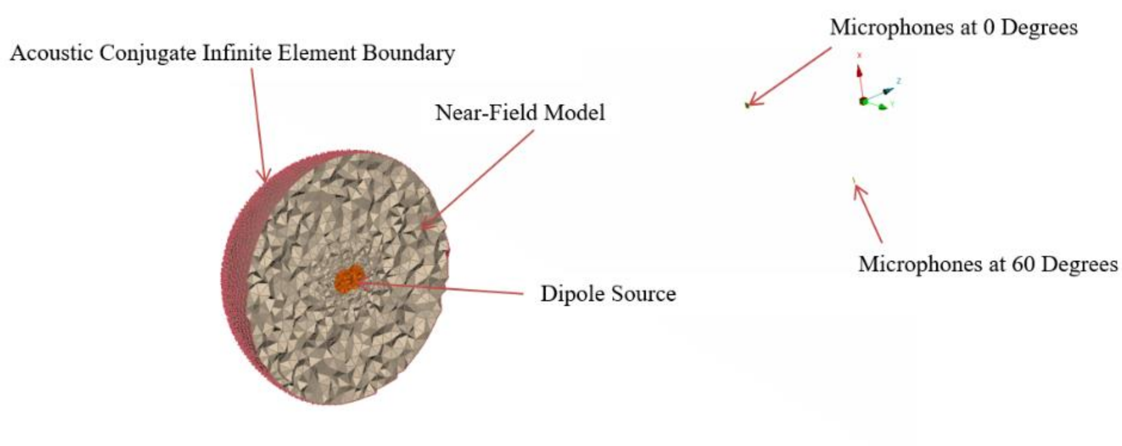


*Figure 6.18* Cross-section view of dipole model and microphone's locations

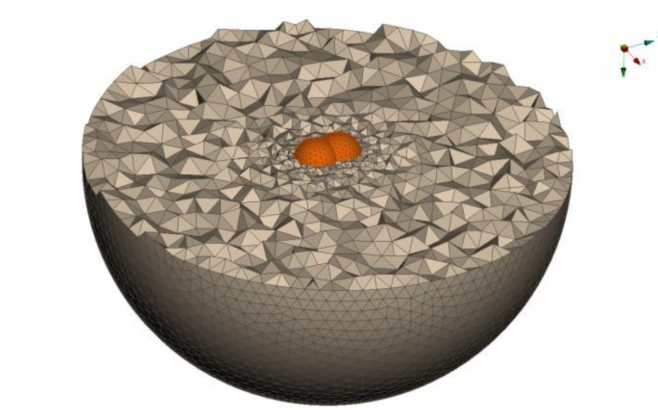

*Figure 6.19* Cross-section of 3-D cavity mesh for near field surrounding dipole

A dipole acoustic source with a volumetric acceleration of magnitude of $10^6$ [$mm^3/s^2$] was used as an input. The pressure magnitude is calculated 1000 mm away at zero degrees and 60 degrees from the front of the dipole speaker (Figure 6.20). Figure 6.21 compares the analytical solution with the numerical FE solution from NASTRAN. The SPL response was calculated using NASTRAN solution sequence 111 (SEMFREQ - Modal frequency response). A very good agreement is observed indicating that the modeling method is correct, and the directivity of the sound pressure is captured.

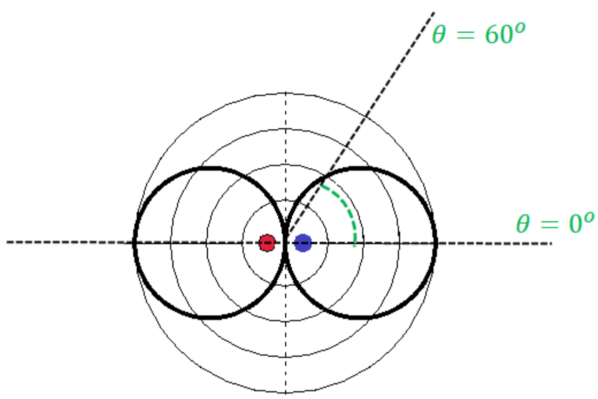


*Figure 6.20* Orientation of dipole response points in far field

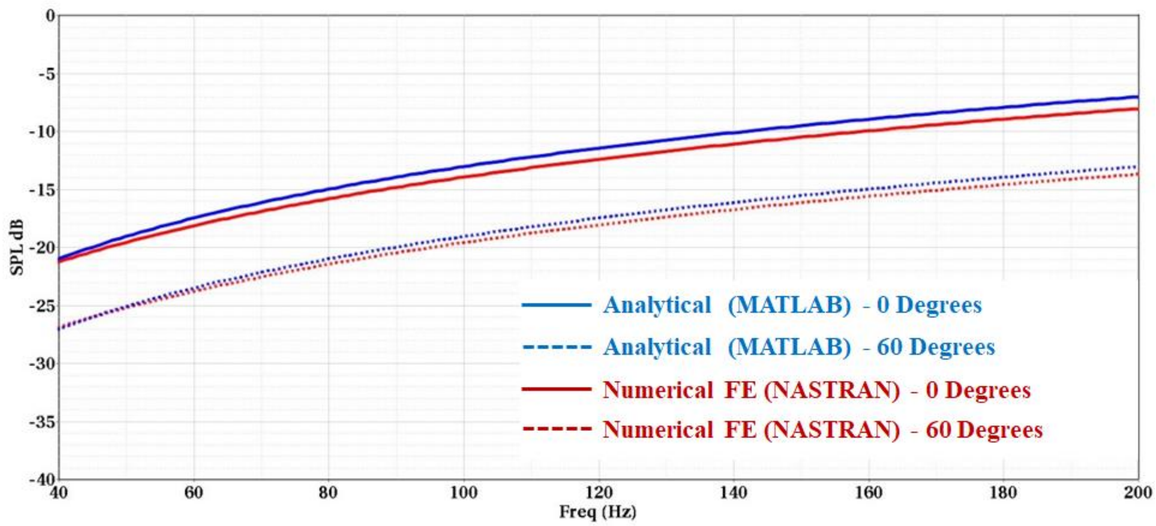


*Figure 6.21* Comparison of response at $0^0$ and $60^0$ in front of dipole between analysis and FE (NASTRAN)

6.6 Modeling of Moving Cone Acoustic Source in Closed Cavity

In many cases the acoustic source is not as simple as a monopole or a dipole source. One of these cases, a moving cone model is considered. While the acoustic dipole provides a basic understanding of loudspeaker operation, a moving cone offers a more comprehensive representation due to its ability to capture the dynamic nature of sound production. Unlike the static nature of the dipole model, a moving cone represents the continuous motion of the loudspeaker diaphragm as it responds to electrical signals. This motion results in varying levels of compression and rarefaction in the air, producing sound waves with complex waveforms and frequencies. Additionally, the moving cone representation allows for the consideration of factors such as resonance, damping, and frequency response, which play crucial roles in determining the loudspeaker's overall performance and fidelity.

The speaker cone which may have a very complex geometry, is coupled to the door cavity and vehicle cavity. Therefore, it is important to develop an analytical model to describe the acoustic field of a moving cone in a closed cavity and develop a FE model to represent this acoustic field. The analytical and the numerical results will be used to verify the accuracy of the FE modeling for the moving cone. We will consider the cone as a rigid plate since its flexibility in the ANC frequency range is negligible as shown by M. Petyt and P. Gelat [53].

We have mentioned that the acoustic pressure obeys the linearized wave equation

$$\frac{1}{c^2}\frac{\partial^2 p}{\partial t^2} - \nabla^2 p = \frac{\partial \dot{q}}{\partial t} \tag{6.45}$$

where $\dot{q}$ is the mass rate (mass per time). Figure 6.22 defines a rectangular cone (plate) moving in the *x* direction. Its area is equal to $(z_2\text{-}z_1)\ (y_2\text{-}y_1)$. The cone is moving with a velocity $v_x$ in the positive *x* direction and is perpendicular to the *x* direction at $x = x_s$.

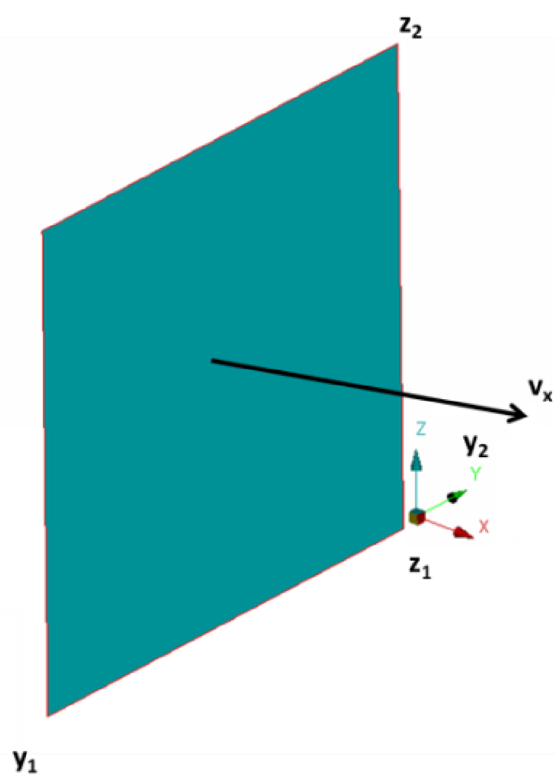


*Figure 6.22* Notation of rectangular moving cone

The mass rate $\dot{q}$ is given by

$$\dot{q} = \rho v_x \delta(x - x_s)\,[h(z - z_1) - h(z - z_2)].\,[h(y - y_1) - h(y - y_2)] \tag{6.46}$$

where $\rho$ is the mass density, $\delta$ is the Dirac delta function, and $h$ is the step function. If

$$F(y) = [h(y - y_1) - h(y - y_2)]$$

$$F(z) = [h(z - z_1) - h(z - z_2)]$$

Equation (6.45) becomes

$$\frac{1}{c^2}\frac{\partial^2 p}{\partial t^2} - \nabla^2 p = \rho\,\dot{v_x} F(y) * F(z) * \delta(x - x_s) \tag{6.47}$$

Like Section 5.5, a modal superposition approach is used, and the acoustic pressure is represented as

$$p(x, y, z, t) = \sum_N A_N(t) * \psi_N(x, y, z) \tag{6.48}$$

where *N* is the mode shape number, $A_N(t)$ is the $N^{th}$ mode participation, and $\psi_N(x, y, z)$ is the $N^{th}$ mode shape.

Using phasor notation, we have

$$A_N(t) = Re[\bar{A}_N * e^{j\omega t}]\ and\, \dot{v_x}(t) = Re[j\omega V_x * e^{j\omega t}] \tag{6.49}$$

where $\bar{A}_N$ is the phasor of $A_N(t)$ and $V_x$ is the magnitude of the harmonic velocity $v_x(t)$. The excitation frequency (i.e., frequency of $v_x(t)$) is $\omega$.

As in section 5.5, the phasor $\bar{A}_N$ is calculated from

$$\textstyle\sum_N Re[(k_N^2 - k^2)\bar{A}_N \psi_N(x, y, z)\, e^{j\omega t}] = Re[\rho\, j\omega V_x F(y) * F(z) * \delta(x - x_s)\, e^{j\omega t}$$

Equating the phasors in the above equation results in

$$\sum_N (k_N^2 - k^2)\bar{A}_N \psi_N(x,y,z) = \rho\, j\omega V_x F(y) * \; F(z) * \delta(x - x_s) \tag{6.50}$$

and multiplication of both sides by $\psi_M(x,y,z)$ and integration over the entire domain (volume of rectangular cavity) yields

$$\sum_N (k_N^2 - k^2)\bar{A}_N \int_V \psi_N(x,y,z) * \psi_M(x,y,z) dV = \rho\, j\omega V_x \int_{z_1}^{z_2} \int_{y_1}^{y_2} \psi_M(x_s,y,z) \quad dydz$$

Using the orthogonality property of the acoustic mode shapes, the above equation yields

$$\bar{A}_N = \frac{\rho\, j\omega V_x \int_{z_1}^{z_2} \int_{y_1}^{y_2} \psi_N(x_s,y,z) \quad dydz}{(k_N^2 - k^2) \quad \int_V \; \psi_N^2(x,y,z) dV} \tag{6.51}$$

The pressure distribution at location $(x,y,z)$ is then given by

$$\begin{aligned} p(x,y,z,t) &= Re\left[\sum_N \bar{A}_N * \psi_N(x,y,z)\, e^{j\omega t}\right] \\ &= Re\left[\sum_N \frac{\rho\, j\omega V_x \int_{z_1}^{z_2} \int_{y_1}^{y_2} \psi_N(x_s,y,z) \quad dydz}{(k_N^2 - k^2) \quad \int_V \; \psi_N^2(x,y,z) dV} \right. \\ &\quad \left. * \psi_N(x,y,z)\, e^{j\omega t}\right] \end{aligned} \tag{6.52}$$

The above pressure can also be expressed as

$$p(x,y,z,t) = Re\left[\bar{P}(x,y,z) e^{j\omega t}\right]$$

where

$$\begin{aligned} \bar{P}(x,y,z) &= \sum_N \frac{\rho\, j\omega V_x \int_{z_1}^{z_2} \int_{y_1}^{y_2} \psi_N(x_s,y,z) \quad dydz}{(k_N^2 - k^2) \quad \int_V \; \psi_N^2(x,y,z) dV} * \psi_N(x,y,z) \\ &= P e^{+j\varphi} \end{aligned} \tag{6.53}$$

is the phasor (complex quantity) of $p(x, y, z, t)$ having a magnitude $P$ and a phase $\varphi$. The acoustic pressure can be finally expressed as

$$p(x, y, z, t) = Pcos(\omega t + \varphi) \tag{6.54}$$

Note that at any resonance (i.e. $k_N^2 = k^2$) the magnitude $P$ of the phasor $\bar{P}(x, y, z)$ (Equation (6.54)) becomes infinite because we have assumed no damping. To avoid this singular condition, we assumed that there is damping equal to a small percentage $\alpha_d$ of stiffness. In this case, Equation (6.54) becomes

$$\bar{P}(x, y, z) = \sum_N \frac{\rho\, j\omega V_x \int_{z_1}^{z_2} \int_{y_1}^{y_2} \psi_N(x_s, y, z) \quad dydz}{[k_N^2(1 + j\omega\alpha_d) - k^2] \quad \int_V \ \psi_N^2(x, y, z) dV} * \psi_N(x, y, z) = Pe^{+j\varphi} \tag{6.55}$$

where the factor $\alpha_d$ can be estimated by measuring the modal damping at a resonance of interest.

We used the same simple rectangular box cavity of previous sections along with a moving cone for the analytical and the FE developments. The moving cone is modeled with a rigid plate as shown in Figure 6.23.

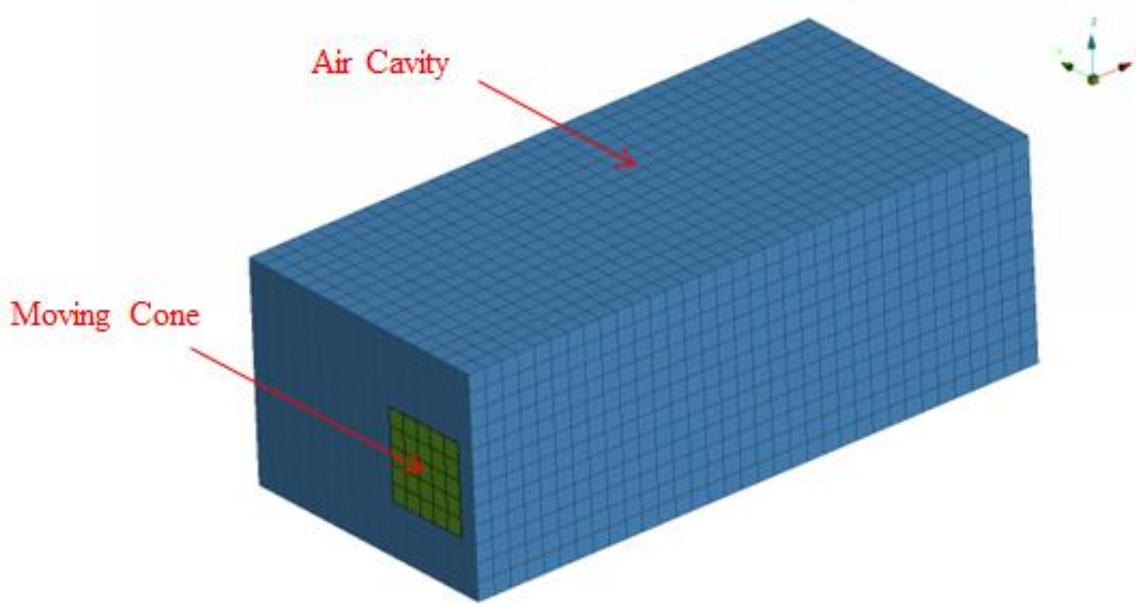


*Figure 6.23* Schematic of rectangular cavity with a moving cone

The dimensions of the moving plate are $L_{py}$=500 mm, $L_{pz}$=500 mm with a thickness of 5 mm and of very "stiff" material. The aim is to avoid having any plate mode shapes in the range of interest (i.e., rigid cone). The cone is excited by a unit acceleration of 1 m/s$^2$. This model represents a pulsating (moving) cone in a closed cavity. The response was calculated at points 2 and 3 (Figure 6.24). An enforced displacement using a NASTRAN SPCD card was used to represent the motion of the cone. The SPL response was calculated using NASTRAN solution sequence 111 (SEMFREQ - Modal frequency response).

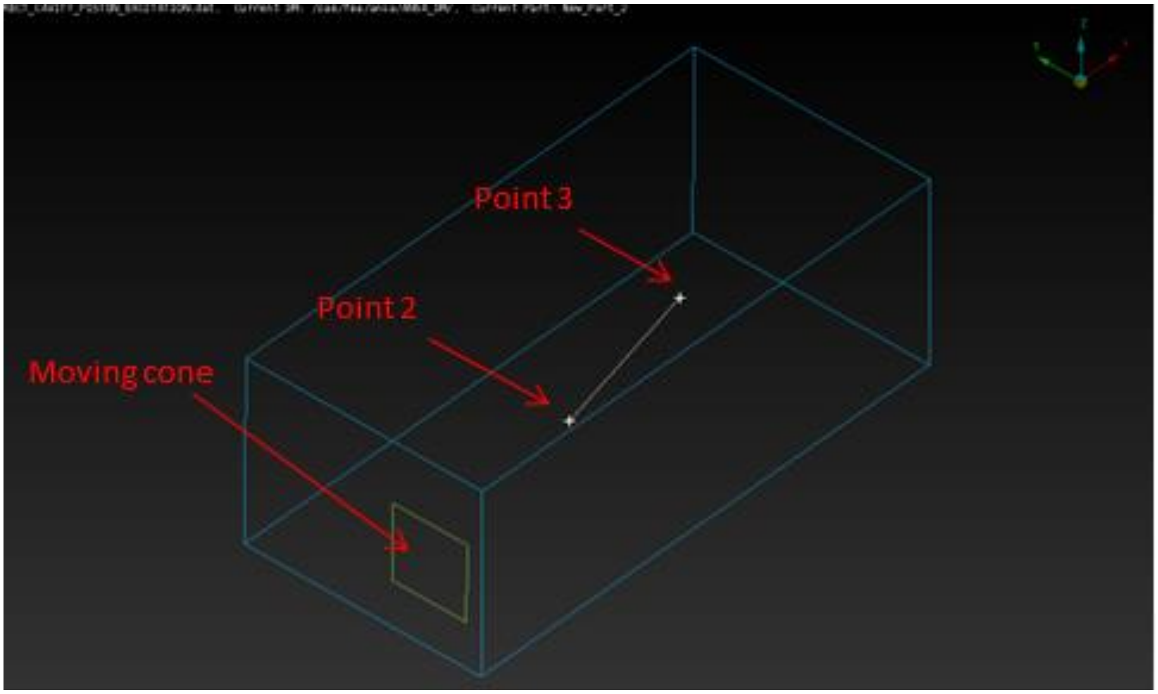


*Figure 6.24* Location of excitation and response points for moving cone example

The analytical acoustic pressures at points 2 and 3 due to the moving cone excitation were compared with the FE model results obtained from NASTRAN. The results shown in Figure 6.25 demonstrate a very good correlation between the FE model and the analytical solution. The FE approach can be thus used to represent a moving cone in a complex geometrical setting with high confidence.

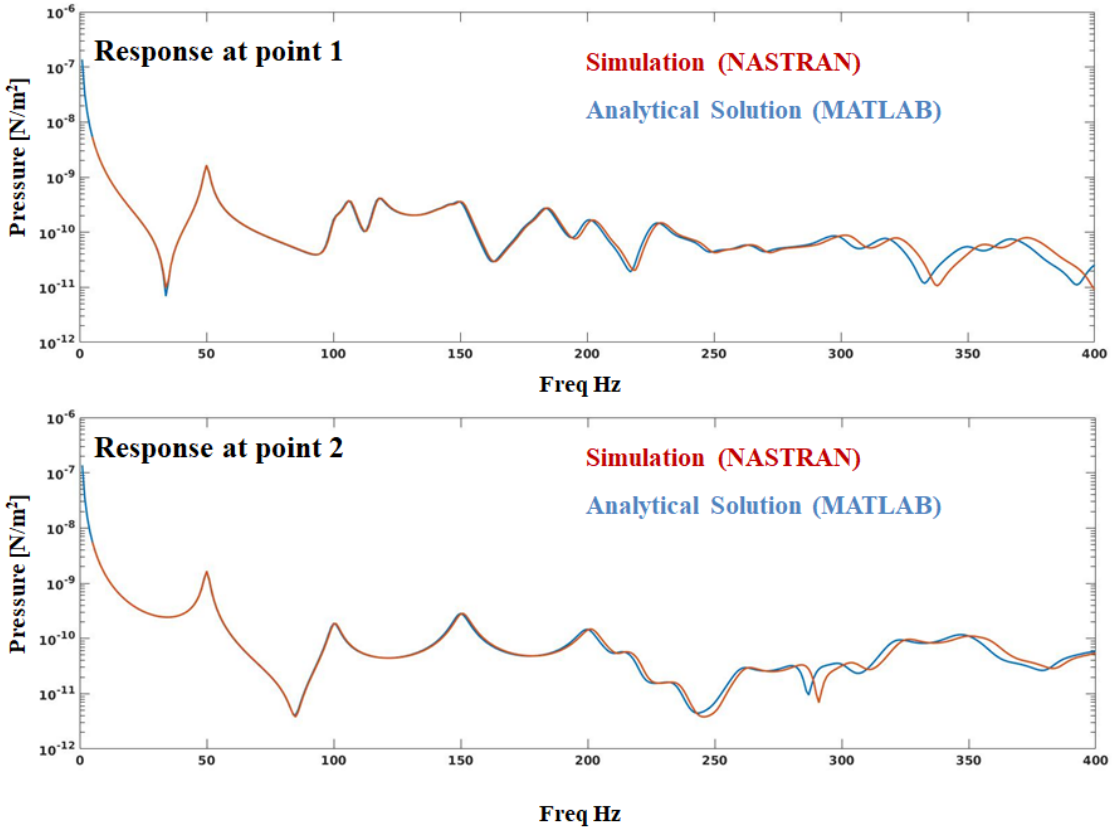


*Figure 6.25* Moving cone acoustic pressure analytical analysis versus FE NASTRAN

6.7 Speaker Modeling as a Baffled Moving Cone (Piston) in Anechoic Room

In this section, we consider the sound field from a vibrating circular piston in an infinite rigid baffle. This modeling is often used for a loudspeaker due to its ability to accurately simulate the loudspeaker dynamic behavior. Using the baffle, which can simulate the speaker enclosure, the model provides a representation of the loudspeaker's performance allowing us to study the effects of frequency response, directivity, and efficiency.

To derive a closed-form solution, the piston comprises many simple sources (monopoles) and thus the response is the sum of all sources radiating in phase. Because of the infinite baffle, each monopole gives rise to an image source which coincides with itself doubling therefore the volume velocity of each monopole.

Let the piston vibrate with a velocity $u_s(t) = Ue^{j\omega t}$ . Then, the phasor of the volume velocity of each elementary monopole is $UdS$. Using linear superposition, the sound pressure radiated by the piston can be evaluated at any position in front of the baffle simply by integrating over the surface of the piston [54]. Thus, we have

$$p = j\omega\rho \int_S \frac{e^{j(\omega t - kh_c)}}{2\pi h_c} UdS \tag{6.56}$$

where $h_c$ is the distance between the observation point $P_o$ and the position on the piston, and $S$ is the surface of the piston of radius $a_c$ as shown in Figure 6.26. Note the factor of two in the denominator due to the contribution of the image sources. The observation point $P_o$ is also at distance $r_c$ from the center of the cone.

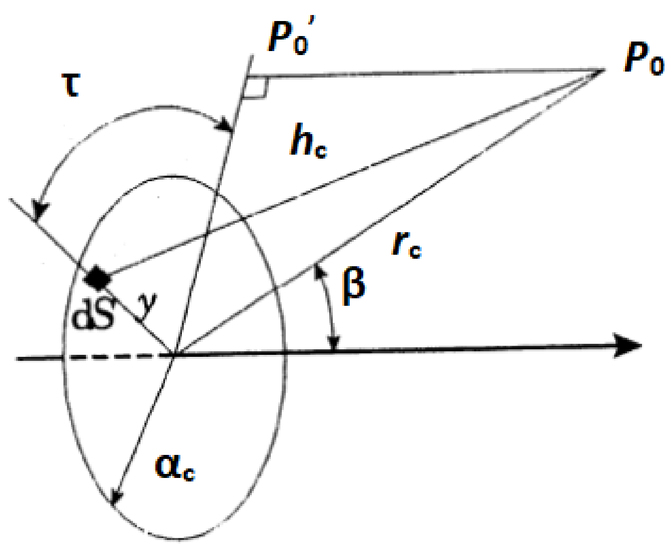


*Figure 6.26* Schematic and variable definition of a moving circular cone (piston)

The far field sound pressure (i.e., pressure at long distances from the center of the piston compared with the piston radius and the wavelength of interest), is calculated by expressing $h_c$ in polar coordinates as

$$h_c = \sqrt{r_c{}^2 + y^2 - 2r_c y sin\beta\, cos\,\tau} \approx r\sqrt{1 - 2\frac{y}{r_c} sin\beta\, cos\,\tau} \tag{6.57}$$

$$\approx r_c - y sin\beta\, cos\,\tau$$

Therefore, the sound pressure becomes

$$p(r_c, \beta) = j\omega\rho \frac{Ue^{j(\omega t - kh_c)}}{2\pi r_c} \int_0^{2\pi} \int_0^{a_c} e^{jky sin\beta\, cos\,\tau} y dy d\tau \tag{6.58}$$

Using the following Bessel functions $J_0(z)$ and $J_1(z)$ (plotted in Figure 6.27)

$$J_0(z) = \frac{1}{2\pi} \int_0^{2\pi} e^{jz cos\mu} d\mu \tag{6.59}$$

and

$$J_1(z) = \frac{1}{z} \int_0^{z} \mu J_0(\mu) d\mu \tag{6.60}$$

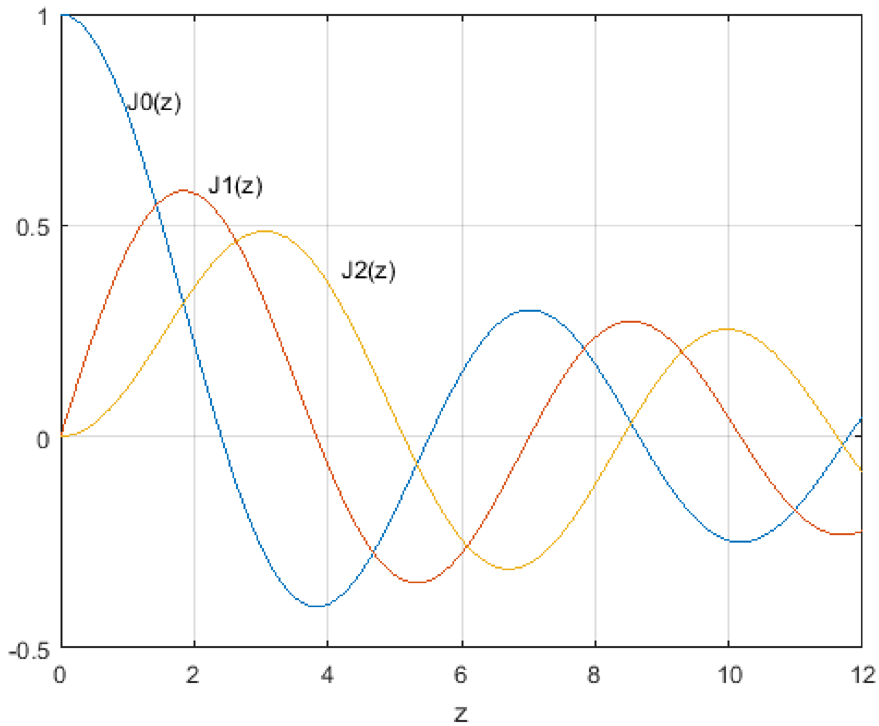


*Figure 6.27* Bessel functions

we obtain the following far field sound pressure,

$$p(r_c,\beta) = \frac{j\omega\rho U}{r_c}\frac{a_c J_1(ka_c sin\beta)}{ka_c sin\beta}e^{j(\omega t-kr)}$$
$$= \frac{j\omega\rho Q}{2\pi r_c}[\frac{2J_1(ka_c sin\beta)}{ka_c sin\beta}]e^{j(\omega t-kr_c)} \tag{6.61}$$

where $Q = \pi {a_c}^2 U$ is the volume velocity generated by the moving cone.

Equation (6.61) can be written as

$$p(r_c,\beta) = \frac{j\omega\rho Q}{2\pi r_c}[R(f,\beta)]e^{j(\omega t-kr_c)} \tag{6.62}$$

The factor in brackets

$$R(f,\beta) = \frac{2J_1(ka_c sin\beta)}{ka_c sin\beta} \tag{6.63}$$

is the piston directivity. It is a frequency dependent function that describes the directional characteristics of the source in the far field. The maximum of the directivity function is one if $\beta$ = 0, indicating maximum radiation in the axial direction for all frequencies. Figure 6.28 shows the directivity for different values of the normalized frequency $ka_c$. Note that the piston is an omnidirectional source (a monopole placed on a rigid surface) at low frequencies. At high frequencies the radiation of the piston is concentrated in a beam along the axial direction.

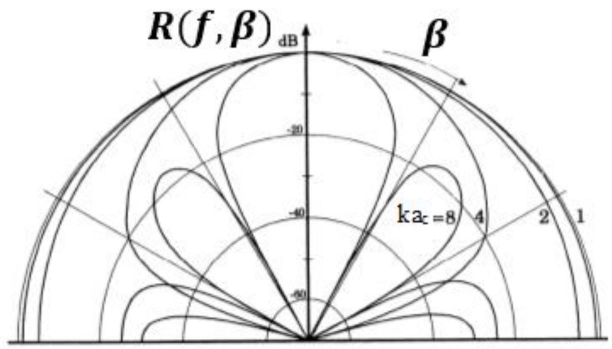


*Figure 6.28* Directivity function $R(f,\beta)$ of the Piston in terms of normalized frequency $ka_c$

The sound pressure along the axis of the piston can be evaluated easily. Since $sin\beta = 0$ on the axis, the distance $h_c$ reduces to

$$h_c = \sqrt{{r_c}^2 + y^2} \qquad or \qquad dh_c = \frac{ydy}{\sqrt{{r_c}^2+y^2}} = \frac{y}{h_c}dy$$

Therefore, the sound pressure on the axis becomes

$$p(r_c, \beta = 0) = \frac{j\omega\rho U}{2\pi} e^{j(\omega t)} \int_0^{2\pi} \int_0^{\sqrt{{r_c}^2+{\alpha_c}^2}} e^{-jkh_c} dh_c d\tau \tag{6.64}$$

$$= \rho c U e^{j(\omega t)} [e^{-jkr_c} - e^{-jk\sqrt{{r_c}^2+{\alpha_c}^2}}]$$

If we define

$$\Delta = \frac{\sqrt{{r_c}^2 + {\alpha_c}^2} - r_c}{2} \tag{6.65}$$

the sound pressure can be written as

$$p = 2j\rho cUe^{j(\omega t - k(r_c + \Delta))} sin\,(k\Delta) \tag{6.66}$$

indicating that the sound pressure is zero if $k\Delta$ is a multiple of π. This happens if $\Delta$ is a multiple of half a wavelength, corresponding to locations

$$r_c = \alpha_c \left[\frac{1}{2n}\frac{\alpha_c}{\lambda} - \frac{n}{2}\frac{\lambda}{\alpha_c}\right] \tag{6.67}$$

on the axis where *n* is a positive integer. Similarly, the sound pressure becomes maximum for

$$2\Delta = \sqrt{{r_c}^2 + {\alpha_c}^2} - r_c = \frac{(2m+1)\lambda}{2}$$

where *m* is a positive integer. This occurs for

$$r_c = \alpha_c \left[\frac{1}{2m+1}\frac{\alpha_c}{\lambda} - \frac{2m+1}{4}\frac{\lambda}{\alpha_c}\right] \tag{6.68}$$

Using a moving cone and a simple hemisphere representing near field (Figure 6.29), a model was developed to predict the acoustic pressure in far field using a FE model in NASTRAN, and then compare it with the derived analytical solution of this section. The moving cone is modeled with a rigid plate.

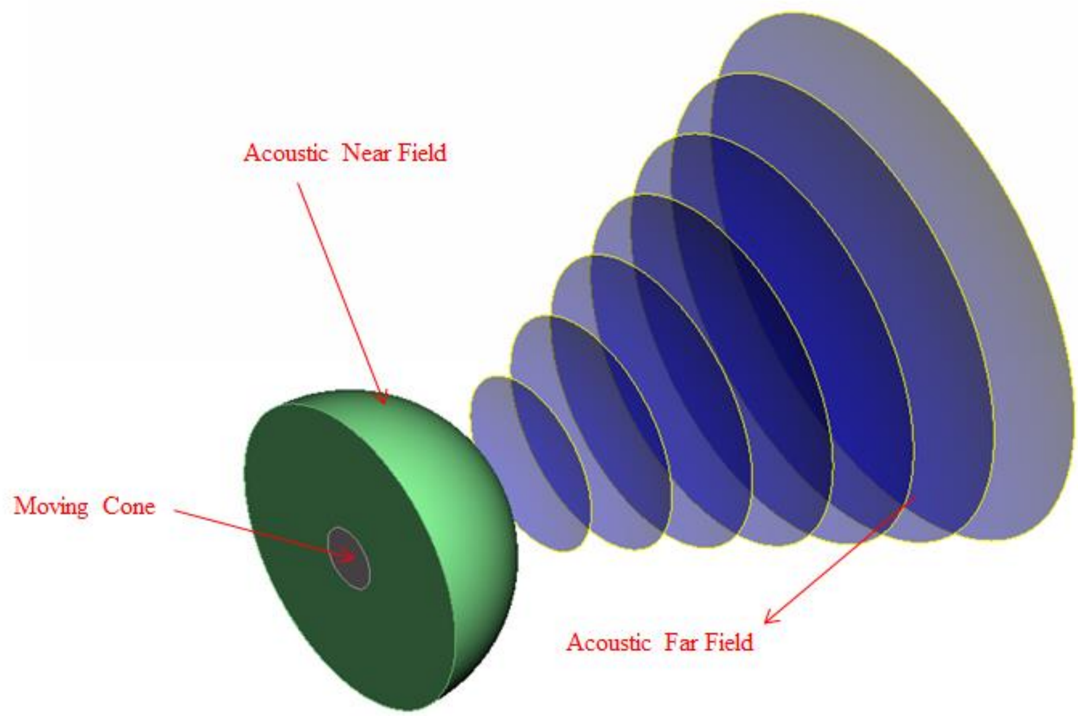


*Figure 6.29* Schematic of moving cone in far field

The near field cavity has a radius of 500 mm and the moving plate has a radius of 100 mm and a thickness of 5 mm. Its material is very “stiff” to avoid having any plate mode shapes in the range of interest (rigid cone). The cone is excited by a unit velocity of 1 mm/s.

The analytical solution is represented by Equation (6.64) and the results are shown in Figure 6.30 indicating how the pressure varies with respect to frequency and cone radius. The directivity of Equation (6.63) is shown in Figure 6.31 indicating that at high frequencies the directivity is more significant. Figure 6.32 shows the FE model for the baffled moving cone. The acoustic near and far fields and transition elements are similar to previous sections. The source is placed at the center of a meshed cavity which is part of the acoustic near field and two microphones were placed at 2 m from the moving cone at different angles. Using NASTRAN solution sequence 111 (SEMFREQ - Modal frequency response) the SPL response at each microphone was calculated.

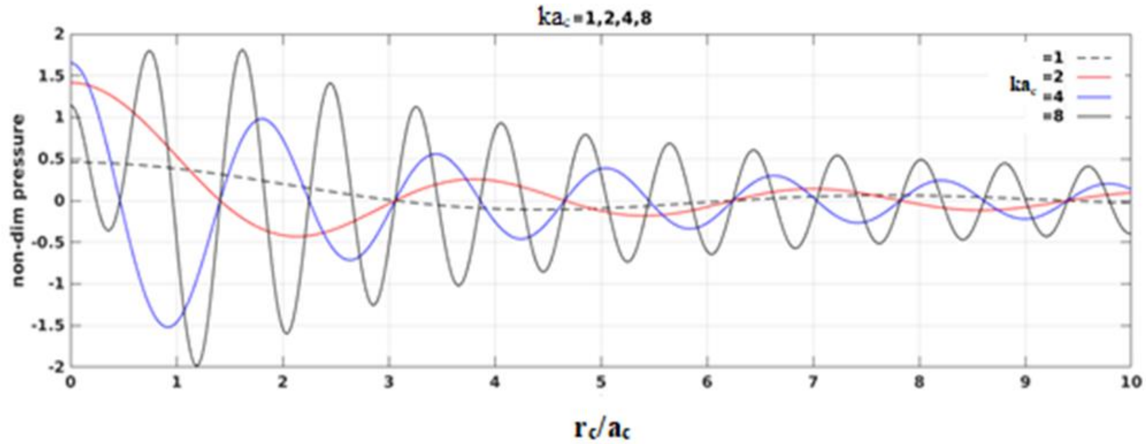


*Figure 6.30* Illustration of analytical solution (Equation 6.64)

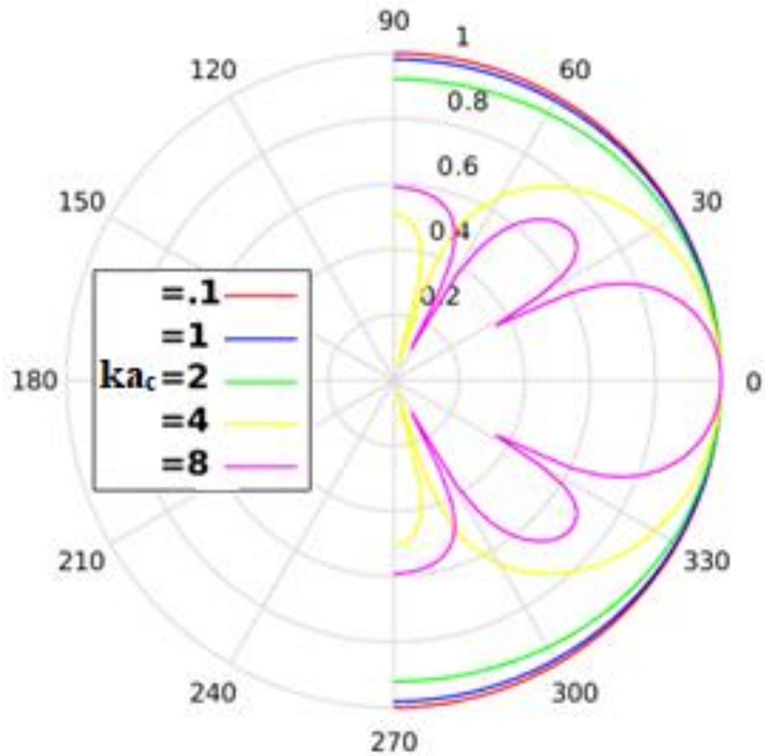


*Figure 6.31* Directivity function for a moving cone

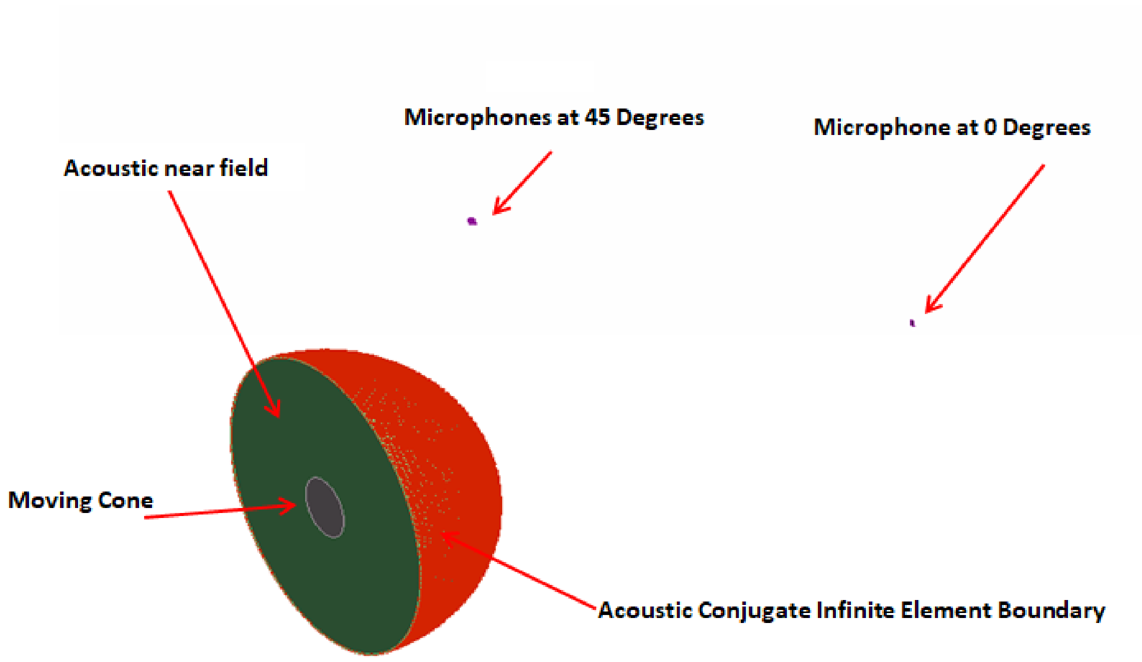


*Figure 6.32* FE modeling of a moving cone in far field

The analytically derived acoustic pressures at angles β = 0 degrees and β = 45 degrees resulting from the excitation of the moving cone are compared with those obtained by the developed NASTRAN approach. As shown in Figure 6.33, there is an excellent agreement between the FE model and the analytical solution. This established FE methodology provides a robust means to represent a moving cone in the far field, even for complex geometries, instilling a high level of confidence in its predictive capabilities.

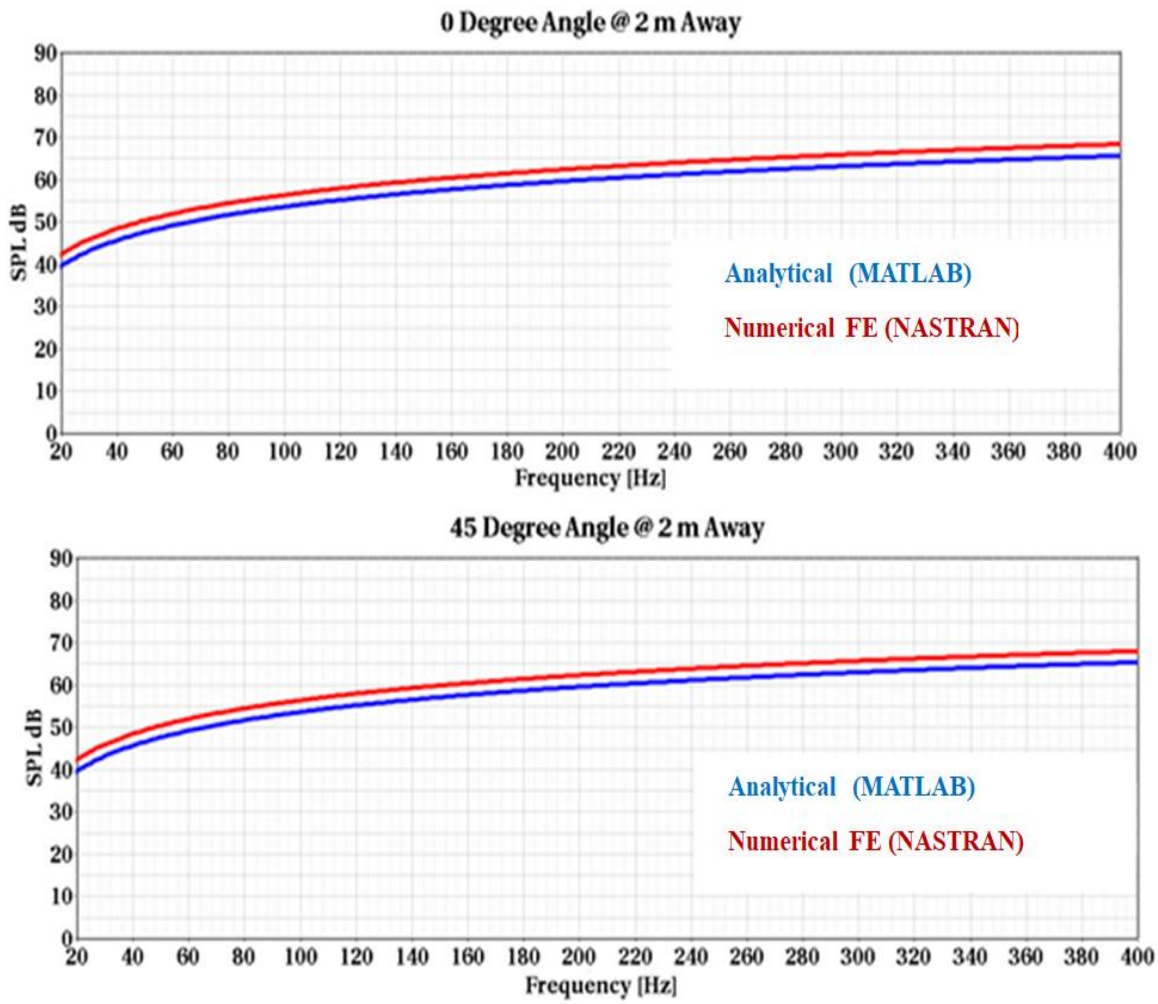


*Figure 6.33* Comparison of SPL at different angles β between analysis and NASTRAN

## 6.8 Non-Baffled Moving Cone (Piston) Model in Anechoic Room

In Section 6.7, we developed a baffled moving cone model in an anechoic room. In this section, we develop a novel moving cone model in a free-field condition avoiding any baffles. This is necessary because a vehicle speaker is not subject to baffling during testing in an anechoic room.

A closed-form solution for a non-baffled moving cone can be obtained using dipole sources. The fundamental concept involves regarding the piston as comprising numerous elementary sources, each formed by individual monopoles. Consequently, the piston is viewed as the aggregate of multiple monopoles, each emitting radiation both in phase and out of phase on either side of the plate, as illustrated in Figure 6.34.

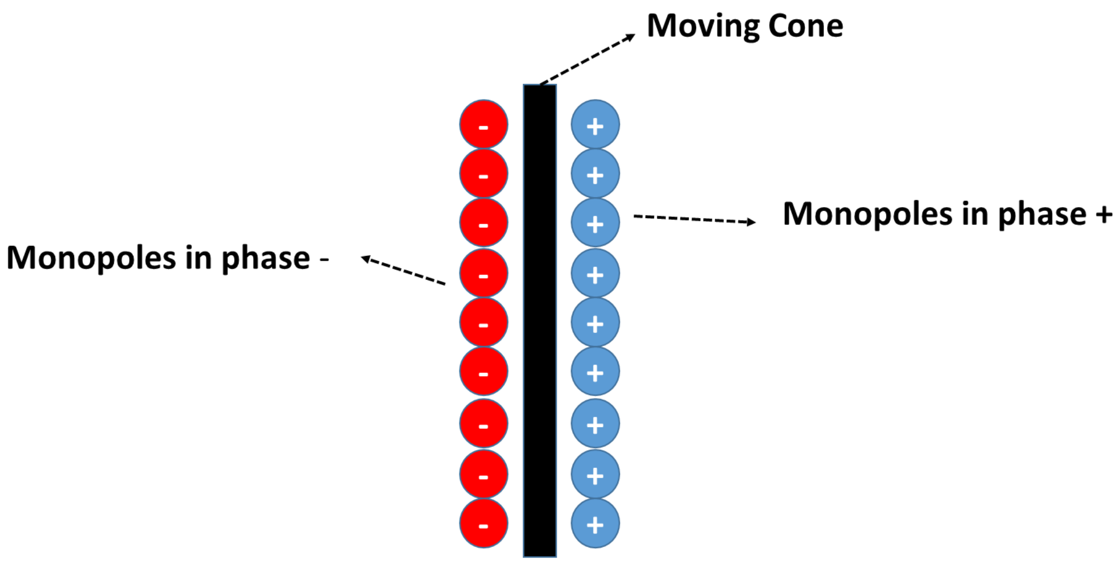


*Figure 6.34* Monopole arrangement to represent a rigid plane surface

Assuming the piston vibrates with the velocity $u_s(t) = Ue^{j\omega t}$, linear superposition allows us to assess the sound pressure radiated by the piston on each side. This can be achieved by integrating over the surface of the piston on each side, enabling evaluation of the sound pressure at any given position in front of the plate as

$$p = j\omega\rho \int_S \frac{e^{j(\omega t - kh_{c2})}}{4\pi h_{c2}} UdS - j\omega\rho \int_S \frac{e^{j(\omega t - kh_{c2})}}{4\pi h_{c2}} UdS \tag{6.69}$$

This is illustrated in Figure 6.35. The solution to Equation (6.69) is,

$$\begin{aligned} p(r_c, \beta) = & \frac{j\omega\rho Q}{4\pi r_{c1}} \left[\frac{2J_1(ka_c sin\beta)}{ka_c sin\beta}\right] e^{j(\omega t - kr_{c1})} \\ & - \frac{j\omega\rho Q}{4\pi r_{c2}} [\frac{2J_1(ka_c sin\beta)}{ka_c sin\beta}] e^{j(\omega t - kr_{c2})} \end{aligned} \tag{6.70}$$

where $r_{c1}$ and $r_{c2}$ are the distances form center of each pole integral to $P_0$. Equation (6.70) is simplified to

$$p(r_c, \beta) = \frac{j\omega\rho Q}{4\pi r_c}\left[\frac{2J_1(ka_c sin\beta)}{ka_c sin\beta}\right] e^{j(\omega t - kr_c)} cos(\beta) kd_p \tag{6.71}$$

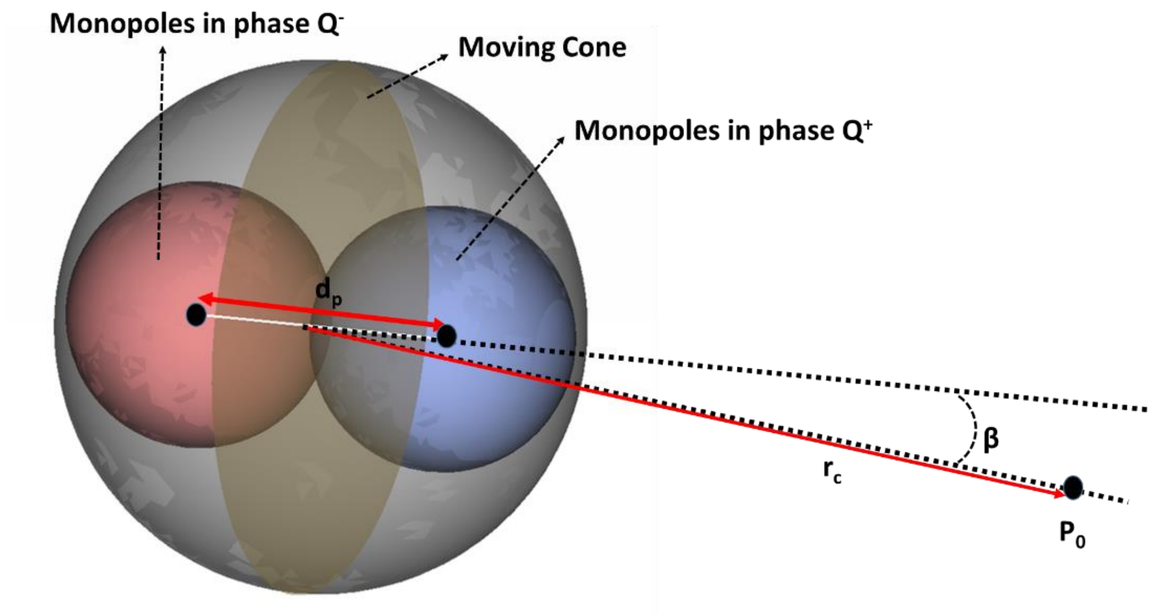


*Figure 6.35* Schematic of moving cone in free field

A FE NASTRAN model is developed using the concept of Figure 6.36. The distance between the microphone and the cone is $r_c$ = 1m, the angle β is zero and the radius of the plate is $a_c$ = 0.1 m. The plate is excited with an enforced velocity of $u_s(t) = 0.005e^{j\omega t}$ $[\frac{m}{s}]$. The analytical solution of Equation (6.71) and the FE model results are plotted in Figure 6.37 . A very good agreement is observed.

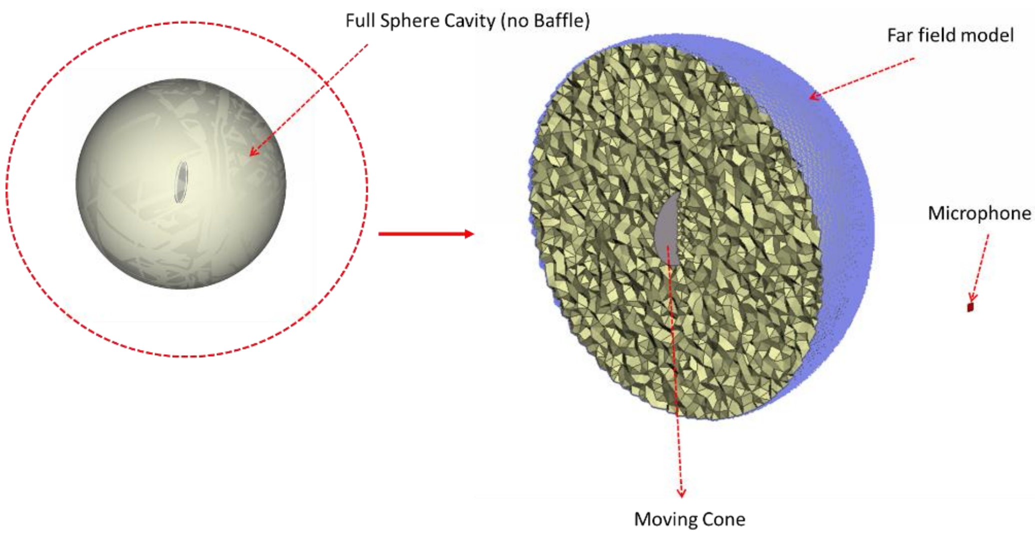


*Figure 6.36* Non-baffled moving cone FE NASTRAN model

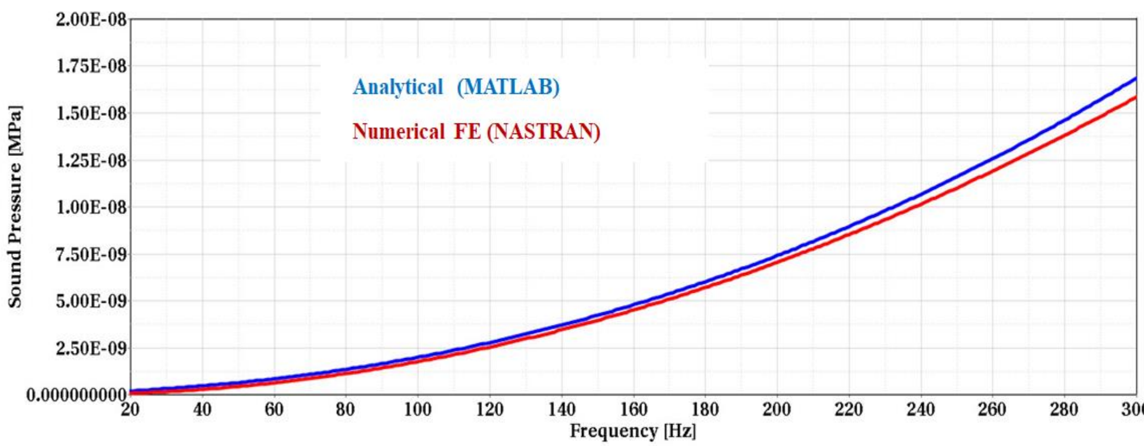


*Figure 6.37* Analytical versus FE SPL for non-baffled cone

6.9 Selection of Best Speaker Model from Developed Representations

The have developed three acoustic source models: a) a monopole acoustic source, b) a dipole acoustic source, and c) a moving cone to represent a speaker. We demonstrated that each of these models is very efficient in generating highly correlated sound signals for both closed cavities and far field FE models. However, as demonstrated, the directivity of the speaker models differs significantly. The solutions for the monopole, dipole, and moving cone exhibit considerable divergence, resulting in distinct directivity patterns. To exemplify this, pressure surface maps of the monopole source and moving cone source for the quantity $\frac{p(r_c,\beta)}{Q}$ were constructed for each case. Figure 6.38 and Figure 6.39 show the directivity of the three acoustic source models in the far field at 300 Hz and 3000 Hz, respectively. At 300 Hz, the moving cone speaker generates a $\frac{p(r_c,\beta)}{Q}$ which is shows low directivity. However, the directivity increases at 3000 Hz (Figure 6.39). The difference at the X axis (front of speaker) is about 75 % and in the orthogonal direction of the speaker the maximum difference is over 100 %. In practical applications, where sound pressure is measured 1 meter from the door and the speaker system, the directivity often plays a significant role. Consequently, the moving cone model emerges as the optimal choice to represent a loudspeaker, particularly at high frequencies. For frequencies below 300 Hz, the difference in directivity between the dipole and moving cone models is negligible.

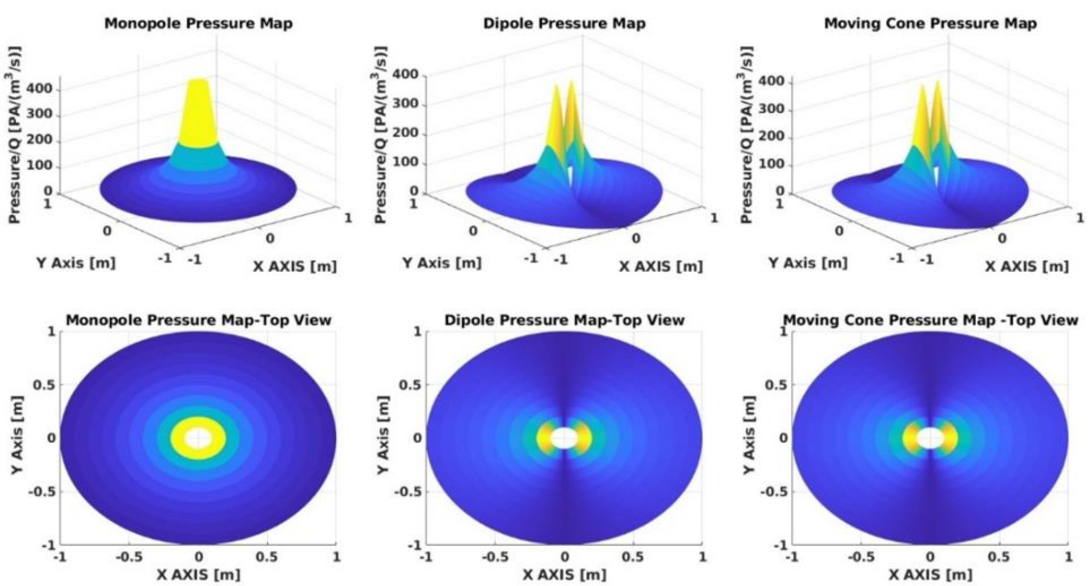


*Figure 6.38* Directivity of different acoustic sources at 300 Hz

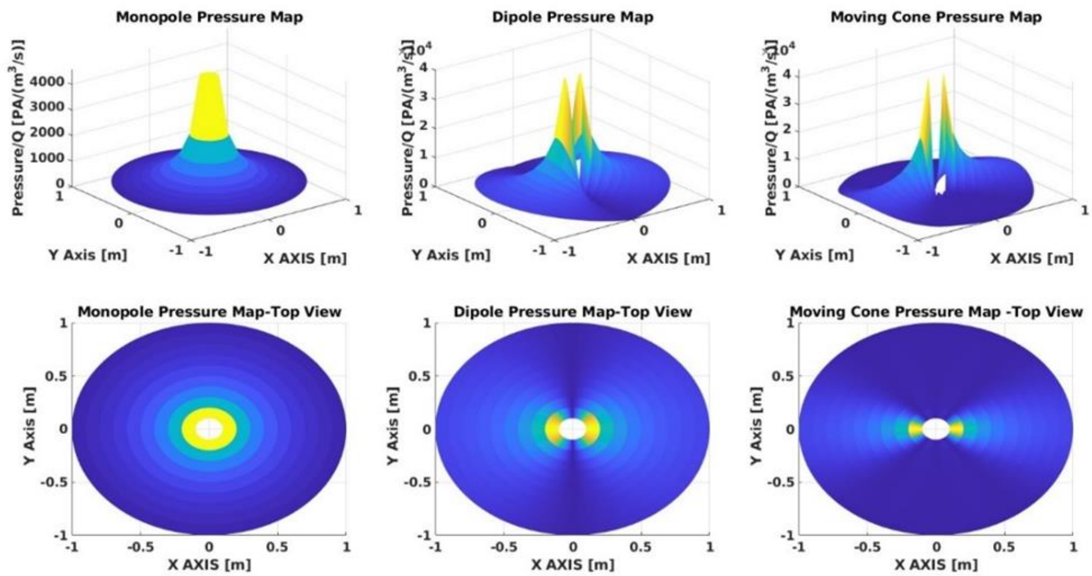


*Figure 6.39* Directivity of different acoustic sources at 3000 Hz

The speaker cone can be of different shapes as shown in Figure 6.40. As Equation (6.61) shows, the geometry of the cone and its curvature drives the pressure and directivity of an actual speaker.

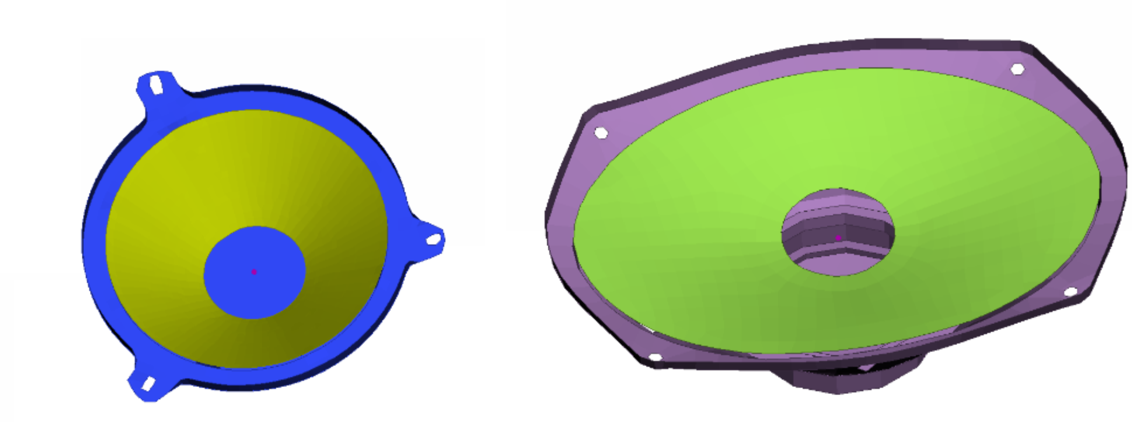

*Figure 6.40* Circular and oval shaped speaker diaphragms

If the speaker cone is modeled as a moving cone, the vibration of the cone can be coupled with the speaker bracket and the door carrier module structurally as shown in Figure 6.41. This coupling is an important factor in speaker modeling in vehicles and it will be discussed in the next chapter.  For these reasons, the best model for a loudspeaker is the moving cone.

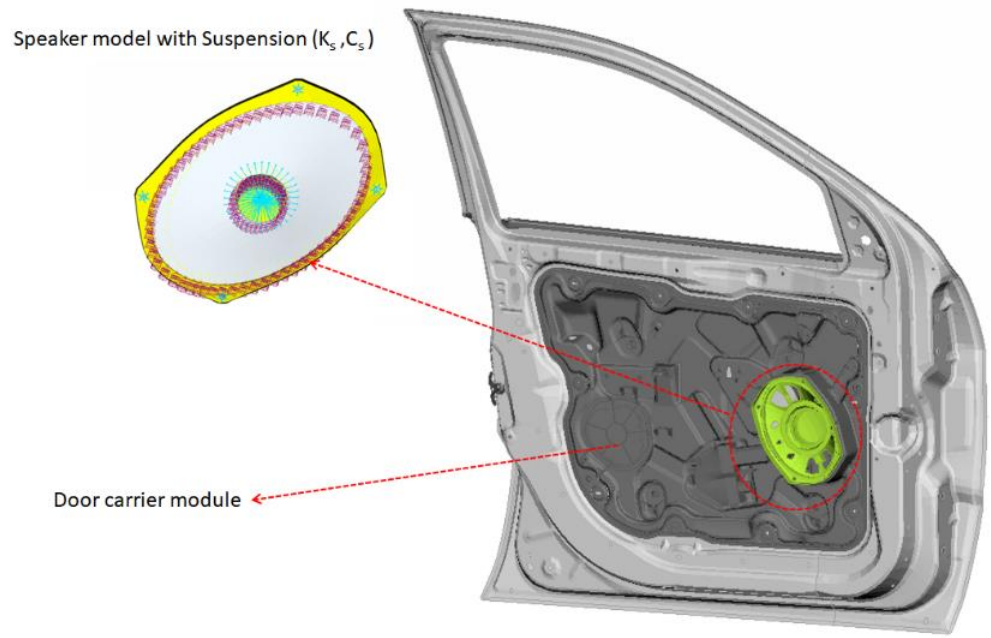


*Figure 6.41* Speaker cone model in door assembly

## 6.10 Experiments to Verify Analytical and FE Speaker Models

To develop a comprehensive finite element model for the representative speaker within a complete vehicle ANC system, it is imperative to conduct component-level testing and correlation. For this, we have chosen a standard 6.5-inch speaker and a 6x9-inch speaker from a full-size SUV (Figure 6.42). Table 6.1 shows all relevant data for the two speakers as provided by the manufacturer. In addition, Figure 6.43 and Figure 6.44 show the speaker sensitivity and speaker impedance function for the 6x9-inch and 6x5-inch speakers, respectively.

*Figure 6.42* 6x9-inch speaker and 6.5-inch speaker for test subject

Table 6.1

*Relevant data for two speakers*

| Speaker | 6x9-inch speaker | 6.5-inch speaker |
| --- | --- | --- |
| ANC frequency range | 40 Hz to 300 Hz | 65 Hz to 300 Hz |
| Total mass of speaker: | 0.889 Kg | 0.862 Kg |
| Speaker resonant frequency | 55 Hz | 58 Hz |
| Mechanical Compliance CMS | 0.375 mm/N | 0.375 m/N |
| Mechanical Resistance MR | 1.68 Kg/s | 1.53 Kg/s |
| Projected area of diaphragm | 0.0228 m2 | 0.01824 m2 |
| ANC max Voltage Planed $V_{max}$ | 3V (Peak) | 3V (Peak) |
| Speaker Sensitivity function $\xi(f)$ | Shown in Figure 6.43 | Shown in Figure 6.44 |
| Impedance function | Shown in Figure 6.43 | Shown in Figure 6.43 |

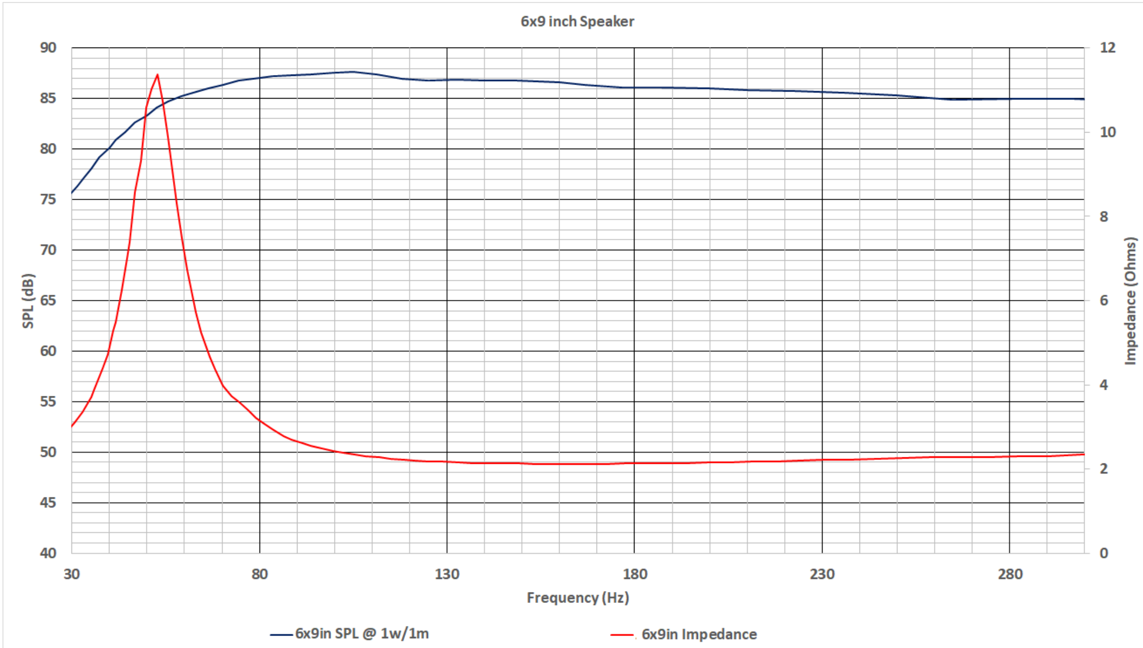


*Figure 6.43* 6x9-inch speaker sensitivity and speaker impedance function

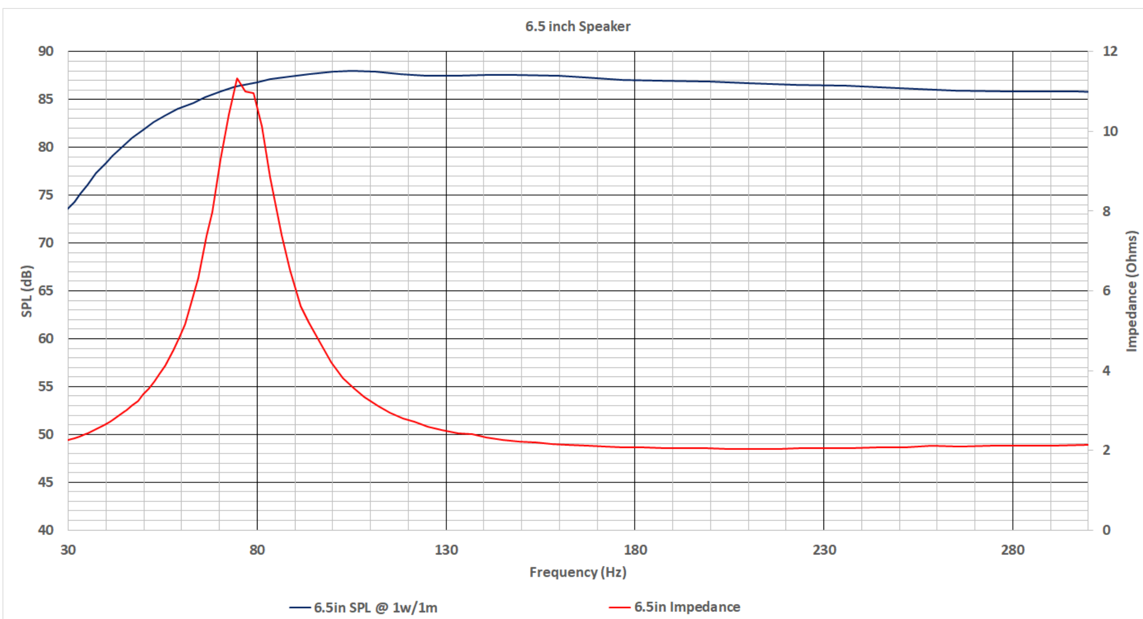


*Figure 6.44* 6.5-inch speaker sensitivity and speaker impedance function

A test was performed in an anechoic room with twelve microphones positioned in exact locations as shown in Figure 6.45. The speaker position was at (0, 0, 0) in (X, Y, Z) coordinate system where positive X is in front of the speaker, Y is across the speaker and positive Z points toward the room ceiling as shown in Figure 6.46. The twelve microphones cover a wide range of distances and angles to establish the accuracy of sound pressure level and directivity predictions. The locations capture the directivity of speakers at different angles and allow us to examine the phase of acoustic pressure at the front and back of the speaker. Table 6.2 shows the precise microphone locations.

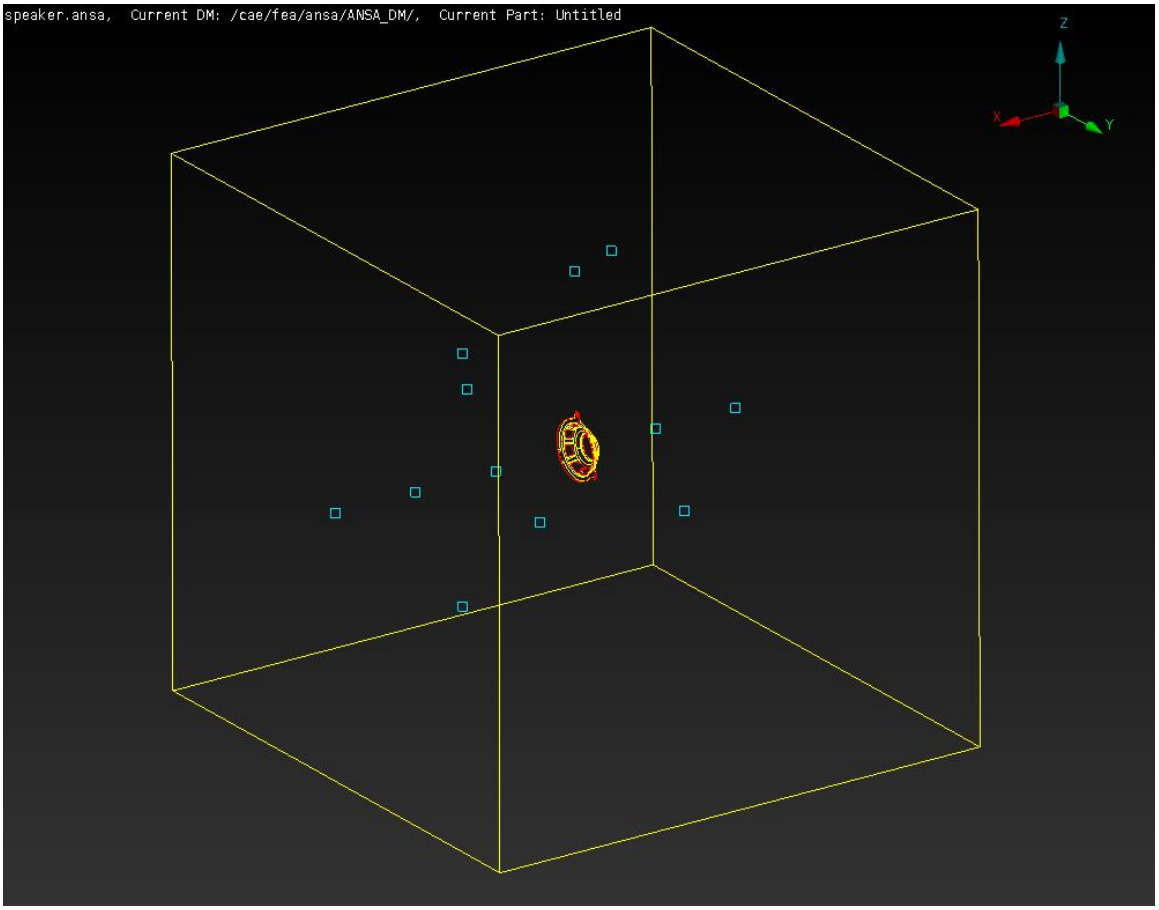


*Figure 6.45* Speaker location at (0,0,0) and microphones points in blue

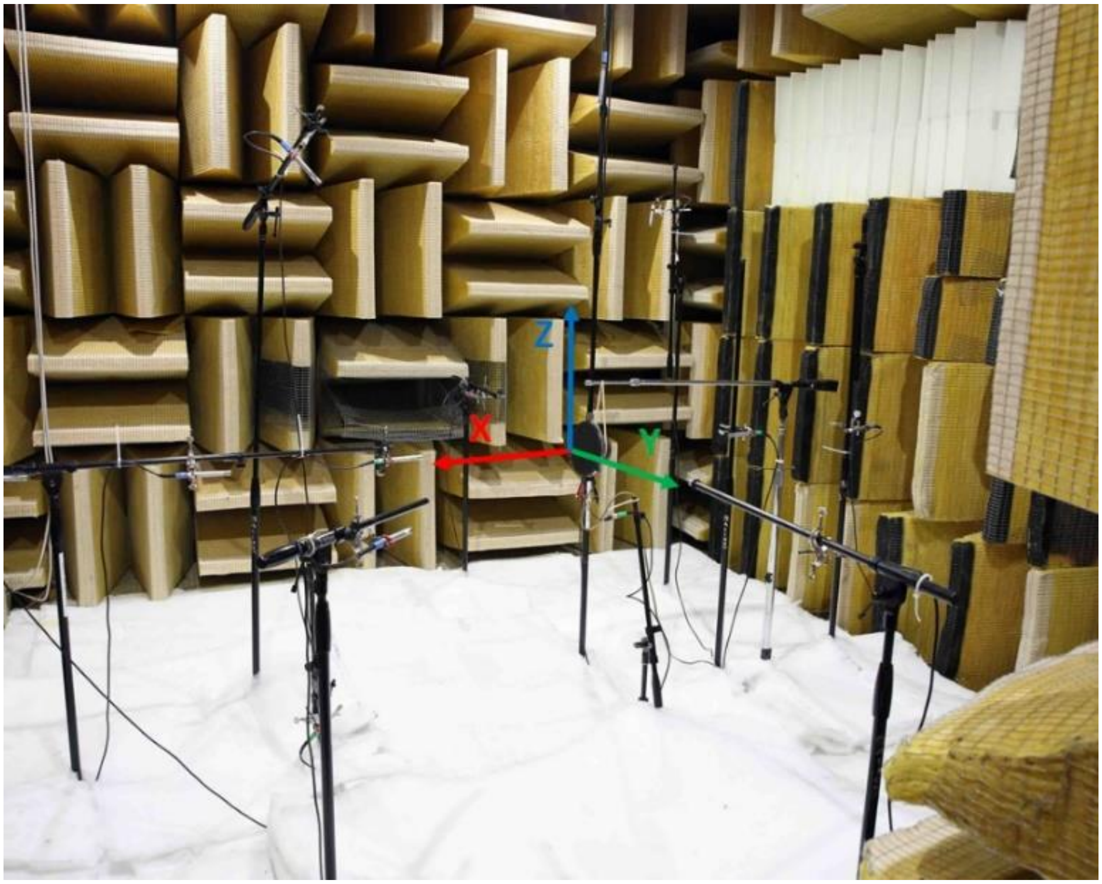


*Figure 6.46* Speaker location at (0,0,0) and microphone's locations

Table 6.2

*Microphone locations precise location with speaker at (0,0,0)*

| Point ID | Location | X (mm) | Y (mm) | Z (mm) |
|---|---|---|---|---|
| 1 | Front of speaker | 500 | 0 | 0 |
| 2 | Front of speaker | 1000 | 0 | 0 |
| 3 | Front of speaker | 1500 | 0 | 0 |
| 4 | Behind of speaker | -500 | 0 | 0 |
| 5 | Behind of speaker | -1000 | 0 | 0 |
| 6 | Adjacent to speaker | 0 | 1000 | 0 |
| 7 | Adjacent to speaker | 0 | -1000 | 0 |
| 8 | Front of speaker out of XY Plane | 706 | 0 | -706 |
| 9 | Front of speaker out of XY Plane | 706 | 0 | 706 |
| 10 | Front of speaker in XY Plane | 706 | 706 | 0 |
| 11 | Adjacent to speaker | 0 | 0 | 1000 |
| 12 | Behind of speaker out of XY Plane | -706 | -706 | 706 |

The floor plan of the anechoic room is 4.115 m x 3.226 m. The room is fitted with 813 mm fiberglass acoustic cones and is covered by 9 inches of acoustic materials (Figure 6.47). The test was performed with the main power feed controlled at the amplifier and probes placed exactly at the speaker terminals to measure the exact current and voltage input. The speaker was suspended by a bungee cord to best match a free-free condition (Figure 6.48).

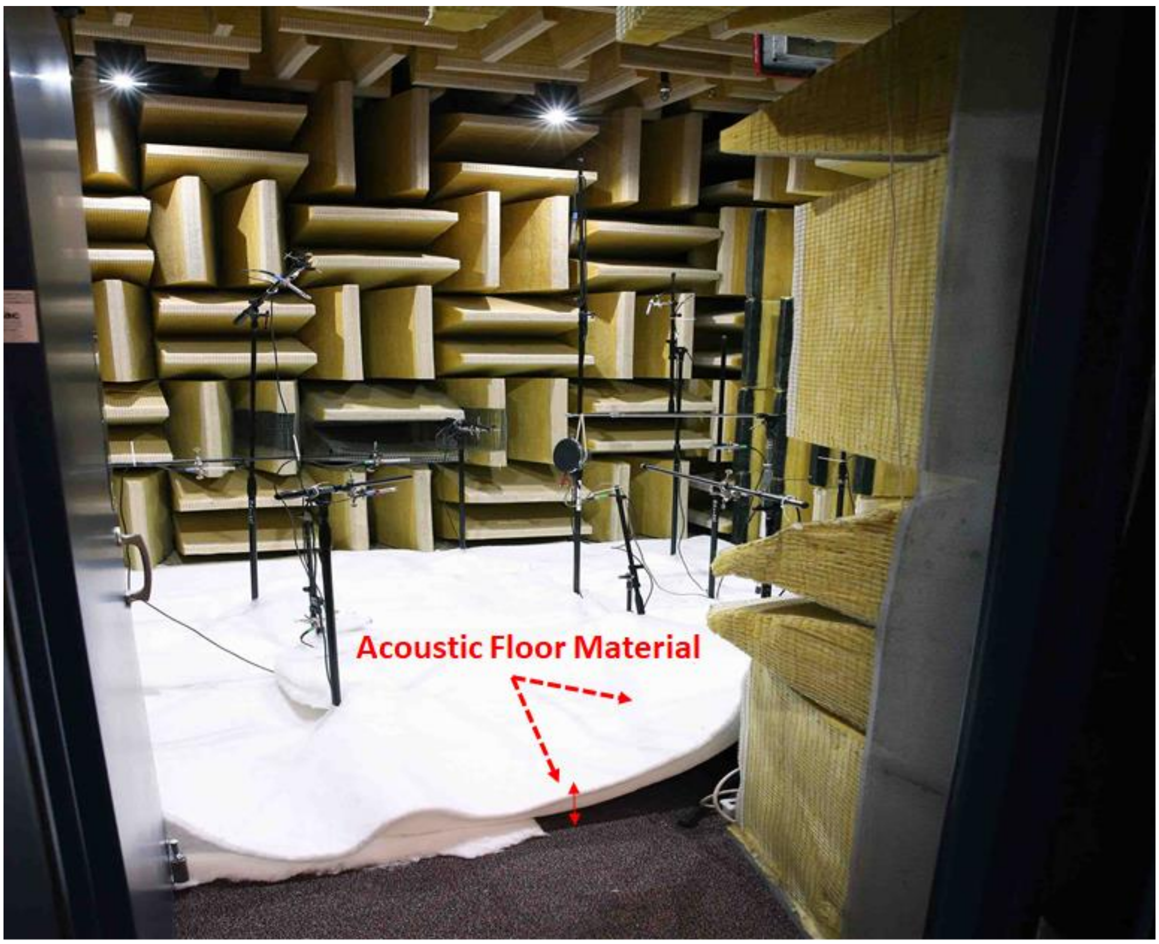


*Figure 6.47* Acoustic material on anechoic room floor

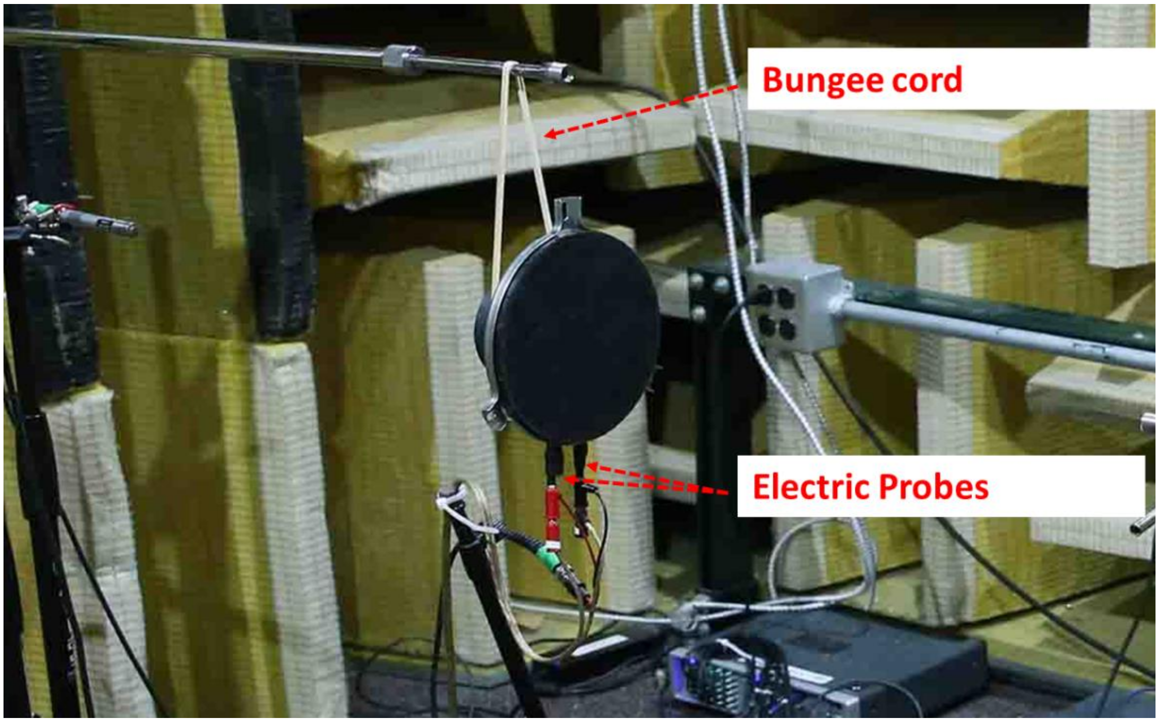


*Figure 6.48* Speaker probes and speaker suspension by a bungee cord

Both the 6x9-inch and the 6.5-inch speakers were tested using varying power inputs. The amplifier for the 6x9-inch speaker was set at 1 Watt and 2 Watts at 1000 Hz to generate the required signal. For each speaker, a constant sine wave of 1 Watts and 2 Watts was applied, and the voltage and current were recorded. Subsequently, a sine sweep spanning the ANC frequency range of 30 to 300 Hz was conducted. This setup was repeated with a 2 Watt amplitude input for the 6x9-inch speaker. Both the 1 Watt and 2 Watts setups were performed for the 6.5-inch speaker.

For both speakers, the sine sweep was performed by maintaining a constant power feed at the amplifier while recording the voltage and current at the probes (Figure 6.49 and Figure 6.50) . Because of the variable speaker impedance, the voltage across the frequency range fluctuates accordingly. Figure 6.51 and 6.52 show the sound pressure amplitude and phase for the twelve microphones at 1-Watt amplifier input.

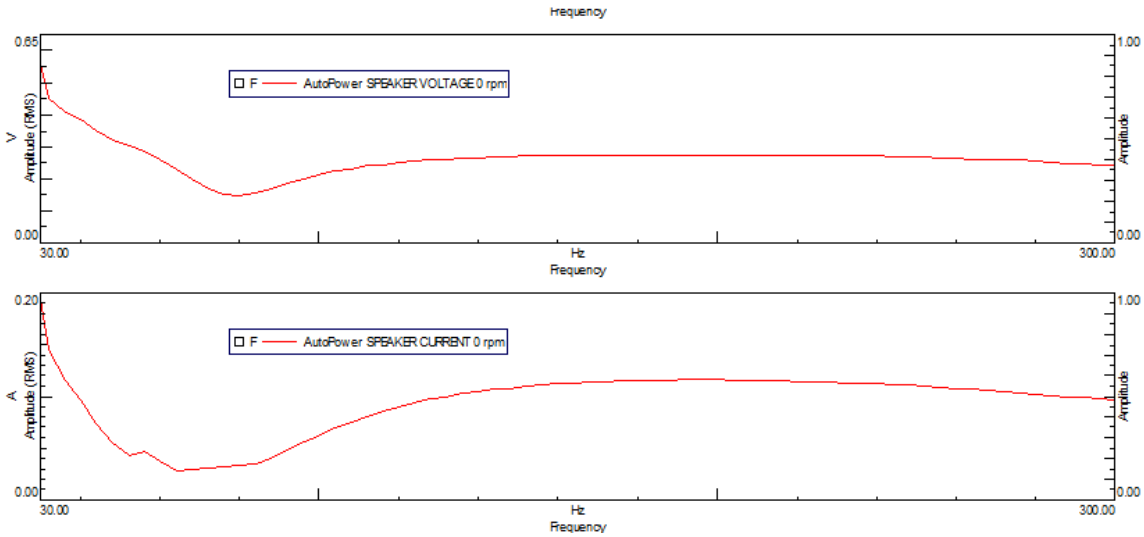


*Figure 6.49* Sine sweep voltage and current for 6.5-inch speaker for 1 Watt power

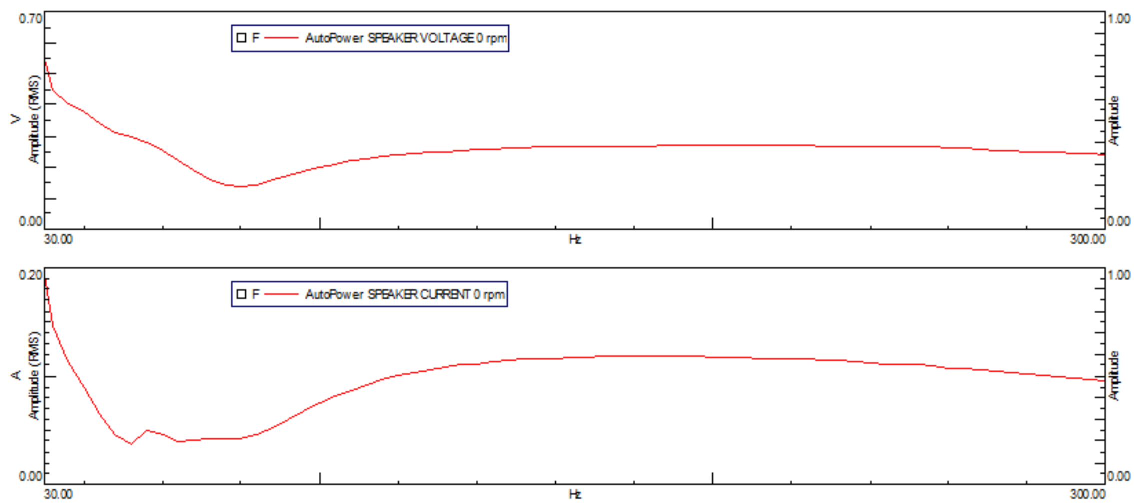


*Figure 6.50* Sine sweep voltage and current for 6x9-inch speaker for 1 Watt power

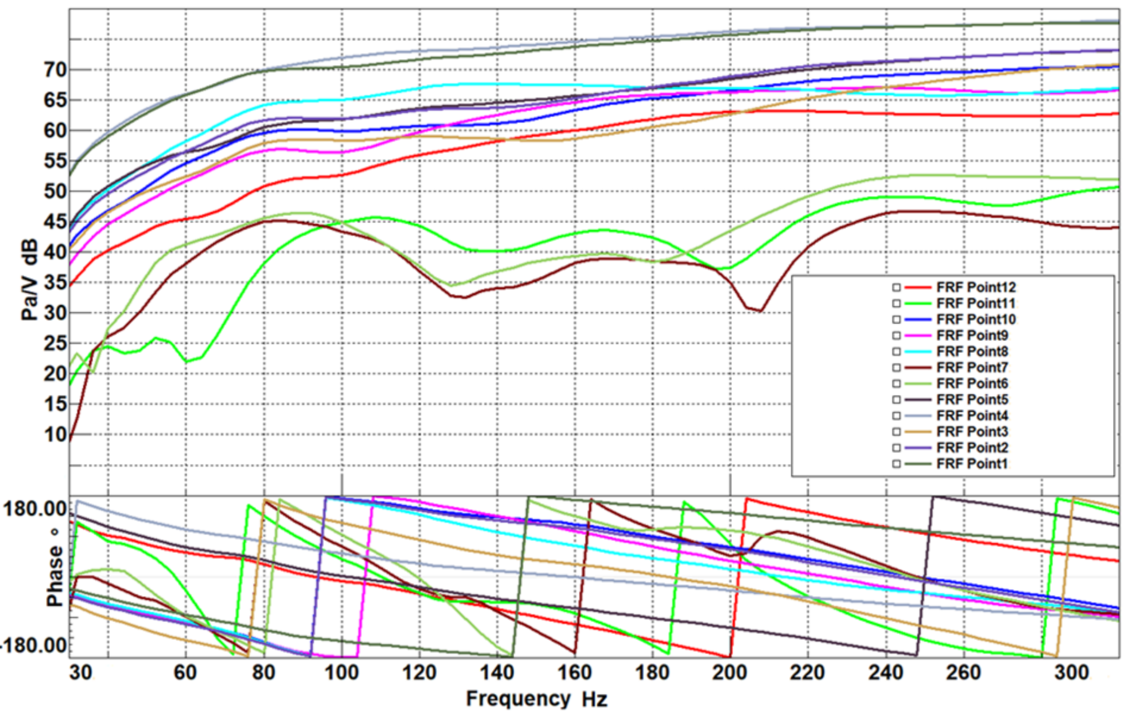


*Figure 6.51* Sine sweep microphone SPL for 6.5-inch speaker

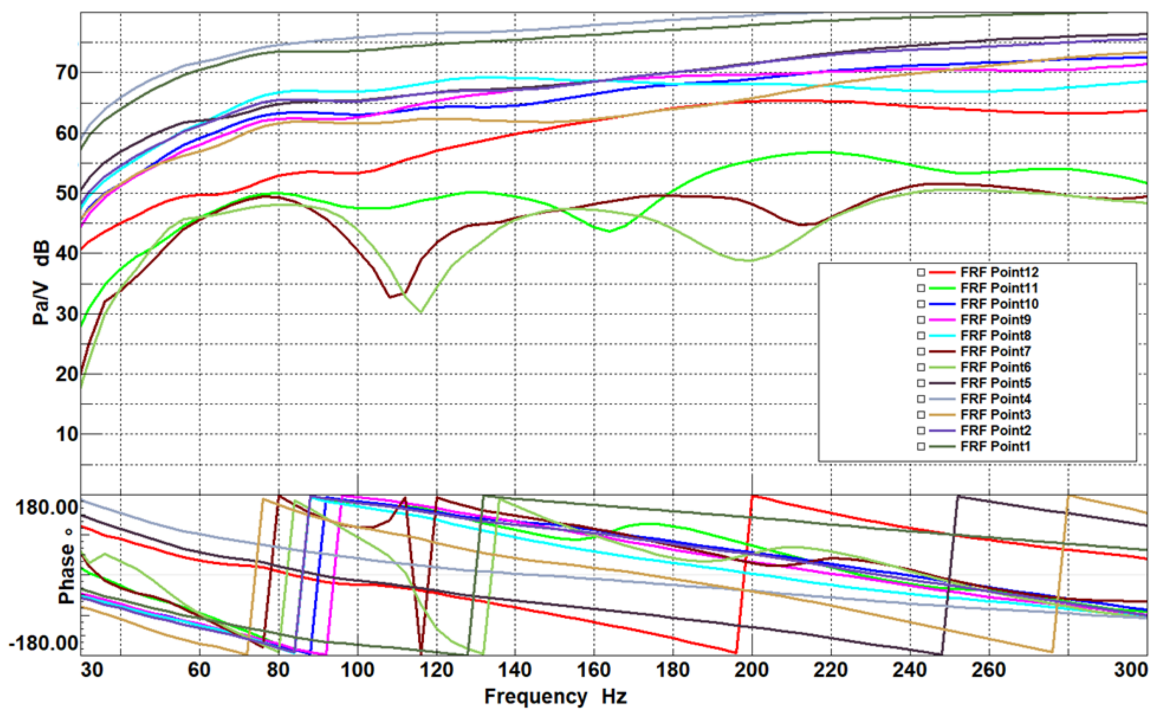


*Figure 6.52* Sine sweep microphone SPL for 6x9-inch speaker

The acoustic tests in the anechoic room were performed to demonstrate the accuracy of the developed FE model as well as the accuracy of the analytical model of Section 6.8 and validate the assumptions used. Equation (6.71) is rearranged to calculate the velocity of a circular speaker cone as

$$U = \frac{1}{\pi {a_c}^2} \frac{p(r_c, \beta)}{\frac{j\omega\rho}{4\pi r_c}\left[\frac{2J_1(ka_c sin\beta)}{ka_c sin\beta}\right] e^{j(\omega t - kr_c)}\, cos(\beta) k d_p}$$

Figure 6.53 shows the experimentally obtained magnitude and phase of SPL for the 6.5-inch speaker at 1 m in front of speaker with a zero angle (Point # 2). This measurement is taken as input and the corresponding diaphragm velocity was calculated using the rearranged form of Equation (6.71). Figure 6.64 shows the calculated velocity amplitude and phase. These results are then used as an enforced velocity input of the diaphragm for the FE model of Figure 6.55.

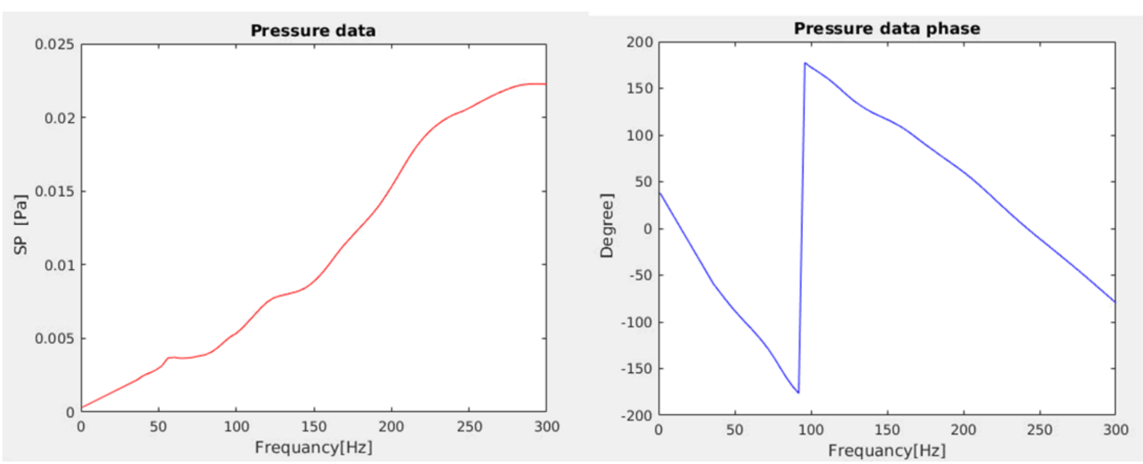


*Figure 6.53* Sound pressure for the 6.5-inch speaker at point 2

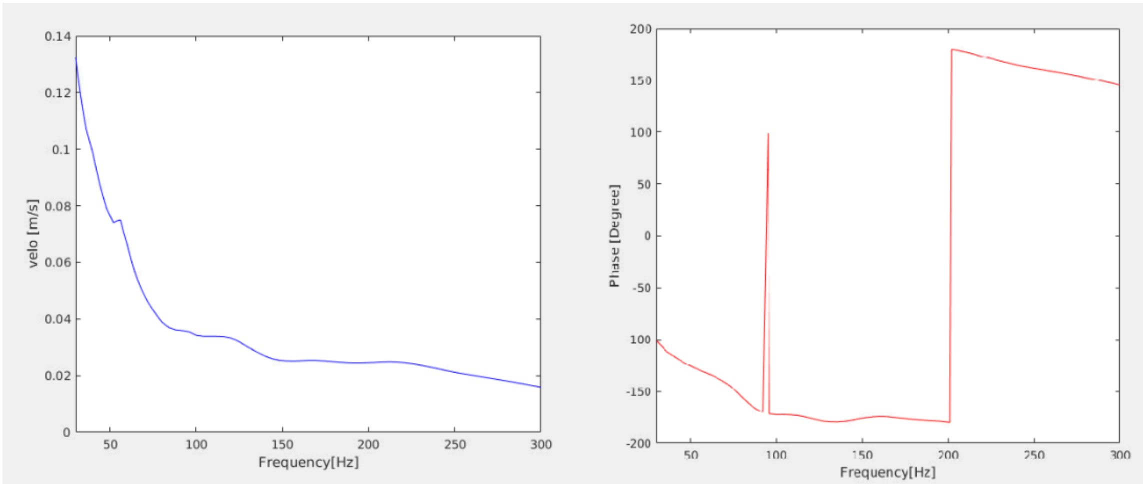


*Figure 6.54* Calculated diaphragm velocity magnitude and phase for point 2

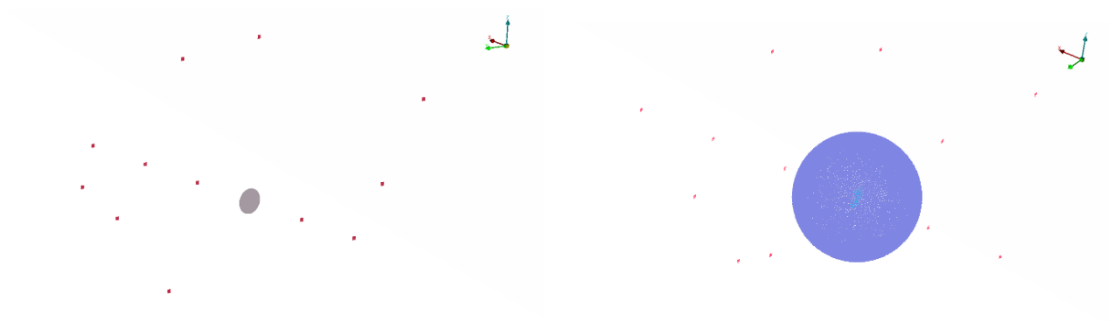

*Figure 6.55* FE model for 6.5-inch speaker with 12 microphones – acoustic near field (left) and full model (right)

The analytical, FE (NASTRAN), and experimental results were obtained for all 12 microphone locations. Points 2 and 9 were specifically chosen to illustrate both in-plane and out-of-plane positions, thus providing comprehensive insights into the results. Figure 6.56 and Figure 6.57 compare the sound pressure for the 6.5-inch speaker and Figure 6.58 compares the phase. All comparisons are excellent. Both the amplitude and phase agree very well across all three methodologies. Furthermore, the speaker's directivity demonstrates favorable characteristics, as evidenced by the good agreement for the out-of-plane point 9.

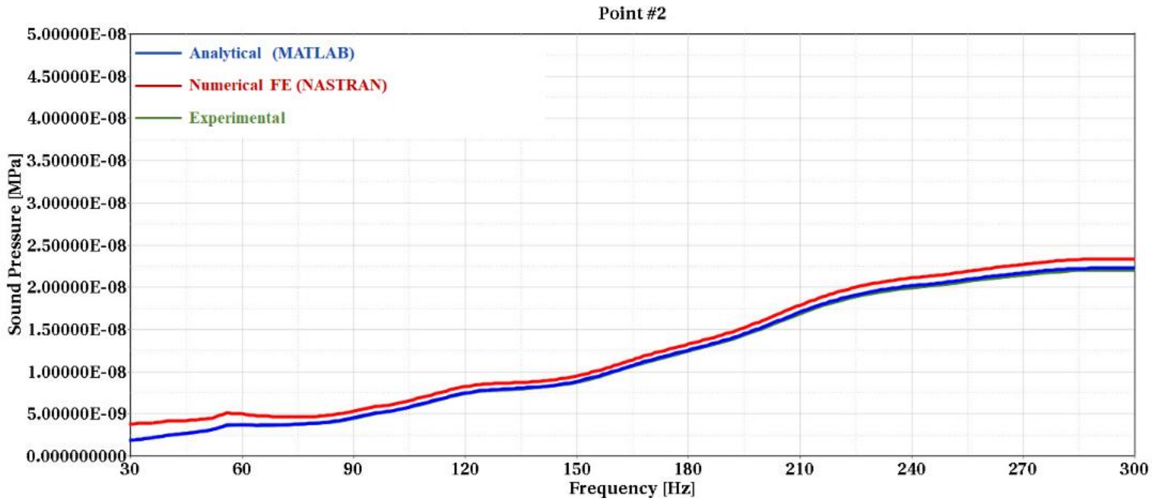


*Figure 6.56* Analytical, FE, and experimental sound pressure at point 2 microphone for 6.5-inch speaker

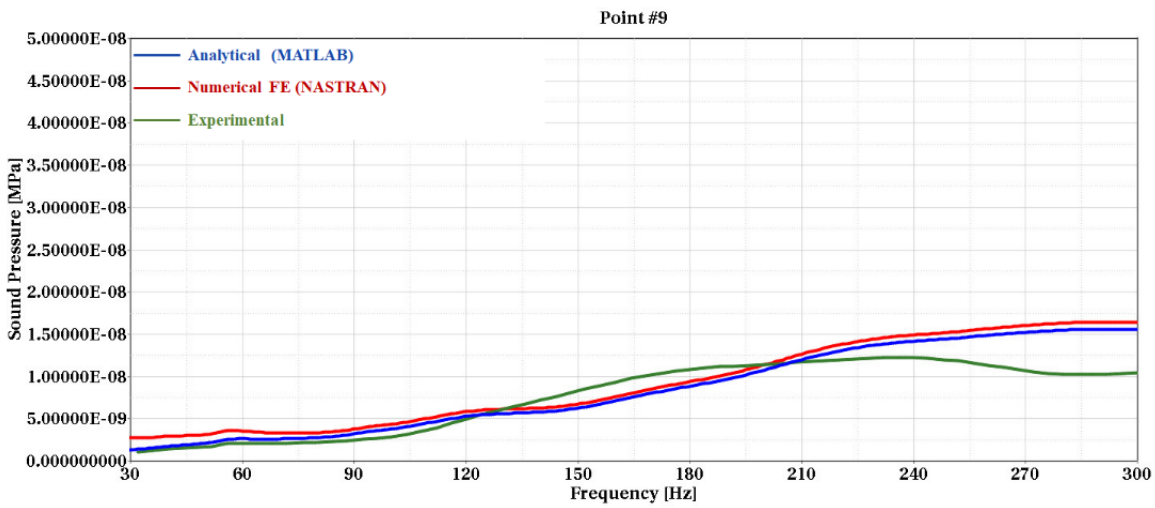


*Figure 6.57* Analytical, FE, and experimental sound pressure at point 9 microphone for 6.5-inch speaker

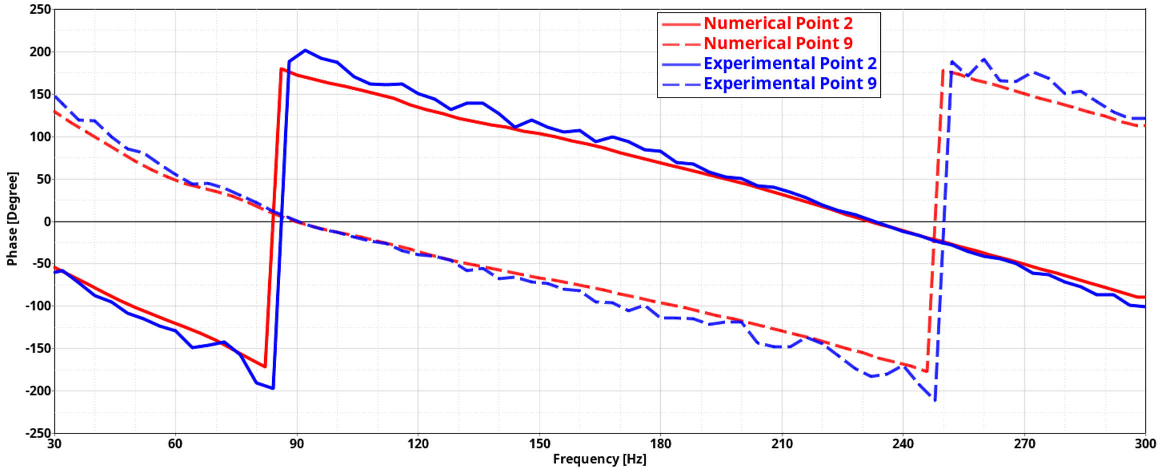


*Figure 6.58* Experimental and FE Microphone sound pressure phase at points 2 and 9 for 6.5-inch speaker

## 6.11 General Shape Speaker CAE Model

In many cases, an exact theoretical formulation for speaker profiles may not be possible. For example, there is no analytical solution for a 6x9 speaker. Consequently, we developed a generalized approach to characterize a speaker using relevant parameters obtained from tests. Based on the speaker's projected area and the dimensions of the ellipse representing it, we can develop a FE model as shown in Figure 6.59 for a 6x9 speaker. The diaphragm of the speaker has radii of 100 mm and 72.6 mm, resulting in a projected area of 0.0228 m$^2$. This FE model is run in a free field with a unit load enforced velocity as shown in Figure 6.60. Figure 6.61 shows the sound pressure for a unit enforced velocity of 1 mm/s at point 2. Using the unit velocity sound pressure, we can estimate the diaphragm velocity through interpolation to obtain the experimental sound pressure of Figure 6.62 at point 2.

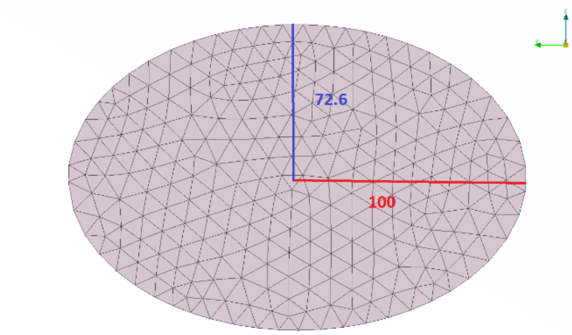


*Figure 6.59* Elliptical flat diaphragm FE model for 6x9 speaker

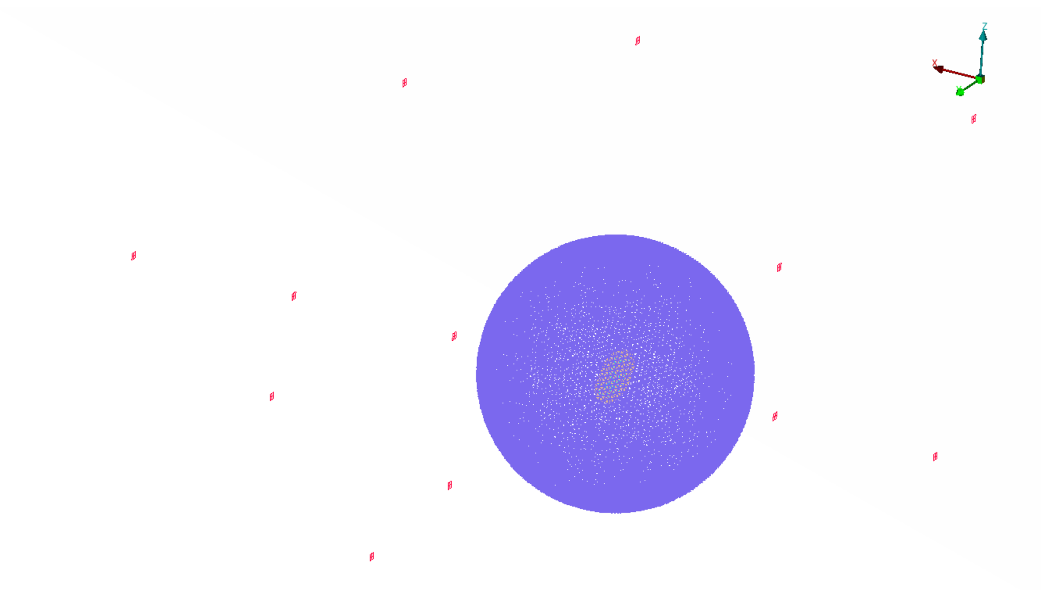

*Figure 6.60* Elliptical flat diaphragm FE model for 6x9 speaker in free field

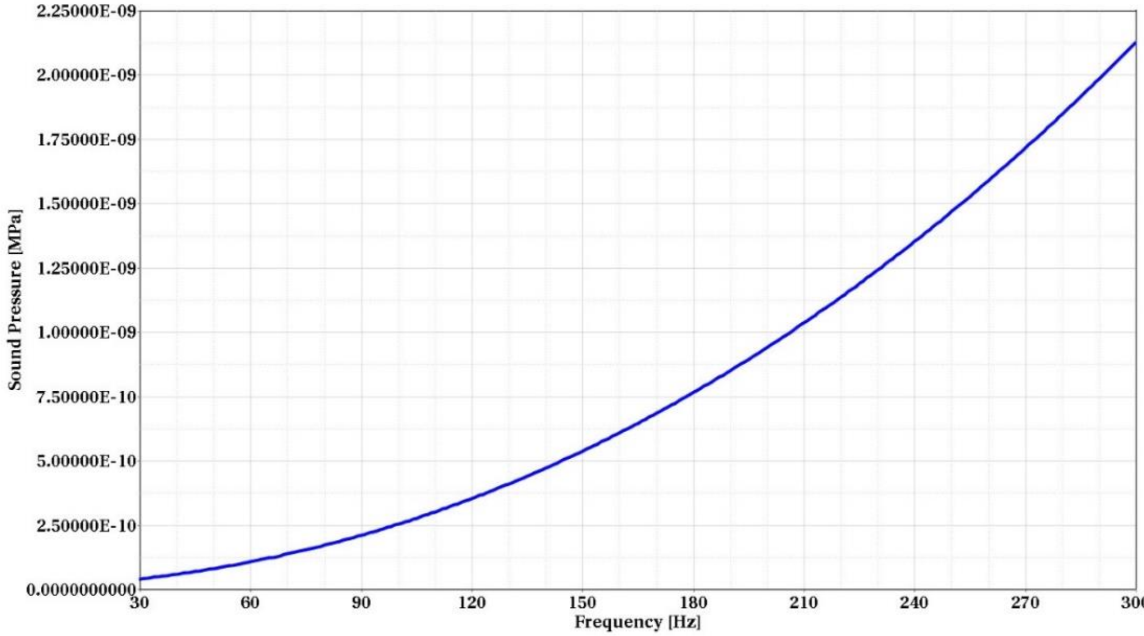


*Figure 6.61* FE model sound pressure at point 2 for a unit load diaphragm velocity of the 6x9-inch speaker

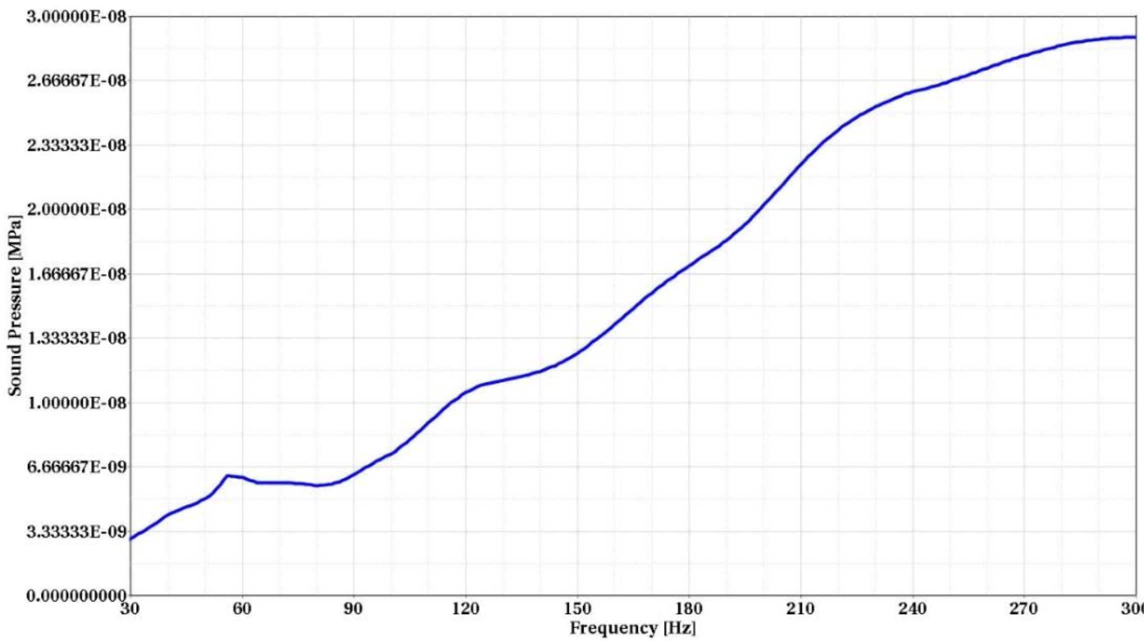


*Figure 6.62* 6x9 inch speaker experimental results

Based on Equation (6.71), the sound pressure response and volumetric velocity vary linearly. Thus, the sound pressure response and the diaphragm velocity vary linearly as well. Using proportional scaling between the plots in Figure 6.61 and Figure 6.62 we can calculate the diaphragm velocity of Figure 6.63.

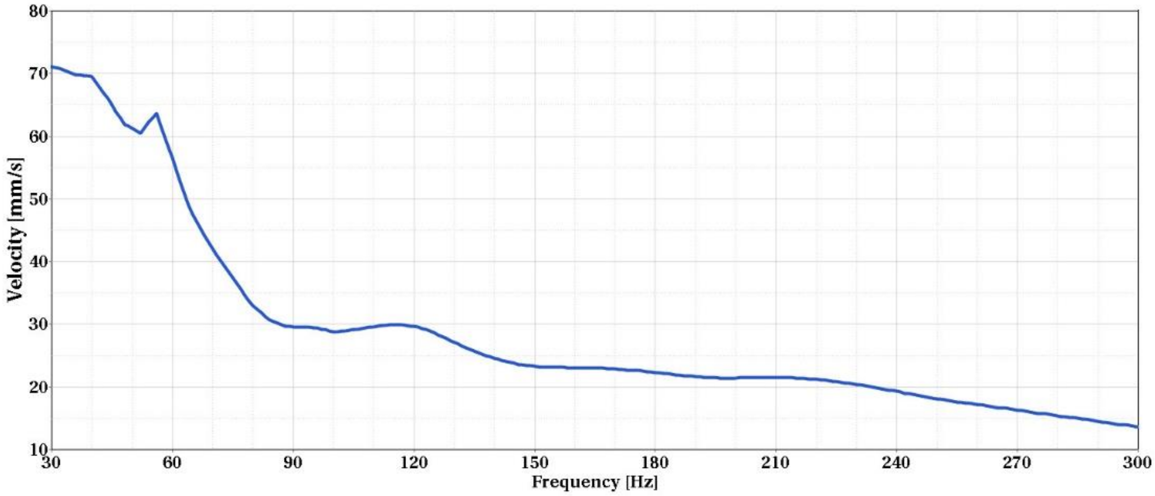


*Figure 6.63* Calculated velocity of diaphragm for point 2

Utilizing this velocity as an input to our FE model enables us to numerically calculate the Sound Pressure Level (SPL) at all twelve points. As shown in Figure 6.64 and Figure 6.65, there is an excellent agreement between the FE predictions and the experimental results. This allows us to characterize any speaker vibro-acoustically, even in the absence of an exact analytical solution, provided we have access to the speaker specifications and are able to conduct a standard sensitivity test. This approach not only facilitates a comprehensive speaker characterization but also enhances our understanding of its vibrational and acoustic behavior, contributing to advancements in audio engineering and design optimization.

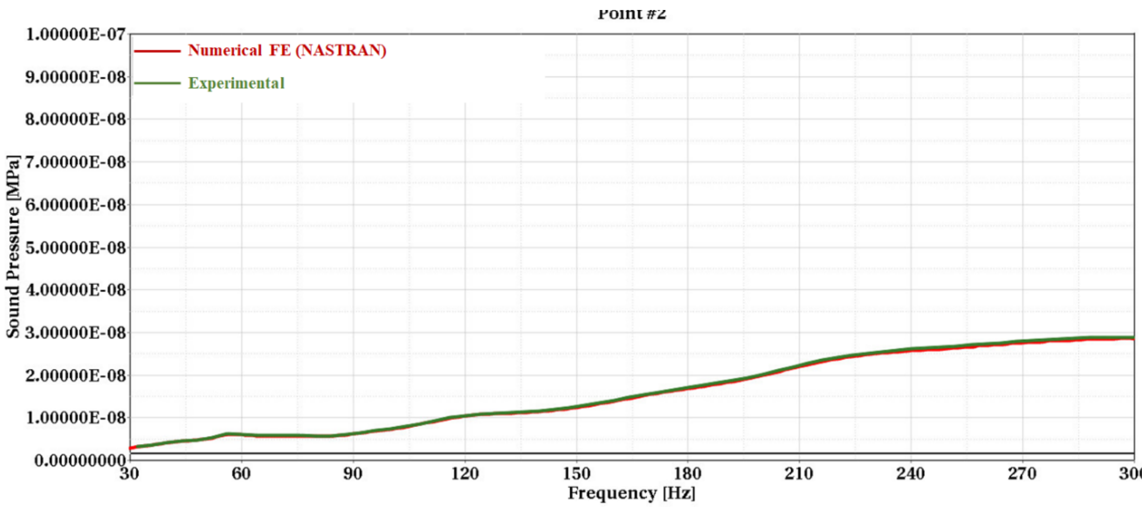


*Figure 6.64* Comparison between experimental and FE sound pressure at point 2 for a 6x9-inch speaker

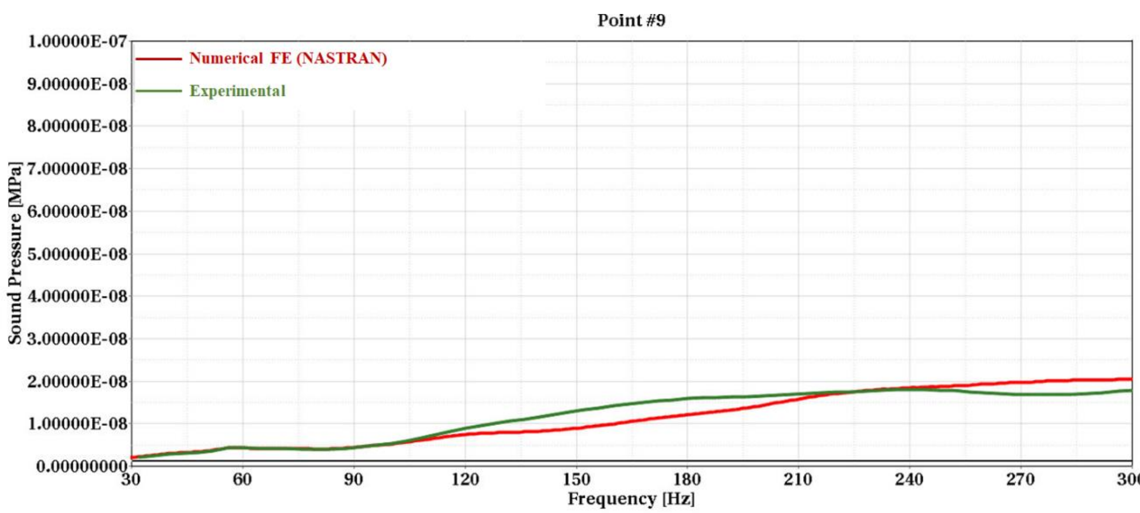


*Figure 6.65* Comparison between experimental and FE sound pressure at point 9 for a 6x9-inch speaker

## 6.12 Speaker Characterization Predictivity with Electrical Input Change

Since the impedance data for the speaker is available, we can use Ohm's law [81] to calculate the electrical power as

$$|P_{EE}(f)| = |\frac{V(f)^2}{R(f)}| \tag{6.72}$$

The acoustic power is linearly proportional to the electrical power used to define the speaker efficiency. Thus, if the impedance function and the acoustic response are known for a given electric power input (i.e., voltage input), we can calculate the acoustic response for different voltage inputs. This is very practical since we assume that the speaker efficiency is constant for comparable voltage inputs. Also, Equation (6.73) shows that the pressure magnitude $|P(r,t)|$ and the input acoustic power $W(f)$ have a quadratic relationship

$$|P(r,t)| = \frac{\frac{1}{2\pi f} \cdot \sqrt{\frac{8\pi c\, W(f)}{\rho}}\rho c k}{4\pi r} \tag{6.73}$$

Using Equation (6.74) we can predict the pressure for an input voltage of 2 Watts using a reference pressure for an input of 1 Watt for example, as shown in Figure 6.66 for the 6x9 speaker.

$$SP\ @\ New\ Voltage$$
$$= \sqrt{\frac{P_{EE\ @\ New\ voltage}}{P_{EE\ @\ Refrance\ voltage}}} * SP\ @\ Refrance\ volatge \tag{6.74}$$

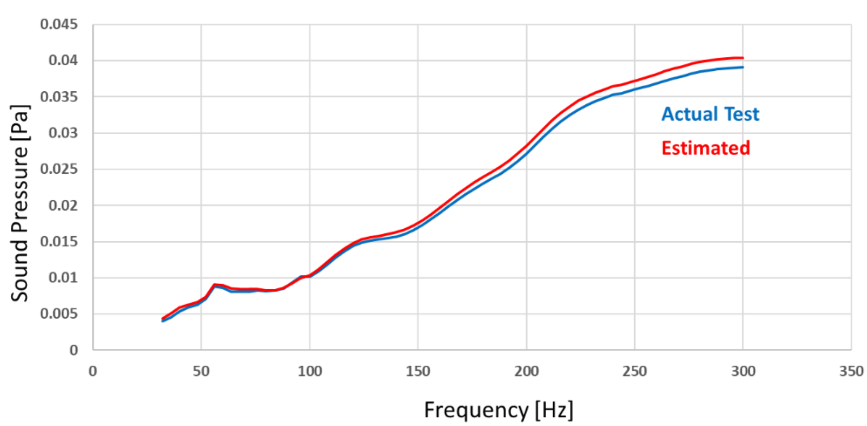


*Figure 6.66* Comparison between estimated and experimental sound pressure for a 2-Watt electrical input at point 2 for a 6x9 speaker

## 6.13 Summary

In this Chapter, we developed a speaker model using limited specifications provided by the speaker's manufacturer. We derived closed-form solutions for the monopole, dipole, and baffled moving cone configurations, and proposed a closed-form solution for the non-baffled moving cone. In addition, for each speaker representation, we developed a detailed FE model, which can be used for any practical application. The results of the FE models agree very well with closed-form solutions.

Our findings indicate that the non-baffled moving cone model is optimal in representing a loudspeaker. The model effectively captures the directivity of sound. Based on testing of multiple speakers, we demonstrated the accuracy of the developed closed-form solutions and the accuracy of developed FE models. Testing results showed that the developed methodology to acoustically characterize a speaker is applicable for complex speaker cone geometries and varying input signals, highlighting the robustness and applicability of the developed approach in real-world applications.

# CHAPTER SEVEN

# LOUDSPEAKER MOUNTING STIFFNESS DESIGN FOR ANC

A speaker in a vehicle door is typically supported by the door carrier module (Figure 7.1). The stiffness of the vehicle door module carrier resists bending deformation when the door opens and closes. There have been several studies conducted on this topic to determine the effects of stiffness on vehicle safety, performance, as well as the user experience including audio performance. Researchers have concluded that the stiffness of the door carrier module is important for several reasons. First is the structural rigidity since the stiffness of the door carrier module helps to improve the overall rigidity of the door. Second is the crash safety. In the event of a collision, a stiff module can help to distribute the impact forces more evenly across the vehicle body, reducing the risk of passenger injury. The third area is durability. A door carrier module with high stiffness can also have improved durability and longevity. It can better withstand the stresses of daily use, such as frequent door opening and closing. A fourth area is noise, vibration, and acoustics. It has been shown that a stiff door can help to reduce the level of noise, vibration, and harshness inside the vehicle. This is because a stiff module absorbs and dampens vibrations that may be transmitted through the vehicle body resulting in a quieter vehicle cabin. Additionally, it has been shown that the door carrier module influences the audio sound quality.

The door carrier module and structure display a vibration response to acoustic loading originating from the loudspeaker, whereas the door cavity exhibits a distinct acoustic response to the same loudspeaker loading. This response may interfere with the loudspeaker output, resulting in alterations to the sound, a phenomenon commonly referred to as "distortion". To date, there exists no comprehensive framework or methodology to comprehend the different distortions that may exist in door speakers and vehicle systems. Furthermore, there is currently no methodology to assess the stiffness requirements for the door speaker attachment points at the component level to optimize active noise cancellation system performance.

*Figure 7.1* Typical door speaker system location (left), door carrier module (middle), and speaker attachment points (right)

## 7.1 Stiffness Requirements for Mounting Loudspeakers

One of the main goals in ANC system prediction is to accurately model the loudspeaker frequency response when integrated into the vehicle door structure. Achieving this requires a good understanding of loudspeaker behavior, as discussed in CHAPTER Six, and a development of detailed finite element models for both the door structure and the vehicle cavity. A loudspeaker converts electrical signals into mechanical vibrations, thereby generating sound waves. It comprises a magnet, a voice coil, a diaphragm, and a suspension. The magnet and voice coil are in a magnetic field, while the diaphragm and suspension are attached to the voice coil.

The application of an electrical signal induces a magnetic field within the voice coil and the permanent magnet moves the voice coil and the diaphragm, producing mechanical vibrations. The diaphragm, which is critical for producing sound waves, is supported and centered by the suspension, also known as the spider, positioned at the base of the speaker.

Figure 7.2 shows the design and assembly details of these components which significantly influence the loudspeaker's overall performance and sound quality.

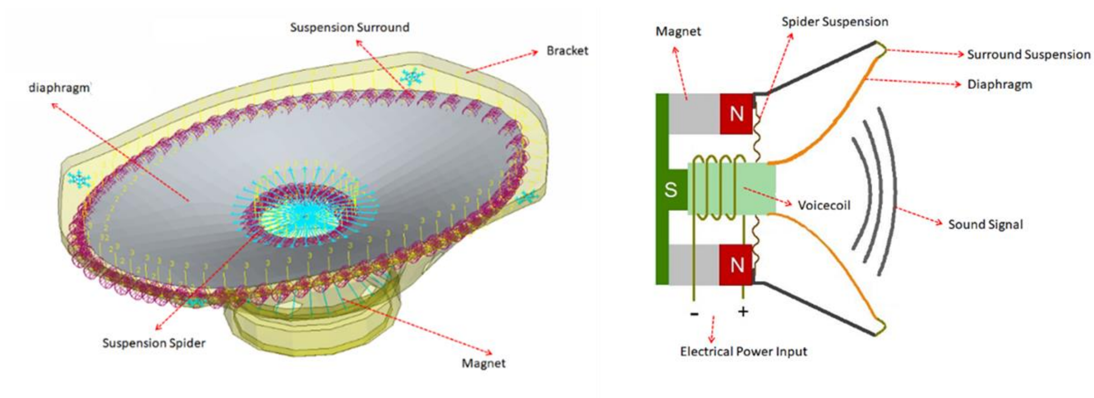


*Figure 7.2* Speaker components

The alteration of speaker frequency response is due to various factors, including the attachment stiffness, the door and cabin acoustic cavities, and the interplay between fluid and door structure, often termed as "loudspeaker sound distortion". Failure to comprehend these distortions can impede the effectiveness of an active noise canceling system. For this reason, this research concentrates on all distortions using an analysis encompassing the speaker mounting stiffness, the door module acoustic coupling and cavity distortions, and the vehicle cavity gain.

The primary aim of this chapter is to obtain the optimal stiffness at loudspeaker attachment points to ensure peak performance of the ANC system. A comprehensive understanding of the distortion induced by door vibration necessitates an accurate measurement of the door stiffness. Consequently, an analytical tool is necessary to quantify the required door attachment stiffness for optimal ANC performance.

## 7.2 Vehicle Loudspeaker Sound Signal Distortions

### 7.2.1 Door Structure Sound Signal Distortion

In a typical setup, a loudspeaker is fixed to the door carrier module. Under operation, the speaker induces door vibrations altering its output sound signal. This is known as door structure sound signal distortion. Figure 7.3 shows a basic loudspeaker model and its equivalent lumped parameter model. The speaker voice coil generates a force, resulting in an acoustic pressure wave, while a resulting reaction force at the mounting location induces door vibrations which in turn, interfere with the produced sound signal. In addition, the vibrating door emits sound that further disrupts the sound generated by the speaker.

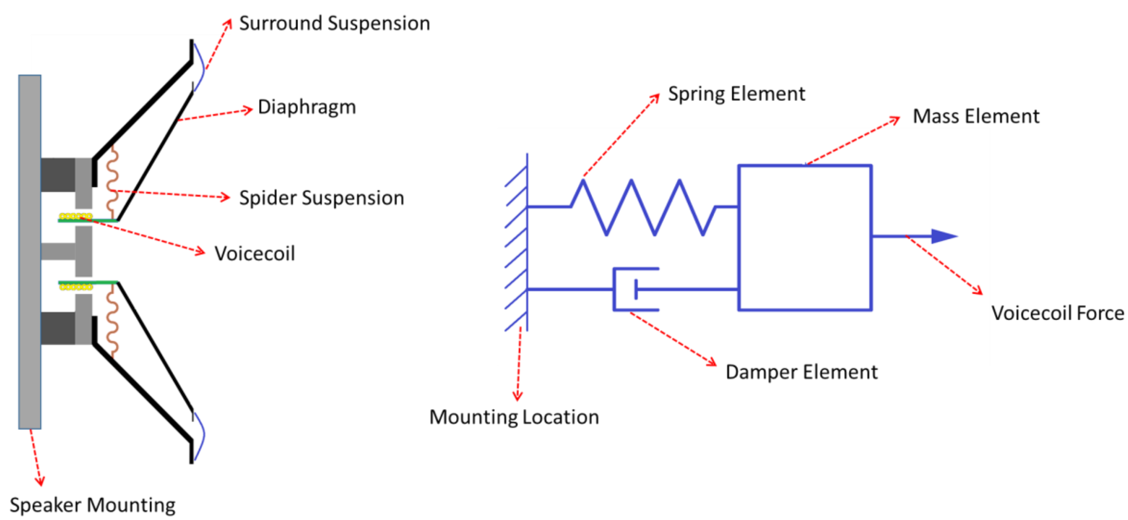


*Figure 7.3* Speaker schematic and lumped parameter model

To illustrate the door structure distortion utilizing a lumped parameter model, Figure 7.4 shows a simplified FE model of a baffled loudspeaker with a circular diaphragm. The lumped parameters representing the speaker spring and damper are integrated into the FE model using a bushing element, while a rigid plate is employed for the speaker diaphragm. The diaphragm is excited by the force of Figure 7.5, while the Sound Pressure Level (SPL) in front of the diaphragm is shown in Figure 7.6. The response point is chosen along the axis of the diaphragm.

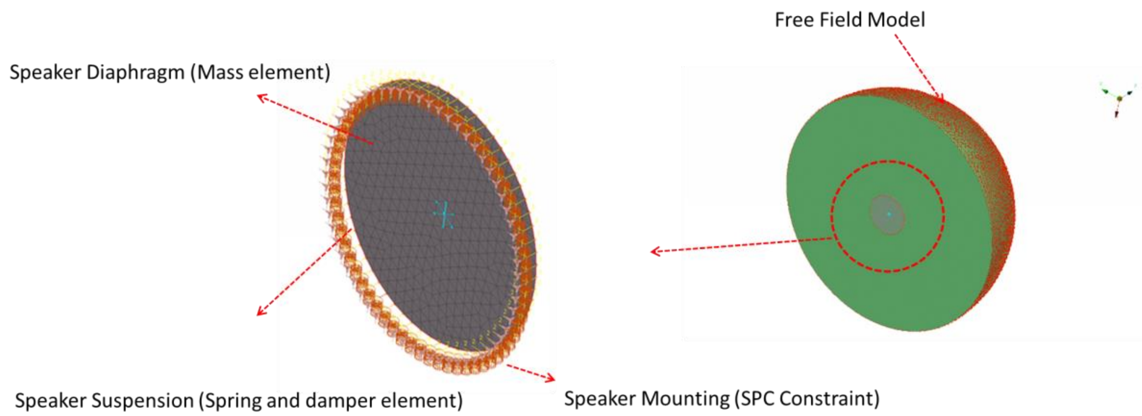


*Figure 7.4* Simplified loudspeaker FE model

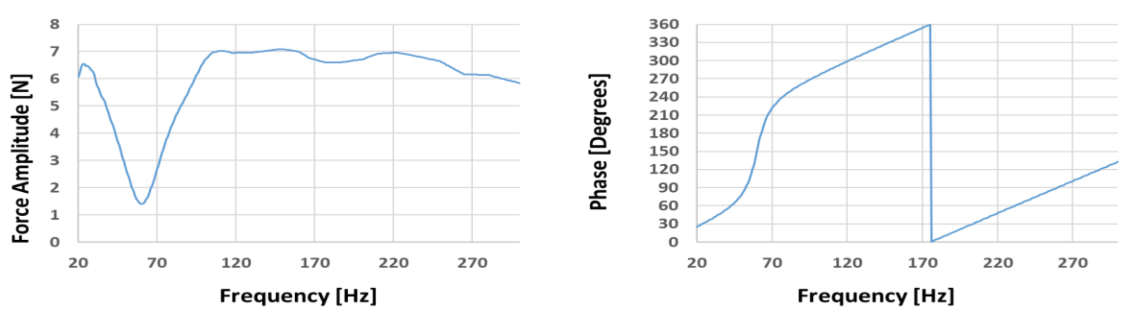


*Figure 7.5* Force exciting the speaker diaphragm

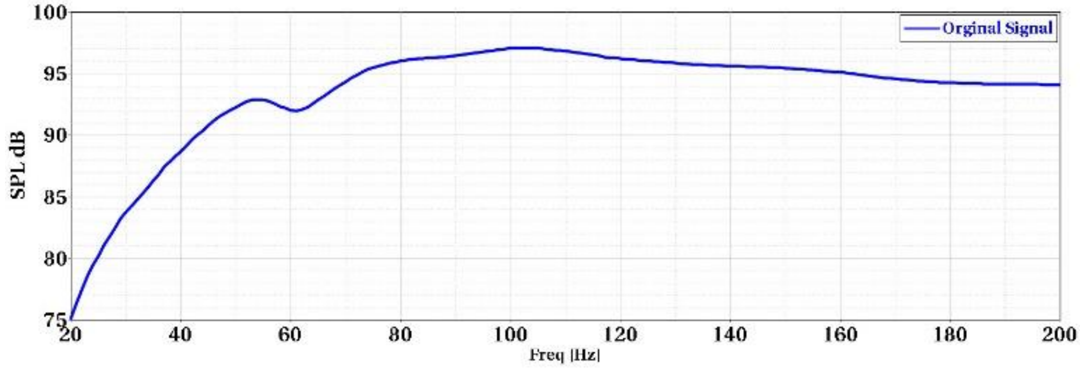


*Figure 7.6* Speaker original SPL

A "door-like" structure is simulated by attaching the diaphragm to a plate (Figure 7.7). The plate, representing the door structure, is firmly constrained along all edges. The plate is designed to exhibit a single pumping mode at 62.0 Hz in the frequency range of 0 to 150 Hz (Figure 7.8).

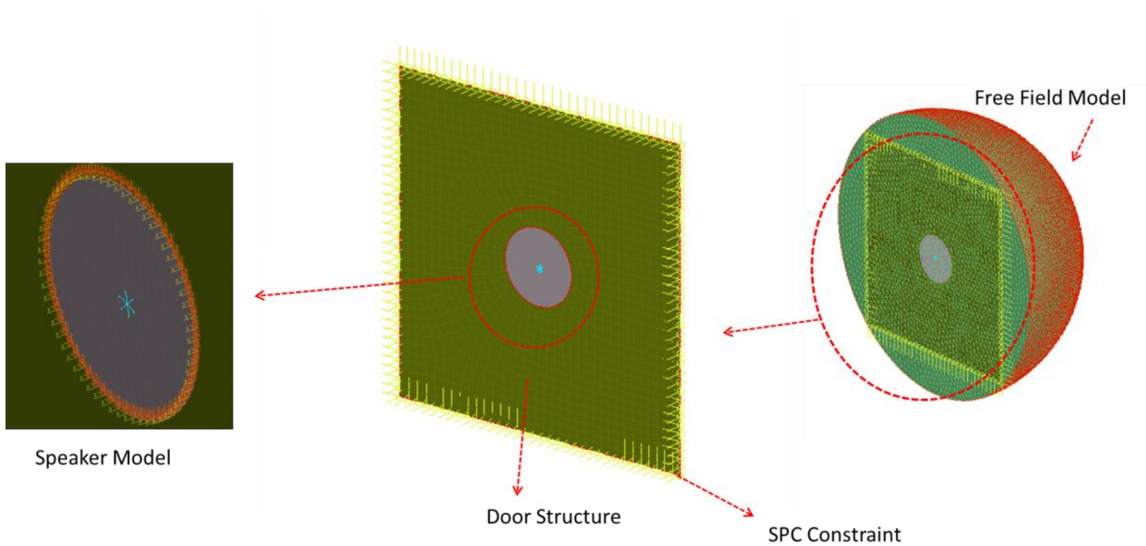


*Figure 7.7* Plate representation of door structure

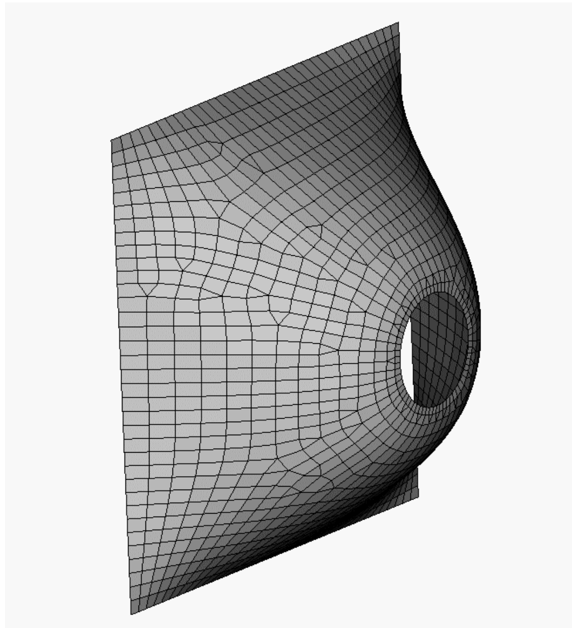

*Figure 7.8* Pumping mode shape of carrier plate at 62 Hz

Figure 7.9 shows the SPL produced by the loudspeaker as it is affected by the door vibrations. The plate mode notably impacts the sound signal around 62 Hz, resulting in a decrease of approximately 8 dB in the speaker's sound generation capacity at that frequency. Moreover, this decline in the speaker's ability to produce sound is not isolated at 62 Hz but spans a range from 55 Hz to 70 Hz. This is known as the speaker mounting structural distortion. Also, the acoustic output from the vibrating door interferes with the acoustic signal. If we consider the acoustic pressure loading on the door in the FE analysis (fluid structure interaction or FSI), the signal distortion differs significantly.

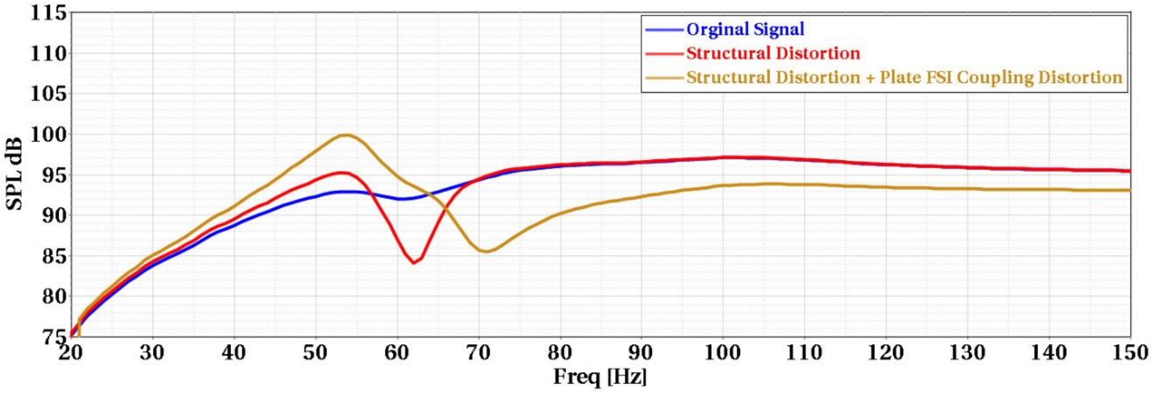


*Figure 7.9* Doors structural and FSI coupling distortions

### 7.2.2 Door Cavity Sound Signal Distortion

Figure 7.10 shows a simplified door closed cavity and a simplified model of the door-mounted loudspeaker to represent a vehicle door cavity. The cavity exhibits a single flexible mode at 120 Hz in the range of 0 to 150 Hz. The mode is a back-and-forth motion as shown in Figure 7.11. Figure 7.12 shows the door cavity distortion in the range from 55 Hz to 125 Hz which aligns with the cavity mode at 120 Hz. This can significantly distort the sound signal.

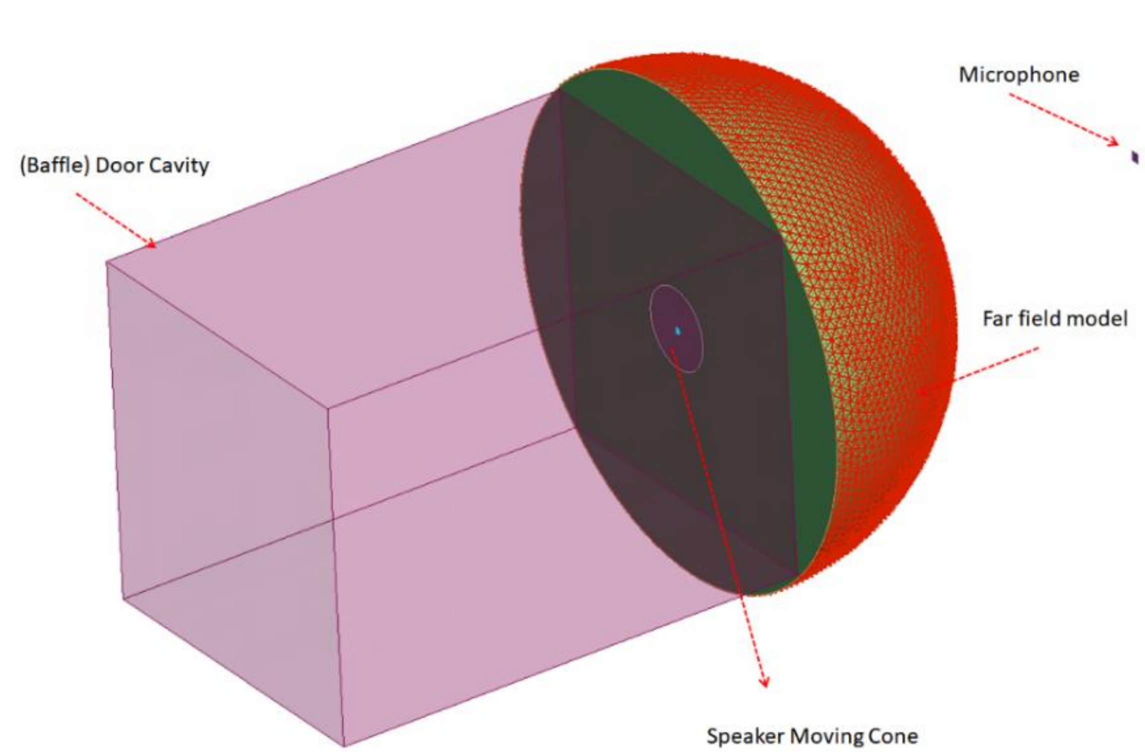


*Figure 7.10* Simplified door cavity

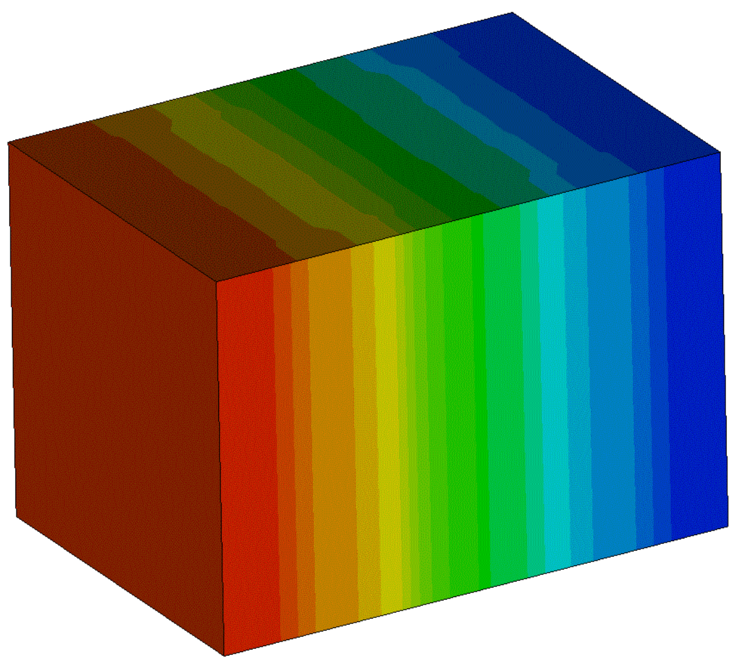

*Figure 7.11* Simplified door cavity mode at 120 Hz

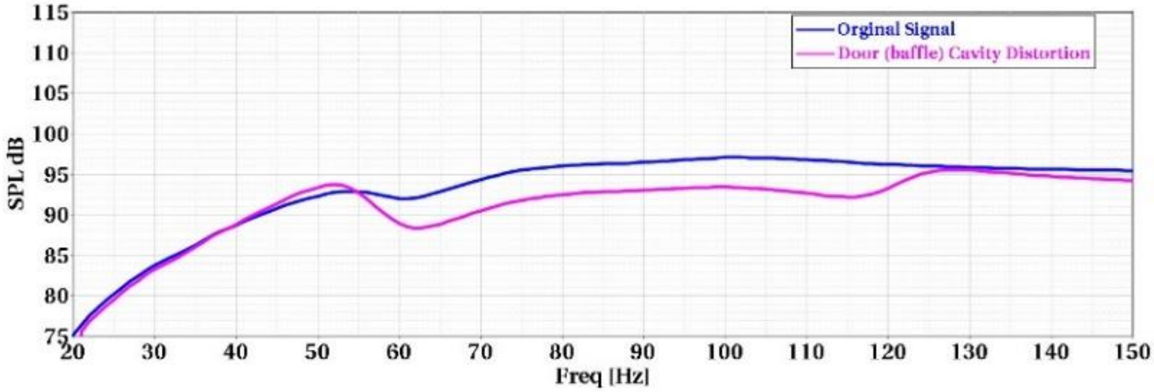


*Figure 7.12* Door cavity distortion

### 7.2.3 Vehicle Cavity Distortion

Figure 7.13 shows the simplified door cavity connected with a simplified vehicle cavity. The latter has three flexible modes at 50.1 Hz, 100.3 Hz, and 106.5 Hz. Figure 7.14 shows the SPL at 1 meter in front of the speaker illustrating the impact of the vehicle cabin's resonance, as indicated by the peaks corresponding to the vehicle cavity's three modes. The SPL reflects the distortion from the door structure and the cavity. However, due to interactions between modes, the peaks and dips are not perfectly aligned. A sound signal in the vehicle cabin may be affected by one or more of these distortions.

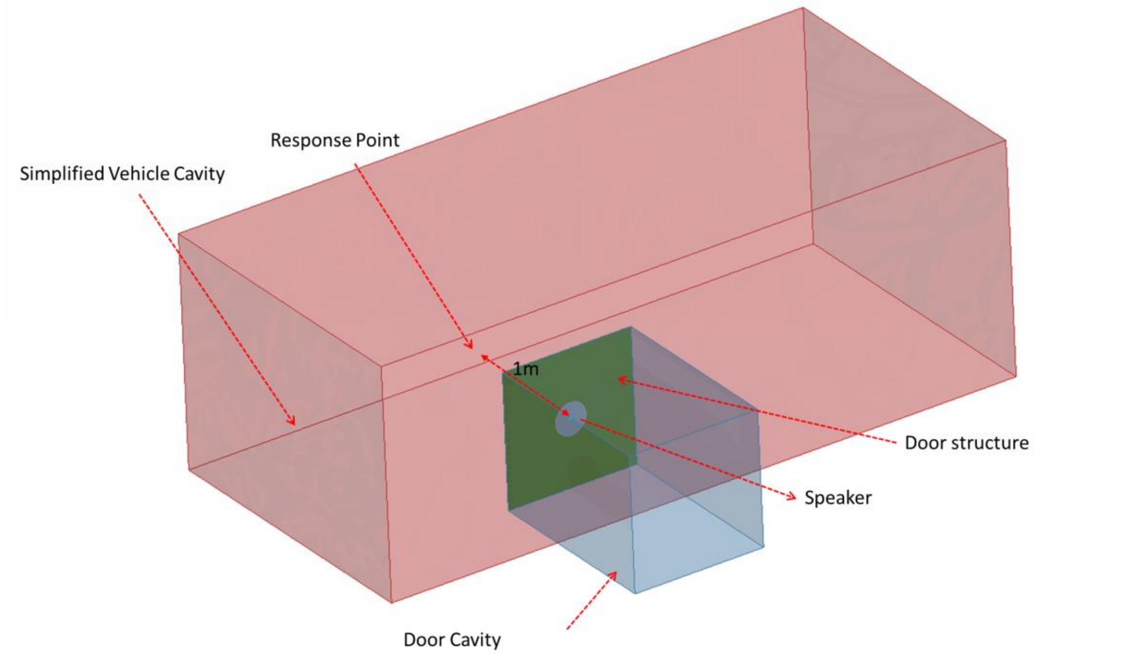


*Figure 7.13* Simplified models for vehicle and door cavities

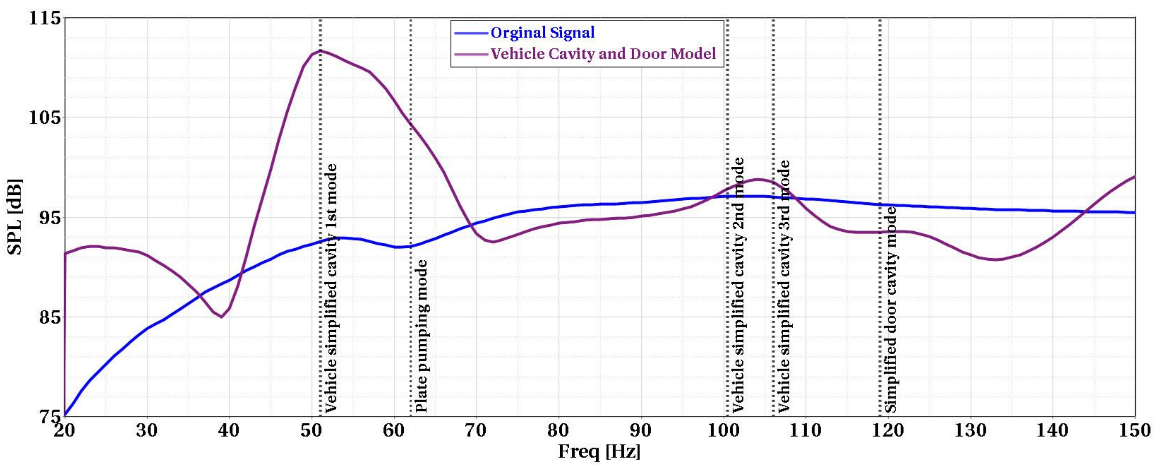


*Figure 7.14* Distortions from vehicle and door cavities

## 7.3 Design of Door Structure for Speaker Mounting

Ensuring proper support of the speaker at its mounting locations is critical as previously highlighted. However, in the initial phases of vehicle design, there is often limited available information on the door soft trim and the speaker specifications. The loudspeaker is typically described using the specifications of Table 6.1 and there is no CAD design available for the speaker bracket.

During the early stages of vehicle development, FE models for the door sheet metal and the carrier module are usually accessible before the completion of the TBIW and the acoustic cavity FE models. Figure 7.15 illustrates an initial FE model for the door assembly, where all soft trims are represented by lumped mass elements. The speaker brackets are typically very stiff. For instance, as shown in Figure 7.16, the door speaker exhibits its first flexible mode at 410 Hz which is well outside the typical ANC frequency range of 25 to 300 Hz. The figure shows the mode shape and modal strain energy of the speaker bracket. Due to sufficient modal separation observed in most cases, the flexible modes of the speaker structure are unlikely to contribute significantly to the ANC vibro-acoustic response. Hence, during the early stages of door structure development, we can simplify the speaker structure using a rigid element and the speaker mass can then be modeled by a lumped mass positioned at the center of this rigid element (Figure 7.17).

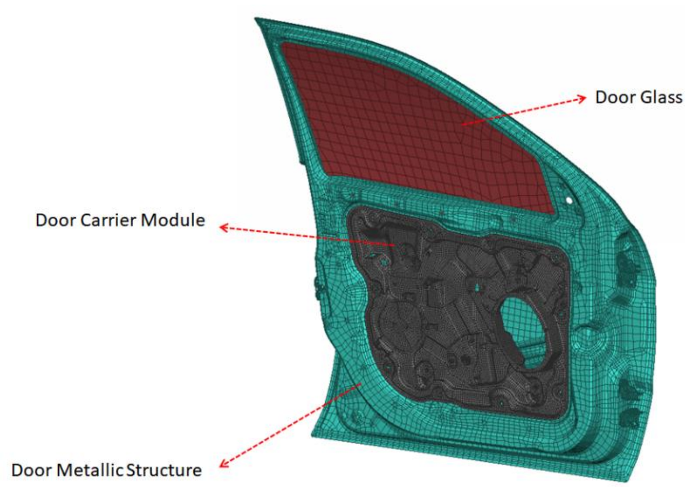


*Figure 7.15* Door structure early development FE model

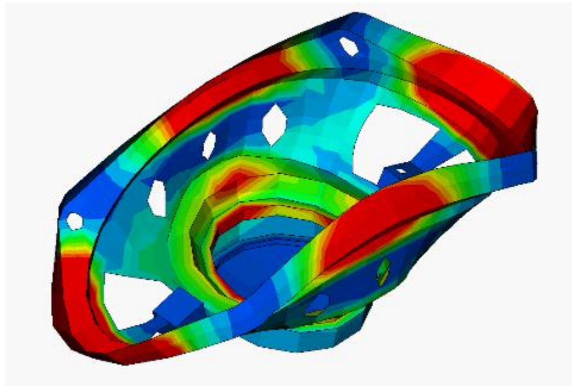

*Figure 7.16* First flexible mode and modal strain energy of speaker bracket

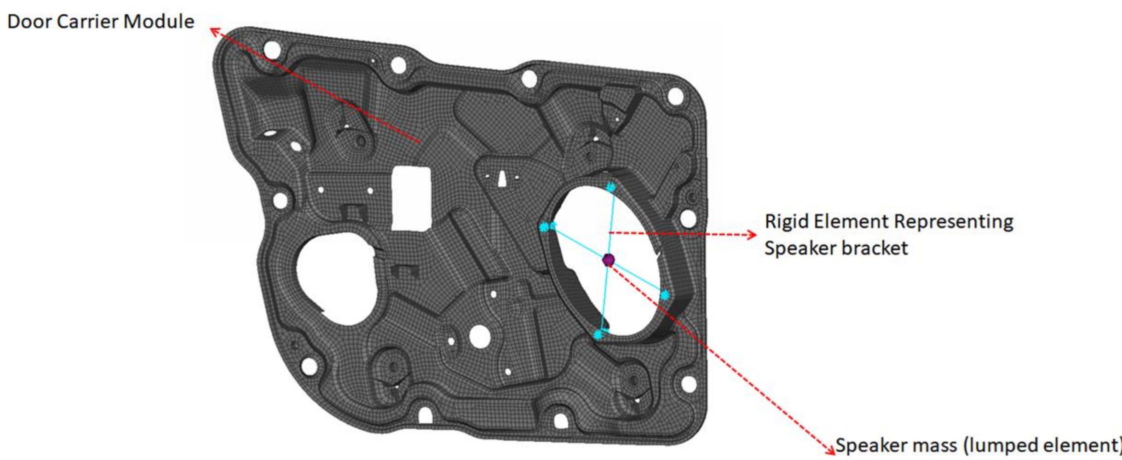


*Figure 7.17* Speaker representation using a rigid element and a lumped mass

As mentioned, the speaker is typically mounted on the door carrier module with a finite compliance at the mounting locations. This compliance introduces magnitude and phase distortions in the measured acoustic pressure compared to a speaker which is rigidly mounted. During the early vehicle development, the door sheet metal and other components undergo constant changes. As a result, the speaker mounting locations on the carrier module is subject to continuous adjustment. Furthermore, to fully evaluate the ANC system, comprehensive models of the TBIW and the car cavity are required (Figure 7.18). These models are typically unavailable during the initial stages of vehicle development, and additionally the process of modeling the far-field cavity and speaker is time consuming. Therefore, there is a critical need for a methodology that can guide the design of door structures during the early stages of product development using basic speaker data and a simplified door FE model.

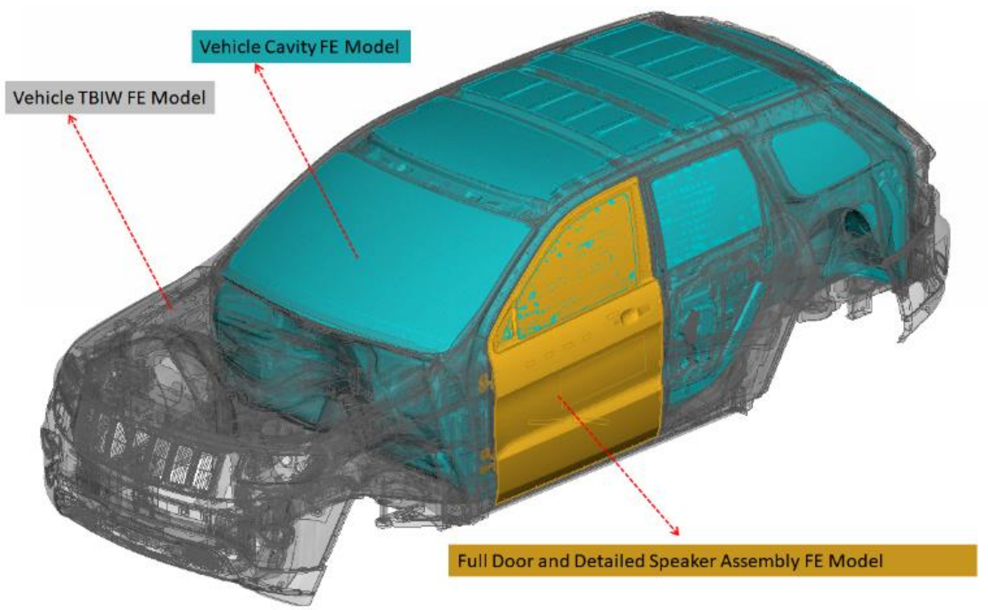


*Figure 7.18* Full vehicle TBIW and door speaker FE model

A method is needed to calculate the magnitude and phase distortion due to the door compliance. For that, the speaker is modeled using either the free-free model of Figure 7.19 or the fixed-free model of Figure 7.20. For the former, *M* is the total speaker mass which is usually much larger than the moving mass $m_d$ of the speaker diaphragm and part of the voice coil mass. Since *M* is much larger than $m_d$, the fixed-free model is used [82]. Thus, the following assumption is used

$$M \gg m_d \tag{7.1}$$

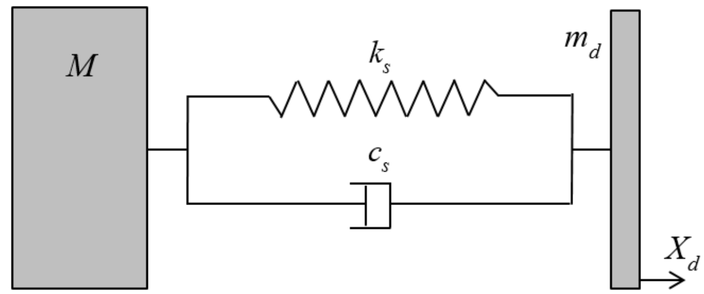


*Figure 7.19* Schematic of free-free speaker model

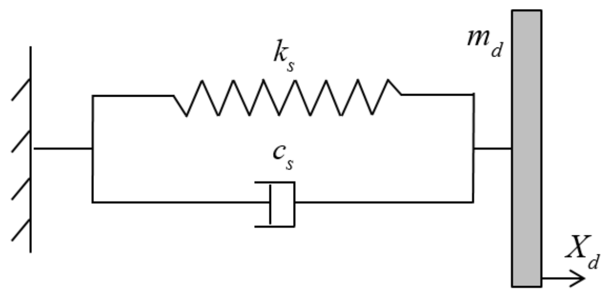


*Figure 7.20* Schematic of fixed-free speaker model

Utilizing the previously developed moving cone (piston) loudspeaker model, we calculate the necessary force on the speaker diaphragm to achieve a required velocity. This process known as "speaker characterization," determines the force required on the speaker diaphragm to generate a measured acoustic pressure at 1 meter from the speaker. Since the applied force on the speaker diaphragm is due to the input electric power supplied to the speaker, we assess the force on the speaker diaphragm in terms varying input power. Thus, the speaker characterization yields a "transfer function" relating the input electric power and the force driving the speaker membrane. Additionally, an FRF sub-structuring approach is employed to quantify the magnitude and phase distortion from the dynamic behavior of the door.

### 7.3.1 Force on a Moving Cone Speaker Diaphragm

As we discussed in Section 6.9, the best representation of a speaker is the moving cone. The total force applied on the loudspeaker diaphragm is denoted $F$ which is the sum of the speaker mechanical force $F_{me}$ and the acoustic force $F_{acu}$. The latter can be calculated by integrating the sound pressure over the diaphragm area

$$F_{acu} = \int_S \; p(r_c, \beta) dS \tag{7.2}$$

Using Equation (6.64) with $\beta = 0$, we get

$$F_{acu} = \int_S \; \rho c U e^{j(\omega t)} [e^{-jkr_c} - e^{-jk\sqrt{{r_c}^2 + {\alpha_c}^2}}] dS \tag{7.3}$$

or

$$\begin{aligned} F_{acu} = \int_S \; pd = \; \rho c \pi {\alpha_c}^2 U e^{j(\omega t)} \bigg[ 1 - \frac{J_1(2k\alpha_c)}{k\alpha_c} \\ + \frac{H_1(2k\alpha_c)}{k\alpha_c} j \bigg] \end{aligned} \tag{7.4}$$

where $H_1$ is the first Struve function and $J_1$ is the first Bessel function.

To calculate the mechanical force on the diaphragm, the following equation of motion of the diaphragm mass $m_d$ is used

$$m_d \ddot{x}(t) + c_s \dot{x}(t) + k_s x(t) = F_{me}(t) \tag{7.5}$$

where $x(t)$ is the displacement of the diaphragm. This equation is solved for a harmonic force signal. The following phasor notation is used

$$F_{me}(t) = Re\big(\bar{F}_{me} e^{j\omega t}\big) \; and \; x(t) = Re(\bar{X} e^{j\omega t}) \tag{7.6}$$

where $\bar{F}_{me}$ is the phasor (complex quantity) of $F_{me}(t)$ and $\bar{X}$ is the phasor of $x(t)$. Note that the frequency of $x(t)$ is the same with the excitation frequency $\omega$. Substitution of Equations (7.6) in Equation (7.5) yields

$$\bar{X} = \frac{\bar{F}_{me}}{[-m_d\omega^2 + j\omega c_s + k_s]} \tag{7.7}$$

Considering that the phasor of the velocity $\dot{x}(t)$ is equal to $j\omega\bar{X}$ , Equation (7.7) yields

$$F_{me} = \frac{\dot{X}((k_s - m_d\omega^2) + j\omega c_s)}{j\omega} \tag{7.8}$$

Recalling that $\dot{X} = U$ where

$$U = \frac{p(r_c, \beta)}{\frac{j\omega\rho\pi a_c{}^2}{4\pi r_c}\left[\frac{2J_1(ka_c sin\beta)}{ka_c sin\beta}\right] e^{j(\omega t - kr_c)}\, cos(\beta) k d_p}$$

we get

$$F_{me} = \frac{p(r_c, \beta)}{\frac{j\omega\rho\pi a_c{}^2}{4\pi r_c}\left[\frac{2J_1(ka_c sin\beta)}{ka_c sin\beta}\right] e^{j(\omega t - kr_c)}\, cos(\beta) k d_p}\Big((k_s - m_d\omega^2) + j\omega c_s\Big).\frac{1}{j\omega} \tag{7.9}$$

Finally total force on the diaphragm is given by:

$$F = F_{acu} + F_{me} \tag{7.10}$$

The analytical estimation of the applied force on the diaphragm was verified experimentally. A predefined sine sweep with 7 Volt input amplitude and zero phase was applied on the speaker and the vibration at the speaker attachment points was measured using accelerometers at each speaker attachment location as shown in Figure 7.21.

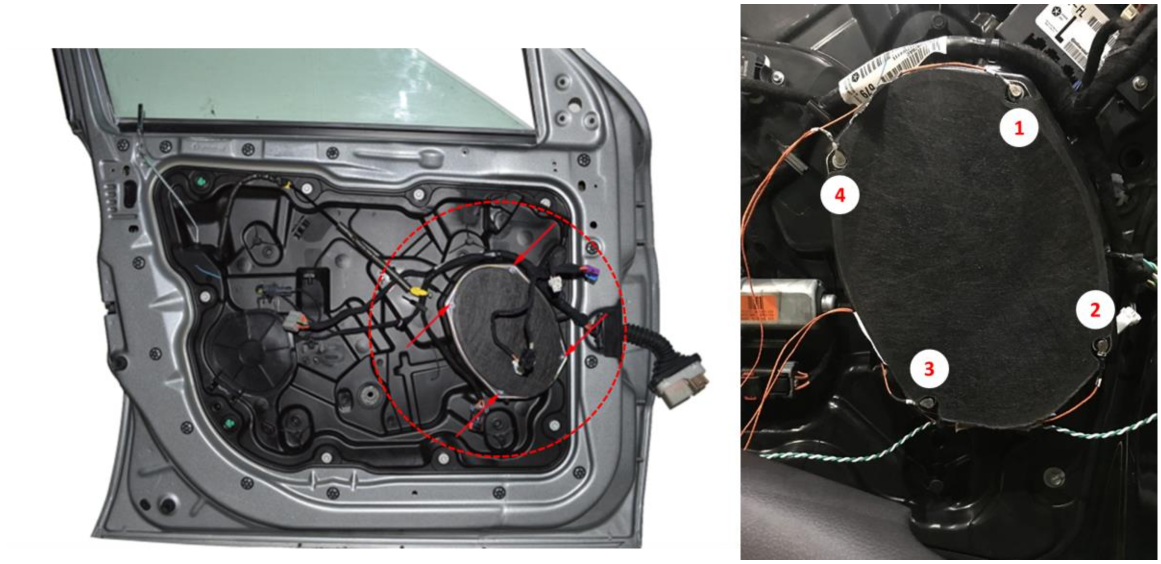


*Figure 7.21* Accelerometer locations on door-speaker assembly

The FEA model of the door-speaker assembly of Figure 7.22 was excited by a force based on Equation (7.10). A 6x9-inch speaker whose specifications are shown in Table 6.1, was used. Figure 7.23 shows the phase between current and voltage for the speaker.

*Figure 7.22* Door FE model for experimental force verification

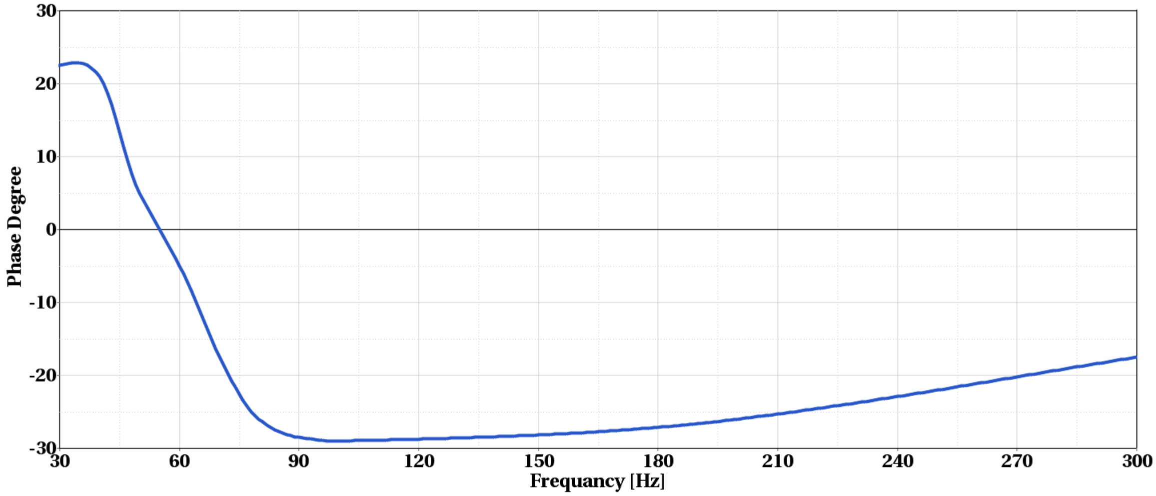


*Figure 7.23* Phase $\phi$ between current and voltage for the 6x9 speaker

The speaker input power is

$$P_{EE}(f) = V(f) * I(f) * cos(\phi) = \frac{V^2}{R} cos(\phi) \tag{7.11}$$

Because the acoustic power is proportional to the electrical power to the speaker, if the acoustic response is known for a given electric power input (i.e., voltage input), we can calculate the acoustic response for a different voltage input. Also, Equation (7.14) shows that the pressure and acoustic power have a quadratic relationship. This relationship holds for low frequencies where *ka* << 1. For the 6x9 speaker, the *ka* is approximately 0.5.

$$|P(r,f)| = \frac{\frac{1}{2\pi f} \cdot \sqrt{\frac{8\pi c\, W(f)}{\rho}} \rho c k}{4\pi r} \tag{7.12}$$

Using scaling (Section 6.12), the force on speaker was calculated for a 7 Volt input (Figure 7.24). This force was used in the door-speaker FE model and the resulting vibration displacement at each attachment point was compared with the experimental results as shown in Figure 7.25. The results show a good agreement indicating that the estimated force on the speaker diaphragm is reasonable.

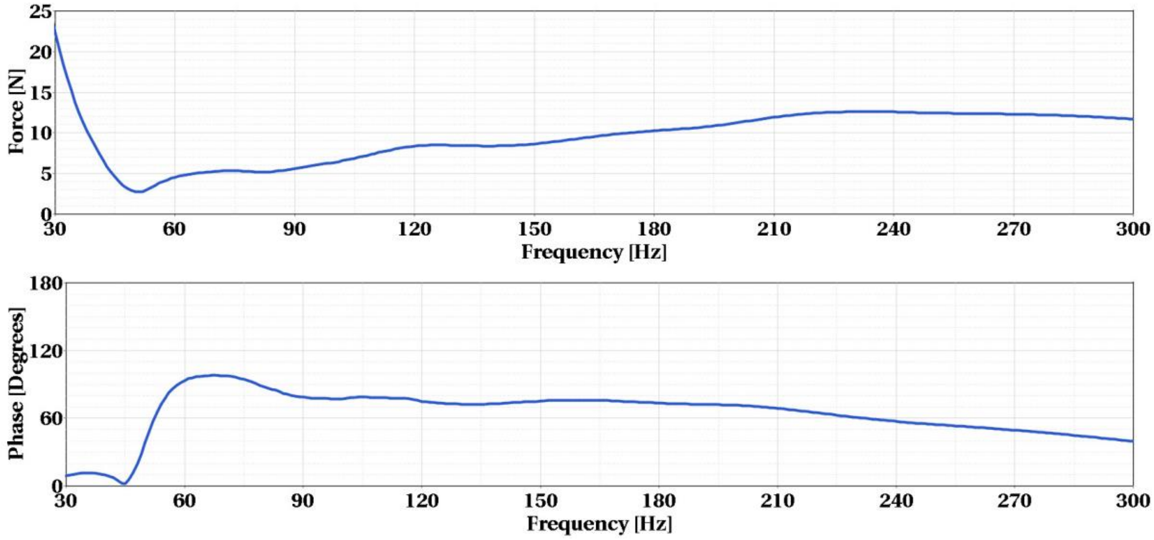


*Figure 7.24* Calculated force on the speaker with 7 Volt input

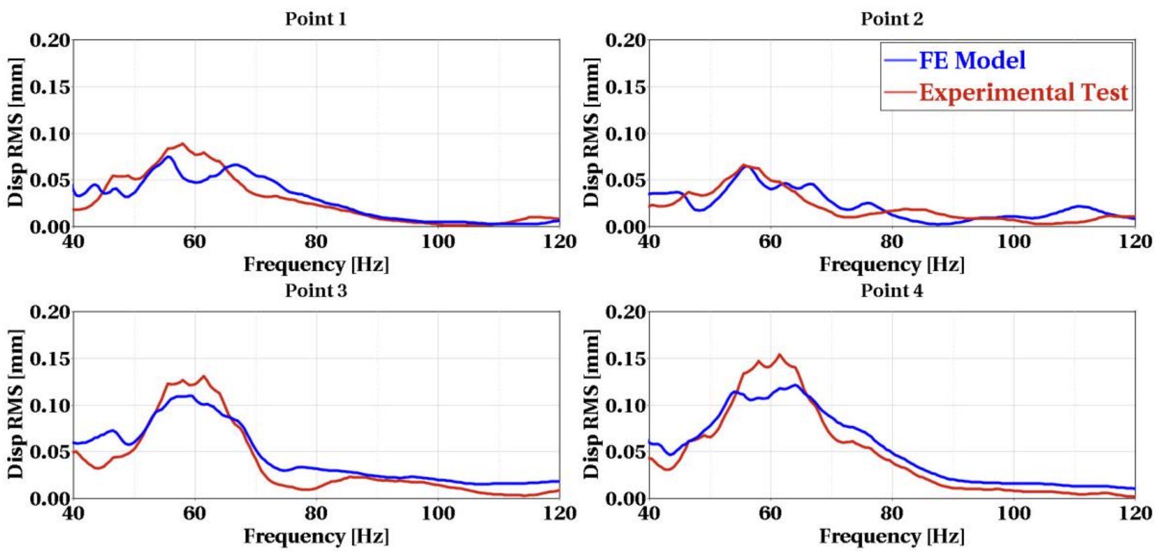


*Figure 7.25* Comparison between FE and experimental response at speaker attachment points

### 7.3.2 FRF Sub-structuring for Door Speaker Vibratory System

The FRF (Frequency Response Function) sub-structuring approach is used to combine the dynamics of the speaker with those of the door. An FRF, denoted by $H$, is defined in the frequency domain and is the ratio of the response phasor $\bar{X}$ over the force phasor $\bar{F}$. Since the force equilibrium on speaker diaphragm is expressed as

$$[-m_d\omega^2 + j\omega c_s + k_s]\bar{X} = \bar{F}$$

the FRF is

$$H = \frac{\bar{X}}{\bar{F}} = \frac{1}{[-m_d\omega^2 + j\omega c_s + k_s]} \quad (7.13)$$

Note that the FRF is complex because there is damping.

Figure 7.26 shows a schematic of the door structure connected in series with the speaker structure. The dynamics of the door are described by the following FRF

$$\bar{X}_2 = H_D\bar{F}_D \quad (7.14)$$

where $H_D$ is the FRF of the door, $\bar{X}_2$ is the displacement phasor at the interface between the door and the speaker, and $\bar{F}_D$ is the force phasor on the door at the interface with the speaker.

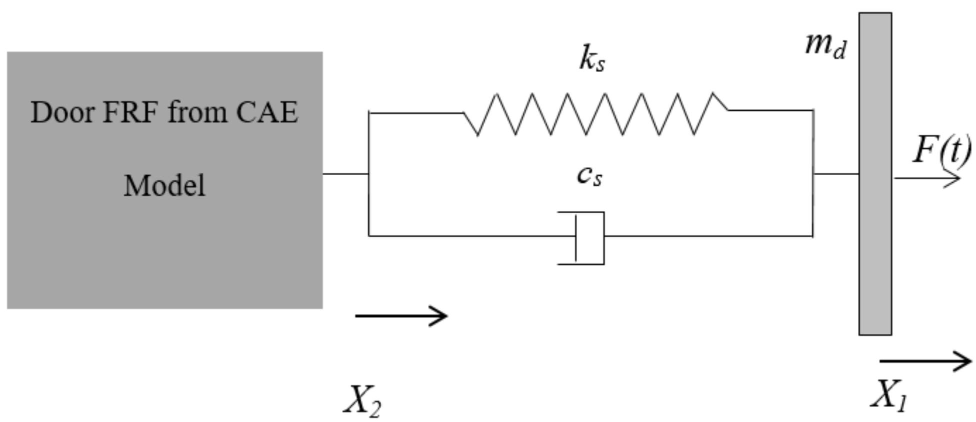


*Figure 7.26* Schematic of door FRF and speaker

Equilibrium of forces at the interface between the door and the speaker yields

$$\bar{F}_D = (\bar{X}_1 - \bar{X}_2)(k_s + j\omega c_s) \quad (7.15)$$

Combining Equations (7.14) and (7.15) results in

$$\bar{X}_2 = \bar{X}_1 - \frac{\bar{X}_2}{\bar{H}_D(k_s + j\omega c_s)}$$

or

$$\bar{X}_1 = [\ 1 + \frac{1}{\bar{H}_D(k_s + j\omega c_s)}]\bar{X}_2 \tag{7.16}$$

The equation of motion of the speaker structure is

$$m_d\ddot{x}_1 + c_s(\dot{x}_1 - \dot{x}_2) + k_s(x_1 - x_2) = F(t)$$

or using phasors

$$(-m_d\omega^2 + j\omega c_s + k_s)\bar{X}_1 - (k_s + j\omega c_s)\bar{X}_2 = \bar{F} \tag{7.17}$$

Substitution of $\bar{X}_1$ from Equation (7.16) into Equation (7.17) yields

$$(-m_d\omega^2 + j\omega c_s + k_s)\left[\ 1 + \frac{1}{\bar{H}_D(j\omega c_s + k_s)}\right]\bar{X}_2 - (j\omega c_s + k_s)\bar{X}_2 = \bar{F}$$

or

$$[(-m_d\omega^2)H_D(j\omega c_s + k_s) + (-m_d\omega^2 + j\omega c_s + k_s)]\bar{X}_2 = \bar{F}H_D(j\omega c_s + k_s)$$

resulting in

$$\bar{X}_2 = \frac{\bar{F}H_D(j\omega c_s + k_s)}{[(-m_d\omega^2)H_D(j\omega c_s + k_s) + (-m_d\omega^2 + j\omega c_s + k_s)]} \tag{7.18}$$

Finally, substitution of $\bar{X}_2$ from Equation(7.18) in Equation (7.16) yields:

$$\bar{X}_1 = \left[\ 1 + \frac{1}{H_D(j\omega c_s + k_s)}\right]\bar{X}_2 = \left[\frac{H_D(j\omega c_s + k_s) + 1}{H_D(j\omega c_s + k_s)}\right]\bar{X}_2$$

or

$$\bar{X}_1 = \left[\frac{H_D(j\omega c_s + k_s) + 1}{H_D(j\omega c_s + k_s)}\right]\frac{\bar{F}H_D(j\omega c_s + k_s)}{[(j\omega c_s + k_s)(1 - m_d\omega^2 H_D) - m_d\omega^2]}$$

or

$$\bar{X}_1 = \left[ \frac{[H_D + \frac{1}{(j\omega c_s + k_s)}]\bar{F}}{(1 - m_d\omega^2 H_D) - \frac{m_d\omega^2}{j\omega c_s + k_s}} \right] \tag{7.19}$$

Equation (7.19) provides the displacement phasor of the speaker moving mass $m_d$ if the door is present. Equations (7.13) through (7.19) describe the FRF sub-structuring method. It allows us to combine the door dynamics with the speaker dynamics using 1) compatibility of displacements at the door-speaker interface and 2) equilibrium of forces at the interface. The phasor $\bar{F}$ of the force $F(t) = \bar{F}e^{j\omega t}$ on the speaker diaphragm is provided by Equation (7.10).

### 7.3.3 Calculation of Speaker Distortion from Door Dynamics

The distorted speaker diaphragm velocity $u^*(t)$ due to the coupling of the speaker with the door is expressed as

$$u^*(t) = Re[j\omega\bar{X}_1 e^{j\omega t}] = Re[\bar{U}^* e^{j\omega t}] \tag{7.20}$$

or using Equation (7.19)

$$u^*(t) = Re[\frac{\left[H_D + \frac{1}{(j\omega c_s + k_s)}\right] j\omega\bar{F}}{(1 - m_d\omega^2 H_D) - \frac{m_d\omega^2}{j\omega c_s + k_s}} e^{j\omega t}] \tag{7.21}$$

Algebra on the phasor of $u^*(t)$ yields:

$$\bar{U}^* = \frac{[H_D + \frac{1}{(j\omega c_s + k_s)}]j\omega\bar{F}}{(1 - m_d\omega^2 H_D) - \frac{m_d\omega^2}{j\omega c_s + k_s}}$$

or

$$\bar{U}^* = \frac{\omega^2 c_s\bar{F} + j\omega\bar{F}[H_D {k_s}^2 + H_D(\omega c_s)^2 + k_s]}{\left[(1 - m_d\omega^2 H_D)\left({k_s}^2 + (\omega c_s)^2\right) - m_d\omega^2 k_s\right] + [m_d\omega^3 c_s]\, j} \tag{7.22}$$

If

$$\alpha_R = \omega^2 c_s \bar{F}$$

$$\alpha_I = \omega \bar{F}[H_D {k_s}^2 + H_D(\omega c_s)^2 + k_s$$

$$\beta_R = \left[(1 - m_d\omega^2 H_D)\left({k_s}^2 + (\omega c_s)^2\right) - m_d\omega^2 k_s\right]$$

$$\beta_I = [m_d\omega^3 c_s]$$

Equation (7.22) can be put in the form

$$\bar{U}^* = \frac{\alpha_R + \alpha_I j}{\beta_R + \beta_I j} = \frac{[\alpha_R\beta_R + \alpha_I\beta_I]}{{\beta_R}^2 + {\beta_I}^2} - \frac{[\alpha_R\beta_I - \alpha_I\beta_R]}{{\beta_R}^2 + {\beta_I}^2} j \tag{7.23}$$

Substitution of Equation (7.22) in Equation (7.23) yields

$$\begin{aligned} u^* &= Re\left(\left[\frac{[\alpha_R\beta_R + \alpha_I\beta_I]}{{\beta_R}^2 + {\beta_I}^2} - \frac{[\alpha_R\beta_I - \alpha_I\beta_R]}{{\beta_R}^2 + {\beta_I}^2} j\right] e^{j\omega t}\right) \\ &= Re[(V_1 + jV_2)e^{j\omega t}] \end{aligned} \tag{7.24}$$

where

$$V_1 = \frac{[\alpha_R\beta_R + \alpha_I\beta_I]}{{\beta_R}^2 + {\beta_I}^2} \qquad\qquad V_2 = -\frac{[\alpha_R\beta_I - \alpha_I\beta_R]}{{\beta_R}^2 + {\beta_I}^2}$$

Since

$$V_1 + V_2 j = \sqrt{{V_1}^2 + {V_2}^2}\, e^{j\varphi_V}$$

and

$$\tan\varphi_V = \frac{V_2}{V_1}$$

Equation (7.24) can be rewritten as

$$u^*(t) = Re\left(\left[\sqrt{{V_1}^2 + {V_2}^2}\, e^{j\varphi_V}\right] e^{j\omega t}\right) = \sqrt{{V_1}^2 + {V_2}^2}\, cos\,(\omega t + \varphi_V) \tag{7.25}$$

providing the distorted diaphragm velocity due to door structure (mounting location) compliance. The magnitude of the distorted velocity is $\sqrt{{V_1}^2 + {V_2}^2}$ and the phase is $\varphi_V$. Using Equation (6.71) and $u^*(t) = Re[\bar{U}^* e^{j\omega t}]$, the distorted sound pressure from the speaker can be written as

$$p(r_c, \beta) = Re[\frac{j\omega\rho {a_c}^2 \bar{U}^*}{4r_c}\left[\frac{2J_1(ka_c sin\beta)}{ka_c sin\beta}\right] e^{j(\omega t - kr_c)} cos(\beta) kd_p] \qquad (7.26)$$

To illustrate the sound distortion described in this section, we used the 6x9 speaker with properties described in Table 6.1. A known force was applied on the speaker diaphragm. The door compliance is $H_D = 5.54 * 10^{-5} e^{j\left(\frac{77}{180}\right)\pi}\ m/N$ if the speaker is attached to a flexible door, and $H_D$ = 0 (ideal case with no distortion) if the door is assumed rigid (Figure 7.27).

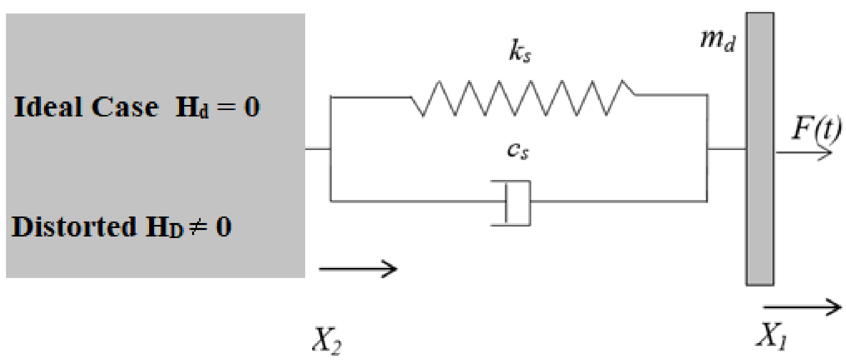


*Figure 7.27* FRF of rigid door versus flexible door

Figure 7.28 shows the velocity of the speaker diaphragm if the door is rigid ($H_D$ = 0) or flexible ($H_D \neq 0$). Figure 7.29 compares the speaker sound pressure at $r = 1m$ from the speaker indicating a sizeable magnitude and phase distortion.

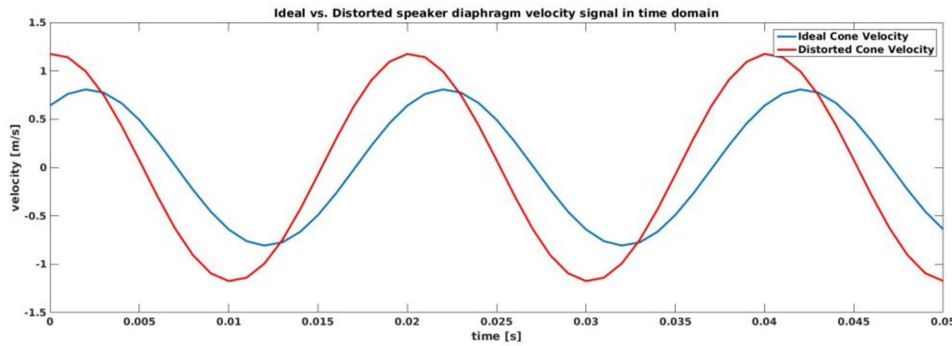


*Figure 7.28* Diaphragm velocity for rigid ($H_D = 0$) and flexible ($H_D \neq 0$) door

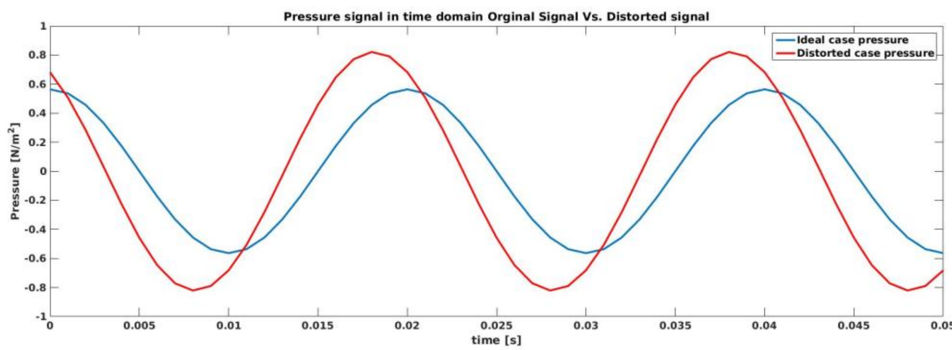


*Figure 7.29* Sound pressure for rigid ($H_D = 0$) and flexible ($H_D \neq 0$) door at 1m from the speaker

## 7.4 A Novel Door Structure Assessment Method for ANC

In Section 7.3 we demonstrated that there is a magnitude and phase distortion of the sound signal if the speaker is mounted on a flexible door. This section introduces a novel method to objectively determine the required door stiffness to achieve optimal speaker sound output with minimal distortion.

Figure 7.30 shows two rigidly mounted speakers. The sound pressure measured at a microphone, equidistantly positioned at 1 meter from each speaker at a specific frequency ω, will be zero if

$$F_1(t) = \bar{F}e^{j\omega t} \; and \; F_2(t) = \bar{F}e^{j\omega t} * \, e^{j\pi}$$

indicating that the forces on the two speakers have equal magnitude and are out of phase.

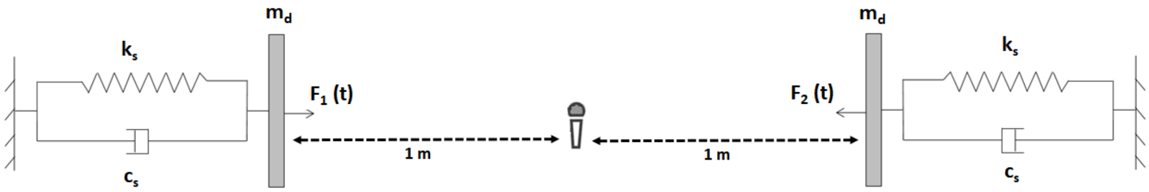


*Figure 7.30* Noise cancelation from rigidly mounted speakers

Now we assume that the speaker on the right is rigidly mounted while the one on the left is attached to a flexible door with a specified FRF (Figure 7.31). If the applied forces $F_1(t)$ and $F_2(t)$ on the two speakers match the ideal case (equal magnitude and out of phase), the sound measured at the microphone will be a nonzero signal due to distortion from the flexible door.

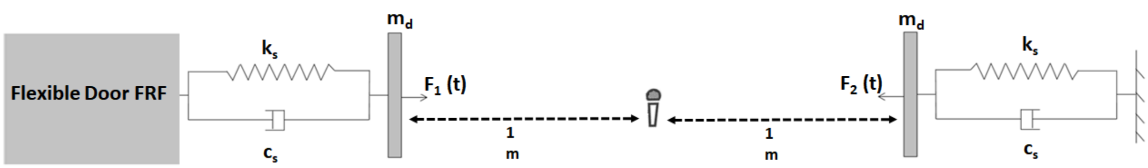


*Figure 7.31* Noise distortion speaker from flexibly mounted speaker

If the sound pressure level (SPL) generated by the single rigidly mounted speaker as of Figure 7.32 is denoted by $P_{Base}$ and the SPL generated by the two speakers of Figure 7.31 is denoted as $P_{distorted}$, we can define $P_{cancellation}$ representing the maximum achievable cancellation as

$$P_{Cancelation} = P_{base} - P_{distorted} \tag{7.27}$$

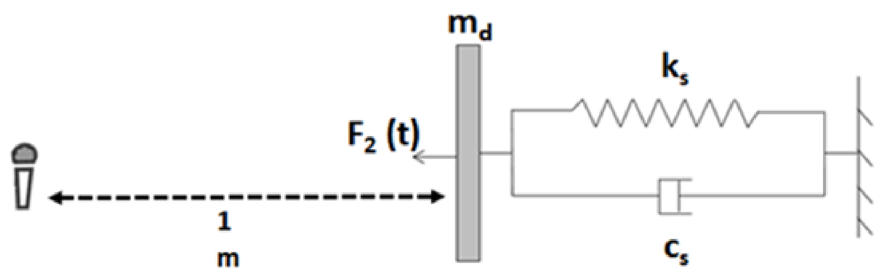


*Figure 7.32* Illustration of the base speaker model

This quantity serves as a metric for assessing the maximum achievable cancellation, under the assumption of an anechoic room environment, where the limiting factor is solely attributed to the door structural distortion.

Consider the FE door model of Figure 7.33, where the door content is typically accessible during the early stages of vehicle development. A point FRF is obtained by exciting the speaker lumped mass and in an orthogonal direction to the mounting plane with a unit force and calculating the response at the same location. Figure 7.34 shows the FRF magnitude and phase.

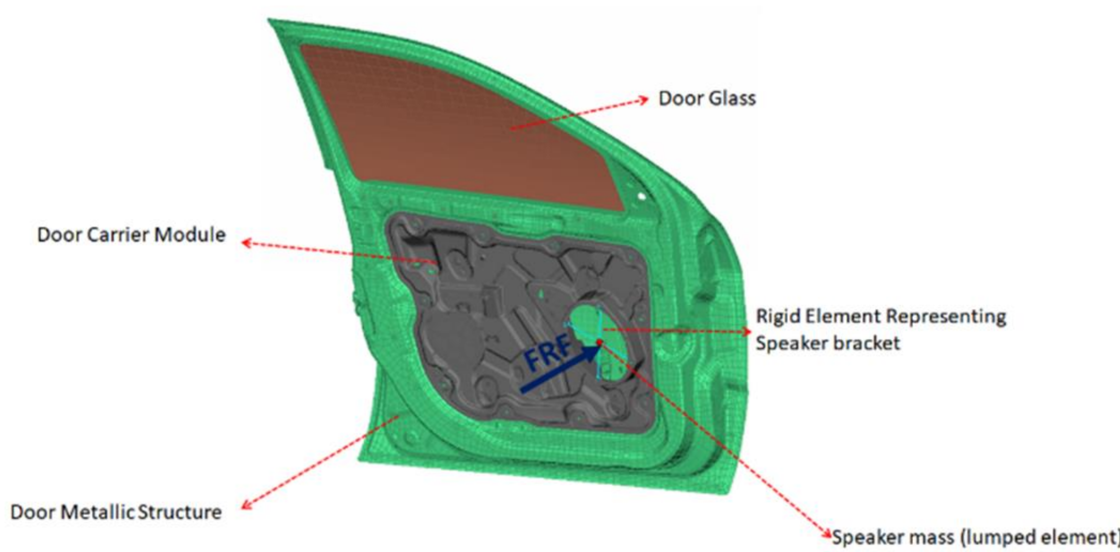


*Figure 7.33* FE door model with simplified speaker and door FRF point

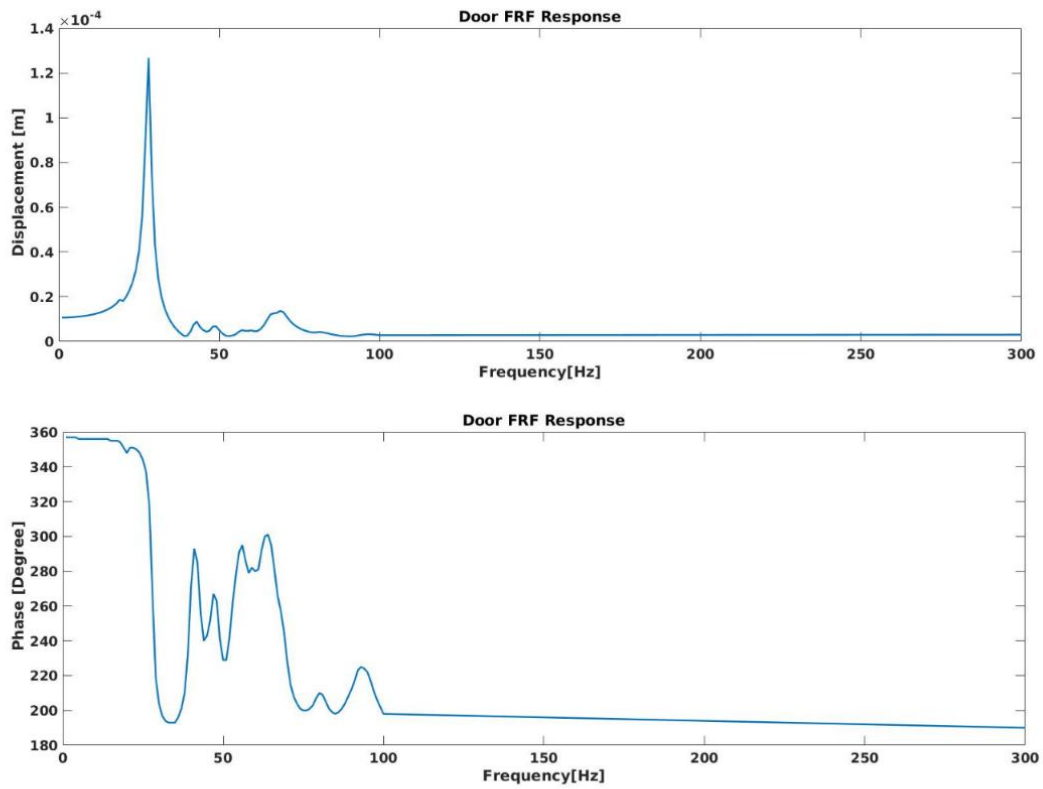


*Figure 7.34* Point FRF for door-speaker model

The point FRF, denoted by $H_D$, is a function of frequency and can be expressed as

$$H_D = H_{DMag} e^{(jwt + H_{DPhase})} \tag{7.28}$$

where $H_{DMag}$ is the FRF magnitude and $H_{DPhase}$ is the FRF phase (Figure 7.34). In this example, the 6x9-inch speaker of Table 6.1 was used with a 3-volt input. Figure 7.36 compares the SPL generated by the single rigidly mounted speaker ($P_{Base}$) with the SPL of the door-mounted speaker using FRF sub-structuring of Figure 7.35 ($P_{distorted}$). Using Equation (7.27) the $SPL_{Cancelation}$ is calculated as shown in Figure 7.37. The drop in SPL cancelation in the 20 to 70 Hz range is related to the door stiffness. This can be used for example, to assign a minimum of 20 dB cancelation for a specific vehicle program.

It should be noted that the speaker cancelation is reduced near cavity modes resulting in a poor ANC performance. Also, this example does not account for the door cavity or vehicle cavity distortions. It rather focuses on the door supporting structure.

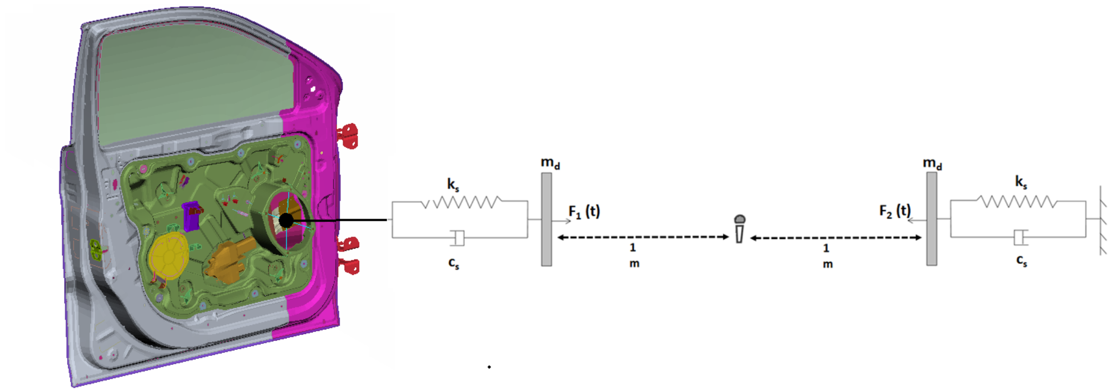


*Figure 7.35* Illustration of FRF sub-structuring door and base speaker

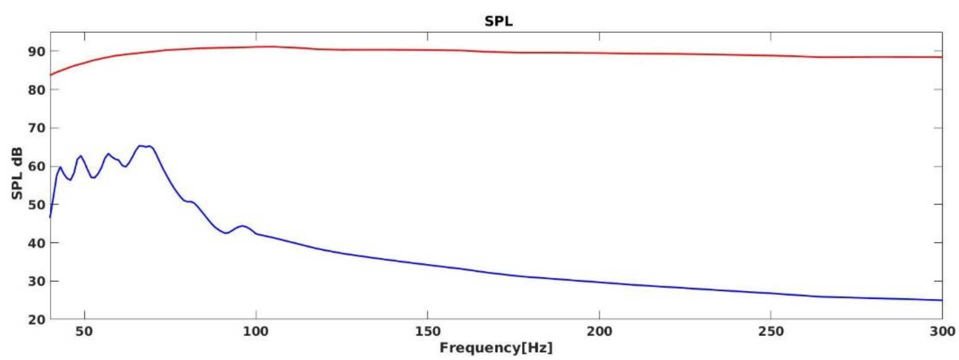


*Figure 7.36* $\mathrm{SPL}_{\mathrm{Base}}$ versus $\mathrm{SPL}_{\mathrm{Distorted}}$

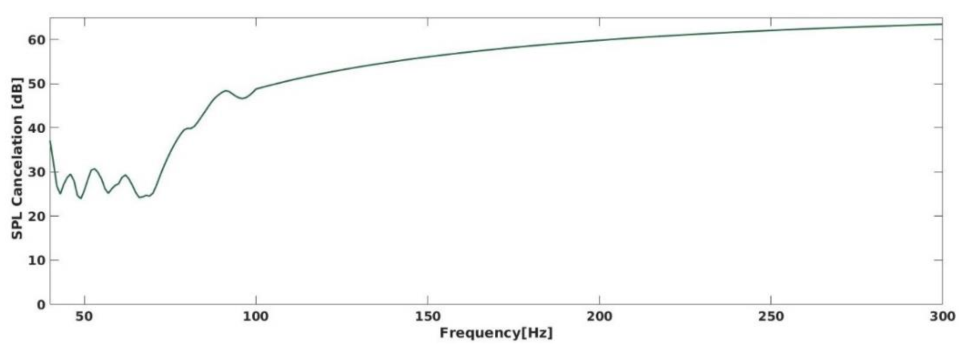


*Figure 7.37* $\mathrm{SPL}_{\mathrm{Cancelation}}$

## 7.5 Summary

This chapter highlighted the importance of optimizing the loudspeaker mounting stiffness in ANC to enhance audio performance. The stiffness of the door carrier module is a significant factor influencing ANC effectiveness. However, the integration of speakers into vehicle doors introduces interactions between structural vibrations and acoustics, resulting in sound signal distortions. This Chapter provided an overview of different distortions but placed emphasis on the door structural distortion.

This Chapter also presented an analytical approach to calculate the force on the speaker diaphragm followed by an experimental verification. In addition, this Chapter introduced a novel method for evaluating the effect of door stiffness on ANC performance. For that, mathematical models were developed to quantify speaker distortion caused by door compliance, enabling an objective assessment of stiffness requirements. A new sub-structuring method was also developed to couple the door and speaker dynamics and assess the effect of this coupling on the speaker SPL.

# CHAPTER EIGHT

# VEHICLE LEVEL ANC PERFORMANCE PREDICTION

Vehicle noise is described by a spectrum indicating a different amplitude at each frequency. Because of the many frequencies in a vehicle noise signal, the ANC system cannot cancel them all. Instead, it selects a narrow band of frequencies and averages out the results. This reduces the vehicle noise, but it cannot cancel it.

Figure 8.1 shows an example of active noise cancelling performance. The black line denotes the Power Train (PT) noise with ANC 'off' at the driver seat microphone location. When the ANC is 'on', the noise at the same location is shown with the red line. We observe that the cancelation is not uniform throughout the frequency range. At the highlighted areas, the ANC system noise attenuation is very small.

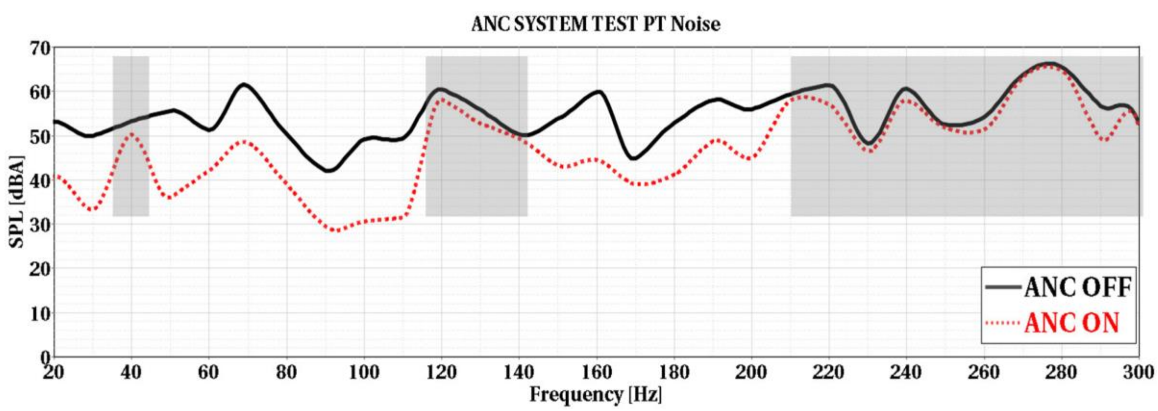


*Figure 8.1* Example plot illustrating ANC system cancelling PT noise

Various factors such as structural resonances, acoustic characteristics, speaker, and microphone placement, among others, significantly impact the ANC performance, potentially hindering its effectiveness. These vehicle-specific characteristics can restrict the ANC system's ability to cancel noise across certain frequency bands or at specific locations in the vehicle cabin. Our proposed method offers a predictive tool for determining the achievable ANC attenuation for noise sources or combinations thereof. Moreover, it enables a comprehensive examination of individual contributions from factors such as speaker and microphone placement, door stiffness, door and vehicle cavity modes, as well as vehicle panel resonances on the overall ANC performance. By focusing on a specific frequency range, a detailed analysis of door and vehicle cavity modes can elucidate the effectiveness of each microphone and speaker location in achieving noise cancelation. This information serves as a basis for optimizing the placement of speakers and microphones to enhance noise cancelation performance.

As previously outlined, a step in developing a predictive ANC model involves acquiring the transfer path (TP) functions from speakers to microphone and receiver points in the vehicle model. Using these TPs, along with the complete Trim Body in White (TBIW), vehicle and door cavities as well as the noise source excitation, we can construct a comprehensive ANC FE model which can then be integrated with an audio management supplier controller.

## 8.1 Vehicle-Speaker Transfer Function FE Model and Experimental Verification

The speaker model of Chapter 6 can be seamlessly integrated into the full TBIW FE model by positioning the speakers in the door structure.

Figure 8.2 shows the incorporation of speakers into the vehicle and door cavities. The speakers are supplied with a constant sine sweep input of 1 volt, and the corresponding response is captured for receiver and microphone points, as shown in Figure 8.3.

Typically, during the initial stages of physical ANC system development, these transfer paths (TPs) are measured for each speaker using prototype vehicles. Using the Simcenter Testlab, experiments were performed using a 1-Volt constant sine sweep input to each speaker and measuring the SPL at microphone locations and passenger-driver ear locations. Figure 8.4 shows the vehicle microphones locations and microphones placed at passenger and driver receiver points in the experimental test setup.

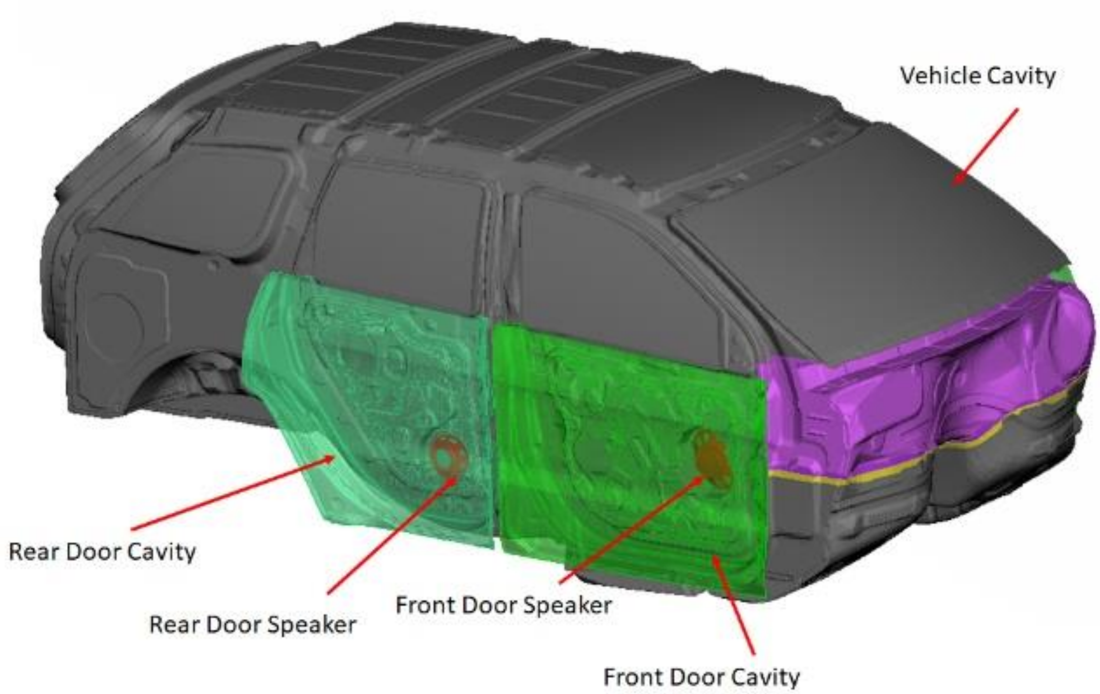


*Figure 8.2* Vehicle speaker integration with vehicle's cavities

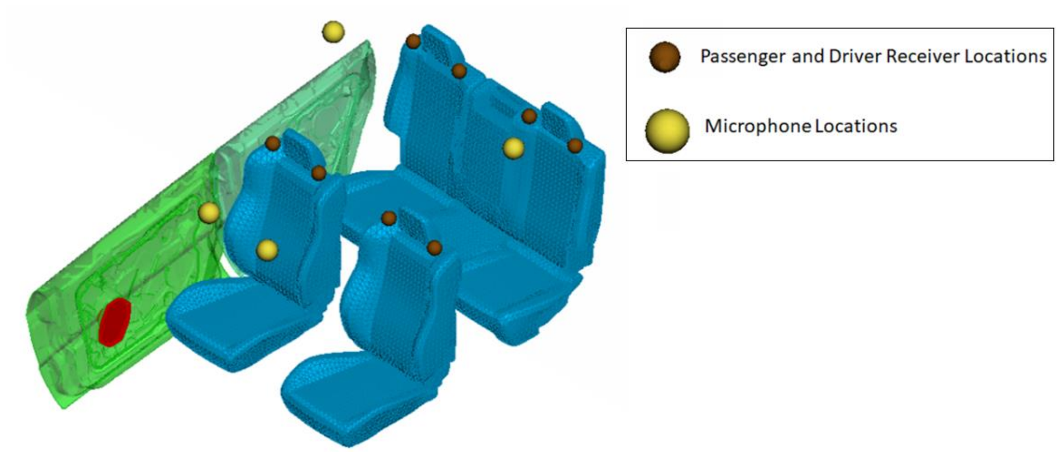


*Figure 8.3* Microphones and passenger and driver receiver locations

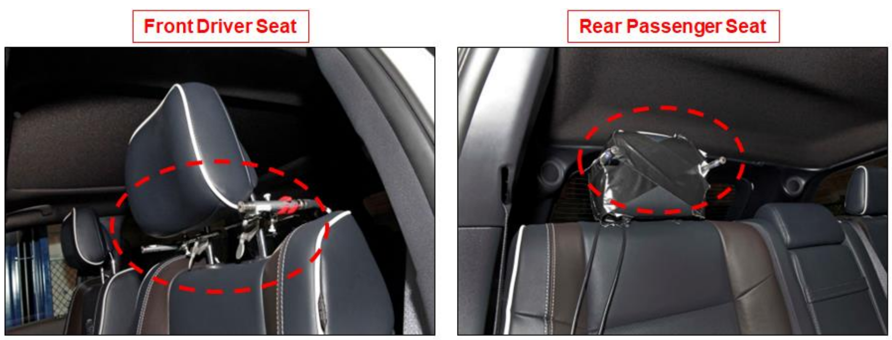


*Figure 8.4* Passenger and driver receiver locations experimental test setup

The calculation based on a FE model of the transfer paths from the speaker to microphones and receiver locations exhibit very good agreement with experimental results. Figure 8.5 shows the transfer path from the left side front door speaker to the driver right ear and the rear right microphone. This study involves four speakers and twelve response points for a total of 48 calculated transfer paths. The transfer paths establish the relationship between the electrical input and the SPL at the acoustic response point.

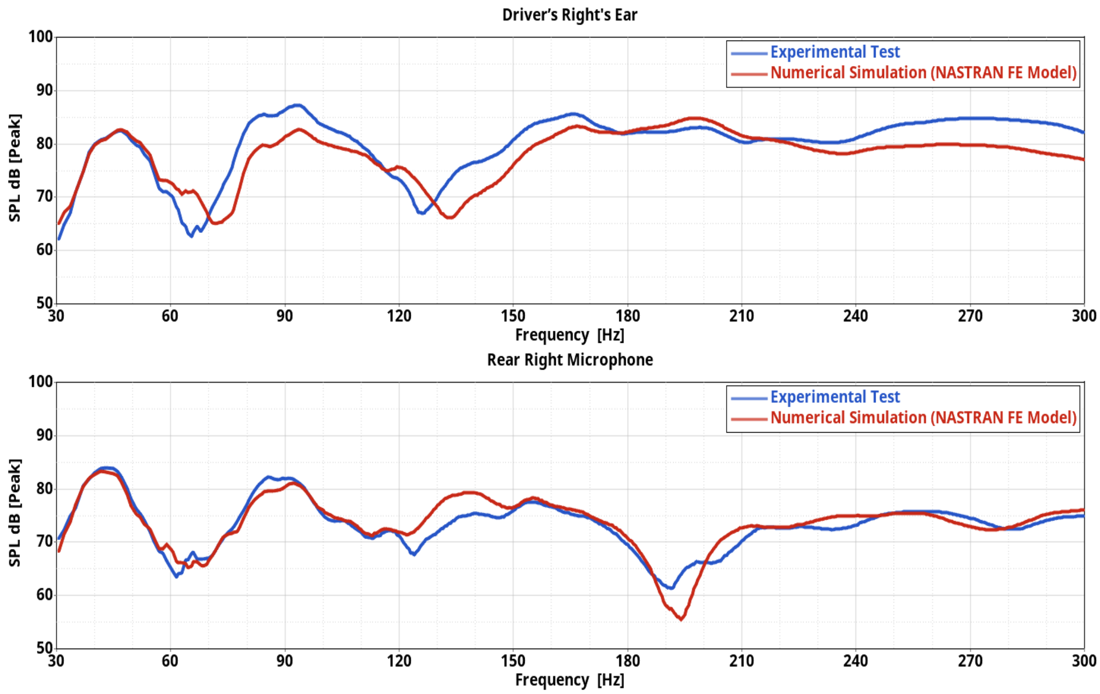


*Figure 8.5* Sample response points correlation for front left speaker TP

## 8.2 An Audio Management Controller Example

To demonstrate the use of an ANC controller in a full vehicle vibro-acoustic FE model, we examine a simplified road noise problem. Road noise analysis has been a focal point of research for several decades. The road profile excites the tire and wheel assembly, transmitting energy to the suspension system, which is then transferred to the body structure, resulting in road noise in the vehicle cabin. Road noise presents numerous challenges, including the random nature of the road profile and the non-linearity in the tire and suspension system, among others. Extensive efforts have been dedicated to modeling various vehicle aspects to establish a well-correlated methodology for road noise. Figure 8.6. illustrates the correlation between experimental results and our developed analytical approach for the vehicle throughout this study. Road noise modeling falls outside the scope of this work and is utilized only as a noise source to showcase ANC performance prediction.

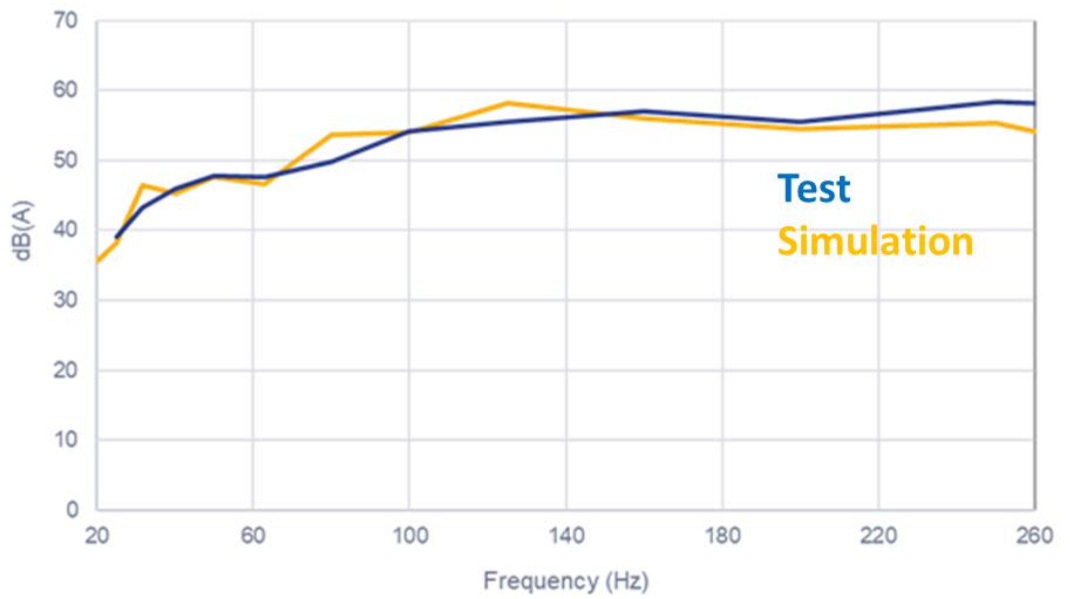


*Figure 8.6* Road noise correlation in 1/3 octave between experiment and simulation

Figure 8.7 shows the SPL of vehicle ANC microphones, and driver ear locations. In Road Noise Cancellation (RNC) systems, accelerometers are strategically placed on the vehicle's body to capture the dominant (anti-node locations) road induced vibrations. These accelerometers detect the vibrations induced by road irregularities and provide valuable insights into the specific noise patterns generated during different driving conditions. After the RNC controller receives this information, the data is seamlessly integrated with the signals from microphones, enabling the RNC system to better understand the nature and intensity of road noise experienced in the cabin.

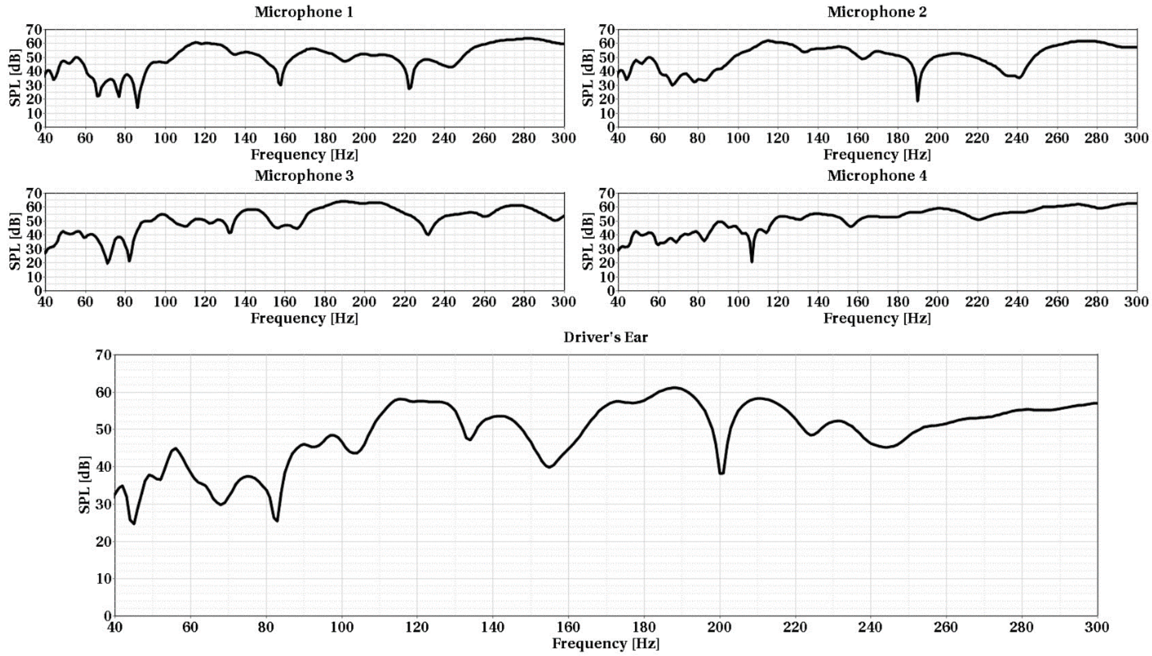


*Figure 8.7* Road noise SPL at ANC microphones and driver's ear

The integration of accelerometers enables RNC systems to dynamically adjust their noise cancelation algorithms in real-time. This dynamic adaptation allows the system to respond swiftly to changes in driving conditions such as variations in road surface texture or driving speed. By continuously analyzing the accelerometer data alongside the microphone data, the RNC system can precisely tailor its noise cancellation strategies to effectively counteract the detected road noise, resulting in a quieter cabin for vehicle occupants.

In this Chapter, we investigate the potential of coupling the speaker anti-noise with road noise to reduce the effect of road noise in the vehicle cabin. Currently, a full RNC model from an audio management supplier is not yet available. Therefore, to illustrate the basic coupling between a speaker anti-noise signal and a full vehicle vibro-acoustic model, we consider a basic ANC optimization problem, as shown schematically in Figure 8.8. For this basic ANC example, we utilize the full vehicle model developed throughout this research, comprising four speakers and four microphones. The front door speakers are 6x9 inches, while the rear door speakers are of the 6.5-inch type (see Table 6.1). The microphone responses to the road excitation are shown in Figure 8.7.

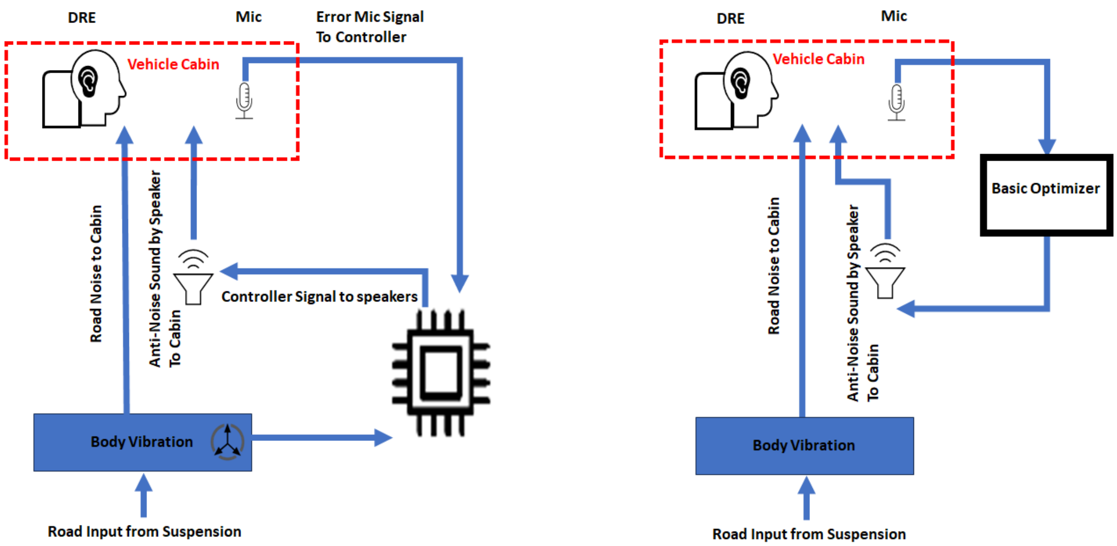


*Figure 8.8* Simplified RNC system (left) and basic ANC optimization problem (right)

The ANC performance is optimized by solving for each Speaker Power Input (SPI), as illustrated in Equation (8.1), using a power input specified in terms of voltage. The power limit (PL), representing the maximum allowed voltage for the speaker input, serves as a constraint. The Sound Pressure from Road Noise (SPRN) is provided by a road noise simulation. Transfer paths (TP) are calculated for each speaker to microphone locations. The Resulting Sound Pressure (RSP) after adding the anti-noise to the excitation road noise in the vehicle cabin is then determined. The optimization problem is stated as

$$Minimize\ \mathrm{RSP} = [\mathrm{SPRN}] + [\mathrm{TP}] \times [\mathrm{SPI}] \tag{8.1}$$

$$subject\ to\ \ 0 \leq [\mathrm{SPI}] \leq [\mathrm{PL}]$$

The design variables comprise the Speaker Power Input (SPI) for each speaker. The resulting sound pressure RSP is a 4x1 matrix that can be expressed as

$$\begin{bmatrix} RSP_{Mic1} \\ RSP_{Mic2} \\ RSP_{Mic3} \\ RSP_{Mic2} \end{bmatrix} = \begin{bmatrix} SPRN_{Mic1} \\ SPRN_{Mic2} \\ SPRN_{Mic3} \\ SPRN_{Mic4} \end{bmatrix} + \begin{bmatrix} TP_{S1\ to\ Mic1} TP_{S2\ to\ Mic1} TP_{S3\ to\ Mic1} TP_{S4\ to\ Mic1} \\ TP_{S1\ to\ Mic2} TP_{S2\ to\ Mic2} TP_{S3\ to\ Mic2} TP_{S4\ to\ Mic2} \\ TP_{S1\ to\ Mic3} TP_{S2\ to\ Mic3} TP_{S3\ to\ Mic3} TP_{S4\ to\ Mic3} \\ TP_{S1\ to\ Mic4} TP_{S2\ to\ Mic4} TP_{S3\ to\ Mic4} TP_{S4\ to\ Mic4} \end{bmatrix} \times \begin{bmatrix} SPI_{S1} \\ SPI_{S2} \\ SPI_{S3} \\ SPI_{S4} \end{bmatrix}$$

where $TP_{S\ x\ to\ Mic\ y}$ is the transfer path of speaker “x” to microphone “y”, all the terms in this equation are complex numbers since both magnitude and phase information are needed. The optimization objective reduces the resulting sound pressure at each microphone. The optimization problem of Equation (8.1) was solved using a gradient-based optimizer and the optimal SPI’s were then applied to the speakers. The optimal ANC performance is shown in Figure 8.9. It should be noted that during the simulation, the speakers generate sound (anti-noise) simultaneously with the road noise input in the vehicle cabin.

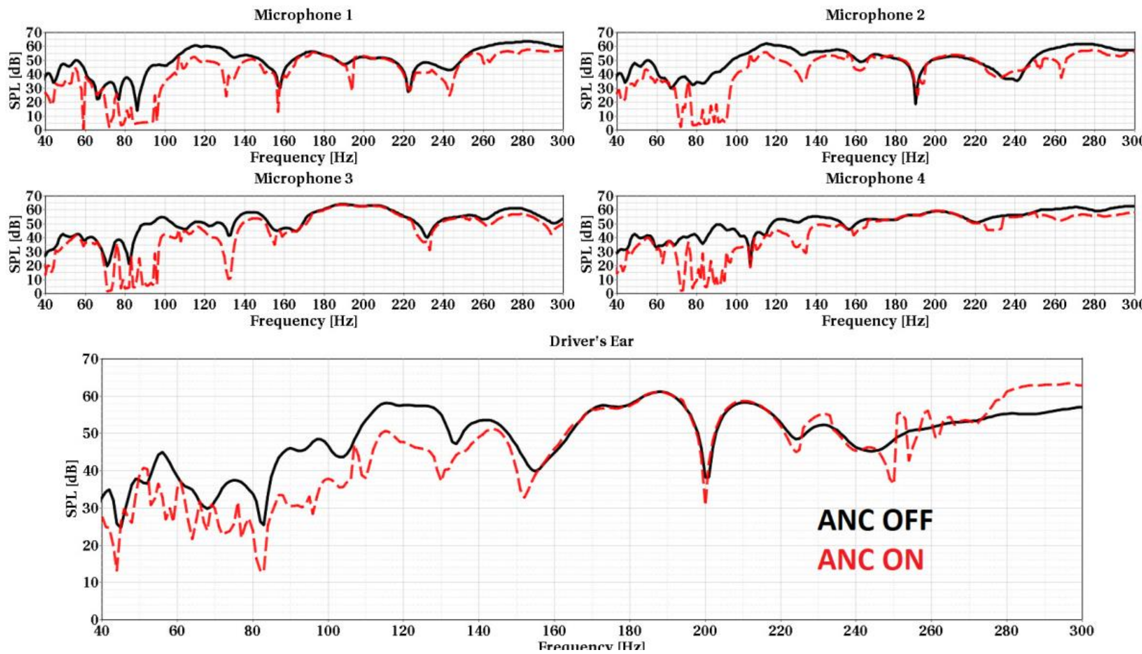


*Figure 8.9* SPL at ANC microphones and driver's ear

In the optimization, weights could be assigned to noise attenuation from each microphone. In our example, equal weights were allocated for sound reduction across all microphones. Note that the front microphone locations are significantly distant from the driver's ear location. Consequently, there is a notable variance in sound reduction between the two front microphones and the driver's ear.

The methodology of this Chapter provides an approach for microphone placement. Proper assignment of weights among all speakers can also be used to improve the ANC performance.

## 8.3 Summary

This Chapter demonstrated the significance of transfer path calculation in the building a predictive ANC model. The transfer paths were computed using the developed comprehensive vibroacoustic FE model, which was validated with experimental data. The Chapter also presented a road noise example demonstrating the effectiveness of the developed ANC system. This study used a basic ANC controller coupled with a full vehicle FE model, enabling real-time prediction of ANC performance.

# CHAPTER NINE

# CONTRIBUTIONS AND FUTURE WORK

## 9.1 Dissertation Contributions

The main contribution of this research is the advancement of the state-of-the-art in predicting and optimizing the performance of an Active Noise Cancellation (ANC) system in vehicles. The developed approach considers the structural and acoustic aspects of ANC systems, diverging from the traditional focus on electronic components and control algorithms. It also enables a virtual prediction of ANC performance using a full vibro-acoustic vehicle model. Additionally, the integration of noise management supplier control systems with predictive ANC models was explored, further enhancing the predictive capabilities of the developed ANC design methodology.

Below are specific contributions:

- Validation and evaluation of a full TBIW vehicle FE model. Chapter 4 provided a comprehensive review of the Full Trim Body in White (TBIW) vehicle FE Model, assessing its suitability for integration into predictive ANC models. Correlation with physical testing demonstrated the accuracy of the developed FE model, and its reliability in capturing the vehicle structural vibration behavior.
- Fundamental analysis of vehicle cavity acoustics. Chapter 5 provided the fundamentals of a vehicle cavity acoustic analysis. Using one-dimensional and three-dimensional closed cavity models, the study validated the efficacy of the developed methodology through correlation with physical testing and FE analysis. Also, the importance of acoustic mode shapes and cavity excitation characteristics in

influencing the system response was emphasized, providing valuable insights for predictive ANC modeling.

- Speaker modeling and representation. Chapter 6 focused on the development and validation of speaker models which are critical for accurate ANC system simulations. Using detailed FE modeling, closed-form solutions and experimental verification, the study demonstrated acoustic models for various speaker and acoustic source configurations, including a monopole, a dipole, a baffled moving cone and a non-baffled moving cone. The optimal representation of loudspeakers, particularly the non-baffled moving cone model, was demonstrated using correlation with physical tests, highlighting the robustness and applicability of the developed speaker models.
- Assessment of loudspeaker mounting stiffness. Chapter 7 demonstrated the critical importance of assessing the loudspeaker mounting stiffness in ANC applications to enhance audio performance. A novel method was proposed to evaluate the door stiffness and quantify the speaker distortion caused by the door compliance. This allows us to optimize ANC performance for realistic vehicle applications.
- Significance of transfer path calculation and predictive ANC modeling. Chapter 8 demonstrated the significance of transfer path calculation in building a predictive ANC model. A road noise example demonstrated the effectiveness of integrating an ANC controller with a full vehicle FE model, enabling real-time prediction and optimization of ANC performance.

The above contributions significantly advance the understanding and prediction of ANC system performance in vehicles, offering valuable insights for predicting ANC performance virtually.

## 9.2 Future Work

- Integrate the developed ANC predictive model with a detailed ANC controller from an audio management supplier to reduce tire noise.
- Develop an ANC predictive model in the time domain to allow its coupling with advanced controllers in the time domain.
- Work with audio management suppliers to enhance and optimize ANC controllers virtually using the developed ANC predictive tool.
- Employ the developed ANC predictive tool to optimize the number and location of speakers, microphones, and accelerometers in a vehicle for a specific noise cancelation strategy.

REFERENCES


[1] N. Zafeiropoulos, J. Zollner and V. Kand, "State-of-the-art Digital Road Noise Cancellation by Harman," in *Automotive Acoustics Conference*, W. Siebenpfeiffer, 2017.

[2] F. Valeri and C. Stirlen, "Practical Uses for Road Noise Cancellation," in *SAE Noise and Vibration Conference & Exhibition - SAE Tecnical Paper: 2021-01-1018*, 2021.

[3] S. Sapuan, M. Osman and Y. Nukman, "State of the Art of the Concurrent Engineering Technique in the Automotive Industry," *Journal of Engineering Design*, vol. 17, no. 2, p. 143–157, 2006.

[4] A. Abbas, W. Elwali, S. Haider, S. Dsouza, M. Sanderson and Y. Segan, "CAE Cooling Module Noise and Vibration Prediction Methodology and Challenges," in *SAE Technical Paper 2020-01-1262*, 2020.

[5] S. Elliott, "A Review of Active Noise and Vibration Control in Road Vehicles," ISVR Technical Memorandum, Southampton, UK, 2008.

[6] W. Rączka and M. Sibielak, Active Noise and Vibration Control, Pfaffikon, Switzerland: Trans Tech Publications Ltd, 2016.

[7] T. Kletschkowski, Adaptive Feed-forward Control of Low Frequency Interior Noise, New York: Springer, 2012.

[8] L. Rayleigh, Theory of Sound V II, Witham: Macmillan, 1896.

[9] P. Lueg, "Process of Silencing Sound Oscillations". United States Patent 2043416, 8 March 1934.

[10] H. Olson and E. May, in *Electronic Sound Absorber*, J. Acoust. Soc. Am, 1953, p. 1130–1136.

[11] H. Olson, "Electronic Sound Absorber". United States Patent US2983790A, 09 May 1961.

[12] L. Beranek, Noise and Vibration Control Engineering Principles and Applications, John Wiley, 1992.

[13] D. Guicking, "Active Control of Sound and Vibration History, Fundamentals, and State of the Art," in *Oscillations, Waves, and Interactions - Sixty Years Drittes Physikalisches Institut*, University Press- Physikalisches Institut, 2007, pp. 107-138.

[14] S. Kuo and D. Morgan, "Active Noise Control: A Tutorial Review," *Proceedings of the IEEE*, vol. 87, no. 6, pp. 943-973, 1999.

[15] J. Bean, "Design and Analysis of an Active Noise Canceling Headrest," Virginia Tech Electronic Theses and Dissertations, Blacksburg, Virginia, 2018.

[16] J. Lefèvre and U. Gabbert, "Finite Element Modelling of Vibro-Acoustic Systems for Active Noise Reduction," *Technische Mechanik*, vol. 25, no. 3, pp. 241-247, 2005.

[17] H. Auweraer, P. Mas, P. Segaert, L. Oliveira, M. da Silva and W. Desme, "CAE-based Design of Active Noise Control Solutions," in *SAE Technical Paper 2007-26-032*, 2007.

[18] D. Xiu and D. Tartakovsky, "Numerical Methods for Differential Equations in Random Domains," *SIAM Journal on Scientific Computing*, vol. 28, no. 3, pp. 1167-1185, 2006.

[19] C. Canuto and T. Kozubek, "A fictitious domain approach to the numerical solution of PDEs in stochastic domains," *Programs and Algorithms of Numerical Mathematics,* vol. 107, no. 2, pp. 46-52, 2006.

[20] L. Parussini and V. Pediroda, "Investigation of multi geometric uncertainties by different polynomial chaos methodologies using a fictitious domain solver," *Computer Modeling in Engineering & Sciences,* vol. 23, no. 1, pp. 29-52, 2008.

[21] A. Nouy, M. Chevreuil and E. Safatly, "Fictitious domain method and separated representations for the solution of boundary value problems on uncertain parameterized domains," *Computer Methods in Applied Mechanics and Engineering,* vol. 200, no. 45-46, pp. 3066-3082., 2011.

[22] A. Nouy, A. Clément, F. Schoefs and N. Moës, "An extended stochastic finite element method for solving stochastic partial differential on random domains," *Computer Methods in Applied Mechanics and Engineering,* vol. 197, no. 51-52, pp. 4663-4682, 2008.

[23] R. Small, "Direct-radiator Loudspeaker System Analysis," *IEEE Trans. Audio and Electroacoustics,* vol. 19, no. 4, p. 269, 1971.

[24] A. Thiele, "Loudspeakers in vented boxes," *Journal of the Audio Engineering Society*, vol. 19, no. 6, p. 382, 1971.

[25] C. Jackman, M. Zampino, D. Cadge, R. Dravida, V. Katiyar and J. Lewis, "Estimating Acoustic Performance of a Cell Phone Speaker Using Abaqus," *SIMULIA Customer Conference,* pp. 14-21, 2009.

[26] Y. Kagawa, T. Yamabuchi, K. Sugihara and T. Shindou, "A finite Element Approach to a Coupled Structural-acoustic Radiation System with Application to Loudspeaker Characteristic Calculation," *Journal of Sound and Vibration*, vol. 69, no. 3, pp. 229-243, 1980.

[27] T. Tsuchiya, Y. Kagawa, M. Doi and T. Tsuji, "Finite Element Simulation of Non-linear Acoustic Generation in a Horn Loudspeaker," *Journal of Sound and Vibration,* vol. 266, no. 5, pp. 993-1008, 2003.

[28] P. Larsen, "Geometrical Stiffness of Loudspeaker Cones A Fine Cone FEM Study," in *ALMA World Cone Symposium*, 2003.

[29] S. Morita, N. Kyono, S. Sakai, T. Yamabuchi and Y. Kagawa, "Acoustic Radiation of a Horn Loudspeaker by the Finite Element Method - A Consideration of the Acoustic Characteristic of Horns," *Journal of the Audio Engineering Society*, vol. 28, no. 7/8, pp. 482-489, 1980.

[30] C. Beltran and J. Spence, "High-Accuracy Wide-Bandwidth Automated Loudspeaker Modeling Using Finite-Element Analysis," *Journal of the Audio Engineering Society,* vol. 1, no. 1, p. 5220, 2000.

[31] M. Rausch, R. Lerch, M. Kaltenbacher, H. Landes, G. Krump and L. Kreitmeier, "Optimization of Electrodynamic Loudspeaker Design Parameters by Using a Numerical Calculation Scheme," *Acta Acustica united with Acustica,* vol. 85, no. 3, pp. 412-419, 1999.

[32] K. Minami and Y. Kajikawa, "A Study on Frequency Response Analysis of Micro-speaker Using Equivalent Circuit and Finite Element Method," in *IEEE 9th Global Conference on Consumer Electronics (GCCE)*, 2020.

[33] K. Jung Ho, K. Jim Tai, K. Jin O and M. Jin Ki, "Acoustic Characteristics of a Loudspeaker Obtained by Vibration and Acoustic Analysis," *Transactions of the Korean Society of Mechanical Engineers,* vol. 21, no. 10, pp. 1742-1756, 1997.

[34] M. Jones, L. Binks and D. Henwood, "Finite Element Methods Applied to the Analysis of High-fidelity Loudspeaker Transducers," *Computers & Structures,* vol. 44, no. 4, pp. 765-772, 1992.

[35] N. Driot, X. Robin, G. Thi and L. Anslinger, "Active Noise Cancellation in a Passenger Car Exhaust System with Finite Elements," in *SIA Automotive NVH Comfort*, 2016.

[36] T. Costes, E. Gaudry, B. De Brye and R. Baudson, "A novel GPU Accelerated Numerical Process for Automotive Loudspeaker Design and Integration Studies," in *SIA NVH Conference,* 2021.

[37] K. Takada and A. Matsuda, "On the Vibrational Analysis of Dome-Type Loudspeakers by the Finite Element Method," *Journal of the Audio Engineering Society - Paper Number: 1346,* 1978.

[38] G. Pellerin, J. Polack and J. Morkerken, "Finite Element Methods and Equivalent Electrical Models for Loudspeaker Characterization," *Journal of the Audio Engineering Society- Paper Number: 5743,* 2003.

[39] M. Hedges and Y. Lam, "Accuracy of Fully Coupled Loudspeaker Simulation Using COMSOL," in *In Proceedings of the COMSOL Conference.,* 2009.

[40] G. Moretti, G. Rizzello, M. Fontana and S. Seelecke, "Finite Element Modelling of the Vibro-acoustic Response in Dielectric Elastomer Membranes," *Electroactive Polymer Actuators and Devices (EAPAD) XXIV,* vol. 12042, no. SPIE, pp. 102-112, 2022.

[41] Y. Hu, "Effects of the Cone and Edge on the Acoustic Characteristics of a Cone Loudspeaker," *Advances in Acoustics and Vibration,* p. 12, 2017.

[42] Y. Shiozawa, R. D'Amico, H. Onitsuka and W. Desmet, "A Multi-physical Loudspeaker Model Including Experimental Modal Information of the Membrane," *Proceedings of ISMA2014 Including US.,* pp. 4317 - 4328, 2014.

[43] E. Segovia, J. Carbaj, A. Espí and J. Ramis, "Numerical Analysis of the Vibrational Behavior of the Moving Assembly of a Dynamic Loudspeaker," *International Journal of Numerical Methods for Calculation and Design in Engineering,* vol. 31, no. 3, pp. 154-160, 2015.

[44] T. Shindo, O. Yashima and H. Suzuki, "Effect of Voice-Coil and Surround on Vibration and Sound Pressure Response of Loudspeaker Cones," *Journal of the Audio Engineering Society,* vol. 28, no. 7/8, pp. 490-499, 1980.

[45] I. A. Aldoshina, A. Voishvillo and V. Mazin, "Modeling of Flux Modulation Distortion in Moving-Coil Loudspeakers by the Finite-Element Method," in *In Audio Engineering Society Convention 9*, 1995.

[46] A. Kaizer and A. Leeuwestein, "Calculation of the Sound Radiation of a Nonrigid Loudspeaker Diaphragm Using the Finite-Element Method," *Journal of the Audio Engineering Society,* vol. 36, no. 7/8, pp. 539-551, 1988.

[47] N. Kyouno, S. Sakai, S. Morita, T. Yamabuchi and Y. Kagawa, "Acoustic Radiation of a Horn Loudspeaker by the Finite Element Method-Acoustic Characteristics of a Horn Loudspeaker with an Elastic Diaphragm," *Journal of the Audio Engineering Society,* vol. 30, no. 12, pp. 896-905, 1982.

[48] O. Yashima, H. Suzuki and T. Shindo, "Applications of the Finite Element Method to the Vibration of a Loudspeaker Diaphragm," *The Journal of the Acoustical Society of America,* vol. 1, no. 1, pp. 80-85, 1978.

[49] M. Bai, C. Liu and R. Chen, "Optimization of Microspeaker Diaphragm Pattern Using Combined Finite Element–Lumped Parameter Models," *IEEE Transactions on Magnetics,* vol. 44, no. 8, pp. 2049 - 2057, 2008.

[50] D. Russell, J. Titlow and Y. Bemmen, "Acoustic Monopoles, Dipoles, and Quadrupoles: An Experiment Revisited," *American Journal of Physics,* vol. 67, no. 1, pp. 660-664, 1999.

[51] P. Argenta, F. Martellotta and L. Soria, "Theoretical and Experimental Study of an Acoustic Monopole Source," in *Audio Engineering Society Convention 144 Audio Engineering Society*, 2018.

[52] J. Vanderkooy, "The Acoustic Center: A New Concept for Loudspeakers at Low Frequencies," Journal of the Audio Engineering Society, Paper Number: 6912, 2006.

[53] M. Petyt and P. Gélat, "Vibration of Loudspeaker Cones Using the Dynamic Stiffness Method," *Applied Acoustics,* vol. 53, no. 4, pp. 313-332, 1998.

[54] F. Jacobsen, T. Poulsen, J. Rindel, A. Gade and M. Ohlrich, "Sound Radiation from a Circular Piston in an Infinite Baffle," in *Fundamentals of Acoustics and Noise Control*, Department of Electrical Engineering, Technical University of Denmark, 2011, pp. 42-47.

[55] D. Keele, "Low-frequency Loudspeaker Assessment by Nearfield Sound-pressure Measurement," *Journal of the Audio Engineering Society*, vol. 22, no. 3, pp. 154-162, 1974.

[56] R. Bücker, "Integration and Lightweight Design in Automotive Doors," in *SAE Symposium on International Automotive Technology - Paper # 2015-26-0242*, 2015.

[57] H. Hyun Na, H. Park, H. Lee and B. Choi, "A Study on the Rattle Index From a Vehicle Door Trim Under Audio System Inputs," SAE Technical Paper: 2013-01-1914, 2013.

[58] N. Narayana, "A Finite Element Method for Effective Reduction of Speaker-Borne Squeak and Rattle Noise in Automotive Doors," in *SAE Noise and Vibration Conference and Exhibition- Paper # 2011-01-1583*, 2011.

[59] D. Lennström, "In-Situ Characterization of Vibrations from a Door Mounted Loudspeaker," in *SAE 10th International Styrian Noise, Vibration & Harshness Congress: The European Automotive Noise Conference Paper # 2018-01-1511*, 2018.

[60] S. Temme, "Enhanced Perceptual Rub & Buzz Measurement for Testing Automotive Loudspeakers," in *AES International Conference on Automotive Audio - Paper # 7*, 2022.

[61] D. Cinanni and C. Sancisi, "Anti-Rattle System Loudspeaker Device," *Journal of the Audio Engineering Society*, vol. 144, no. 1, p. 9915, 2018.

[62] V. Cook and A. Ali, "Spherical Beamforming and Buzz, Squeak and Rattle (BSR) Testing," in *SAE Braking Systems and NVH Considerations - Paper # 2009-01-2114*, 2009.

[63] K. Kim, C. Kim and J. Kim, "A Study on the Optimization of Body Structure for Rattle Noise by Exciting Woofer Speakers," in *SAE Noise and Vibration Conference and Exhibition - Paper # 2009-01-2110*, 2009.

[64] J. Weber and I. Benhayoun, "Squeak & Rattle Simulation - A Success Enabler in the Development of the New Saab 9-5 Cockpit without Prototype Hardware," in *6th International Styrian Noise, Vibration & Harshness Congress - Sustainable NVH solutions inspired by ecology and economy - Paper # 2010-01-1423*, 2010.

[65] L. Gagliardini, A. CLOIX, P. Chartrain and O. Ponte-Felgueras, "Trimmed Door Audio Response Hybrid Modeling Assessment," in *SAE 10th International Styrian*

*Noise, Vibration & Harshness Congress: The European Automotive Noise Conference - Paper # 2018-01-1508*, 2018.

[66] L. Gagliardini, R. Leneveu, A. Cloix and A. Durr, "Door Audio Response Hybrid Modeling and Assesment," SAE Technical Paper: 2017-01-1849, 2017.

[67] L. Gagliardini, A. CLOIX, P. Chartrain and O. Ponte-Felgueras, "Trimmed Door Audio Response Hybrid Modeling Assessment," SAE Technical Paper: 2018-01-1508, 2018.

[68] S. Paik, M. De Geest and K. Vansant, "Interior Acoustic Simulation for In-car Audio Design," *Journal of Sound & Vibration*, vol. 47, no. 1, pp. 10-17, 2013.

[69] T. Reaburn and T. Skszek, "Ultra-Light Weight Automotive Door: Design and Validation," in *WCX World Congress Experience - Paper # 2018-01-0111*, 2018.

[70] Y. Tay, C. Lim and H. Lankarani, "A Finite Element Analysis of High-energy Absorption Cellular Materials in Enhancing Passive Safety of Road Vehicles in Side-impact Accidents," *International Journal of Crashworthiness,* vol. 19, no. 3, pp. 288-300, 2014.

[71] S. Roth, J. Oudry, M. El-Rich and H. Shakourzadeh, "Influence of Mesh Density on a Finite Element Model's Response Under Dynamic Loading," *Journal of Biological Physics and Chemistry,* vol. 9, no. 4, pp. 210-219, 2009.

[72] S. Rao, Mechanical Vibrations – 5th Edition, Prentice Hall, 2011.

[73] J. Woodhouse, "Linear Damping Models for Structural- Vibration," *Journal of Sound and Vibration*, vol. 215, no. 3, pp. 547-569, 1998.

[74] A. Nilsson and B. Liu, Vibro-Acoustics, Volume 1 Second Edition, London: Springer Heidelberg New York Dordrecht London, 2012.

[75] L. Kinsler, A. Frey, A. Coppens and J. Sanders, Fundamentals of Acoustics, 4th ED, John Wiley & Sons, Limited, 2002.

[76] MSC.Software, MSC Nastran Quick Reference Guide, Newport Beach, CA: MSC Software, 2013.

[77] Siemens, *Simcenter Qsources Picture,* https://www.qsources.be/simcenter-qsources/q-med/, 2014.

[78] B. Peeters, M. El-kafafy, G. Accardo, T. Knechten, K. Janssens, J. Lau and L. Gielen, "Automotive Cabin Characterization By Acoustic Modal Analysis," in *Proceedings of the JSAE Annual Congress*, 2014.

[79] G. Accardo, M. El-Kafafy, B. Peeters, F. Bianciardi, D. Brandolisio, K. Janssens and M. & Martarelli, "Experimental Techniques, Rotating Machinery, and Acoustics, Volume 8: Experimental Acoustic Modal Analysis Of An Automotive Cabin," in *Proceedings of the 33rd IMAC, A Conference and Exposition on Structural Dynamics*, 2015.

[80] H. Lin, T. Bengisu and Z. Mourelatos, Lecture Notes on Acoustics and Noise Control, Springer, 2021.

[81] J. Eargle, "Details Of the Magnatic Circuit," in *Loudspeaker Handbook*, Springer, 2003, pp. 55-59.

[82] G. Jin, T. Ye and Z. Su, Structural Vibration, Springer Heidelberg New York Dordrecht London, 2015.

[83] J. Blauert and N. Xiang, Acoustics for Engineers, Springer-Verlag Berlin Heidelberg, 2008.

[84] I. Kido, A. Nakamura, T. Hayashi and M. and Asai, "Suspension Vibration Analysis for Road Noise Using Finite Element Model," *Proceedings of the 1999 Noise and Vibration Conference*, vol. 1, no. 1, p. 342, 1999.

[85] M. Brinkmeier, U. Nackenhorst, S. Petersen and E. Otto von, "A finite element approach for the simulation of tire rolling noise," *Journal of sound and vibration,* vol. 309, no. 1-2, pp. 20-39, 2008.

[86] L. Sangiuliano, R. Boukadia, E. Deckers, W. Desmet and C. Claeys, *Reduction of Structure-Borne Tyre/Road Noise through Rubber Resonant Metamaterials in Tyres,* 12th International Styrian Noise, Vibration & Harshness Congress: The European Automotive Noise Conference: SAE Technical Paper 2022-01-0954, 2002.

[87] A. Guellec, J. J. Marie Cabrol and B. V. d. Nieuwenhof, *Optimization of Trim Component and Reduction of the Road Noise Transmission Based on Finite Element Methods,* 10th International Styrian Noise, Vibration & Harshness Congress: The European Automotive Noise Conference: SAE Technical Paper 2018-01-1547, 2018.

[88] Chulwoo Jung and L. Nam Young, "Analyzing Effects of Upperbody on Road Noise of Platform-Sharing Vehicles," *SAE International Journal of Vehicle Dynamics, Stability, and NVH*, vol. 130, no. 1, p. 10EJ, 2021.

# RELATED PUBLICATIONS

Journal Papers

- Abbas, A., Mourelatos, Z.P. Elwali, W. and Latcha M., "Acoustic Speaker Finite-element Modeling for Vehicle Active Noise Cancelation," in preparation, *Journal of Sound and Vibration*, 2024.
- Abbas, A., Mourelatos, Z.P., " Loudspeaker Mounting Stiffness Design for ANC Application," in preparation, *Computers and Structures*, 2024.
- Abbas, A., Mourelatos, Z.P. and Haider, S., "Vehicle Vibro-acoustics Finite-element Modeling for Active Noise Cancelation Prediction and Design," in preparation, *Computers and Structures*, 2024.